Optimization of Phosphorus Removal and Mineral Characterization in Aerated Anaerobic Digestate with Divalent Cation Addition

Caitlyn Ann Harris

Thesis submitted to the faculty of the Virginia Polytechnic Institute and State University in partial fulfillment of the requirements for the degree of

Master of Science
In
Environmental Engineering

Amy J. Pruden
William R. Knocke
Christopher A. Wilson

December 18, 2024
Blacksburg, VA

Keywords:
Phosphorus, Struvite Precipitation, Nutrient Recovery, Biosolids, Modeling

Optimization of Phosphorus Removal and Mineral Characterization in Aerated Anaerobic Digestate with Divalent Cation Addition

Caitlyn Harris

Academic Abstract

Struvite and other minerals often form at WRRFs when phosphorus-rich activated sludge from EBPR processes undergo anaerobic digestion. Without proper control, these minerals can cause scale deposits that clog pipes and damage dewatering equipment. However, managing when and where these minerals form allows for phosphorus recovery as a sustainable fertilizer or its sequestration into Class A biosolids, creating a nutrient-rich soil product. This approach can reduce phosphorus recycling in solids handling, prevent scaling issues, and enhance the value of biosolids as a marketable, sustainable product. In a digested solids storage tank that is in between anaerobic digestion and final dewatering, precipitation was removed in a controlled pilot setup by manipulating variables such as mixing, aeration to achieve a low solids retention time (SRT) post aerobic digestion (PAD) and by chemical addition. Optimizing this via pilot testing can reduce struvite buildup, enhance phosphorus removal, and provide additional benefits such as nitrogen and COD removal. The pilot setup at Hampton Roads Sanitation District's Atlantic Treatment Plant (ATP) consisted of four 45-gallon tanks operated as daily batch fed continuously stirred tank reactors with a 3-day SRT. Aeration and chemical addition of $Mg(OH)_2$ and $Ca(OH)_2$ at varying Ca^{2+}+Mg^{2+}:P ratios were tested under different aeration settings of constant, pH or dissolved oxygen (DO) setpoints. Results showed that DO setpoint-controlled aeration stabilized pH and DO and enhanced OP-P and NH_3-N removal, with maximum OP-P removal of 97 percent achieved at a Ca^{2+}+Mg^{2+}:P ratio of 1.3:1. NH_3-N removal, mainly from struvite precipitation, averaged 10–20 percent, with no nitrification observed likely due to free ammonia inhibition. Alkalinity reduction exceeded predicted levels, suggesting additional coprecipitation reactions occurred. Aeration and mixing consistently achieved about 20 percent total COD removal across the pilot in microaerobic conditions. The chemical equilibrium model Visual MINTEQ was also explored to determine the effects of pH, temperature, chemical choice and dose on minerology. A validated model could then be used to predict scaling potential and characterize minerals formed at WRRFs to better treat these nuisance scaling minerals and determine their potential for harvesting or sequestration as a nutrient-rich product. With the increasing need to not only remove but recover nutrients for beneficial reuse, it is imperative to deepen the understanding of successful phosphorus precipitation in biosolids and how it can be optimized and modified for various solids handling configurations.

Optimization of Phosphorus Removal and Mineral Characterization in Aerated Anaerobic Digestate with Divalent Cation Addition

Caitlyn Harris

General Abstract

Nutrient removal, particularly phosphorus (P) and nitrogen (N), is essential in wastewater treatment to prevent eutrophication and its harmful impacts on aquatic ecosystems and water quality. Phosphorus, while a pollutant in excess, is also a critical and non-renewable resource essential for food and fertilizer production, with limited global supplies and rising demand. A common phosphorus recovery source the industry has turned to are Water Resource Recovery Facilities (WRRFs), which process billions of gallons of wastewater daily. Enhanced Biological Phosphorus Removal (EBPR) is a process that takes advantage of microorganisms in wastewater to divert phosphorus from the liquid to the solids stream. In solids handling, this excess phosphorus can be recovered in the form of phosphorus minerals, most notably struvite, and can be utilized as a sustainable biosolid product for beneficial land application. However, struvite, if not properly controlled, can lead to costly maintenance issues by forming scale in piping and dewatering equipment. By optimizing phosphorus recovery and directing where these mineral formations occur, WRRFs can reduce scaling risks, recycle phosphorus, and produce a sustainable fertilizer alternative. A pilot setup at Hampton Roads Sanitation District's Atlantic Treatment Plant (ATP) consisted of four 45-gallon tanks operated as daily batch fed continuously stirred tank reactors with a low solids retention time (SRT). Various aeration settings were tested for pH adjustment and the addition of two chemicals were tested, $Mg(OH)_2$ and $Ca(OH)_2$, at varying Ca^{2+}+Mg^{2+}:P ratios to supplement phosphorus mineral precipitation. Phosphorus precipitation was successful in each trial and a maximum of 97 percent phosphorus removal was achieved, along with additional benefits such as nitrogen and COD removal. A chemical equilibrium model was also explored to predict scaling potential and characterize minerals formed at WRRFs to better treat these nuisance scaling minerals and determine their potential for harvesting or sequestration as a nutrient-rich product. Optimizing this approach at the pilot scale can improve plantwide efficiency at ATP and provide other WRRFs an optimized operational strategy to prevent nuisance scaling while producing a marketable biosolids product, thereby enhancing the sustainability of phosphorus management in wastewater treatment.

Acknowledgements

I would like to thank my advisor Chris Wilson, and the rest of the team of mentors at HRSD, which includes Dana Gonzalez, BJ Ward, Jeff Nicholson, and Holley Anne Matel. I would also like to thank Shubhashini Oza. Thank you for the endless hours on teams calls, answers to all my questions, and random office/lab visits. You all have taught me so much. Thank you for your mentorship and continued support as I enter the next chapter of my career.

I want to give a huge thank you to Arba Willamson and Shelby Creely for your long, hard work on the pilot build out and maintenance with me. I truly could not have done it without your carpentry, electrical, instrumentation, plumbing, fitting, and operator brilliance.
I also want to thank my undergraduate lab assistant, Nathan Bennett.

Finally, I give thanks to all the friends and family I have made throughout my time at VT and the ones that continued to love and support me from home in Texas. I love you all and can't thank you enough.

Dedication

I dedicate this work to my mom, Dawn. You are my guiding light.

Table of Contents

Lists of Tables

Lists of Figures

List of Abbreviations

ACP – Amorphous Calcium Phosphate

AD – Anaerobic Digestion

A/O – Anaerobic/Aerobic

AOB – Ammonia Oxidizing Bacteria

ARE – Aeration Basin Effluent

ATP – Atlantic Treatment Plant

Ca^{2+} – Calcium Ion

$CaCO_3$ – Calcium Carbonate, Calcite

$Ca(OH)_2$ – Calcium Hydroxide

CaP – Calcium Phosphate

COD – Chemical Oxygen Demand

CSTR – Continuously Stirred Tank Reactor

DCP – Dicalcium Phosphate

DCPD – Dicalcium Phosphate Dihydrate

DEQ – Department of Environmental Quality

DF – Dilution Factor

DO – Dissolved Oxygen

DOC (SHM) – Dissolved Organic Carbon (Stockholm Humic Model)

DSST – Digested Solids Storage Tank

EBPR – Enhanced Biological Phosphorus Removal

EDS- Energy Dispersive X-ray Spectrometry

EPA – Environmental Protection Agency

FOG – Fats, Oils, and Grease

GBT – Gravity Belt Thickener

HAP – Hydroxyapatite

HRSD – Hampton Roads Sanitation District

HRT – Hydraulic Retention Time

IAP – Ion Activity Product

K_{sp} – Solubility Product

lb/day – Pounds per Day

LPM – Liters Per Minute

MAP – Magnesium Ammonium Phosphate

Mg – Magnesium

Mg^{2+} – Magnesium Ion

MGD – Million Gallons per Day

mg/L – Milligram per Liter

$Mg(OH)_2$ – Magnesium Hydroxide

N - Nitrogen

NH_3-N – Ammonia as Nitrogen

NH_4^+ – Ammonium Ion

NO_2^- – Nitrite

NO_3 – Nitrate

NOB – Nitrite Oxidizing Bacteria

NPW – Non-Potable Water

OCP – Octacalcium Phosphate

OHOs – Ordinary Heterotrophic Organisms

OP-P – Orthophosphate as Phosphorus

ORP – Oxidative Reduction Potential

PAD – Post Aerobic Digestion

PAOs – Polyphosphate Accumulating Organisms

P – Phosphorus

PO_4^{3-} - Phosphate Ion

RWI – Raw Water Influent

sCOD – Soluble Chemical Oxygen Demand

SEM – Scanning Electron Microscope

SI – Saturation Index

SND – Simultaneous Nitrification and Denitrification

SRF – Struvite Recovery Facility

SRT – Solids Retention Time

TAN – Total Ammonia Nitrogen

TCP – Tricalcium Phosphate

TH-AD – Thermally Hydrolyzed Anaerobic Digestate

THP – Thermal Hydrolysis Process

TP – Total Phosphorus

TS – Total Solids

VA – Volatile Acids

VFA – Volatile fatty Acid

VS – Volatile Solids

VSR – Volatile Solids Reduction

WAS – Waste Activated Sludge

WASSTRIP – Waste Activated Sludge Stripping To Remove Internal Phosphorus

WRRF – Water Resource Recovery Facility

XRD – X-Ray Diffraction

1. Introduction

The removal of nutrients, particularly phosphorus (P) and nitrogen (N), from wastewater has long been essential in treatment processes to prevent excess discharge into freshwater bodies, which can lead to eutrophication. This nutrient buildup causes harmful effects on aquatic ecosystems, including dissolved oxygen (DO) depletion and disruptions in drinking water treatment (Liu et al., 2016). While excess phosphorus is an issue, phosphorus is also an essential nutrient and a valuable non-renewable resource that is becoming increasingly limited by its consumption for global food production, and most commonly, fertilizer production (Wilfert et al., 2015). The global phosphorus demand is increasing every day and is estimated to be exhausted within the next 50-100 years, with the expected global peak in phosphorus production predicted to occur around 2030 (Cordell et al., 2009). These excessive phosphorus uses all point to a need for phosphorus recycling and recovery. A common phosphorus source the industry has turned to is wastewater.

Water Resource Recovery Facilities (WRRFs) nationwide process approximately 34 billion gallons of wastewater per day (EPA, 2023). Total Phosphorus (TP) in WRRFs influent typically range from 5-20 mg/L with effluent TP limits as low as 0.1-1 mg/L. Phosphorus originates from human waste, food wastes, cleaning products and detergents, and anti-corrosion products (Shraddha et al., 2018). Therefore, the advancement of technologies aimed at not only the removal, but the recycling and recovery of phosphate species from waste streams is immensely advantageous in establishing a sustainable phosphorus future.

There are a variety of techniques to remove and recover phosphorus species from wastewater, including chemical treatment, enhanced biological phosphorus removal (EBPR), as well as crystallization and harvesting. A common method of chemical treatment is dosing a metal salt, such as iron or aluminum-based salts, and removing or sorbing phosphorus as a metal coprecipitate in the solids. However, this chemical addition adds to treatment and chemical costs as well as increases the amount of solids produced, which leads to increased hauling and disposal costs. EBPR processes exercise the natural metabolic capabilities of polyphosphate-accumulating organisms (PAOs) in activated sludge to store carbon anaerobically and uptake phosphorus aerobically, which can then be diverted to the solids stream to be further treated or disposed of in solids handling. EBPR is regarded as an ecologically friendly and cost-effective means of phosphorus removal that allows WRRFs to meet discharge limits and to minimize contributions to eutrophication in water bodies (Kamika et al., 2014). However, this leads to highly concentrated amounts of nitrogen and phosphorus in the solids stream, which must also be handled properly. This presents an opportunity for resource recovery through biosolids to be used as a sustainable alternative to synthetic fertilizers, but land application of these class A biosolids must also be regulated by state agronomic rates for P or N to protect the environment from eutrophication risks from soil runoff (Gilmour et al., 2003).

In the Clean Water Act, the U.S. Environmental Protection Agency (EPA) established the Standards for the Use or Disposal of Sewage Sludge, or the Part 503 rule, which limited pathogens and pollutants in biosolids intended for land application to protect environmental and human health. In the state of Virginia, the Virginia Department of Environmental Quality (DEQ) monitors biosolid application rates based on biosolid nutrient analysis and is namely managed on a nitrogen agronomic basis (9VAC25-32-356 Virginia DEQ). However, a case study determined that repeated land application of class A biosolids according only to agronomic nitrogen rates can result in excessive phosphorus buildup in soils, which may contribute to eutrophication in the event of soil runoff (Qiong et al., 2012, Penn and Sims 2002). Therefore, both nutrients must be considered in class A land application rates and area coverage. If biosolids are properly managed, resource recovery through wastewater treatment is a viable option.

According to a study completed in 2011, 22% of the agricultural phosphorus demand can be met through the recovery of phosphorus in wastewater (Mihelcic et al., 2011). Phosphorus recovery is utilized by combining EBPR with phosphorus containing mineral harvesting, such as struvite ($MgNH_4PO_4 \cdot 6H_2O$, or MAP) (Le Corre et al., 2009). Struvite and other common minerals formed in wastewater treatment can spontaneously form when the constituent concentrations exceed the solubility product (Le Corre et al., 2009). Struvite most commonly forms when phosphorus rich activated sludge from EBPR processes is coupled with anaerobic digestion. Anaerobic conditions within the digester cause the release of both ammonium and phosphate as part of volatile solids reduction (VSR) and from polyphosphate stored in the biomass (Booker et al., 1999). Cambi Thermal Hydrolysis Process (THP) can exacerbate this by allowing an increased total solid (TS) loading to anaerobic digesters. Cambi THP utilizes extreme heat and pressure prior to anaerobic digestion which leads to many benefits such as increased volatile solids reduction (VSR), increased gas yield, improved cake dryness, and decreased solids viscosity allowing for increased digester loading (Haug, 1977; Stuckey and McCarty, 1978; Wilson and Novak, 2009; Higgins et al., 2017). These benefits in increased load to the digesters and increased VSR lead to higher concentrations of P and N within and post digestion and enhance the possibility of struvite formation. Struvite precipitation is a well understood route to phosphorus recovery and can be utilized as a marketable fertilizer product (Doyle et al., 2003).

Where these phosphorus containing minerals such as struvite can be beneficial for resource recovery, if they are not properly controlled to be sequestered in biosolids or harvested, the minerals may form scale deposits at inopportune locations around the plant leading to issues that clog piping networks and damage final dewatering equipment over time (Doyle et al., 2003). Therefore, these minerals are often perceived as a nuisance that affect treatment process efficiency and cause maintenance issues. However, if proper control of where and when these phosphorus containing minerals form is maintained, phosphorus can be harvested as a pure, sustainable, slow-release fertilizer, such as struvite, or phosphorus can be sequestered into class A biosolids to create a nutrient-rich soil blend product for beneficial and

responsible land application. This phosphorus recovery would not only reduce the phosphorus recycle in solids handling leading to spontaneous scaling and damage to plant equipment and operations, but it could also valorize biosolids into a marketable product.

1.1 Research Motivation

Solids utilized throughout pilot testing were real solids from Hampton Road Sanitation District's (HRSD) Atlantic Treatment Plant (ATP). ATP is a 54 MGD, high-rate facility with an anaerobic/aerobic (A/O) process configuration and ocean outfall. Figure 1 below depicts the plant process schematic.

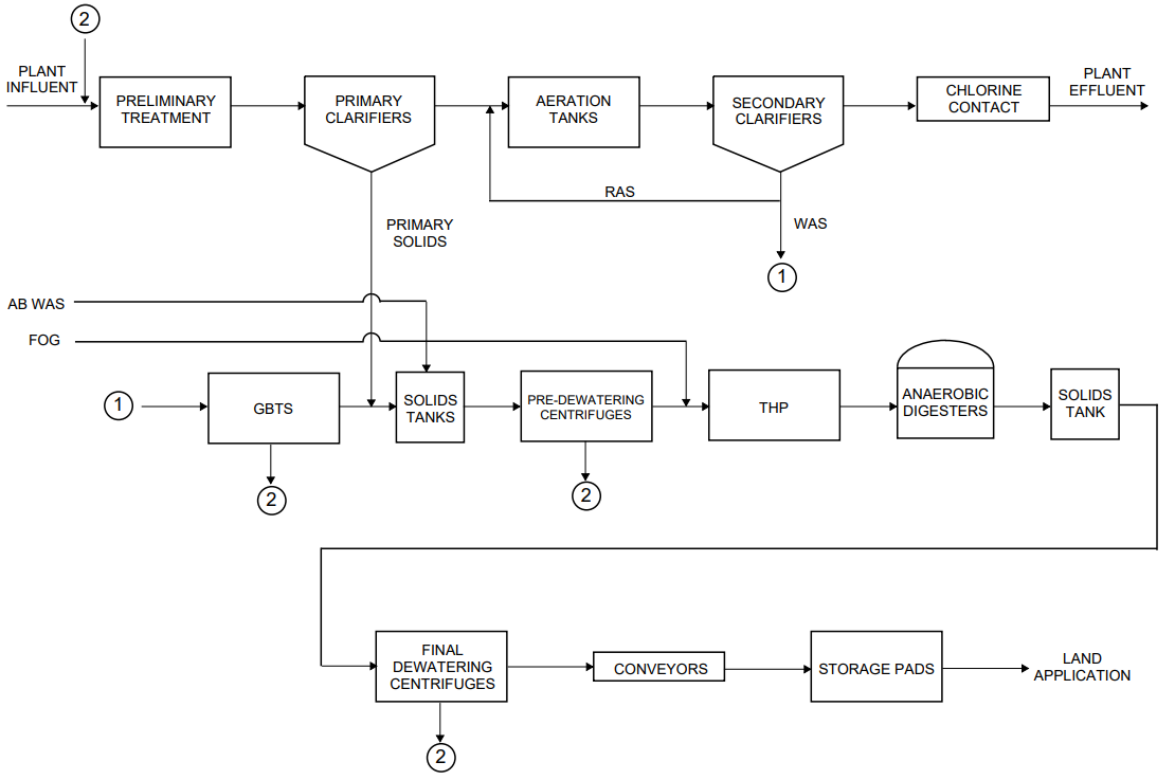

Figure 1: Process schematic of HRSD's Atlantic Treatment Plant.

Within the A/O configuration, the plant utilizes an anaerobic selector to promote better solids settling and to control filaments. As a result of this, the plant indirectly achieves about 75% EBPR in the liquid stream. The solids then consist of a blend of waste activated sludge from this EBPR process and fermented primary solids, as well as addition from fats, oils, and grease (FOG). The solids undergo thermal hydrolysis pretreatment in a Cambi B6-4 unit before anaerobic codigestion and are then stored in the anaerobic, mixed digested solids storage tank (DSST) for about 3 days. The solids then are dewatered with centrifuges to form Class A biosolids for land application. Due to the EBPR solids' exposure to anaerobic digestion, the plant is experiencing scaling issues within the digesters and on final dewatering equipment. ATP is also experiencing an increased phosphorus recycle load around the plant in

the dewatering centrate/filtrate lines and does not currently have an outlet for phosphorus removal or recovery within their solids handling treatment.

A total phosphorus (TP) mass balance was completed using plant data from 2022-2024 (Figure 2). Atlantic received on average 2106 lbs P/day in the raw water influent (RWI) during this time. With about 75% TP removal achieved in the liquid stream, that sent about 521 lbs P/day to the ocean outfall and the remaining 1585 lbs P/day were diverted to solids handling. The total solids (TS) content in solids handling after gravity belt thickeners (GBT) was 6-7%, digester feed was about 10% and after anaerobic digestion TS was about 4-5% on a dry weight basis. As shown in Figure 2, there are large phosphorus sinks around the aeration basins (ARE), the GBTs, in the pre-dewatering feed, as well as around the THP and digesters. About 1135 lbs P/day were removed with the cake during this time, which accounted for about 54% TP removal of the incoming TP in the RWI. Due to increased loading to the digesters from a THP and soluble phosphorus in dewatering filtrates/centrates, TP in the recycle lines has increased over this time period, leading to continuous treatment of TP. From the GBT filtrate, pre-dewatering centrate, and the final dewatering centrate, about 2696 lbs P/day were recycled to the head of the plant. This heavy recycle load increases the phosphorus available around the plant to form scaling precipitates that lead to the phosphorus sinks within digesters and on dewatering equipment that can clog and damage equipment, increase maintenance and clean out costs, and hinder treatment efficiency overall.

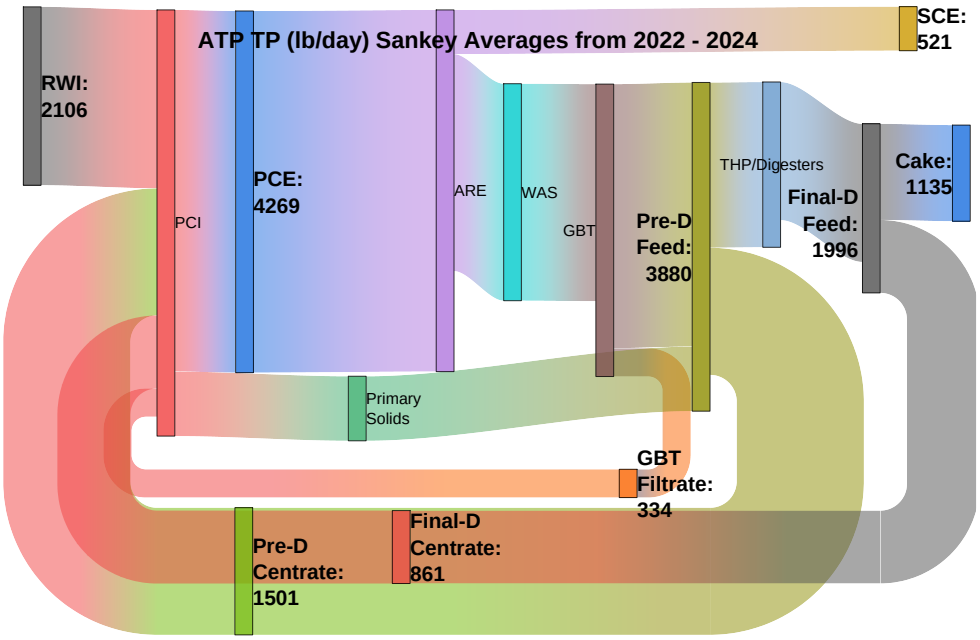

Figure 2: Total Phosphorus (TP) mass balance in the form of a Sankey diagram for the Atlantic Treatment Plant from 2022-2024.

Performing a TP mass balance can help identify where phosphorus may be precipitating along solids treatment lines and offer insight into removal points. However, additional

analysis is necessary to identify the specific type of precipitate formed, which is essential for determining the most effective treatment approach. There are many different phosphorus containing minerals that may form at WRRFs with various solubility conditions that must be understood to determine how to best control the formation of these precipitates for future nutrient harvesting or sequestration potential. As many WRRFs struggle with similar issues of phosphorus recycles and nuisance scaling, the research and modeling work presented in this thesis can potentially be valuable across the industry.

The overall objective of the research presented in this thesis was to optimize phosphorus removal at HRSD's Atlantic Treatment Plant, aiming to reduce phosphorus recycle loads and minimize nuisance scaling around the plant. Chapter 2 includes a literature review of the current state of knowledge on the common minerals that scale at WRRFs, factors influencing precipitation reactions, and nutrient recovery technologies in operation. Chapter 3 reviews the materials and methodology for the startup, operation, chemical addition, sampling, and clean out pilot procedures that were utilized in both manuscripts. The focus of Chapter 4 was to experimentally determine the optimal pilot operation for phosphorus removal and understand the effects. The first objective was to evaluate and understand the impacts of mixing, aeration at various settings, and chemical addition of two chemicals at various Ca^{2+}+Mg^{2+}:P ratios on the optimization of phosphorus sequestration to class A biosolids. The second objective of Chapter 4 was to determine pilot operational impacts on other parameters such as nitrogen removal, alkalinity, and COD removal. Knowledge acquired from experimental results on the pilot scale will directly influence design modifications and operation in a future plant upgrade at HRSD's ATP. Insights gained from this investigation also possess potential benefits for other WRRFs that desire to decrease phosphorus loads in the solids recycle lines and nuisance scaling in a more cost-effective manner than some commercially available technologies. The focus of Chapter 5 was to understand pilot operational effects on minerology using modeling and solids analysis. The first objective was to evaluate and understand the impacts of pH, temperature, and chemical addition of two chemicals at various Ca^{2+}+Mg^{2+}:P ratios on phosphorus removal and mineral formation utilizing the modeling software Visual MINTEQ. The second objective was to characterize the solids formed with SEM/EDS, XRD, and Raman Spectroscopy to calibrate and validate the model. The results of this study will enhance our understanding regarding scaling minerals likely to form within anaerobic digestion pretreated with a THP, post anaerobic digestion and on downstream equipment, as well as in a potential post aerobic digestion (PAD) setup. A validated model could then be used to predict scaling potential and characterize minerals formed at other WRRFs to better treat these nuisance scaling minerals and determine their potential for harvesting/sequestration as a nutrient-rich product. With the increasing need to not only remove but recover nutrients for beneficial reuse, it is imperative to deepen the understanding of successful phosphorus precipitation in biosolids and how it can be optimized and modified for various solids handling configurations.

2. Literature Review

2.1 Common WRRF Minerals

The following minerals have long posed issues at WRRFs that cause disruption to treatment efficiency and damage to equipment. A shift in the perspective on phosphorus containing scaling minerals to be used for resource recovery or as sustainable fertilizers rather than just a nuisance has led to more research on understanding how to control the conditions in which they form. The minerals can generally be categorized as magnesium ammonium phosphates (MAP), calcium phosphates (CaP), or other phosphate containing minerals, including aluminum and iron salts, as well as carbonates and sulfides. Not only phosphorus containing minerals were included in this literature review to assess other effects from scaling minerals and coprecipitation reactions affecting P-containing mineral formation. Mineral classification as relevant or not was determined within the context of anaerobic digestion (AD) and post aerobic digestion (PAD) experiments. While many other minerals are important to WWRF scaling, most research in the literature revolves around those that can also be utilized to recover phosphorus, most notably struvite, brushite, and vivianite.

2.1.1 Magnesium Phosphates

Struvite, k-struvite ($KMgPO_4{\cdot}6H_2O$), dittmarite ($MgNH_4PO_4{\cdot}H_2O$), newberyite ($MgHPO_4{\cdot}3H_2O$), bobierrite ($Mg_3(PO_4)_2{\cdot}8H_2O$), and cattiite ($Mg_3(PO_4)_2{\cdot}22H_2O$) have all been noted in solutions containing magnesium, ammonium, and phosphate ions (Massey et al., 2009; Daneshgar et al., 2018). K-struvite is an analog of struvite, where the K^+ ion can replace the NH_4^+ ion. It has been noted to precipitate in the pH range of 8.5-11.5 and requires a Mg:K:P ratio of 2:1:2 to significantly precipitate (Xu et al., 2015). Due to struvite's range of insolubility overlapping with K-struvite as well as ample amounts of ammonium in the anaerobic digestion system, K-struvite is unlikely to precipitate with respect to struvite (Shih and Yan, 2016).

Dittmarite, the monohydrate form of struvite, has been noted as an intermediate reaction product before reaching the more stable mineral state of struvite (Zhang et al., 2010). Dittmarite can be formed within wastewater treatment processes, however, formation requires a greater magnesium concentration than struvite (NH_4:Mg:P of 1:1.25:1) and a pH of 10.7 for maximum precipitation, making it not as likely to form before struvite within the conditions created by AD or PAD (Atalay and Whitehead, 2018).

Newberyite and bobierrite are two main magnesium phosphate compounds that may precipitate, but strongly depend on operating conditions. Newberyite has been hypothesized to be the product of struvite decomposition (Sutor, 1968). Newberyite can narrowly coprecipitate with struvite but requires a high Mg^{2+}:P ratio and is only less soluble than struvite at a pH less than 6, with a minimum solubility at a pH of 5.85. Moreover, the induction time of nucleation, or the time it takes for the first crystal growth to occur, at 25°C and a supersaturation ratio of 4 for struvite is about two days, whereas newberyite needs about one week. This all renders this

mineral not as likely to form as struvite within or downstream of anaerobic digestion, however it is still an important mineral to consider for coprecipitation possibilities (Abbona et al., 1982). In the same test on determining the effects of pH and concentration on magnesium phosphate crystallization, Abbona et al., 1982 also tried to supersaturate the solution with respect to other magnesium phosphates such as bobierrite and cattiite but were ultimately never observed as precipitates in the pH ranges tested and, therefore, left out of the consideration of the study. It was noted that in the high pH solutions used, bobierrite was much more supersaturated than cattiite, yet struvite still ultimately formed instead of bobierrite or cattiite. It has been reported in another study that bobierrite requires a very slow reaction time that extends past conventional solid residence times in anaerobic digestion and is, therefore, excluded from consideration in the time frame of wastewater treatment (Mamais et al., 1994). Musvoto et al., 2000 also used this source as reason to not include either of these trimagnesium phosphates at both states of hydration (bobierrite and cattiite) in their model and stated them to have low precipitation rates, and not likely to precipitate in a pH range of 6-9. However, there is newer evidence to suggest cattiite can co-precipitate with K-struvite in urine solutions in a pH range of 9-11 and if the initial Mg^{2+} concentration in solution is 10 mmol/L or higher (Wei et al., 2023). More research is required on trimagnesium phosphate minerals, so they were not considered significant minerals of interest to this study. Due to struvite having a range of insolubility, kinetics, and constituent makeup ideal for anaerobic digestion or PAD, struvite has a great tendency to crystalize and will, therefore, be the focus of the following section.

2.1.1.1 Struvite

Struvite is a mineral with equimolar concentrations of magnesium, ammonium, and phosphate. Struvite scale deposits have long been a nuisance around wastewater treatment processes and dates back to 1937 when it was first observed as a crystalline material inside a multi-stage sludge digestion system by Rawn et al., 1937. Struvite is orthorhombic in crystal structure and generally has a white and sparkly appearance. The mineral has a molecular weight of 245.4 g/mol, which means that when forming struvite, every pound of phosphorus yields 7.9 lbs of struvite, and every pound of magnesium and ammonium-N yields 10.1 and 17.5 lbs of struvite, respectively. Struvite has a density of 1.7 g/cm^3 and a thermodynamic solubility product (pK_{sp}) that experimentally ranges from 9.94 to 13.27 at 25°C (Abbona et al., 1982; Ohlinger et al., 1998). Struvite's solubility is low in water, 180 g/mL, at 25°C making it a feasible "slow release" fertilizer choice as it is less likely to leach (Munch and Barr, 2000, Le Corre et al., 2009, Ohlinger et al., 1998, and Aka et al., 2023).

The precipitation reaction for struvite is represented by Equation 1 (with n = 0, 1, or 2, dependent on the solution pH):

$$Mg^{2+} + NH_4^+ + H_nPO_4^{n-3} + 6H_2O \rightarrow MgNH_4PO_4 + 6H_2O + nH^+ \quad (1)$$

The formation of struvite is complex as it depends on a multitude of factors such as thermodynamics, mass transfer between liquid-solid equilibrium, kinetics, pH, supersaturation

of the solution, mixing intensity, temperature, and the existence of foreign ions (Booker et al., 1999, Le Corre et al., 2009). According to Equation 1, the formation of struvite releases a hydrogen ion (H^+) in solution, which causes a drop in pH and consumes alkalinity, indicating the necessary continued alkalinity requirement throughout the struvite precipitation process. Magnesium concentration within wastewater treatment plants is influenced by the local service area water supply and is typically in the range of 10-20 mg/L. Magnesium is often the limiting element in the treatment of anaerobic digestate that is ammonium and phosphate rich, indicting a need for additional external Mg as well to reach the required 1:1:1 Mg:N:P ratio (Munch and Barr, 2000; Lui et al., 2018). The solubility of struvite decreases as pH increases, with a wide ideal range of precipitation identified as 7-11. It has been noted by many sources that struvite is the least soluble, and therefore most likely to form, at pH 9 (Munch and Barr, 2000; Yan and Shih, 2016; Buchanan et al., 1994; Doyle and Parsons, 2002).

Struvite formation is particularly common within and post anaerobic digestion due to the transition from anaerobic digester headspace conditions to atmospheric CO_2 pressure. The Henderson-Hasselbach equation (Equation 2) can be used to describe what happens to pH as the partial pressure of CO_2 decreases from about 35% within anaerobic digestion to atmospheric partial pressure of CO_2 around 0.03%.

$$pH = pK_a + \log\left(\frac{[HCO_3^-]}{[H_2CO_3]}\right) \quad (2)$$

Henry's Law can also be substituted into Equation 2 to describe the relationship between carbon dioxide and carbonic acid (Equation 3). The Henry's Law constant is 0.03, and the pKa,1 for the carbonate system is 6.3.

$$pH = 6.3 + \log\left(\frac{[HCO_3^-]}{0.03 \times pCO_2}\right) \quad (3)$$

Assuming a bicarbonate alkalinity of 7500 mg/L as $CaCO_3$ within the digesters, at a partial pressure of CO_2 of 35% within the anaerobic digester, the pH is calculated to be 7.6. When exposed to the atmospheric CO_2 partial pressure of about 0.03%, the pH would increase to 10.6. As struvite is most likely to form at higher pH ranges, this transition promotes struvite formation. Areas of high turbulence (dewatering equipment, propellers, centrifuges, gravity belt thickeners, pumps, heat exchangers) and areas that can cause a local velocity or pressure drop (pipe bends and elbows, Figure 3) also promote this CO_2 partial pressure drop to equilibrium, raise the pH, and lead to struvite scale. This phenomenon throughout the treatment process combined with solids streams of enhanced phosphate concentrations (within and downstream of digestion) cause struvite to precipitate (Ohlinger et al., 1999).

Figure 3: Scale within a removed pipe bend at HRSD's Atlantic Treatment Plant transporting digestate to the final dewatering centrifuges.

Controlling the solution pH and supersaturation with respect to struvite via chemical addition could control where struvite forms, and safeguard digesters and downstream equipment from scaling.

2.1.2 Calcium Phosphates

Calcium phosphates include a large and complex variety of potential scaling minerals. This family includes (but is not limited to) amorphous calcium phosphate (ACP – $Ca_3(PO_4)_2$), as well as crystalline minerals such as: dicalcium phosphate dihydrate, commonly referred as brushite (DCPD – $CaHPO_4{\cdot}2H_2O$), dicalcium phosphate, or monetite (DCP – $CaHPO_4$), tricalcium phosphate, commonly referred to as whitlockite (TCP – $Ca_3(PO_4)_2$), octacalcium phosphate (OCP – $Ca_8H_2(PO_4)_6{\cdot}5H_2O$), and apatites such as hydroxyapatite (HAP – $Ca_{10}(PO_4)_6(OH)_2$) (Daneshgar et al., 2018). In order of increasing solubility these are: hydroxyapatite, whitlockite, octacalcium phosphate, monetite, and brushite (Abbona et al., 1986). However, the order of minerals to precipitate from a solution that is supersaturated is not only dependent on the thermodynamic solubility product, but kinetics as well, which is still heavily debated in the scientific community.

In a study done by Abbona et al., 1986 at Ca+Mg = P concentrations ranging from 10 to 500 mM, brushite precipitated first at low pH (3-5), above pH 5, ACP began to form, and at a pH above 6, ACP was coprecipitated with struvite. Struvite was precipitated with brushite only at Mg:P above 0.8, and monetite and newberyite only formed at higher Ca+Mg = P concentrations of 500 mM. Abbona et al., 1986 goes on to discuss that among these, brushite

and ACP are most favored to precipitate first with increasing pH and can then be further transformed into the more stable forms of hydroxyapatite, monetite, and whitlockite. Root et al., 1990 found that when the pH ranges from 7 to 9, ACP can be transformed into the precursor OCP phase, and then into HAP. Whereas if the pH is 9 or higher, that intermediate conversion to OCP is omitted and ACP is immediately transformed into HAP. Likewise, Meyer, 1983 found the kinetics to favor OCP when the pH is less than 9.25, and apatite to preferentially form at a pH higher than 9.25. Other studies suggest that OCP is formed from the conversion of α-tricalcium phosphate (α-TCP) at initial pHs from 5.7-7.7 (Monma and Goto, 1983; Markovic et al., 1993). Another study suggests OCP likely forms from the hydrolysis of brushite at pH 5-6 (Lu and Leng, 2004).

These calcium phosphate phase transformations depend on several solution factors such as Ca^{2+} and total phosphate concentrations, $Ca:PO_4$ ratio, and the presence of phosphoproteins (Arnold, 1950; Cheng, 1985; Furedi-Milhofer et al., 1971). Mixing can also affect the kinetics of the shift from OCP to apatite. A stationary buffer solution supersaturated with respect to OCP remained supersaturated with OCP, but when stirred, precipitation occurred much more rapidly and decreased the degree of supersaturation with respect to OCP. Meaning, the slow diffusive mass transport in a less mixed environment delayed the decrease in supersaturation with respect to OCP and created a slightly acidic environment that aided growing OCP crystals rather than shifting towards apatite (Iijima et al., 1998). Simpson, 1966 found CO_2 to enhance OCP precipitation at 25°C and discovered that OCP precipitation increased when the partial pressure of CO_2 increased from 0.046 to 10% at a pH around 7.2-7.3. Therefore, this research suggests OCP formation may be favored over apatite within anaerobic digesters in WRRFs.

ACP has been shown to form at pH values between 7.4-9.25 and have a $Ca:PO_4$ ratio around 1.5, which is highly similar to that of TCP of the same molecular formula. ACP forms spontaneously in rapidly mixed solutions with sufficient Ca^{2+} and phosphate ions that they quickly coalesce into irregular and hydrated clusters that are extremely unstable, leading to a rapid change into a crystal form such as brushite, or to a more stable form such as OCP or apatite (Chow, 2001). The amorphous to crystalline transformation is highly dependent on solution conditions. At pH 7.4, the transformation from ACP to a crystalline form is 5 times faster at 37°C than 20°C, and at 25°C the aqueous lifetime of ACP was less than 0.3 hours at pH 7.4 as compared to over 9 hours between pH 10 and 10.5 (Eanes and Meyer, 1977; Meyer and Eanes 1978). However, the initial presence of inorganic ions such as Mg, carbonate, and pyrophosphate have been shown to extend the lifetime of ACP in solution (Eanes and Posner, 1968). LeGeros and LeGeros, 1984 also found that if Mg is present in solution, it can delay or even prevent ACP from ever transforming into a crystalline state. These research findings point to conditions within anaerobic digesters to be conducive to the shift from ACP to more stable minerals such as brushite or OCP.

Monetite has fast formation kinetics from ACP and brushite, however Abbona et al., 1986 showed it to only form if concentrations of Ca+Mg = P were as high as 500 mM but is still

quite unlikely as ACP will immediately first form and reduce the calcium and phosphate concentrations below this critical value for monetite precipitation. Another study showed monetite to only be the least soluble salt below pH 4.2 (Chow, 2001).

Hydroxyapatite is known as the most thermodynamically stable calcium phosphate; however, its formation is constrained by very slow kinetics, which is commonly thought to be outside of the typical timeline of WRRFs operating conditions (Mamais et al., 1994; Johnsson and Nancollas, 1992). It has been noted that whitlockite also has sluggish kinetics. Both HAP and TCP were not considered relevant minerals to the WRRF timescale due to the conversion kinetics taking a minimum of one months to a number of years, which is thought to be outside of the solids retention time (SRT) of conventional anaerobic digesters (Musvoto et al., 2000; Mamais et al., 1994).

The range of insolubility for calcium phosphates coincides with that of struvite, therefore, the extent to which a calcium phosphate forms heavily affects struvite coprecipitation and production (Root, 1990). This CaP literature review helped determine which minerals were most important to consider within and post anaerobic digestion at WRRFs, within PAD experiments, and how they relate to struvite formation. Brushite is insoluble at pH ranges less than 7, and would, therefore, be more relevant to pre-digested sludge, or unaerated sludge, however, due to its significance in other P harvesting mechanisms such as CalPrex™, this mineral was considered relevant (Stumm and Morgan, 1996). ACP is insoluble at a pH greater than 6, but the lifespan of the mineral is heavily debated within the scientific community, therefore, it has been noted as a relevant calcium phosphate to wastewater treatment (Johnsson and Nancollas, 1992; Lu and Leng, 2004). OCP was considered a relevant mineral to WRRFs. Lastly, monetite, TCP, and HAP were not considered relevant minerals due to their conditions for formation not aligning with the context of AD and PAD.

2.1.3 Other Salts – Carbonates, Iron and Aluminum Salts and Oxides, and Iron Sulfides

Other important minerals to phosphorus recovery and scaling minerals at WRRFs are carbonates and aluminum and iron salts. There are three possible varieties of the $CaCO_3$ crystalline structure, including calcite, aragonite, and vaterite. Calcite ($CaCO_3$) is the most thermodynamically stable form of calcium carbonates at ambient temperature and atmospheric pressure and is insoluble in alkaline environments (Roques and Girou, 1974). Musvoto et al., 2000, determined that the rate of $CaCO_3$ formation relies most on the presence of Mg, Fe, phosphate, and dissolved organics, which can slow down kinetics and increase solubility. Magnesite ($MgCO_3$) is the most thermodynamically stable form of magnesium carbonate and precipitates in a pH range less than 10.7, therefore, it is relevant within the context of AD and PAD. Mixtures of Ca and Mg carbonates exist such as dolomite ($CaMg(CO_3)_2$) and huntite ($CaMg(CO_3)_4$). However, neither are well understood, and Mamais et al., 1994 was unsuccessful in precipitating dolomite at atmospheric conditions.

Both dolomite and huntite have been left out of consideration for wastewater treatment plant scaling minerals. Also often ignored are calcium hydroxide ($Ca(OH)_2$) and brucite ($Mg(OH)_2$) as they precipitate at pH ranges greater than 9.5 and would most likely not precipitate in the presence of other precipitating minerals mentioned above (Mamais et al., 1994; Musvoto et al., 2000).

Iron salts are also a viable option for P reuse, especially at plants that dose iron for chemical phosphorus removal, odor control, or as a coagulating agent (Park et al., 2006a). This purposeful iron dosing at WRRFs leads to elevated concentrations in activated sludge, which concentrates in solids streams and can impact P precipitation. At WRRFs, iron phosphates form most likely as minerals in the presence of orthophosphate and dissolved iron or via adsorption of orthophosphates onto the surface of iron oxides. Although many exist, relevant iron phosphates in literature are vivianite ($Fe_3(PO_4)_2{\cdot}8H_2O$) and strengite ($FePO_4{\cdot}2H_2O$). The optimal conditions for vivianite formation are a pH range of 6-8, a Fe:P ratio around 2:1, and reduced environments, which is why it has commonly been found throughout solids handling treatment (Wilfert et al., 2015). Vivianite, like struvite, is increasing in popularity as a highly valuable wastewater recovery product that has beneficial slow release, fertilizer-like qualities when land applied (Wu et al., 2019). The pH range of insolubility of vivianite also overlaps with that of struvite, and they have been noted to coprecipitate together. Mamais et al., 1994 discovered that a dose of Fe (using $FeCl_3$) up to 13.5 mM, struvite will still be supersaturated in solution along with vivianite, but at higher Fe dosages, struvite will no longer precipitate. Strengite is formed when ferrous is oxidized to ferric iron and can directly precipitate with phosphorus at a pH less than 6. Due to this lower pH of insolubility, it is not likely to form in the context of AD and PAD.

Siderite ($FeCO_3$) formation has equilibrium conditions that overlap with vivianite formation and is strongly tied to the dissociation of carbonic and phosphoric acid. This makes the distinction between whether vivianite or siderite formation occurs highly dependent on the alkalinity or pH of the solution. Postma, 1980 found that towards the lower pH range of formation (6-8), the stability of vivianite increases relatively to siderite. Jiang and Tosca, 2019 also discovered that at similar solution saturation and 25°C, siderite growth kinetics is about seven orders of magnitude slower than calcite kinetics, making it less likely to form if calcium is readily available.

Some common iron oxides, both ferrous and ferric, include goethite (α-$Fe^{3+}O(OH)$), hematite (Fe_2O_3), ferrihydrite ($Fe^{3+}{}_{10}O_{14}(OH)_2$), and am-FeOOH. Unlike iron phosphate minerals which usually form in the presence of OP-P and dissolved iron, iron oxides can remove phosphorus by binding OP-P onto their solid surfaces via adsorption complexes. The more amorphous the iron oxide the more surface area available for a higher orthophosphate adsorption capacity (Wilfert et al., 2015). Guzman et al., 1994 discovered that the relative affinity for phosphate decreased in order of goethite, hematite, to ferrihydrite. Iron oxide and OP-P interactions can be complex, so most of the focus found in literature in the wastewater context has been focused on iron-phosphate salts, namely vivianite.

Aluminum in sludge is often caused by Al salt addition in drinking water treatment to remove natural organic matter, and in wastewater treatment as coagulating and chemical phosphorus removal agents (Park et al., 2006a). Aluminum phosphorus salts exist such as variscite ($AlPO_4 \cdot 2H_2O$) and wavellite ($Al_3(PO_4)_2(OH)_3 \cdot 5H_2O$), which are both more common in low pH, weathered phosphatic soils. However, neither mineral is a viable P recovery option in this AD and PAD context as their formation requires a pH range of 3-6 and 4-5.5, respectively (Azam et al., 2019). However, orthophosphate has been shown to adsorb onto Al oxides such as diaspore (AlO(OH)), boehmite (AlO(OH)), and gibbsite (Al(OH)3). At 25°C and 1 atmospheric pressure, the thermodynamic stabilities of these minerals increase from gibbsite, boehmite, to diaspore (Peryea and Kittrick, 1988). The hydroxyl groups on these aluminum oxides facilitate phosphate adsorption and adsorb phosphate in the pH range of 2 to 9, with maximum adsorption observed at pH 4 (Tanada et al., 2003). Although Al-P salts are important in chemical P removal, the focus was shifted to these three Al hydroxides as a means for P removal in the conditions present in AD and PAD.

There are three naturally occurring iron sulfides minerals to note: mackinawite ($Fe_{(1+x)}S$, where x = 0.0057 to 0.06) with a tetragonal crystalline structure, pyrrhotite (ranging from Fe_7S_8 to FeS) with a monoclinic nickel arsenide mineral structure, and pyrite (FeS_2) with a cubic mineral structure (Meyer et al., 1958). Iron sulfides are important to understand around WRRFs due to the high likelihood of scaling formed when high iron loads from ferric dosing is combined with sulfide in anaerobic digesters or sulfate in PAD. Studies have shown that significant levels of corrosion and degradation to water management systems is due to the oxidation of gaseous sulfide to sulfuric acid, which can be prevented by iron-sulfide complexation (Rebosura et al., 2018). In all cases of iron sulfide synthesis, mackinawite is initially produced before following equilibrium to form other species (Smith and Miller, 1975). A study done by Berner et al., 1967 reported that mackinawite was unstable compared to another iron sulfide mineral, troilite, which is stoichiometrically the same as pyrrhotite, FeS. The scaling potential of these minerals is linked to pH and the sulfide concentration. One study found that at lower sulfide concentrations between 15 to 1700 mg/L the minerals formed mainly consisted of pyrrhotite and pyrite (Sardisco et al., 1963). Another study noted mackinawite to be preferred to form in the initial pH range of 6.5 to 8.8, and pyrrhotite or pyrite could only dominate outside of this pH range (Sardisco and Pitts, 1965). Generally, the order of formation has been found to be a mackinawite scale that is then transformed or covered by pyrrhotite and pyrite, which was therefore taken as guidance for iron sulfide scale (Meyer et al., 1958). These minerals are important for WRRF scaling mineral characterization and indirectly to P recovery as they can affect iron concentrations, which affects P concentrations available for precipitation.

Lastly, barite ($BaSO_4$) is another mineral of interest. Wastewater treatment plants can promote conditions for exogenous sulfate to interact with divalent cations like Ba^{2+}, if present, and form barite scale. Ruiz-Agudo et al., 2015 showed the effects of pH on the nucleation and growth of barite at 22°C and found that growth rates increased at a pH above

10. In experiments conducted by Esteves et al., 2023 at a Ba:SO_4 ratio of 1:1, and an initial pH range of 2 to 7, they determined barium precipitation was strongly impacted by pH. At a pH less than 2, barium precipitation was undetectable, but between pH 2-5, an increase in precipitation rates was observed, and comparable barium precipitation rates in the pH range of 5-7. Barite was considered relevant within the context of AD and PAD.

2.2 Precipitation Chemistry

Crystal formation occurs in two stages: nucleation (precipitation begins) and crystal growth (progress of crystals until equilibrium is reached) (Jones, 2002). These mechanisms are complex and depend most on solubility and saturation, which likewise are dependent on a multitude of factors such as thermodynamics, pH, temperature, mixing intensity, mass transfer between liquid-solid equilibrium, kinetics, and the existence of foreign ions (Booker et al., 1999, Le Corre et al., 2009).

2.2.1 Solubility

Solubility is defined as the amount of substance (moles/L or mg/L) that can be dissolved under certain conditions of temperature and pressure. Every crystal has a solubility product (K_{sp}), which is an equilibrium constant describing a precipitate dissolving in pure water to give its constituent ions, shown in Equation 5 based on the general reaction in Equations 4 (Snoeyink and Jenkins, 1980).

$$A_zB_{y(s)} \leftrightarrow zA^{y+} + yB^{z-} \quad (4)$$

$$K_{sp} = \frac{\{A^{y+}\}^z\{B^{z-}\}^y}{\{A_zB_{y(s)}\}} \quad (5)$$

The solubility product considers the ionic strength (I) and the activity (a_i) of an ionic species and can be calculated below for struvite using Equation 6.

$$K_{sp} = a_{Mg^{2+}} \times a_{NH_4^+} \times a_{PO_4^{3-}} \quad (6)$$

Where a_i is the activity of the ith ion in solution and is described as $a_i = \gamma_i \cdot [C_i]$; γ_i is the activity coefficient of the species and $[C_i]$ is the total concentration in solution. Predicting mineral formation can be difficult in matrices such as wastewater due to the many different free ions (i.e., the ionic activity) that are available at a given pH to react with the component ions making up the mineral of interest (Snoeyink and Jenkins, 1980).

Snoeyink and Jenkins also introduced the concept of a conditional solubility product, which is dependent on solution conditions other than common ions present, seen in Equation 7.

$$P_s = C_{T,M} \times C_{T,A} \quad (7)$$

Where $C_{T,M}$ is the total concentration of the metal ion M in all possible complex forms, and $C_{T,A}$ is the total concentration of the anion A in all possible complex forms. This method of calculating the solubility product can be helpful because it ignores the side reactions of anions and cations. However, P_s is dependent on solution properties such as pH and concentrations of species that may form complexes. The conditional solubility product is at a minimum when the product of the ionization fractions is at a maximum; this corresponds to a

minimum pH value as well, known as the pH of minimum solubility. The conditional solubility product and the solubility product, K_{sp} can be related. If α_M = the fraction of $C_{T,M}$ present as the free metal ion, $[M^+] = \alpha_M(C_{T,M})$, and if the same is true for α_A equaling the fraction of $C_{T,A}$ present as the free anion, $[A^-] = \alpha_A(C_{T,A})$, then

$$K_{sp} = [M^+][A^-] \tag{8}$$

or

$$K_{sp} = \alpha_M \alpha_A (C_{T,M})(C_{T,A}) \tag{9}$$

So that,

$$K_{sp} = \alpha_M \alpha_A P_s \tag{10}$$

Combining Equations 7-10 in terms of struvite one can see

$$P_s = C_{T,Mg} C_{T,NH4}, C_{T,PO4} = \left(\frac{K_{sp}}{\alpha_{Mg^{2+}} \alpha_{NH_4^+} \alpha_{PO_4^{3-}} \times \gamma_{Mg^{2+}} \gamma_{NH_4^+} \gamma_{PO_4^{3-}}} \right) \tag{11}$$

The conditional solubility product also allows for a fast evaluation of the state of the crystal in solution (Snoeyink and Jenkins, 1980).

- If $P_s < C_{T,Mg} \times C_{T,PO4} \times C_{T,NH4}$, the solution is oversaturated and struvite will precipitate until equilibrium is reached.
- If $P_s > C_{T,Mg} \times C_{T,PO4} \times C_{T,NH4}$, the solution is undersaturated with respect to struvite and will not precipitate.
- If $P_s = C_{T,Mg} \times C_{T,PO4} \times C_{T,NH4}$, then the solution is at equilibrium.

The solubility product can also be defined thermodynamically by the free energy change that comes with the dissolution of a solid, expressed as an equilibrium constant. The solubility product, K_{sp}, also follows the Arrhenius form shown in Equation 12.

$$K_{sp} = exp\left(\frac{-\Delta G^\circ}{RT}\right) \tag{12}$$

Where ΔG° is the standard Gibbs free energy change of the reaction, R is the ideal gas constant, and T is the absolute temperature. This adds the thermodynamic dependence on precipitation reactions to describe a reactions reversibility, spontaneity, and temperature dependence. The solubility product can be used to understand mineral formation and dissolution (Stumm and Morgan, 1996).

In Table 1 below are the pK_{sp} values found in visual MINTEQ (Gustafsson, 2008), and in literature at 25°C for all relevant solids to this project listed in section 2.2 Common WWTP Minerals.

Table 1: Common scaling minerals found in WWTPs, along with their chemical equation, the conditions in which each mineral may form, the pKsp values listed in Visual MINTEQ at 25°C and the pKsp values commonly found in literature at 25°C.

Precipitate	Chemical Equation	Condition	pK_{sp} (25°C) Visual MINTEQ	pK_{sp} (25°C)	Reference
Magnesium Phosphates					
Struvite (MAP)	$Mg^{2+}+ NH_4^+ + HPO_4^{2-} + 6H_2O \leftrightarrow MgNH_4PO_4 \cdot 6H_2O + H^+$	7 < pH < 11	13.26	13.26	Ohlinger et al. (1998)
K-struvite	$Mg^{2+}+ K^+ + PO_4^{3-} + 6H_2O \leftrightarrow MgKPO_4 \cdot 6H_2O$	8.5 < pH < 11.5	-	12.2	Xu et al. (2015)
Dittmarite	$Mg^{2+}+ NH_4^+ + PO_4^{3-} + H_2O \leftrightarrow MgNH_4PO_4 \cdot H_2O$	pH = 10.7, struvite intermediate	-	13.36	Atalay and Whitehead (2018)
Newberyite	$Mg^{2+}+ HPO_4^{2-} + 3H_2O \leftrightarrow MgHPO_4 \cdot 3H_2O$	High Mg^{2+}:P, pH < 6	18.175	5.51	Abbona et al. (1981)
Bobierrite	$3Mg^{2+}+ 2PO_4^{2-} + 8H_2O \leftrightarrow Mg_3(PO_4)_2 \cdot 8H_2O$	Slow reaction time, pH outside of 6-9	23.28[A]	25.2	Musvoto et al. (2000)
Cattiite	$3Mg^{2+}+ 2PO_4^{2-} + 22H_2O \leftrightarrow Mg_3(PO_4)_2 \cdot 22H_2O$	Low precipitation rate	23.28[A]	23.1	Mamais et al. (1994), Scott et al. (1991)
Calcium Phosphates					
Amorphous Calcium Phosphate (ACP)	$3Ca^{2+} + 2PO_4^{3-} + xH_2O \leftrightarrow Ca_3(PO_4)_2 \cdot xH_2O$	pH > 6	25.5, 28.25[B]	25.5	Musvoto et al. (2000)
Brushite (DCPD)	$Ca^{2+} + HPO_4^{2-} + 2H_2O \leftrightarrow CaHPO_4 \cdot 2H_2O$	pH < 7	18.995	6.6	Stumm and Morgan (1996)
Monetite (DCPA)	$Ca^{2+} + HPO_4^{2-} \leftrightarrow CaHPO_4$	Fast formation from ACP, DCPD	19.275	6.04	Johnsson and Nancollas (1992)
Whitlockite (TCP)	$3Ca^{2+} + 2PO_4^{3-} \leftrightarrow Ca_3(PO_4)_2$	Slow formation from ACP, DCPD	-	32.6	Musvoto et al. (2000)
β-Tricalcium Phosphate	$3Ca^{2+} + 2PO_4^{3-} \leftrightarrow \beta - Ca_3(PO_4)_2$	Slow formation from ACP, DCPD	28.92	24	Mamais et al. (1994)
Octacalcium	$8Ca^{2+} + 2HPO_4^{2-} + 4PO_4^{3-} + 5H_2O \leftrightarrow Ca_8H_2(PO_4)_6 \cdot 5H_2O$	Thermodynamically favorable when pH ≥	47.95	36.48	Lu and Leng (2004)

phosphate (OCP)		6.3, Hydrolysis of brushite			
Hydroxyapatite (HAP)	$5Ca^{2+} + 3PO_4^{3-} + OH^- \leftrightarrow Ca_5(PO_4)_3OH$	Slow	44.333	58.6	Kumar et al. (2004)
Carbonates and Hydroxides					
Calcite	$Ca^{2+} + CO_3^{2-} \leftrightarrow CaCO_3$	Stable at 25°C, atmospheric P, and alkaline pHs	8.48	8.42	Strumm and Morgan (1981)
Magnesite	$Mg^{2+} + CO_3^{2-} \leftrightarrow MgCO_3$	Stable at pH < 10.7	7.46	7.46	Strumm and Morgan (1981)
Dolomite	$Ca^{2+} + Mg^{2+} + 2CO_3^{2-} \leftrightarrow CaMg(CO_3)_2$	Not precipitated at atmospheric conditions	16.54, 17.09[C]	16.7, 17.09[C]	Strumm and Morgan (1981); Nordstrom et al. (1990)
Calcium Hydroxide	$Ca^{2+} + 2OH^- \leftrightarrow Ca(OH)_2$	pH > 9.5	-	5.2	Strumm and Morgan (1981)
Brucite	$Mg^{2+} + 2OH^- \leftrightarrow Mg(OH)_2$	pH > 9.5	17.1	11.16	Strumm and Morgan (1981)
Siderite	$Fe^{2+} + CO_3^{2-} \leftrightarrow FeCO_3$	Less stable than vivianite, slower formation than calcite	10.59	10.7	Mamais et al. (1994)
Other Phosphate Salts, Oxides, and Sulfides					
Vivianite	$Fe^{2+} + PO_4^{3-} + 8H_2O \leftrightarrow Fe_3(PO_4)_2 \cdot 8H_2O$	6 < pH < 8, Fe:P = 2:1	37.76	33	Mamais et al. (1994)
Strengite	$Fe^{3+} + PO_4^{3-} + 2H_2O \leftrightarrow Fe(PO_4) \cdot 2H_2O$	pH < 6	26.4	33.1	Makitie (1966)
Variscite	$Al^{3+} + PO_4^{3-} + 2H_2O \leftrightarrow Al(PO_4) \cdot 2H_2O$	3 < pH < 6	22.07	30.6	Makitie (1966)
Diaspore	$Al^{3+} + O^{2-} + H_2O \leftrightarrow Al_2O_3 \cdot H_2O$	Can adsorb phosphate at pH 2-9	6.873	6.75	Tanada et al. (2003), Peryea and Kittrick (1988)
Boehmite	$Al^{3+} + O^{2-} + H_2O \leftrightarrow Al_2O_3 \cdot H_2O$	Maximum phosphate adsorbed at pH 4	8.578	7.49	Tanada et al. (2003), Peryea and

					Kittrick (1988)
Gibbsite	$Al^{3+} + O^{2-} + 3H_2O \leftrightarrow Al_2O_3 \cdot 3H_2O$	Can adsorb phosphate at pH 2-9	7.74	7.76	Tanada et al. (2003), Peryea and Kittrick (1988)
Mackinawite	$Fe_{(1+x)}S$, where x = 0.057 to 0.064	First iron sulfide to form, 6.5 < pH < 8.8	3.6	3.64	Sardisco and Pitts. (1965), Morse and Arakaki (1993)
Pyrrhotite	$Fe_{(1-x)}S$, where x = 0.14 to 0	Formation from mackinawite, low sulfide concentrations	2.95[D]		Smith and Miller (1975)
Pyrite	$Fe^{2+} + 2HS^- \leftrightarrow FeS_2$	Formation from mackinawite, low sulfide concentrations	18.508	18.479	Robie and Waldbaum (1968)
Barite	$Ba^{2+} + SO_4^{2-} \leftrightarrow Ba(SO_4)$	Increasing precipitation rates 2 < pH < 7, faster growth rates 10-12	9.98	9.97	Nordstrom et al. (1990)

[A] Waters of Hydration not specified in Visual MINTEQ.

[B] List in Visual MINTEQ as either Ca3(PO4)2 (am1) or Ca3(PO4)2 (am2), respectively.

[C] Dolomite (disordered), Dolomite (ordered), respectively.

[D] Listed as FeS (ppt) in Visual MINTEQ

The pH at which a mineral may precipitate is one of the most important factors controlling the crystallization process as it is linked to both solubility and supersaturation. Every mineral has a pH range of insolubility based on conditional solubility product, as shown in Table 1 (Snoeyink and Jenkins, 1980). A study conducted by Yan and Shih, 2016 utilized quantitative XRD analysis to determine struvite content at various pH values and interfering cation levels. For example, phosphorus removal was greater than 90% at pH 7.5, and continued to increase as the Ca:Mg molar ratio increased up to 1:1 due to calcium phosphate formation. At pH 11, magnesium had the highest precipitation efficiency, but struvite had the lowest purity, indicating that at a pH greater than 9, magnesium phosphates may form over struvite (Yan and Shih, 2016). This indicates that pH as well as ion content in solution control precipitation reactions and can lead to multi-phase precipitates.

pH can be adjusted in various ways, including through chemical addition or physical processes like mixing and aeration. Common chemicals used for pH manipulation such as caustic (NaOH) can cause an increase in pH into a more insoluble range for a specific mineral. While effective, NaOH has drawbacks such as additional chemical costs and rapid pH adjustment, which has been shown to sharply increase the saturation of magnesium precipitation reactions such as the formation of bobierrite and magnesite to be favored over struvite (Zeng and Li, 2006).

Alternatively, aeration can be used to strip CO_2 from solution. Merkel and Krauth, 1999, demonstrated the use of aeration for pH elevation, which has the advantage of slowly raising the pH in a manner that does not require additional reagents and providing optimal conditions for struvite formation. During aeration, CO_2 stripping involves a transformation of dissolved CO_2 in solution into CO_2 gas and commonly occurs when anaerobic digestate encounters atmospheric air in an attempt to reach equilibrium, as described by Equation 3. CO_2 stripping efficiency depends on characteristics of the influent such as temperature, initial dissolved CO_2 gas concentration, as well as the flow rates of the influent, effluent, and aeration rate (Korchef et al., 2011). For instance, a study by Saidou et al., 2009 found that phosphorus removal increased up to 78% with increased airflow rates and pH adjustments above 6.5. Likewise, gases become less soluble at increased temperatures, and thus can increase the likelihood of CO_2 to volatilize when coupled with exposure to atmospheric conditions or areas of local turbulence. For example, the Henry's constant (pK_H) for $CO_{2(g)}$ increases from 1.41 at 20°C to 1.64 at 40°C, reaffirming a lower solubility with increased temperature (Snoeyink and Jenkins, 1980).

Temperature can affect precipitation reactions by influencing crystal solubility, and morphology. Multiple studies show an inverse relationship between the solubility product of struvite and temperature, indicating that struvite is more insoluble and likely to form at lower temperatures. Where Aage et al., 1997 found via radiochemical methods the pKsp for struvite decrease from 13.3 at 10°C to 12.4 at 50°C, Burns and Finlayson, 1982 via pH and concentration measurements saw a decrease in pKsp from 13.1 at 25°C to 13.0 at 35°C, and Bhuiyan et al., 2007 measured a decrease in struvite pKsp from 14.0 at 15°C to 13.01 at 35°C. These data explain why struvite scaling is very common within the pipe bends of heat exchangers for Cambi THP units that are used to cool the sludge down post thermal hydrolysis as well as downstream of heated anaerobic digestion. These data also explain the mesophilic temperature range that is common in digesters and digestate from 20°C to 45°C is the most common working temperature for struvite studies on the lab and full scale.

2.2.2 Saturation

Saturation describes the potential for a crystal to form in a solution and can exist in the three phases previously stated: undersaturated, equilibrium or metastable, and oversaturated. Solutions can be defined by the ionic activity product (IAP), which is a measure of how

many ions are dissolved within solution. All minerals have a specific IAP, which can be calculated as Equation 12.

$$IAP = \{M^+\}\{X^-\} \quad (12)$$

Comparing the IAP and K_{sp} can help determine whether a precipitate is thermodynamically favorable to form, i.e. the level of saturation. If the IAP is less than the K_{sp}, then the solution is undersaturated, if the IAP is equal to the K_{sp} the solution is at equilibrium, and the solution is supersaturated if the IAP is greater than the K_{sp}. The saturation index (SI) can be used to compare the degree of saturation between different minerals, shown in Equation 13, where z is the number of component ions.

$$SI = log\left(\frac{IAP}{K_{sp}}\right)^{1/z} \quad (13)$$

Again, saturation can now be described as undersaturated when the SI is less than 1, at equilibrium when the SI equals 0, and supersaturated when the SI is greater than 1 (Stumm and Morgan, 1996).

The presence of foreign ions in solution significantly impacts mineral saturation. Struvite formation is heavily impacted by calcium ions, which can be present at high levels in real wastewater. Pastor et al., 2008 determined if the Ca:P molar ratio is as high as 0.5:1, the precipitate will likely switch from struvite to a calcium phosphate. Le Corre et al., 2005 confirmed if the Ca:Mg molar ratio is 1:1 or greater, struvite formation can be limited or completely inhibited by the formation of ACP. Another study analyzed the inhibitory effects of calcium and ferric ions on struvite formation and found that both significantly inhibited struvite formation (Yan and Shih, 2016). Struvite content in precipitates formed (wt. %) decreased as Ca:Mg molar ratios increased to favor calcium, and the mineral formed switched from struvite to hydroxyapatite at a Ca:Mg molar ratio of 2:1. Ferric ions were added to solution in the form of ferric chloride at an Fe:Mg molar ratio of 1:5. Compared to the similar Ca:Mg molar ratio of 1:5 test, ferric ions at this molar ratio caused the struvite weight percentage to decrease to 60% at pH 7.5, whereas calcium ions caused the struvite weight percentage to be 83% at the same pH, indicating that ferric ions may inhibit struvite crystallization more strongly than calcium and likely transition the mineral formed to a ferric phosphate. The reverse situation is also inhibitory; Abbona et al., 1986 confirmed that the presence of magnesium ions in solution have inhibitory effects on crystallization of calcium phosphate solutions. It was stated that background concentrations of magnesium ions can favor the formation of ACP over other crystalline calcium phosphates and can delay or even prevent the conversion of ACP to a crystalline form.

Wastewater can contain various heavy metals that can affect the purity of struvite, or the purity of other minerals formed. Divalent metal ions such as Mn^{2+}, Fe^{2+}, Zn^{2+}, Cu^{2+}, Co^{2+}, and Cd^{2+} have all been noted to replace Mg^{2+} in the structure of struvite at room temperature. By the same mechanism, monovalent cations can replace NH_4^+ in struvite's crystal structure such as K^+, Rb^+, and Ti^+, and was observed in the experiments conducted by Andrade and Schuiling, 2001. These impurities can cause minerals to be less crystalline, which is indicated

by a decrease in relative intensity peaks when subjected to XRD analysis. In the same study conducted by Yan and Shih, 2016, as Ca:Mg molar ratios increased to favor calcium, the relative intensity of XRD peaks for struvite decreased as well.

Supersaturation within a solution is required for spontaneous crystallization to occur, but more kinetics information is needed to determine if certain precipitates are possible within the wastewater treatment time frame.

2.2.3 Crystallization

2.2.3.1 Nucleation and Crystal Growth

Crystal formation is the occurrence of a solid and can be divided into two phases: nucleation and crystal growth. Nucleation is the birth of the crystal, or the first and original occurrence of ions combining together, which is controlled by reaction kinetics. Crystal growth is the further development of that crystal until equilibrium is reached and is controlled by mineral growth kinetics. Mullin, 1992 describes the rate of nucleation, J, as the number of nuclei formed per unit time per unit volume and can be described in Equation 14 below.

$$J = A\ exp\left[\frac{16\pi\gamma^3\nu^2}{3k^3T^3(ln\Omega)^2}\right] \quad (14)$$

Where A is a kinetic factor, k is the Boltzmann constant (1.3805×10^{-23} J/K = R/N, with R being the gas constant = 8.314 J/K/mol and N is the Avogadro number = 6.023×10^{-23} mol^{-1}), Ω is the supersaturation ratio, γ is the interfacial tension, or surface energy, between the crystal and solution, ν is the molecular volume, and T is the absolute temperature. Nucleation rate is, therefore, dependent on temperature, the degree of saturation, and the interfacial tension, with supersaturation being the most important factor in initiating the start of nucleation.

Induction time, or the time a solution containing precipitate constituents takes to form the first measurable form of the precipitate, is also important to the crystallization process. This time frame includes the nucleation time as well as the time it takes the crystal to grow to a detectable size, or growth time (Jones, 2002). Induction time also depends on the degree to which a solution is supersaturated, temperature, and the presence of other ions or impurities in solution (Ohlinger et al., 1999). Agitation has also been shown to influence nucleation, with Mullin (1992) finding that nucleation can be induced by mixing.

Many studies highlight the effects of agitation on induction time. For example, with no agitation and a supersaturation ratio of Ω = 2.5, spontaneous precipitation of struvite had an induction time of 24 hours (Abbona and Boistelle, 1985). However, with constant agitation via a magnetic stirrer at a similar saturation ratio (Ω = 2.27), the induction time was reduced to 42 minutes (Bouropoulos and Koutsokos, 2000). This suggests that agitation reduces the time needed for crystallization by enhancing nucleation.

Following nucleation is crystal growth, which is the further development of the mineral until equilibrium is reached. Growth rate is controlled by mass transfer and mechanisms of surface integration. Mass transfer describes the transfer of solutes in solution to the surface of the nucleated crystal via diffusion or convection or both (Mullin, 1992). In diffusion theory, it is assumed that the crystallization rate was governed by the difference in concentration between the solid surface and the bulk solution. Nerst, 1904 hypothesized that molecules of the solute had to transfer through a stagnant film around the growing crystal face in order to attach and grow, with the stagnant film thickness being dependent on the degree of agitation of the system. Jones, 2002 described crystal growth rate (G) as the variation in crystal size (L) versus the time it takes (t), shown in Equation 15.

$$G = \frac{dL}{dt} = k_g \sigma^g \quad (15)$$

Where k_g represents the growth constant and σ^g the relative supersaturation with g = 1 for diffusion-controlled growth and g = 1-2 or >2 for surface integration-controlled growth. Theoretical principles for crystal growth are difficult to establish from experimental results, so often more practical parameters for crystal growth are considered such as measuring the disappearance of solid phase constituent ions (i.e. Mg, N, P) and fitting an assumed rate equation to determine rate constants.

Agitation plays a critical role in both induction time and crystal growth rate. While some studies, such as Ohlinger et al., 1999, show minimal influence of mixing energy on struvite induction time, there is consensus that agitation impacts the growth rate. In their study, with mixing speeds varying from 360-1060 rpm, struvite crystals formed under higher mixing intensities grew at a rate of 22.4 g/(m²·d), compared to 1.8 g/(m²·d) in quiescent conditions. The increased mixing led to more compact and less elongated crystals, suggesting that high energy promotes surface integration growth and reduces transport limitations. Nucleation rates can also be accelerated by high-speed mixing, as demonstrated by Durrant et al., 1999. Mixing energy not only affects nucleation but also helps minimize boundary layers around growing crystals, facilitating quicker attachment and growth of the solute molecules. Thus, increased turbulence and agitation reduce induction time and enhance overall crystallization kinetics, supporting faster and more efficient crystal formation.

2.2.3.2 Struvite Kinetics

The kinetics of struvite growth have been well studied in literature but have not quite converged as it can depend on many parameters such as the supersaturation ratio, pH, temperature, mixing intensity, and organic solids content. Ohlinger et al., 1999 determined the struvite nucleation process to most strongly depend on the supersaturation level, but the growth rate to be transport-limited and most strongly dependent on the mixing intensity. Later, Ohlinger et al., 2000 reported that struvite formation followed a pseudo first order kinetic relationship, with a rate constant estimated as 4.2 h^{-1} at a pH of 8.3. Nelson et al.,

2003 confirmed that struvite kinetics fit a first-order model, with the rate constant increasing with pH: 3.7 h^{-1} at pH 8.4, 7.9 h^{-1} at pH 8.7, and 12.3 h^{-1} at pH 9. However, Bouropoulos and Koutsoukos, 2000 observed second-order kinetics when struvite concentrations were oversaturated in solution. Other authors have found struvite kinetics to depend on mixing intensity and Mg:P ratios as well, with increasing kinetic rate constants as mixing intensity increased and as the Mg:P ratio increased (Ven Rensburg et al. 2003; Quintana et al. 2005). Rahaman et al., 2008 completed a comprehensive study to determine which process parameters most effected struvite precipitation kinetics out of supersaturation (9.64 – 1.13), pH (7.6-8.5), Mg:P ratio (1:1 – 1.6:1), degree of mixing (70 – 100 rpm), and seeding conditions (seeded vs unseeded) at 20°C and determined that the supersaturation ratio, and therefore pH, and the Mg:P ratio had the greatest impact on struvite kinetics, whereas the mixing intensity and seeding conditions tested had minimal impact on OP-P removal. Therefore, all of these parameters are important to consider in phosphorus precipitation experiments.

The pH change induced by struvite formation is another important kinetic factor. According to equation 1, the reaction of struvite formation causes a release of protons, which leads to a reduction in pH of the solution. Therefore, the pH change can be used as an indicator of the nucleation of struvite (Bouropoulos and Koutsoukos, 2000). The reduction in pH induced by struvite's formation indicates how fast the reaction and crystallization occurs. This study also found that the higher the initial pH of solution, the faster the reaction speed. However, the study stated that in real wastewaters, the existence of alkaline ions and other foreign substances will impose different pH decreases due to buffer capacity (Liu et al., 2018). This is important to note especially for the case of anaerobic digestate undergoing the significant pH change from a digester headspace to atmospheric CO_2 concentrations, as well as many other dynamic chemical, physical, and biological changes that may be buffering this system.

Solution pH can also affect crystal growth rate and size. Ohlinger et al., 1999 demonstrated that higher pH leads to increased supersaturation and faster growth rates. However, Moulessehoul et al., 2017 found that in lower pH values of 8.5 and 8.7 as compared to higher pH values tested of 10.5 and 11.8, struvite had faster induction times for crystal growth, which lead to larger and more crystalline aggregates confirmed by XRD and SEM analysis. Shaddel et al., 2019 further found that while particle size decreased as pH increased, the production of struvite fines (<10 μm) was highest at pH 9.5, indicating a tradeoff between precipitation efficiency and the potential loss of fines during harvesting. Therefore, despite pH 9 being commonly listed peak insolubility for struvite, many struvite recovery facilities aim for a pH range of 7.4-8.0 to minimize fines production (Wisdom et al., 2017).

Temperature is another key factor influencing struvite crystallization kinetics. Jones, 2002 noted that high temperatures tend to favor diffusion-controlled crystal growth within solution, while lower temperatures favor surface integration-controlled growth, requiring a

surface to scale onto. Jones also states the rate of precipitation is often increased at higher temperatures. Boistelle et al., 1983 demonstrated struvite crystals grow in a “rectangular and prismatic” way at 25°C and more “square and thick” growth was seen at the increased temperature of 37°C. Experiments by Abbona et al., 1982 showed that higher temperatures significantly favored the precipitation of newberyite over struvite, while Babic-Ivancic et al., 2002 found that elevated temperatures accelerated the transformation of struvite into newberyite, particularly in the presence of high magnesium concentrations and low pH levels, thus showing temperature effects on the nature of the crystal formed.

Recent studies have examined the impact of organic solids on struvite formation and revealed varying effects depending on the concentration and solids type. Tarragó et al., 2018 observed a decrease in phosphorus recovery from 99.3% to 93.5% as the solids load increased from 0.16 to 10.73 g TSS/L/day. They found that suspended solids acted as nuclei which enhanced heterogeneous nucleation and agglomeration during struvite crystallization, but also limited individual crystal sizes. Without solids, crystal sizes around 200 μm were obtained, while the presence of solids reduced this size to about 100 μm due to an increase in nucleation sites, which favored nucleation over crystal growth. Likewise, Ping et al., 2016, found that high concentrations of total suspended solids (in the range of 116–194 mg/L) could inhibit struvite precipitation and reduce particle size by half.

Muhmood et al., 2021 studied the effects of organic substances in poultry slurries on struvite formation and found that particulate and colloidal organic substances slowed the precipitation reaction but increased struvite particle size by 70% and 40%, respectively. Humic substances were found to hinder struvite formation through adsorption and ionic exchange, and organic acids present in anaerobic digestate, such as citric, succinic, and acetic acids, interfered with crystallization (Song et al., 2014). Citric acid had the strongest inhibitory effect. Muhmood et al., 2021 also noted that that within the pH range of 8-9, higher organic solids content in digested solids led to more significant nutrient recovery inhibition. This was hypothesized to be due to the higher prevalence of humic acid and other similar substances at these lower pH ranges compared to some high pH values tested. Negatively charged humic acid substances can complex with the necessary positive components for struvite formation such as Mg^{2+} and NH^{4+}. The greatest inhibition occurred in samples containing a mix of particulate, colloidal, and dissolved organic matter, while the least inhibition was observed in samples with only dissolved organics. Organic substances also slowed the rate of struvite precipitation, doubling the reaction time, with particulate substances having the slowest reaction speed, followed by colloidal and dissolved substances.

Precipitation chemistry is complex and depends most on solubility, saturation, and crystal growth kinetics. Therefore, a deep understanding of the multitude of factors affecting precipitation chemistry is required, such as thermodynamics, pH, temperature, mixing

intensity, mass transfer between liquid-solid equilibrium, kinetics, the existence of foreign ions, and solids characteristics.

2.3 Current P Recovery Technologies

For WRRFs that have low effluent phosphorus limits such as 2 mg/L or below, or desire to decrease the overall phosphorus recycle load on the plant, there are several current innovative technologies that enhance the common P removal and recovery strategies already in place.

2.3.1 Ostara Technologies

Ostara has two relevant technologies: the Ostara Pearl® and WASSTRIP®. These are often coupled together for maximum struvite recovery efficiency.

2.3.1.1 Ostara Pearl

The Ostara Pearl® is an upflow moving bed reactor that enables continuous struvite crystallization. The Pearl® reactor is designed to remove phosphorus from the nutrient-rich pre- or post-anaerobic digestion thickening and dewatering liquors via the controlled precipitation of struvite. Magnesium (as $MgCl_2$ or MgO) and caustic are dosed to the influent of the reactor to supersaturate struvite as well as raise the pH to induce precipitation. The Pearl® reactor is also seeded initially with struvite particles around 1 mm in diameter to advance the nucleation step into crystal growth. The reactor is designed in a three-tier fashion to allow three separate flow controls to optimize the suspension of growing crystals in the middle, the fines to be maintained at the top and ideally the collection of the largest particles to develop and fall out at the base. The resulting products are treated effluent discharged from the top of the reactor with a reduced nutrient content and pure, slow-release struvite particles harvested out of the base marketed as a fertilizer called Crystal Green® (Ostara Nutrient Recovery).

Ostara claims up to 85% P and 40% N removal rates, and a generated revenue from Crystal Green to offset operating costs. At HRSD's Nansemond Wastewater Treatment Plant a Struvite Recovery Facility (SRF) utilizing the Ostara Pearl® 500 reactors dosed with $MgCl_2$ salt has operated for 10 years and achieved about 85% recovery of phosphorus. Since 2018, HRSD has piloted and been in transition to use the cheaper alternative of MgO. However, the generation of too fine of struvite crystals to be harvested, or fines, have been reported which can cause upsets like lower fertilizer production than expected and loss of P removal to fines in the effluent. Efforts are currently in place at Nansemond to reduce the fines loss by installing lamella plate settlers to assist in collection of these fines.

2.3.1.2 WASSTRIP

The Waste Activated Sludge Stripping To Remove Internal Phosphorus (WASSTRIP®) process was developed by Clean Water Services to reduce struvite precipitation in digesters

fed with nutrient-rich EBPR sludge and to divert more P to a struvite crystallizer such as the Ostara Pearl®. The WASSTRIP® process acts as a side stream anaerobic tank to induce the release of P by PAOs (along with magnesium and potassium counter ions) before anaerobic digestion. However, due to no digestion occurring in the WASSTRIP® process the centrate is still low in ammonia and does not promote the precipitation of struvite and, therefore, better protects the digesters from scale build up. The P rich supernatant is then directly sent to and combined with dewatering liquors in the Pearl® for improved struvite harvesting. WASSTRIP® also claims to reduce the negative effects of EBPR on dewaterability. The hydraulic retention time (HRT) for the WASSTRIP® process is dependent on the P content and volatile fatty acid (VFA) availability in WAS. WASSTRIP® can be operated endogenously on waste activated sludge (WAS) alone if sufficient VFAs are present to be absorbed, or VFAs can be supplemented to accelerate P release and reduce the HRT required (Gysin et al., 2018).

2.3.2 Centrisys CNP Technologies

Centrisys CNP has two relevant technologies: MagPrex™, which is a struvite recovery technology, and CalPrex™, which is a brushite recovery technology.

2.3.2.1 MagPrex™

Different from those technologies described above, CNP's MagPrex™ increases the pH of a solution by stripping CO_2 via aeration rather than adding a chemical base. Magnesium is added in the form of $MgCl_2$ to enhance struvite formation. MagPrex™ operates on anaerobic digestate and before polymer conditioning and final dewatering. Struvite can either be harvested as crystals or sequestered in the biosolids. This process can reduce phosphorus recycle loads around a plant and protect downstream dewatering equipment from struvite formation. CNP claims up to 90% OP removal, 3% higher TS in cake which also reduces disposal costs, and 20-30% reduction in polymer use (Centrisys CNP - MagPrex). The HRT for this process is on the scale of a few hours. The Metro Wastewater Reclamation District in Denver, Colorado piloted this process in 2016 and reported a 20% reduction in polymer demand and a 10% decrease in cake hauling costs. Orthophosphate conversion was as high as 90%, however it was estimated that only 20% of P was actually recovered due to the production of fines and difficulty to capture the struvite crystals into the biosolids, which was supported by the increase of particulate phosphorus measured in the centrate (Wisdom et al., 2017). Higher concentrations of magnesium have been reported to affect the size of struvite crystals formed, and purity due to an increased potential of Mg precipitates forming (Korchef et al., 2011). Too short of an SRT used has also been hypothesized in this thesis to affect crystal maturity and size. This study illustrates the need for a further understanding of the phosphorus removal mechanism via sequestration into biosolids.

2.3.2.2 CalPrex™

Similar to WASSTRIP, CNP's CalPrex™ technology acts as a side stream anaerobic tank to induce the release of P by PAOs after a P-release fermentation tank and prior to anaerobic digesters to reduce the potential for struvite formation in the digesters. However, CalPrex™ doses calcium hydroxide to recover phosphorus in the form of brushite as a comparable, high-quality fertilizer. This operates on an SRT of 12-36 hours prior to anaerobic digestion and can provide a low oxygen environment that promotes 60% of P solubilization without additional chemicals at Bio-P plants. Brushite ($CaHPO_4 \cdot 2H_2O$) is formed at a pH less than 7, so no caustic or aeration addition is required for pH elevation as compared to P recovery as struvite. Also different from struvite, brushite does not require ammonium. The downside of this is there is no additional N removal benefit with brushite. CNP claims CalPrex can divert 70% of soluble P from the digesters, and reduce up to 50% TP in biosolids, and reduce disposal costs up to 50% (Centrisys CNP – CalPrex).

2.3.3 Post-Aerobic Digestion

Post-Aerobic Digestion (PAD) is an advanced digestion process that applies anaerobic digestion followed by aerobic digestion. PAD can provide total nitrogen removal without the need for a supplemental carbon source or alkalinity, as well as additional volatile solids reduction (VSR), which can reduce biosolids for disposal. This aerobic digestion can help to treat the high nutrient and soluble organic loads after anaerobic digestion. Ammonia removal occurs in PAD reactors and can fully rely on the available carbon content leaving the anaerobic digester (Bauer et al., 2016). Aerobic microbes in PAD reactors that complete this ammonia removal do not have enough carbon to increase their biomass as they do in activated sludge; therefore, they undergo endogenous decay, which leads to additional VSR. In a study at a 9-day digester SRT, the average VSR observed was additional 32 ± 5.8% and the average ammonia removal was 81 ± 2.3% with complete denitrification (Menniti et al., 2010). Novak et al., 2009 reported 12% VSR and 90% TAN removal in a PAD digester at an SRT of 5 days. These studies suggest additional research is needed for the plausibility of additional VSR and nitrification occurring in PAD at an SRT as low as 3 days and high ammonia concentrations in anaerobic digestate. The likelihood of partial nitrification or nitritation occurring is important as it would consume alkalinity and therefore alter the pH and solubility of precipitates in this system that are favored to form.

Whether nitrification occurs in PAD systems also depends on competition with Ordinary Heterotrophic Organisms (OHOs). Solids content of PAD is much higher than mainstream processes, which results in higher oxygen uptake rates, and leads to low or non-detectable dissolved oxygen concentrations. This environment helps promote the postulated nitrogen removal mechanism of simultaneous nitrification and denitrification (SND) or short cut nitrogen removal. However, heterotrophic organisms exist that are capable of both nitrification and denitrification under aerobic conditions. Aerobic systems with low DO environments (< 1 mg/L) and negative ORP values can support denitrification as SND or

nitritation/denitritation (Novak et al., 2011; Sabba et al., 2022). Nitritation/denitritation (nitrite shunt) can utilize nitrite rather than conventional nitrate as an intermediate and further reduce nitrite directly to nitrogen gas via denitritation (Roots et al., 2020). OHOs have been shown to thrive in carbon-rich and low DO environments, which promotes out competition for NOB (McNamara et al., 2022). Winkler et al., 2012 similarly noted that these conditions are more ideal for OHOs due to their fast growth rates and lead to this competition for nitrite. Understanding the biological activity that occurs within PAD is just as important as the physical and chemical processes and must be considered with the other goals of this project.

2.3.3.1 Relationship Between Nitrogen and pH in PAD

Nitrogen and pH have a crucial connection to one another in the context of PAD. Nitrogen can be removed in this system via precipitation in the form of struvite, via ammonia stripping, or via partial nitrification/nitritation. pH change is both the cause and effect of all three of these phenomenon's occurring.

As previously discussed, in order for struvite to form, the solution pH must be high enough to enter the range of insolubility for struvite. If struvite forms, alkalinity is consumed and thus the pH of the solution decreases (Equation 1). Struvite is the most likely precipitate to form at WRRFs that can contribute to nitrogen removal via precipitation. Therefore, if the pH shifts from any of these following mechanisms, it could lead to a shift in solubility in favor of a different mineral's formation that might not contribute to nitrogen (or even phosphorus) removal.

Nitrogen can also be removed in PAD via the transfer of ammonium to ammonia and subsequent volatilization. In aqueous solutions, total ammonia exists as both free ammonia and ammonium ions as shown in equation 16.

$$NH_4^+ + H_2O \leftrightarrow NH_3 + H^+ \quad (16)$$

Ammonium (NH_4^+) is an acid and ammonia (NH_3) is its conjugate weak base, together they act as a solution buffer. The equilibrium constant for ammonium ($K_{NH_4^+}$) can then be written as Equation 17, which is known to be $10^{-9.3}$ (Stumm and Morgan, 1996).

$$K_{NH_4^+} = \frac{[NH_3][H^+]}{[NH_4^+]} = 10^{-9.3} \quad (17)$$

Arranging the above expression gives Equation 18 below, which can be used to solve for the pH of the solution.

$$\frac{[NH_4^+]}{[NH_3]} = \frac{[H^+]}{K_{NH_4^+}} \quad (18)$$

Therefore, the ratio of ammonium to ammonia directly influences the pH of a solution and vice versa. As the pH increases towards the $K_{NH_4^+}$ more ammonium is converted to ammonia, which can then be transferred from the liquid to gas phase and removed via volatilization or stripping. The equilibrium between ammonium and ammonia is continuously satisfied with changing pH and stripping. Conventional ammonia stripping processes require a pH range of 10-12 (Gustin and Marinsek-Logar, 2011). However, lower pH values have still been shown to contribute to ammonia stripping. In this same study by Gustin and Marinsek-

Logar, 2011, using an ammonia stripping column, a pH range of 8.5-11.0 was tested to measure the effects on ammonia removal efficiency, and it was shown to have the greatest effect compared to temperature and the air to liquid flowrate ratio. At the lowest pH tested of 8.5, they measured ammonia removal efficiency to be 27.4%, which continued to increase as pH increased. Therefore, moderate ammonia stripping can still occur at these lower pH values tested (pH 8.5) as a nitrogen removal mechanism.

Nitrogen can also be removed from PAD systems via partial nitrification or nitritation, which consumes alkalinity. Determination if nitrification is occurring in a PAD system focused on phosphorus removal is crucial, as it can cause a decrease in pH which can alter the phosphate mineral formed. Nitrification can be inhibited by many factors such as alkalinity, DO, temperature, SRT, and substrate concentration (NH_3). Alkalinity is required for nutrient removal in PAD reactors. Ammonia removal requires 7.14 mg/L as $CaCO_3$ per 1 mg N/L oxidized. Likewise, 3.57 mg/L as $CaCO_3$ of alkalinity is produced per 1 mg N/L reduced during denitrification. Low carbonate alkalinity (<100 mg/L as $CaCO_3$) has been reported as inhibitory to nitrification rates, as alkalinity in the carbon form, and not just as added hydroxide, is the inorganic carbon source for AOB and NOB (Biesterfeld et al., 2003). Nitrifying bacteria are also extremely sensitive to DO concentrations. The oxygen half-saturation coefficient for aerobic autotrophs ($K_{O,A}$) is higher than that of aerobic heterotrophs ($K_{O,H}$) which indicates that nitrifiers are much more affected by a decrease in oxygen concentration than heterotrophs (Grady et al., 2011). There is a minimum SRT required for nitrifier growth, or the SRT at which point washout of nitrifiers begins, and this SRT is heavily dependent on both DO concentration and temperature. The minimum SRT required for nitrification increases as either DO or temperature decrease (Grady et al., 2011). This can be calculated with Equation 19, provided by the same textbook:

$$\Theta_{c\,min} = \frac{K_S + S_{SO}}{S_{SO}(\hat{\mu}_A - b_A) - K_S \cdot b_A} \quad (19)$$

Where $\Theta_{c\,min}$ is the minimum SRT, K_s is the half saturation constant for the substrate, S_{SO} is the initial readily biodegradable substrate concentration, $\hat{\mu}_A$ is the maximum specific growth rate for autotrophs, and b_A is the decay coefficient for autotrophs.

Research points to the predominant nitrogen removal mechanism in PAD being short-cut nitrogen removal. Nitrite production rates were several orders of magnitude greater than nitrate and after studying the microbial community in PAD reactors, meaning AOBs were much more abundant than NOBs (Sabba et al., 2022). The nitrogen removal pathway heavily effects aeration requirements and carbon demand, such as short cut N removal requires less oxygen and carbon than SND.

Now the question becomes: can nitrification occur at the operation pH of a PAD reactor focused on CO_2 stripping and phosphorus precipitation? The interaction of factors such as pH and inhibitory compounds influences the rate of nitrification. High concentrations of most notably ammonia and nitrite in high organic or ammonia nitrogen containing solids streams have been shown to inhibit nitrifiers. When NOB (Nitrobacter) are inhibited, nitrite will accumulate, and when AOB (Nitrosomonas) are inhibited, ammonia will accumulate

(Anthonisen et al., 1976). Solution pH directly contributes to this phenomenon and can increase free ammonia levels (FA). FA is a substrate for AOB, it also has potentially inhibitory effects on nitrification at high concentrations. The FA concentration depends on pH, temperature, and ammonium concentration (Anthonisen et al. 1976). FA has been shown to more easily inhibit NOB than AOB, as inhibitory levels of FA for each are between 0.1 to 1.0 mg/L and 10-150 mg/L, respectively (Anthonisen et al., 1976). Due to the nitrogen removal pathway most likely being via a nitrite shunt in PAD, NOB can further be suppressed depending on reactor pH and ammonium accumulation (Sabba et al., 2022).

McNamara et al., 2022 concluded that in healthy PAD reactors, the pH should be around 6.0-7.5 to decrease the potential accumulation of inhibitory compounds such as free ammonia. Optimal pH for AOB is about 7.8 and varies between 6.2 and 8.2 for NOB (Alleman et al., 1985). pH values above 8 can directly result in more free ammonia. This elevated free ammonia leads to a negative feedback loop for nitrogen removal in that nitrification inhibition leads to a buildup of total ammonia and consequently more toxic free ammonia (McNamara 2022). In a full-scale PAD reactor operated at Denver's Northern Treatment Plant, lime addition is supplemented for phosphorus precipitation. This pH increase from the lime addition converts CO_2 to dissolved carbonate, and the calcium precipitates with phosphorus to help remove dissolved phosphorus that otherwise gets recycled to the head of the plant. This excess lime addition raised solution pH to about 8.0, and lead to toxic free ammonia levels greater than 10 mg N/L which inhibited nitrification and decreased PAD performance efficiency (McNamara, 2022). Overall, high ammonia levels coupled with pH values above 8 in a PAD reactor may lead to inhibition of any partial nitrification occurring.

2.4 Controlling Precipitation Reactions for Phosphorus Recovery and Mineral Characterization

Within the literature review outlined above, the importance of phosphorus recovery in biosolids via precipitation reactions and how to control these reactions is addressed. A deep understanding of mineral solubility and saturation, crystal formation and growth, and all other factors affecting precipitation chemistry such as pH, temperature, mixing intensity, and foreign ions is required. There has been commercial success with phosphorus recovery technologies and side stream nutrient removal mechanisms such as PAD, however, issues remain around the optimization of phosphorus removal in specific cases such as phosphorus recovery loss due to fines, chemical and aeration costs, and characterizing the minerals formed within such a system.

Therefore, a pilot experimental setup utilized aeration for pH control and chemical addition of $Mg(OH)_2$ and $Ca(OH)_2$ to anaerobic digestate on a 3-day SRT to optimize phosphorus removal, understand the effects on N and COD removal, and characterize the minerals formed. The 3-day SRT is longer than commercial P recovery technologies and is hypothesized to allow more time for crystal growth to better sequester phosphorus in biosolids and diminish losses due to fines. The 3-day SRT is also shorter than traditional PAD

processes, and challenges whether additional benefits such as solids destruction and ammonia removal can also be achieved on this scale. A long-term pilot operation testing aeration control settings, $Ca(OH)_2$ versus $Mg(OH)_2$ and various Ca^{2+}+Mg^{2+}:P dosages at this SRT can be significant to plants that desire to decrease phosphorus loads in the solids recycle lines and nuisance scaling in a more cost effective manner than some commercially available technologies. Parameters measured in each pilot test were modeled with the chemical equilibria software Visual MINTEQ to determine the effects of pH, temperature, chemical choice and dose on minerology. The precipitates formed within pilot testing were then analyzed with Scanning Electron Microscope (SEM), Energy Dispersive X-ray Spectroscopy (EDS), X-Ray Diffraction (XRD) analysis, and Raman Spectroscopy to calibrate and confirm the model results. A validated model could then be used to predict scaling potential and characterize minerals formed at WRRFs to better treat these nuisance scaling minerals and determine their potential for harvesting/sequestration as a nutrient-rich product. Both a pilot project such as this as well as the Visual MINTEQ modeling work on it are missing from the current body of knowledge.

3. Materials and Methodology

3.1 Solids Characteristics

Solids utilized throughout pilot testing were real solids from Hampton Road Sanitation District's Atlantic Treatment Plant (ATP). ATP is a high-rate facility with an A/O process configuration and ocean outfall. Within the A/O configuration, the plant utilizes an anaerobic selector to promote better solids settling and to control filaments. As a result of this, the plant indirectly achieves good EBPR in the liquid stream. The solids then consist of a blend of waste activated sludge from this EBPR process and fermented primary solids, as well as addition from fats, oils, and grease (FOG). The solids undergo thermal hydrolysis pretreatment in a Cambi B6-4 unit before anaerobic codigestion and are then stored in the anaerobic, mixed DSST for about 3 days. The solids then are dewatered with centrifuges to form Class A biosolids for land application. Due to the EBPR solids' exposure to anaerobic digestion, the plant is experiencing scaling issues within the digesters and on final dewatering equipment. As an effort to solve this problem, an ongoing pilot study was set up. The pilot was set in place after anaerobic digestion and before final dewatering with a SRT of 3 days to simulate the DSST and determine the optimal operation for OP-P removal and struvite control. The pilot influent flows directly from the DSST and is nutrient-rich digestate with typical phosphorus concentrations between 800 – 1000 mg/L and an ammonia-nitrogen concentration around 2400 – 2800 mg/L. Typical influent magnesium and calcium concentrations range from 5 – 12 mg/L and 15 – 30 mg/L, respectively. Digestate typically has a pH of around 7.5, and a temperature around 35°C. Alkalinity in digestate ranges from 7000 – 8000 mg as $CaCO_3$/L.

3.2 Pilot Design

The pilot setup at ATP consisted of four tanks (Figure 4). Each tank was 11 feet tall with a volume of about 44 gallons. Simulating the DSST, the tanks were operated as daily batch fed continuously stirred tank reactors (CSTRs) mixed by pump recirculation with a 3-day SRT. The mixing pumps had a tank turnover rate of less than two minutes (Equation 62 in Appendix B). Digestate was passed through a 2 mm basket screen before being fed to the tanks to screen out fibrous material and additional grit to protect pilot equipment. The tanks were aerated with fine bubble diffuser membranes at the base of each tank which could be operated at constant or intermittent air flow rates, on a DO setpoint, or pH setpoint. Each tank contained probes to record online measurements of temperature, DO, and pH (INSITE IG®). The tanks were temperature controlled to best match the temperature in the pilot to the temperature of digestate within the DSST. In the summer months temperature was controlled with heat exchangers flushing Non-Potable Water (NPW), i.e. treated secondary effluent, around the mixing lines at a setpoint of 35ºC, and in the winter each tank was wrapped with fiberglass insulation panels to maintain heat. Effluent samples from each tank, as well as the pilot influent (e.g. digestate), were gathered throughout each test at the end of the 24-hour batch waste and feed timer to track steady state characteristics.

Figure 4: Pilot scale set up featuring the control tank 1, and tanks 2, 3, and 4 from left to right.

The chemical injection set up utilized positive displacement chemical feed pumps which pulled chemical from a continuously mixed tank to spike or dose the pilot tanks on an hourly timer at the desired dosage ratios directly into the recirculation line. The chemical dosage was followed by a NPW flush to clean the feed lines and push any remaining chemical into the tanks (Figure 5).

Figure 5: Chemical dosing setup for the pilot.

Figure 6 exhibits the setup during pilot trials.

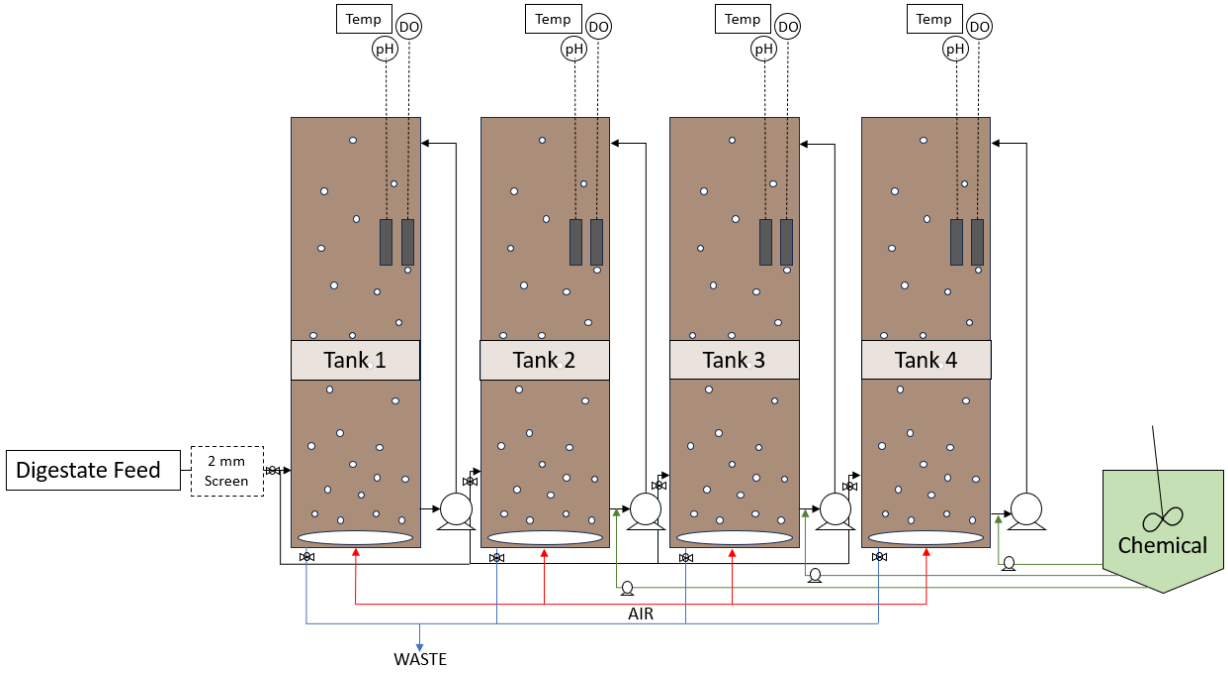

Figure 6: Pilot scale schematic featuring the control tank 1, and tanks 2, 3, and 4 from left to right, waste and feed lines, diffusers, probes, mixing pumps, and chemical injection.

3.3 Pilot Operation

After pilot build out and start up (June 2023 – April 2024), the pilot was operated during the months of April through October of 2024. Six campaigns were conducted on the pilot scale to determine the effects of aeration and mixing and chemical addition of magnesium in the form of $Mg(OH)_2$ (Thioguard via Premiere Magnesia) or calcium in the form of a $Ca(OH)_2$ slurry at various Ca^{2+}+Mg^{2+}:P molar dosage ratios. To determine the optimal aeration operation, aeration was controlled at a constant aeration setting of 5 LPM, at a DO setpoint of 0.2 mg/L, and at various pH set points. To determine the optimal chemical dose for each chemical, different dosage ratios of $Mg(OH)_2$ and $Ca(OH)_2$ were tested. The tanks were dosed at Ca^{2+}+Mg^{2+}:P molar dosage ratios of 0:1 (control), 0.25:1, 0.5:1, and 1:1 in Campaigns 1-4, and increased up to 1.3:1 and 1.6:1 for Campaign 5. The effects of mixing versus no mixing were also explored in Campaign 4.1. Finally, campaign 6 tested aeration controlled by pH setpoints at pH 7.5, 8, 8.5, and 9. One variable was changed at a time to determine the individual impact of each parameter tested to narrow down to the optimal operational efficiency. Table 2 below details the operating conditions for each campaign conducted.

Table 2: Operational conditions for each testing campaign including: test name, chemical injected, Ca^{2+}+Mg^{2+}:P ratio dosed to tanks 1-4, respectively, the aeration setting, and mixing condition.

Test Name	*Chemical Injected*	*Dosages in Tanks 1-4 (Ca+Mg:P)*	*Aeration Setting*	*Mixing*
Campaign 1	$Mg(OH)_2$	0, 0.25:1, 0.5:1, 1:1	Constant: 5 LPM	Yes
Campaign 2	$Mg(OH)_2$	0, 0.25:1, 0.5:1, 1:1	DO setpoint: 0.2 mg/L	Yes
Campaign 3	$Ca(OH)_2$	0, 0.25:1, 0.5:1, 1:1	Constant: 5 LPM	Yes
Campaign 4	$Ca(OH)_2$	0, 0.25:1, 0.5:1, 1:1	DO setpoint: 0.2 mg/L	Yes
Campaign 4.1	$Ca(OH)_2$	0, 0.25:1, 0.5:1, 1:1	DO setpoint: 0.2 mg/L	No
Campaign 5	$Mg(OH)_2$	0, 1:1, 1.3:1, 1.6:1	DO setpoint: 0.2 mg/L	Yes
Campaign 6	None	None	pH setpoints: 7.5, 8, 8.5, 9	Yes

3.4 Pilot Start Up Procedure

A pilot start up procedure was followed prior to each campaign to provide consistent methods. The pilot tanks were first filled with fresh digestate. The DO probes were zeroed, and the pH probes were calibrated on a two-point scale with solution buffers at pH 7 and 10. Before beginning a chemical injection test, the tanks were operated at the aeration and mixing setting that was to be used in the testing period and online data recordings were checked for stability in pH and DO measurements. Influent and effluent samples were collected three times a week for the following analyses: orthophosphate (TNT 845), ammonia (TNT 833), total alkalinity (TNT 870), water hardness (Ca^{2+}, Mg^{2+}, and $CaCO_3$) (TNT 869), total chemical oxygen demand (COD) (TNT 823), and soluble COD (TNT 822) defined at 0.45 micron filter size, all with HACH TNTplus Vial Tests, as well as total solids (TS), and volatile solids (VS) via standard methods (2540 G - 1991). Sample collection continued until the standard deviation of each tank normalized to the combined average for all the tanks was under 5% for each parameter measured to ensure stability and comparability across the pilot tanks. This usually required 3 SRTs (a nine-day period). Once the tanks were performing similarly, chemical could be introduced and could be assumed to be the only independent variable. Prior to chemical addition, another sample was collected and analyzed for soluble metals via filtering and ICP-AES (EPA 200.7 rev 4.4) and volatile acids via standard methods (5560 C - 2011) by the HRSD's Central Environmental Lab (CEL). Table 3 below displays the pilot laboratory analysis and methods.

Table 3: Pilot laboratory Analysis.

Parameter	Method
Ortho Phosphate	Hach TNT 845, Ascorbic Acid
Ammonia	Hach TNT 833, Salicylate
Total Alkalinity	Hach TNT 870, Colormetric
Water Hardness	Hach TNT 869, Metalphthalein
Soluble COD	Hach TNT 822, Filtered, Reactor Digestion
Total COD	Hach TNT 823, Reactor Digestion
Total Solids, Volatile Solids	Standard Methods 2540 G - 1991
Soluble Metals	Filtered, ICP-AES (EPA 200.7 rev 4.4)
Total Volatile Acids	Standard Methods 5560 C - 2011

Influent and pilot effluent analysis performed with Hach tubes were used to monitor the efficiency of the pilot process. This efficiency is predominantly determined by how much phosphorus is removed from the system as a precipitate. Phosphorus removal, calculated by Equation 20, is important when monitoring precipitation reactions as it can infer how well the digestate is being treated for phosphorus and how much struvite may be produced in the reactor to be sequestered into the Class A biosolids.

$$Phosphorus\ Removal\ (\%) = \left(\frac{Influent\ Phosphorus\left(\frac{mg\ PO4-P}{L}\right) - Effluent\ Phosphorus\left(\frac{mg\ PO4-P}{L}\right)}{Influent\ Phosphorus\left(\frac{mg\ PO4-P}{L}\right)}\right) \times 100 \quad (20)$$

This equation assumes phosphorus removed has been precipitated from the system and phosphorus is either sequestered as a phosphorus mineral in the biosolids or released from the system as soluble phosphorus or as small fines in the effluent. Phosphorus removal can be calculated for OP-P or TP-P removal. OP-P removal is measured to quantify the soluble phosphorus removed from the digestate.

3.5 Magnesium Hydroxide Addition Pilot Tests

Magnesium hydroxide ($Mg(OH)_2$) in the form of Thioguard via Premiere Magnesia was injected in campaigns 1, 2, and 5 for supplemental magnesium addition. Prior to each campaign, a batch of chemical was made and diluted by a factor (DF) of 20 to prevent chemical clogging. The chemical slurry was made down in the 15-gallon, conical chemical tank pictured in Figure 4. The 20X slurry was prepared by determining the necessary $Mg(OH)_2$ mass to add to the 15-gallon tank, and the remainder of the tank volume was filled with NPW. The manufacturer listed density for thioguard of 1.45 g/mL was used. The mass of $Mg(OH)_2$ product was solved for using equation 21:

$$Mass\ of\ Mg(OH)_2\ (g) = \frac{Total\ volume\ (gal)}{DF} \times 3785.41 \frac{mL}{gal} \times Mg(OH)_2\ density\ \left(\frac{g}{mL}\right) \quad (21)$$

Once the diluted chemical solution was made, it was mixed with a caframo overhead impeller that rested on a frame seated on the chemical tank at 400 rpm to keep the $Mg(OH)_2$ in suspension.

Pilot campaigns were conducted under specific Ca^{2+}+Mg^{2+}:P ratios. A ratio of Ca^{2+}+Mg^{2+}:P rather than simply Ca^{2+}:P or Mg^{2+}:P to account for background ions within both thioguard and the carbide lime slurry used as chemicals, as well as within digestate. To achieve a desired Ca^{2+}+Mg^{2+}:P ratio it was necessary to measure the background OP, Ca^{2+}, and Mg^{2+} levels in digestate, and dose $Mg(OH)_2$ appropriately. HRSD's CEL first analyzed the neat $Mg(OH)_2$ chemical as a solid for total Ca^{2+} and Mg^{2+} (mg/kg) using the EPA 6010D method (SW-846). This wet weight can be converted to mmol/L using the following equations for both calcium and magnesium, then the concentrations can be summed to determine the Ca^{2+}+Mg^{2+} mmol/L in $Mg(OH)_2$.

$$Ca^{2+}\left(\frac{mg}{kg\ wet}\right) \times \left(\frac{1\ kg}{1000\ g}\right) \times Mg(OH)_2\ density\ \left(\frac{g}{mL}\right) \times \left(\frac{1000\ mL}{1\ L}\right) \div 40 \frac{mg}{mmol} \quad (22)$$
$$= Ca^{2+}\left(\frac{mmol}{L}\right)$$

$$Mg^{2+}\left(\frac{mg}{kg\ wet}\right)\times\left(\frac{1\ kg}{1000\ g}\right)\times Mg(OH)_2\ density\ \left(\frac{g}{mL}\right)\times\left(\frac{1000\ mL}{1\ L}\right)\div 24.3\frac{mg}{mmol} \quad (23)$$

$$= Mg^{2+}\left(\frac{mmol}{L}\right)$$

$$Ca^{2+} + Mg^{2+}\ in\ Mg(OH)_2 = Ca^{2+}\left(\frac{mmol}{L}\right) + Mg^{2+}\left(\frac{mmol}{L}\right) \quad (24)$$

Next, the measured calcium, magnesium, and phosphorus levels in digestate must be considered. These values were measured during the start up period of the pilot using the methods for orthophosphate and Ca^{2+} and Mg^{2+} via water hardness described in Section 3.4. All four pilot tank effluent Ca, Mg, and P concentrations were then averaged for this calculation. Therefore, the dosage of $Mg(OH)_2$ depends on the steady state levels of Ca, Mg, and P values already normalized to mixing and the aeration setting to be used in that specific campaign. This dosing calculation method considers differences in influent concentrations and pilot performance across each campaign, as well as maximizes chemical utilization for OP-P removal. The Ca^{2+}+Mg^{2+}:P ratio is then:

$$(Ca^{2+} + Mg^{2+}\ in\ Mg(OH)_2) + (Ca^{2+} + Mg^{2+}\ in\ pilot\ effluent) : P\ in\ pilot\ effluent$$

To achieve a desired dosage ratio, the $C_1V_1 = C_2V_2$ equation was used, and the correct $Mg(OH)_2$ volume can be solved for as V_1. Where:

$C_1 = (Ca^{2+} + Mg^{2+}\ in\ Mg(OH)_2)$

V_1 = $Mg(OH)_2$ volume to add

$C_2 = (desired\ ratio \times P\ in\ pilot\ effluent) - (Ca^{2+} + Mg^{2+}\ in\ pilot\ effluent)$

V_2 = Pilot volume

The total $Mg(OH)_2$ volume required for the tank to immediately reach the desired dosage ratio can be calculated by plugging in the entire tank volume to V_2. This is referred to as the spike dose volume. The $Mg(OH)_2$ volume required for the tank to continue to be at the desired dosage ratio throughout waste and feed can be calculated by plugging in a third of the tank volume to V_2. This is referred to as the daily dose volume. The hourly dose volume is then the daily dose volume divided by 24 hours. Each calculated dosage volume was then multiplied by 20 to account for the dilution factor.

Once the chemical solution was made and the dosage volumes were calculated, the chemical feed pumps were calibrated and timed. The chemical feed pumps pictured in Figure 5 pull from the base of the chemical tank and inject directly into the mixing lines of tanks 2-4 on an hourly on/off timer. The time on for each chemical pump must be solved based on the known desired volume and the flow on each chemical feed pump which can be set. The time on and off required to reach the desired volume can be determined with the equations below.

$$Pump\ time\ on\ (sec) = \frac{desired\ vol\ (mL)}{pump\ flow\left(\frac{mL}{min}\right)} \times \frac{60\ sec}{1\ min} \quad (25)$$

$$Pump\ time\ off\ (sec) = 3600\ \text{sec} - Pump\ time\ on \quad (26)$$

The volumes were measured and the pump speeds were tuned until the correct dosage volume was reached consistently.

To begin each campaign with $Mg(OH)_2$, first the chemical feed pumps and timers were calibrated for the spike dose volume. On the test start day, the spike dose volume was injected into the tanks via the chemical feed pumps and timers directly after that day's waste and feed cycle. This spike dose was the only dose administered on the first day of the test to immediately start the tanks off at their desired dosage ratios. The following day 1 of the test, the chemical feed pumps and timers were recalibrated to the hourly dose volumes. Once the waste and feed cycle for this day passed, the tanks were then only at 2/3 of their desired dosage ratio and require a new daily dose volume. The chemical feed pumps and timers were then turned on to begin administering the hourly dose volume to slowly bring the tanks back up to their desired dosage ratio over the course of the day. Chemical feed proceeded like this, shown in Figure 7, for the remainder of each campaign.

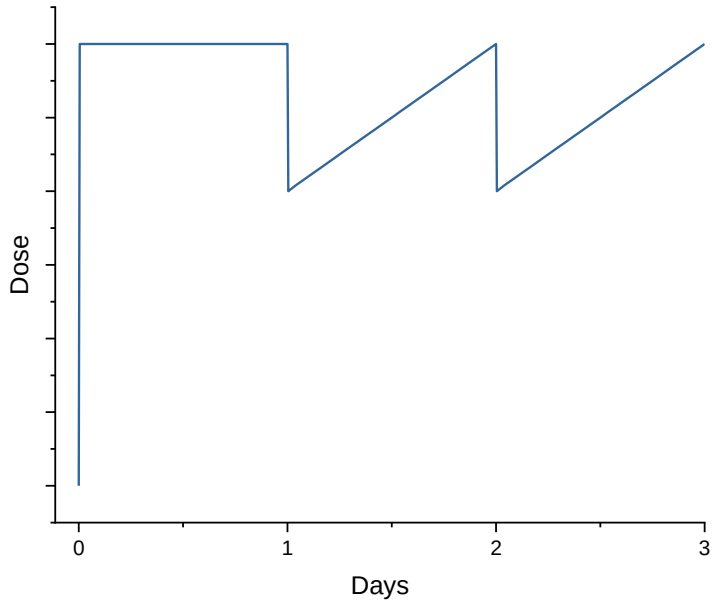

Figure 7: Example of chemical dosing in each test.

3.6 Calcium Hydroxide Addition Pilot Tests

Calcium hydroxide ($Ca(OH)_2$) in the form of a carbide lime slurry via a byproduct created by Arc3 Gases was injected in campaigns 3 and 4 for supplemental calcium addition. For campaign 3, a batch of chemical was made and diluted by a factor (DF) of 20 to follow the same chemical make down protocol as campaigns 1 and 2. The chemical slurry was made down in the 15-gallon, conical chemical tank pictured in Figure 5. The 20X slurry was prepared by determining the necessary $Ca(OH)_2$ mass to add to the 15-gallon tank, and the remainder of the tank volume was filled with NPW. A manufacturer listed density for the slurry of 1.317 g/mL was used. The mass of $Ca(OH)_2$ product was solved for using the same procedure and Equation 21 as described for $Mg(OH)_2$. The dosing volume calculations, chemical feed pump calibrations, and timings were also similarly followed for $Ca(OH)_2$

addition as described above. However, throughout campaign 3 issues with dosing began and clogging was observed. The lines pulling chemical from the chemical mixing tank to the three-way value before traveling through the chemical feed pumps to the tanks were removed and flow was obstructed. Once this was observed, the lines were replaced, and the existing chemical batch was doubled in dilution to a factor of 40. This seemed to aid in preventing clogging for the most part. Therefore, for campaign 4 onwards a DF of 40 was used for $Ca(OH)_2$ and daily dose volume checks were completed to make sure flow was not obstructed.

The testing start up procedure for $Ca(OH)_2$ injection was also followed exactly as described for $Mg(OH)_2$ as beginning with a spike dose volume, proceeded by hourly dosage volumes for the remainder of the testing period.

3.7 Pilot Clean Out Procedure and Scale Sample Collection

Following the conclusion of each campaign, and prior to the start up procedure for the next campaign, a pilot clean out procedure was followed. This clean out procedure was important to remove any residual chemical in the tanks and equipment to begin the next chemical injection test as a fresh start. The mixing pumps were first unplugged. The tanks were drained of pilot effluent and filled with water. Water was continuously flushed in and out of each tank using the manual feed and waste valves. Aeration was turned on to a maximum to suspend any grit at the base of the tanks to be flushed out with the water rinse. The mixing pumps were plugged back in to cycle through with water for cleaning. Each tank was filled and drained of NPW until the overflow drained water was clear. This procedure was followed every campaign and was referred to as the pilot clean out procedure.

Another pilot clean out procedure was followed if a scale sample from the base of the tanks needed to be collected. This was referred to as the complete pilot clean out procedure. In this procedure, the mixing pumps were first unplugged, and the pilot tanks were drained of pilot effluent. The tank was not yet rinsed with NPW to not disturb the scale sample at the base of the tank. Each pilot tank had to be unbolted from the diffuser base and lifted up with a JLG lift. Once lifted, the remaining scale sample of settled grit at the surface of the diffuser could be collected for scale analysis. The remainder of the complete pilot clean out procedure was then followed. The diffusers were removed and soaked in citric acid cleansing solution for 15 minutes to remove any hardened scale fouling the diffuser. The tank was flushed with water to rinse any remaining pilot effluent out, the mixing pumps were cleaned, the mixing lines were snaked and cleaned, and the probes were cleaned. The pilot was then secured back together and was ready for the next test start up. This complete pilot clean out procedure was followed after preliminary pilot testing to collect a scale sample of aerated digestate prior to chemical injection, as well as after campaign 4 and 5 to collect a scale sample supplemented with calcium and magnesium.

4. Manuscript 1 – Optimization of Phosphorus Removal with Low Solids Retention Time Post Aerobic Digestion of Thermally Hydrolyzed Wastewater Solids with Divalent Cation Addition

Intended Authorship of this manuscript: Caitlyn Harris, BJ Ward, Jeff Nicholson, Holly Anne Matel, Dana Gonzalez, Chris Wilson

- *Harris: Conceptualization, experimental design, data collection, analysis, writing lead*
- *Ward, Nicholson, Matel, Gonzalez: Conceptualization*
- *Wilson: Conceptualization, experimental design, analysis, writing support, review*

4.1 Abstract

This pilot study investigated the impacts of mixing, aeration at multiple different settings, and chemical addition of $Mg(OH)_2$ and $Ca(OH)_2$ at various dosages on phosphorus (OP-P) removal from thermally hydrolyzed, anaerobically digested solids. Phosphorus removal via sequestration into class A biosolids can decrease phosphorus recycles within solids handling and centrate flows, as well as control and diminish opportunities for nuisance scaling mineral formation, such as struvite, at WRRFs that damage equipment and treatment efficiency. At a SRT of 3 days, the pilot provided a longer reaction time for crystal formation than many traditional struvite recovery facilities that have issues with struvite capture, but a shorter SRT than traditional PAD operation. The pilot also investigated if benefits from PAD such as nitrogen removal and COD removal could be achieved at this scale. Six pilot campaigns were conducted to test the effects of aeration at a constant flow rate of 5 LPM, at a DO setpoint of 0.2 mg/L, and at pH setpoints of 7.5, 8, 8.5, and 9. $Mg(OH)_2$ and $Ca(OH)_2$ were injected at various Ca^{2+}+Mg^{2+}:P ratios of 0 (control), 0.25:1, 0.5:1, 1:1, 1.3:1, and 1.6:1, and the effects of mixing were studied. Pilot results indicated aeration on a DO setpoint provided more stability to pH and DO measurements than constant aeration, which had a direct improvement on OP-P removal, NH_3-N removal, the formation of precipitates, and alkalinity removal. Both $Mg(OH)_2$ and $Ca(OH)_2$ addition effectively removed OP-P, with improved efficiency as the Ca^{2+}+Mg^{2+}:P ratio increased. At the higher 1:1 dosage, the performance of these two chemicals and aeration settings converged, showing no statistically significant difference in their phosphorus removal efficiency. The maximum OP-P removal achieved was 97% with aeration on a DO setpoint and $Mg(OH)_2$ addition at a ratio Ca^{2+}+Mg^{2+}:P of 1.3:1. NH_3-N removal averaged around 10-20%, with more efficient removal measured in the tests aerated at a DO setpoint. Ammonia-N removal was assumed to be due to mostly to precipitation as struvite, with moderate ammonia stripping available at the pH values measured in these tests. No nitrification was observed in PAD most likely due to FA inhibition. Alkalinity removal in each test surpassed what was calculated as the alkalinity consumption due to the predicted struvite formation, indicating that further coprecipitation reactions with struvite could be occurring. Finally, implementing aeration and

mixing on TH-AD solids consistently achieved about 20% total COD removal across the pilot. However, when the influence of mixing was eliminated, total COD removal decreased by nearly half, suggesting that physical shear from the mixing pumps played a significant role in breaking down colloidal COD into soluble forms, which were more readily biodegradable.

4.2 Introduction

Phosphorus is an essential nutrient and a valuable non-renewable resource that is becoming increasingly limited due to its heavy consumption for global food production, particularly in the production of fertilizers (Wilfert et al., 2015). As a result, the development of technologies within wastewater treatment focused not only on the removal but also the recycling and recovery of phosphorus from waste streams is crucial to establishing a sustainable phosphorus future. A shift in the perspective on phosphorus-containing scaling minerals, once considered a nuisance, has led to their recognition as valuable resources for recovery and use as sustainable fertilizers, inspiring further research on controlling the conditions in which they form.

At WRRFs, struvite ($MgNH_4PO_4 \cdot 6H_2O$) and other precipitates have consistently presented operational challenges. These precipitates typically occur when phosphorus-rich activated sludge from EBPR processes is combined with anaerobic digestion. Anaerobic conditions in the digester release both ammonium and phosphate due to volatile solids reduction (VSR) and the release of polyphosphate stored in the biomass (Booker et al., 1999). Technologies such as Cambi's thermal hydrolysis process (THP) have gained popularity due to their ability to increase VSR, gas yield, and cake dryness, while reducing solids viscosity, which allows for higher digester loading (Haug, 1977; Stuckey and McCarty, 1978; Wilson and Novak, 2009; Higgins et al., 2017). However, the increased loads and VSR from THP lead to elevated concentrations of phosphorus and nitrogen in digesters, enhancing the potential for struvite formation. This leads to high levels of phosphate and ammonium ions in downstream solids handling, which can result in mineral scaling that clogs piping and damages dewatering equipment.

Struvite and other phosphorus minerals can be recovered and used as slow-release fertilizers or sequestered into biosolids for beneficial land application. This not only yields a marketable product but also protects downstream plant operations and reduces phosphorus recycling. Understanding how to control the formation of these minerals is key to mitigating operational challenges and leveraging their potential for phosphorus recovery.

Understanding and controlling these precipitation reactions can be complex as they are influenced by several chemical and physical factors. Crystal formation occurs in two primary stages: nucleation, where precipitation begins, and crystal growth, during which the crystals continue to develop until equilibrium is reached (Jones, 2002). These stages are affected by solubility and saturation, which depend on multiple variables such as thermodynamics, pH, temperature, mixing intensity, and the presence of foreign ions (Booker et al., 1999; Le Corre

et al., 2009). Precipitate formation is most predominantly determined by the pH as it is related to both the solids solubility product (K_{sp}) and the saturation in solution (Snoeyink and Jenkins, 1980). Several authors have shown that the solubility of struvite decreases as pH increases, with maximum likelihood of formation in the wide pH range of 7-11, depending on the type of wastewater and plant operating conditions (Buchanan et *al*., 1994, Moulessehoul et *al*., 2017). The pH of a solution can be manipulated via CO_2 stripping from agitation and aeration as demonstrated by Merkel and Krauth, 1999, allowing for controlled struvite formation without additional reagents. The effectiveness of CO_2 removal varies with factors like temperature, initial dissolved CO_2 levels, and aeration flow rates (Korchef et al., 2011), and CO_2 solubility decreases with increasing temperature, further enhancing CO_2 volatilization and promoting conditions favorable to struvite crystallization (Snoeyink and Jenkins, 1980). The formation of struvite also affects pH. According to Equation 27, the reaction of struvite formation causes a release of protons, which leads to a reduction in pH of the solution. Therefore, the pH change can be used as an indicator of the nucleation of struvite (Bouropoulos and Koutsoukos, 2000).

$$Mg^{2+} + NH_4^+ + H_nPO_4^{n-3} + 6H_2O \rightarrow MgNH_4PO_4 + 6H_2O + nH^+ \quad (27)$$

Temperature has a significant effect on mineral solubility, morphology, and kinetics. Studies show an inverse relationship between struvite solubility and temperature, indicating that struvite is more likely to form at lower temperatures (Burns and Finlayson, 1982; Bhuiyan et al., 2007). Additionally, high temperatures promote the formation of alternative mineral phases, such as newberyite formation instead of struvite, especially in solutions with high magnesium concentrations and low pH levels (Babic-Ivancic et al., 2002). Jones, 2002 noted that the rate of precipitation is often increased at higher temperatures. Likewise, Boistelle et al., 1983 demonstrated struvite crystal growth to differ with temperature, with a "rectangular and prismatic" crystal structure at 25°C and more "square and thick" growth was seen at the increased temperature of 37°C.

The dynamics of crystal nucleation and growth are also important to understanding the crystallization process. Induction time, which depends on supersaturation levels, temperature, and ion concentration, has been shown to reduce with mixing. Studies demonstrated that nucleation could be induced with mixing, and that the induction time could be reduced from 24 hours to 42 minutes with constant agitation at a similar supersaturation ratio (Mullin, 1992; Abbona and Boistelle, 1985; Bouropoulos and Koutsoukos, 2000). Mixing also influences the rate of struvite crystal growth, which has been shown to increase with higher mixing intensities and Mg ratios (Ven Rensburg et al., 2003; Quintana et al., 2005).

Another influential factor is the presence of foreign ions, such as calcium and ferric ions, which have been shown to inhibit struvite formation. Struvite requires a Mg:N:P molar ratio of 1:1:1, and is most often magnesium limited in wastewater systems. Pastor et al., 2008 demonstrated that at a pH above 8 and a Ca:P molar ratio of 0.5:1 or higher can shift precipitation from struvite to a calcium phosphate. Le Corre et al., 2005 confirmed that a Ca:P molar ratio of 1:1 or greater hinders struvite formation by promoting ACP instead.

Studies have also shown that the presence of divalent and monovalent ions can alter mineral purity and induce mixed mineral formations. Yan and Shih, 2016 tested similar molar ratios of Ca:Mg and Fe:Mg of 1:5 and found that both decreased the struvite content in precipitates formed (wt. %), with hydroxyapatite formation in the Ca trials and likely a ferric phosphate formation in the Fe trials. Another study found that background contents of magnesium ions can favor the formation of ACP rather than a crystalline form of a CaP (Abbona et al., 1986). Together, these factors emphasize the need to consider physical and chemical conditions in optimizing phosphorus removal processes in wastewater treatment systems.

There has been commercial success with phosphorus recovery technologies and side stream nutrient removal mechanisms such as PAD, however, issues remain around the optimization of phosphorus removal in specific cases such as phosphorus recovery loss due to fines, chemical and aeration costs, and characterizing the minerals formed within such a system. Limited research exists on the mechanisms involved in phosphorus sequestration in PAD. Therefore, a pilot experimental setup utilized aeration for pH control and chemical addition of $Mg(OH)_2$ and $Ca(OH)_2$ to thermally hydrolyzed anaerobic digestate collected from Hampton Road Sanitation District's Atlantic Treatment Plant (ATP) on a 3-day SRT. The study had two primary objectives: to evaluate and understand the impacts of mixing, aeration at various settings, and chemical addition of two chemicals at various Ca^{2+}+Mg^{2+}:P ratios on

1) primarily the optimization of phosphorus sequestration to class A biosolids, and
2) other parameters such as nitrogen removal, alkalinity, and COD removal.

The 3-day SRT is longer than commercial P recovery technologies and is hypothesized to allow more time for crystal growth to better sequester phosphorus in biosolids and diminish losses due to fines. The 3-day SRT is also shorter than traditional PAD processes, and challenges whether additional benefits such as solids destruction and ammonia removal can be achieved on this scale. Knowledge acquired from experimental results on the pilot scale will directly influence design modifications and operation in a future plant upgrade at HRSD's ATP. Insights gained from this investigation also possess potential benefits for other WRRFs that desire to decrease phosphorus loads in the solids recycle lines and nuisance scaling in a more cost-effective manner than some commercially available technologies. Furthermore, this research will expand upon phosphorus recovery mechanisms in biosolids and contribute to more sustainable and efficient resource management in wastewater treatment, which is imperative in the future of solids handling.

4.3 Materials and Methodology

4.3.1 Pilot Design

The pilot setup at ATP consisted of four tanks (Figure 8). Each tank was 11 feet tall with a volume of about 44 gallons. Simulating the DSST, the tanks were operated as daily batch fed continuously stirred tank reactors (CSTRs) mixed by pump recirculation with a 3-

day SRT. The mixing pumps had a tank turnover rate of less than one minute (Equation 62 in Appendix B). Digestate was passed through a Rosedale Model 6, 2 mm basket strainer before being fed to the tanks to screen out fibrous material and additional grit to protect pilot equipment. The tanks were aerated with 7" fine bubble diffuser membranes by EDI Flexair at the base of each tank which could be operated at constant or intermittent air flow rates, or via Dissolved Oxygen (DO) setpoints. Each tank contained probes to record online measurements of temperature, DO, and pH. The tanks were temperature controlled with heat exchangers at a setpoint of 35ºC to best match the temperature in the pilot to the temperature of digestate within the DSST. Effluent samples from each tank, as well as the pilot influent (e.g. anaerobic digestate), were gathered throughout each test at the end of the 24-hour batch waste and feed timer to track steady state characteristics. The samples were analyzed for orthophosphate, ammonia, water hardness (Ca^{2+} ions, Mg^{2+} ions, and hardness as $CaCO_3$), alkalinity, total chemical oxygen demand (COD), and soluble COD (defined at a 0.45 µm filter size) all with HACH TNTplus Vial Tests, as well as volatile acids via standard methods (5560C-2011), total solids (TS), and volatile solids (VS) via standard methods (1684). Before beginning a chemical injection test, the tanks were operated at the aeration and mixing setting that was used in the testing period and for all variables listed above the standard deviation of each tank normalized to the combined average for all the tanks must be under 5% to ensure stability and comparability across the pilot tanks. This usually required 3 SRTs (a nine-day period).

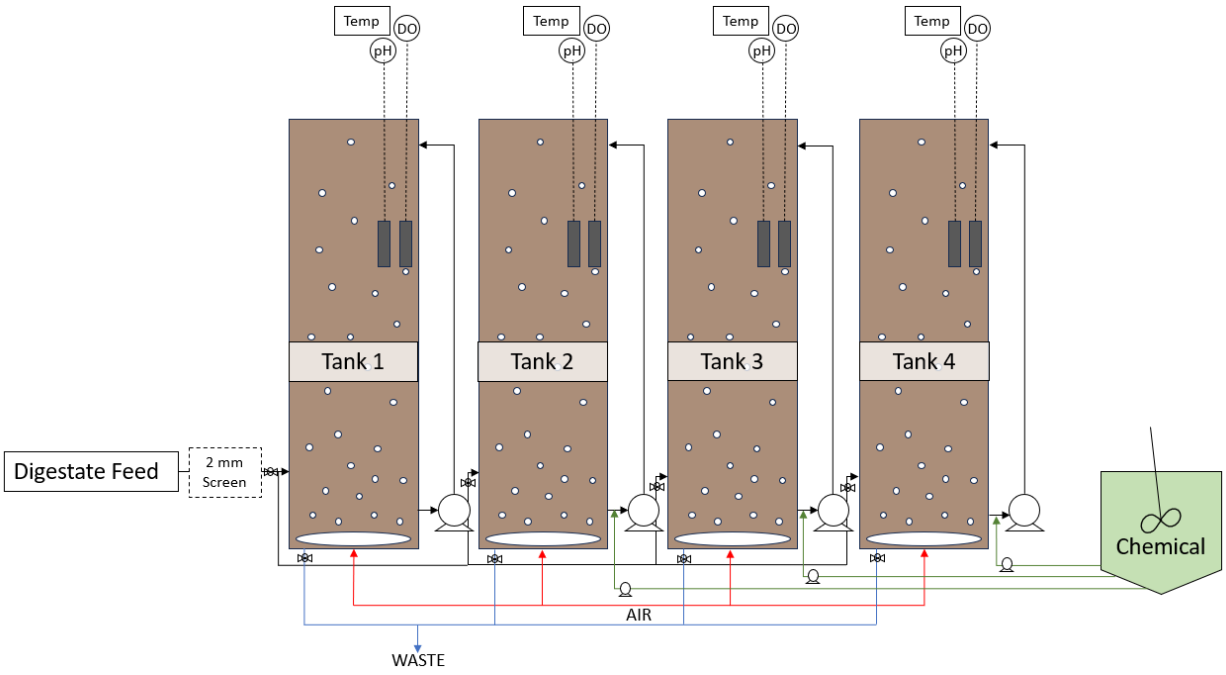

Figure 8: Pilot scale schematic featuring the control tank 1, and tanks 2, 3, and 4 from left to right, waste and feed lines, diffusers, probes, mixing pumps, and chemical injection.

4.3.2 Pilot Testing – Chemical Addition

The chemical injection utilized positive displacement chemical feed pumps which drew chemical from a continuously mixed tank to spike or dose the pilot tanks on an hourly timer at the desired dosage ratios directly into the recirculation line. The chemical dosage was followed by a Non-Potable Water (NPW), i.e. treated secondary effluent, flush to clean the feed lines and push any remaining chemical into the tanks (Figure 5).

Six campaigns were conducted on the pilot scale to determine the effects of aeration and mixing and chemical addition of magnesium in the form of $Mg(OH)_2$ (Thioguard via Premiere Magnesia) or calcium in the form of a $Ca(OH)_2$ slurry at various Ca^{2+}+Mg^{2+}:P molar dosage ratios. To determine the optimal aeration operation, aeration was controlled at a constant aeration setting of 5 LPM, at a DO setpoint of 0.2 mg/L, and at various pH set points. To determine the optimal chemical dose for each chemical, different dosage ratios of $Mg(OH)_2$ and $Ca(OH)_2$ were tested. The tanks were dosed at Ca^{2+}+Mg^{2+}:P molar dosage ratios of 0:1 (control), 0.25:1, 0.5:1, and 1:1 in Campaigns 1-4, and increased up to 1.3:1 and 1.6:1 for Campaign 5. The effects of mixing versus no mixing were also explored in Campaign 4.1. Finally, campaign 6 tested aeration controlled by pH setpoints at pH 7.5, 8, 8.5, and 9. One variable was changed at a time to determine the individual impact of each parameter tested to narrow down to the optimal operational efficiency. Table 4 below details the operating conditions for each campaign conducted.

Table 4: Operational conditions for each testing campaign including: test name, chemical injected, Ca^{2+}+Mg^{2+}:P ratio dosed to tanks 1-4, respectively, the aeration setting, and mixing condition.

Test Name	*Chemical Injected*	*Dosages in Tanks 1-4 (Ca+Mg:P)*	*Aeration Setting*	*Mixing*
Campaign 1	$Mg(OH)_2$	0, 0.25:1, 0.5:1, 1:1	Constant: 5 LPM	Yes
Campaign 2	$Mg(OH)_2$	0, 0.25:1, 0.5:1, 1:1	DO setpoint: 0.2 mg/L	Yes
Campaign 3	$Ca(OH)_2$	0, 0.25:1, 0.5:1, 1:1	Constant: 5 LPM	Yes
Campaign 4	$Ca(OH)_2$	0, 0.25:1, 0.5:1, 1:1	DO setpoint: 0.2 mg/L	Yes
Campaign 4.1	$Ca(OH)_2$	0, 0.25:1, 0.5:1, 1:1	DO setpoint: 0.2 mg/L	No
Campaign 5	$Mg(OH)_2$	0, 1:1, 1.3:1, 1.6:1	DO setpoint: 0.2 mg/L	Yes
Campaign 6	None	None	pH setpoints: 7.5, 8, 8.5, 9	Yes

4.4 Results and Discussion

4.4.1 Pilot Performance

To test the effects of aeration, mixing and $Mg(OH)_2$ or $Ca(OH)_2$ addition, the tanks were operated for 9 days as well mixed, aerated systems and dosed to various Ca^{2+}+Mg^{2+}:P ratios. Figure 9 A-F displays the pH and DO measurements for each campaign 1-6, respectively. Fluctuations in pH and DO correspond to the daily waste and feed. The introduction of a fresh third of digestate to the tank volume led to an increase in temperature, a decrease in pH, and a decrease in DO. The temperature stabilized, and pH and DO began to increase as the day progressed. Data was lost the first few days of campaign 4, and in both the $Ca(OH)_2$ injected tests there were errors in pH probe calibration, but the last few days of pH measurements were taken to be correct (Figure 9 C and D). Data was also lost the first two days of campaign 5, and a power outage caused the pilot to lose aeration during days 7 and 8 of campaign 5. Table 5 displays the averages and standard deviations for each variable for discussion.

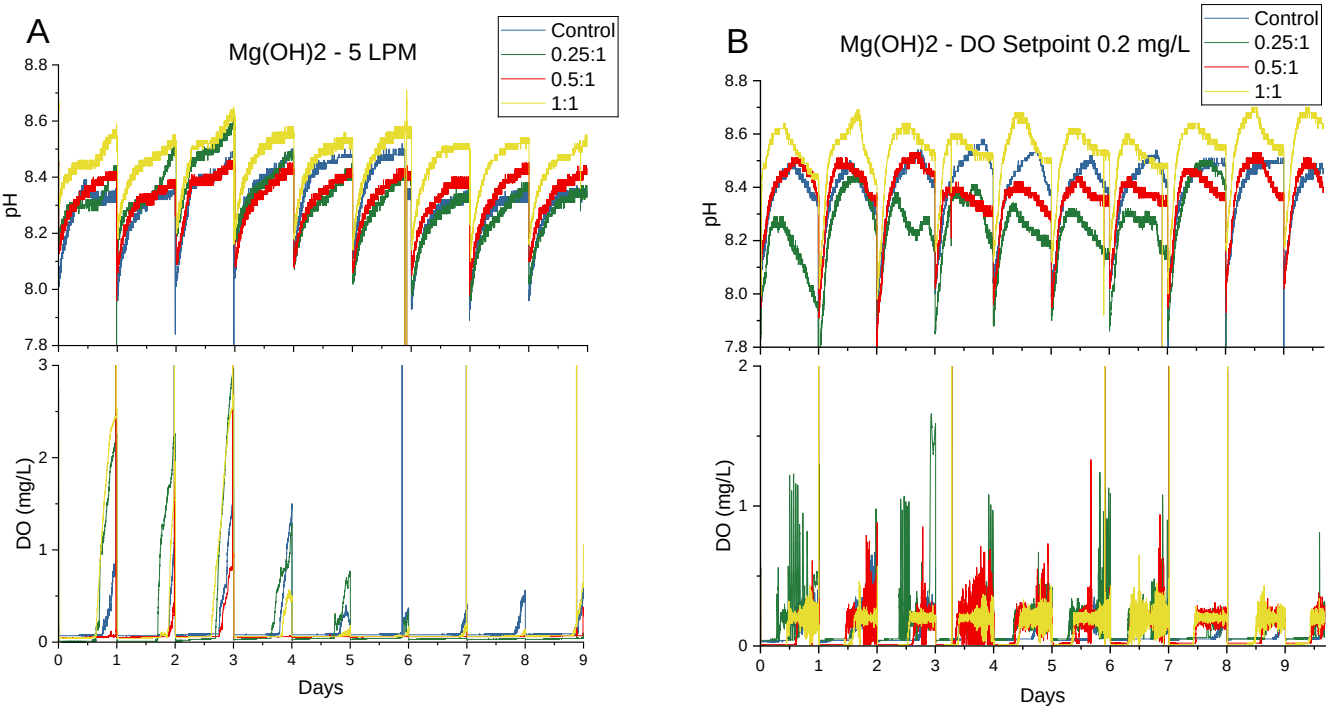

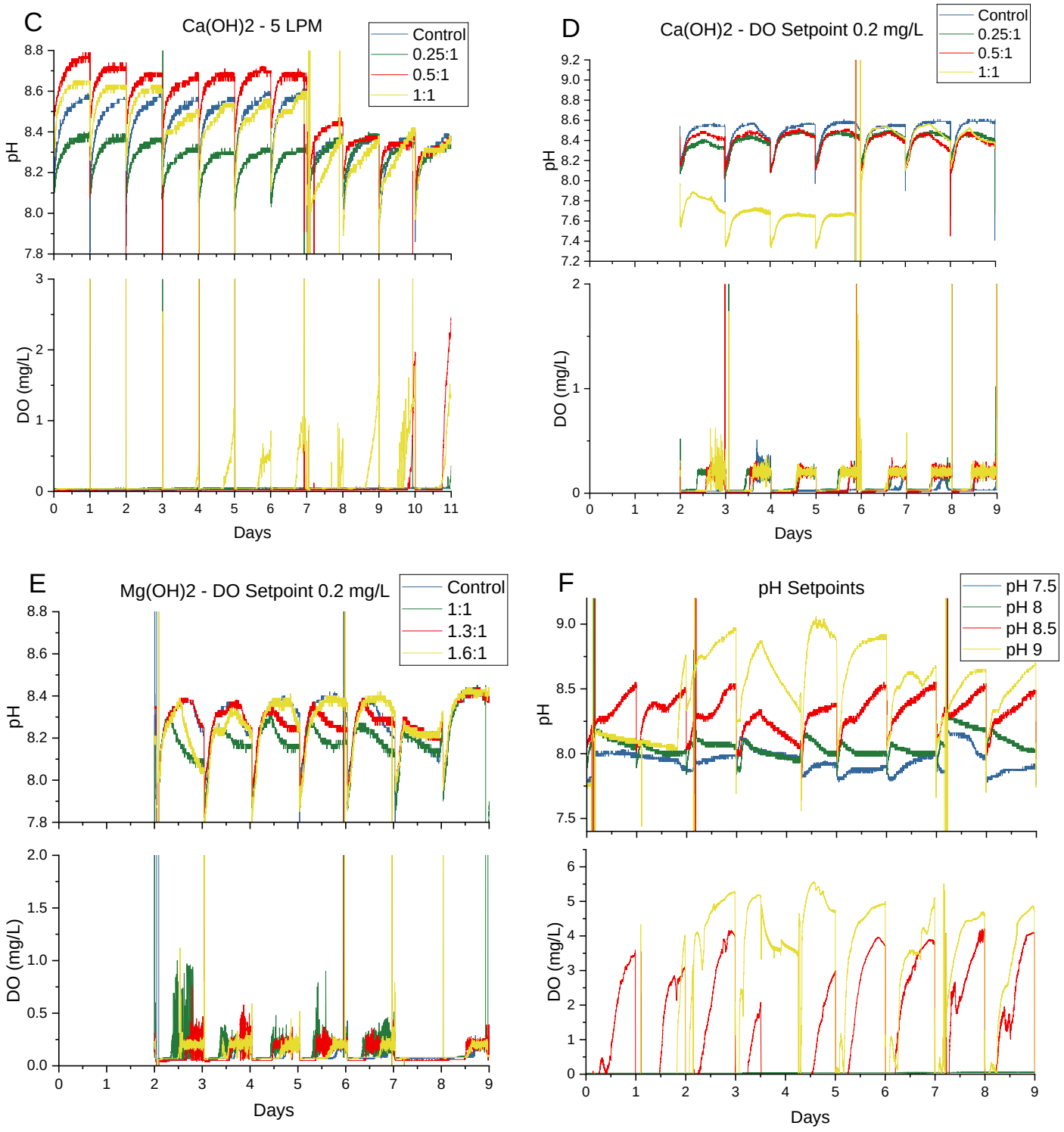

Figure 9 A-F: pH and DO online measurements across the 9-day testing period for the control, and chemically dosed tanks at 0.25:1, 0.5:1, and 1:1 Ca^{2+}+Mg^{2+}:P ratios dosed with $Mg(OH)_2$ at A. constant aeration at 5 LPM, and B. DO setpoint 0.2 mg/L, or dosed with $Ca(OH)_2$ at C. constant aeration at 5 LPM, and D. DO setpoint 0.2 mg/L. Figure 9 E shows the pH and DO online measurements across the 9-day testing period for the control, and chemically dosed tanks

at 1:1, 1.3:1, and 1.6:1 Ca^{2+}+Mg^{2+}:P ratios dosed with $Mg(OH)_2$ and aerated at a DO setpoint of 0.2 mg/L, and Figure 9 F displays the same data for the test with no chemical addition aerated at pH setpoints of 7.5, 8, 8.5, and 9.

Table 5: Average values for pH, DO (mg/L), airflow demands (LPM), and temperature (°C) and the standard deviation measured across campaigns 1-6.

	Average pH ± std.	Average DO (mg/L)	Average Airflow Demands ± std. (LPM)	Average Temperature ± std. (°C)
Campaign 1:				
Tank 1 – control	8.3 ± 0.49	0.2 ± 0.24	5.0 ± 0.14	35.3 ± 3.06
Tank 2 – 0.25:1	8.3 ± 0.49	0.2 ± 0.53	5.0 ± 0.25	32.4 ± 5.24
Tank 3 – 0.5:1	8.3 ± 0.48	0.1 ± 0.11	5.0 ± 0.24	33.8 ± 2.41
Tank 4 – 1:1	8.4 ± 0.49	0.2 ± 0.50	5.0 ± 0.12	34.9 ± 2.87
Campaign 2:				
Tank 1 – control	8.4 ± 0.13	0.1 ± 0.10	13.1 ± 4.41	34.4 ± 1.05
Tank 2 – 0.25:1	7.8 ± 0.73[A]	0.2 ± 0.22	10.3 ± 5.37	34.5 ± 0.95
Tank 3 – 0.5:1	8.4 ± 0.13	0.1 ± 0.14	10.9 ± 4.71	35.0 ± 0.40
Tank 4 – 1:1	8.5 ± 0.13	0.1 ± 0.12	10.6 ± 4.46	35.0 ± 0.42
Campaign 3:				
Tank 1 – control	8.3 ± 0.83	0.0 ± 0.11	5.2 ± 1.13	34.0 ± 3.54
Tank 2 – 0.25:1	8.2 ± 0.81	0.1 ± 0.11	5.0 ± 0.45	34.7 ± 3.55
Tank 3 – 0.5:1	8.5 ± 0.85	0.1 ± 0.29	5.0 ± 0.46	35.0 ± 2.34
Tank 4 – 1:1	8.4 ± 0.85	0.2 ± 0.29	5.0 ± 0.40	34.4 ± 3.55
Campaign 4:				
Tank 1 – control	8.5 ± 0.11	0.1 ± 0.08	14.6 ± 2.46	35.3 ± 0.31
Tank 2 – 0.25:1	8.4 ± 0.10	0.1 ± 0.11	11.0 ± 4.46	37.2 ± 0.81
Tank 3 – 0.5:1	8.4 ± 0.10	0.1 ± 0.13	12.2 ± 3.78	35.9 ± 0.53
Tank 4 – 1:1	8.4 ± 0.10[B]	0.1 ± 0.13	11.4 ± 4.32	36.4 ± 0.77
Campaign 4.1[C]:				
Tank 1 – control	8.8 ± 0.10	0.1 ± 0.00	15.3 ± 0.06	34.1 ± 0.50
Tank 2 – 0.25:1	8.7 ± 0.08	0.1 ± 0.00	15.0 ± 0.02	33.8 ± 0.45
Tank 3 – 0.5:1	8.7 ± 0.08	0.0 ± 0.00	15.1 ± 0.02	34.2 ± 0.39
Tank 4 – 1:1	8.8 ± 0.07	0.1 ± 0.00	15.0 ± 0.02	34.0 ± 0.42
Campaign 5:				
Tank 1 – control	8.3 ± 0.12	0.1 ± 0.08	9.1 ± 13.65	34.9 ± 0.66
Tank 2 – 1:1	8.2 ± 0.20	0.2 ± 0.25	6.9 ± 7.31	35.2 ± 0.75
Tank 3 – 1.3:1	8.3 ± 0.12	0.1 ± 0.10	8.9 ± 6.76	35.0 ± 0.79
Tank 4 – 1.6:1	8.3 ± 0.12	0.1 ± 0.09	10.1 ± 6.92	35.0 ± 0.81
Campaign 6:				
Tank 1 – pH 9	8.6 ± 0.54	3.8 ± 1.41	19.2 ± 15.93	33.4 ± 3.05
Tank 2 – pH 7.5	7.9 ± 0.52	0.0 ± 0.16	0.0 ± 1.78	33.5 ± 3.51
Tank 3 – pH 8	8.0 ± 0.53	0.0 ± 0.16	0.0 ± 4.68	34.9 ± 2.61
Tank 4 – pH 8.5	8.3 ± 0.56	1.7 ± 1.50	17.5 ± 7.14	34.5 ± 2.66

[A] pH probe in tank 2 failed on day 8 of test.

[B] pH data only averaged on days 6-9, when calibration issue was resolved.
[C] Data collected during last 24 hours only

The pH values for campaign 1-5 mostly hovered around 8.3 to 8.5, with less variability in the tests that controlled aeration on a DO setpoint as compared to constant aeration. In the magnesium and calcium supplemented trials with constant aeration, the constant aeration at 5 LPM provided predictable pH manipulation via CO_2 stripping, with a gradual increase up to the maximum pH over the course of each testing day (Figure 9 A and C). Due to each tank having the same constant airflow of 5 LPM, any pH increase measured in the chemically dosed tanks above the control pH can be assumed to be attributed to the addition of alkalinity from $Mg(OH)_2$ or $Ca(OH)_2$. The average pH values for each tank were similar between campaigns 1 and 3, hovering between 8.2 and 8.5, but this increased pH past the control due to alkalinity addition can be seen in the highest dosed tank 1:1 in both campaigns. The drop in pH in the control, the 0.5:1, and the 1:1 dosed tanks in the $Ca(OH)_2$ test at 5 LPM constant aeration was due to pH probe calibration issues (Figure 9 C). In the magnesium and calcium supplemented trials with aeration controlled on a DO setpoint of 0.2 mg/L, each tank had different aeration demands to hit that DO setpoint, which led to less predictable, but more stable pH values (Figure 9 B and D). This unconstrained airflow (up to 15 LPM) led to the tanks reaching slightly higher maximum pHs as tests with constant aeration, and the tanks reached the peak pH faster, and maintained it for longer. This increase in pH stability due to a DO setpoint controlled aeration can statistically be seen in the lower standard deviations in pH averages in campaigns 2, 4, and 5 (Table 5). More stable pH values were perhaps beneficial for attempting to control precipitation as it is an important factor. Difficulty in pH probe calibration occurred in campaign 4 in the 1:1 dosed tank but was resolved by the end of the steady state period, so data shown for campaign 4 tank 4 is only averaged over days 6-9 when the issue was resolved.

Aeration control via constant aeration or on a DO setpoint both created a microaerobic or suboxic testing environment on average ($\leq$ 0.2 mg/L). In the magnesium and calcium supplemented trials with constant aeration at 5 LPM, low and unstable DO levels across the tanks were measured (Figure 9 A and C). In campaign 1, DO was measurable in all four tanks from about 2:00 am to 10:30 am for the first three days but decreased to non-detectable levels by day 6. This decline in DO could be due to the high solids content in digestate, which results in higher oxygen uptake rates, and leads to low or non-detectable DO concentrations. OHOs could be the cause of this oxygen depletion and have been shown to thrive in carbon-rich and low DO environments (McNamara et al., 2022). The constant 5 LPM aeration setting is not high enough for the oxygen demand required for consistent measurable DO. In the magnesium and calcium supplemented trials with aeration on a DO setpoint of 0.2 mg/L, each tank had similar DO levels throughout the tests and averaged close to the setpoint. As shown in Figure 9 B and D, all tanks in both campaigns were able to consistently reach the setpoint, but, again, not until receiving aeration for about 12-14 hours each day of the campaign. This means that even though the DO was more consistently measurable in this aeration setting than

the constant aeration setting, about half of the total SRT is spent oxygen starved. According to Table 5, the average DO levels across campaign 2 and 4 aerated on a DO setpoint were just as low as campaigns 1 and 3 aerated at 5 LPM (≤ 0.2 mg/L), but had more consistent measurable DO levels, which can be seen in the lower standard deviations. Overall, in both aeration controls, the pilot system was operated predominantly in a low DO or microaerobic environment.

The airflow demands were also measured online throughout each test to determine the air flow rate required to hit the DO or pH setpoints. In Table 5, the airflow demands in campaigns 1 and 3 aerated constantly at 5 LPM averaged approximately at the setpoint. In campaigns 2, 4, and 5 aerated on a DO setpoint of 0.2 mg/L, the air demand averaged from 6.9 – 14.6 LPM in order to reach this setpoint. In both campaign 2 and 4, tank 1 struggled to hit the setpoint, indicated by the slightly lower average DO levels than the other tanks, and the higher air demands utilized in Table 5. This could be due to a fouled air diffuser struggling to efficiently dispense air bubbles due to grit build up at the base of the tank. Between campaigns 4 and 5 a full pilot clean-out procedure was completed to collect scale samples from the tanks. Aerated at the same DO setpoint, campaign 5 had much lower air demands as compared to campaign 4 with freshly cleaned diffusers. This is important to note in an experiment involving precipitation reactions while aerating solids, as these maintenance concerns did play a role in the experimental results.

Campaign 6 was aerated at pH setpoints of 7.5, 8, 8.5, and 9 with no chemical addition. However, the first two days of this test, two tanks were trialed as duplicates at pH 7.5, one at pH 8, and the last tank at pH 8.5. A minimum pH of 7.5 was selected to try to match the pH within the anaerobic digesters and DSST. However, an average pH of 7.9 ± 0.52 was the minimum pH achieved (Table 5). The average air demand to reach the pH setpoint was 0.0 ± 1.78 LPM, meaning that the tank diffused the minimal amount of air possible, yet the pH was still unable to decrease low enough to reach the setpoint. This may be due to the difference in headspace makeup of an anaerobic digester with a CO_2 partial pressure of 35% to atmospheric air in the pilot, which caused an immediate stripping of some CO_2 even without additional aeration, leading to the higher pH (Equation 3). Therefore, after 2 days one of the duplicated tanks aerated on a pH setpoint of 7.5 was increased to pH 9 to determine the minimum and maximum pH values the pilot could reach. This can be seen in the increase in the pH 9 labeled line in Figure 9 F. The tank aerated at pH setpoint 8 successfully maintained the setpoint with an average pH of 8.0 ± 0.53. To hit this setpoint, again no air was needed, and the airflow demand was 0.0 ± 4.68 LPM. Measurable DO in both of the lower pH setpoint tanks was zero due to the diffusers being essentially off. With the high pH setpoints the opposite problem occurred by both pH 8.5 and 9 being unattainable now due to lack of aeration. The tank aerated to pH 8.5 averaged 8.3 ± 0.56 with an air demand of 17.5 ± 7.14 LPM required to reach this average. In this tank the maximum liters of air per minute allowed through the diffusers was increased to 20 LPM from the previous maximum of 15 LPM to aid in achieving a higher pH. Even with this extension in provided air, the average fell short of the set point.

Measurable DO in this tank was higher than previously seen in tests aerated constantly or on a DO setpoint, reaching an average of 1.7 ± 1.50 mg/L. In the tank aerated on a setpoint of pH 9, the average pH fell even shorter, at 8.6 ± 0.54, with an air demand of 19.2 ± 15.93 LPM required to reach this average. In this tank, the maximum liters of air per minute allowed through the diffusers was increased to 27 LPM on day 3, however, this caused an over foaming event which led to a major volume loss of the tank on day 4 of this test, thus interrupting all results due to a change in the SRT. The tank was refilled and the maximum liters per minutes was decreased to 22 LPM on day 6, thus the slight decrease in measured pH on days 6-9 of this test seen in Figure 9 F, to minimize foaming. Measurable DO in this test was again higher than tests aerated constantly or on a DO setpoint and averaged 3.8 ± 1.41 mg/L. Therefore, this campaign answered the question of the minimum and maximum achievable pH values possible from aeration and mixing alone. However, due to the tanks aerated at pH setpoints of 7.5 and 9 not accurately achieving these values and not maintaining the correct SRT, the samples taken from these tanks cannot be used to accurately describe the effects of aeration at these pH values. Overall, pH aeration control proved to be quite difficult on this scale due to foaming issues, difficulties in maintaining proper calibration of pH probes in this harsh sludge matrix, and differences in the CO_2 concentrations in the pilot headspace compared to the anaerobic digesters.

Lastly, the average temperatures for all campaigns remained closely aligned with the temperature control setpoint of 35°C. Table 5 displays these consistent temperature averages with little variability. Temperature consistency provided stability throughout the testing periods, as it is correlated to the solubility of minerals.

4.4.2 OP-P removal

The pilot reactors reached a steady state in OP-P removal after the first SRT in the campaigns. Thus, the OP-P concentrations (mg P/L) and removal efficiencies reported in Figure 10 were averaged across the steady state period, which includes triplicate samples taken on days 3, 6, and 9 for the pilot influent and effluents of campaigns 1-4. Significant OP-P removal was measured in each campaign, with increased OP-P removal as the chemical dose increased.

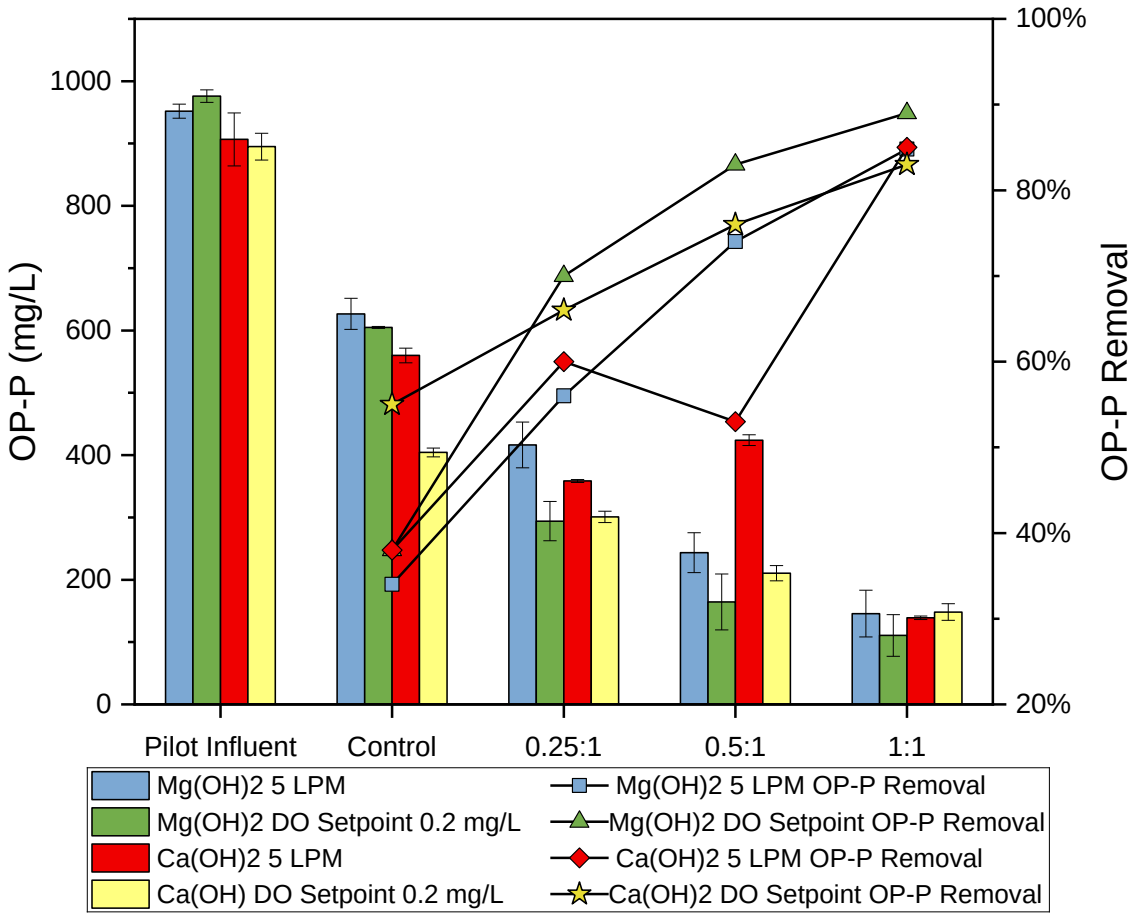

Figure 10: OP-P (mg P/L) averaged across the steady state period of each test and the OP-P removal efficiency of each pilot tank from the pilot influent for campaigns 1-4 at Ca^{2+}+Mg^{2+}:P dosage ratios of 0, 0.25:1, 0.5:1, and 1:1.

In the $Mg(OH)_2$ dosed trials at each aeration setting, the reduction in OP-P concentrations with increasing chemical dosage exceeded a standard deviation between dosage levels. In the $Mg(OH)_2$ dosed tests at a constant 5 LPM and at a DO setpoint of 0.2 mg/L, the control cases reported 34% and 38% OP-P removal, respectively, from the effects of aeration and mixing alone. OP-P removal was slightly greater in the DO setpoint test than the constant 5 LPM aerated test in the control cases due to the previously explained relationship between unconstrained airflow that allows for more CO_2 stripping leading to higher pHs and, therefore, more OP-P removal. However, the OP-P removal measured in the control tanks on days 3, 6, and 9 aerated at either constant or a DO setpoint in the magnesium supplemented tests were not significantly different from each other (p value = 0.09), indicating that the aeration setting statistically had a minimal impact on OP-P removal in the control cases. This OP-P removal measured in the control tank of each test could be considered the baseline for

OP-P removal as chemical was introduced, so any OP-P removal above 34% and 38% was attributed to the magnesium supplementation in campaigns 1 and 2, respectively.

In the $Mg(OH)_2$ dosed test at constant 5 LPM aeration, with increasing Ca^{2+}+Mg^{2+}:P dosage ratios of 0.25:1, 0.5:1, and 1:1 the OP-P removal increased to 56%, 74%, and 85%, respectively. Subtracting the baseline OP-P removal of 34% due to aeration and mixing in this test, the phosphorus removal due to $Mg(OH)_2$ addition in each tank would then be 22% in the 0.25:1 dosed tank, 40% in the 0.5:1 dosed tank, and 51% OP-P removal in the 1:1 dosed tank. Theoretically, if magnesium was the limiting constituent in the formation of struvite that requires a 1:1:1 molar ratio of Mg:NH_4^+:P, and the $Mg(OH)_2$ added was effective to its fullest reaction potential, the 0.25:1 dosed tank could remove 25% OP-P, the 0.5:1 dosed tank could remove 50% OP-P, and the 1:1 dosed tank could remove 100% of OP-P. Considering the OP-P removal in each tank completed solely by the $Mg(OH)_2$ addition, this means the 0.25:1 dosed tank achieved 88% of the expected OP-P removal, the 0.5:1 dosed tank achieved 80% of the expected OP-P removal, and the 1:1 dosed tank achieved 51% of the theoretical OP-P removal (Equation 28). All the tanks were limited in the OP-P removal expected. Therefore, the highest dosed tank with $Mg(OH)_2$ at 1:1 aerated at 5 LPM had the highest OP-P removal overall, but the lower dosed tanks yielded more OP-P removal per amount of chemical added, as calculated in Equation 28 below.

$$\%\ Yield\ of\ OP-P\ Removal = \frac{Actual\ OP-P\ removal}{Theoretical\ OP-P\ removal} \times 100 \quad (28)$$

In the $Mg(OH)_2$ dosed test at a DO setpoint of 0.2 mg/L, with increasing Ca^{2+}+Mg^{2+}:P dosage ratios of 0.25:1, 0.5:1, and 1:1 the OP-P removal increased to 70%, 83%, and 89%, respectively. The same percent yield calculation of actual OP-P removal measured compared to the removal expected after subtracting off the baseline OP-P removal achieved in the control of this test at 38% was completed. The 0.25:1 dosed tank achieved 128% of the expected OP-P removal, the 0.5:1 dosed tank achieved 90% of the expected OP-P removal and the 1:1 dosed tank achieved 51% of the theoretical OP-P removal (Equation 28). Similar to the $Mg(OH)_2$ test completed at 5 LPM, the same test now aerated on a DO setpoint yielded more OP-P removal per $Mg(OH)_2$ dosed at lower dosages as compared to the highest 1:1 dosage, and even exceeded the expected OP-P removal in the 0.25:1 dosed tank. This increased OP-P removal via aeration on a DO setpoint as well as increased OP-P removal yield can be explained by the unconstrained airflow resulting in increased pH values for longer portions of the day, or an increased aerobic SRT.

When comparing the OP removal efficiencies measured per tank across days 3, 6, and 9 aerated at either constant 5 LPM or a DO setpoint of 0.2 mg/L, overall they were not statistically different except for in the tank dosed at a Ca^{2+}+Mg^{2+}:P ratio of 0.25:1. Therefore, this suggests that between the two $Mg(OH)_2$ dosed tests, the aeration setting had minimal influence on OP-P removal, with both approaches achieving comparable performance.

In the $Ca(OH)_2$ dosed tests at a constant 5 LPM and at a DO setpoint of 0.2 mg/L, the control cases reported 36% and 55% OP-P removal, respectively, from the effects of aeration and mixing alone. This difference in control tanks on days 3, 6, and 9 were statistically different (p value = 0.0004). In the $Ca(OH)_2$ dosed test at a DO setpoint, the control tank averaged higher OP-P removal than the control tanks in the other three tests completed. This could be due to the tank struggling to hit the DO setpoint, averaging higher air demands, which increased the control pH values. From Table 4, one can see that the control in campaign 4 averaged an airflow rate of 14.6 ± 2.46 in order to hit the DO setpoint of 0.2 mg/L and resulted in an average pH throughout the test of 8.5 ± 0.11, whereas the control in campaign 2 aerated on the same DO setpoint averaged an air demand of 13.1 ± 4.41 and a pH of 8.4 ± 0.13. As this high of an air demand was only seen in the control of this test, this could have been attributed to a fouled diffuser. However, an increased OP-P removal in the control tanks aerated on a DO setpoint as compared to constant aeration at 5 LPM, perhaps on a lesser extent, was still expected due to increased pHs due to CO_2 stripping.

In the $Ca(OH)_2$ dosed test at constant 5 LPM aeration, issues with clogging events in the chemical feed occurred on days 2-6 of the test. The $Ca(OH)_2$ slurry used in this test was much thicker than the $Mg(OH)_2$. Once this was recognized, remediation was attempted by replacing feed lines and increasing the dilution ratio of the chemical make down, but ultimately these OP-P values were affected. OP-P removal rates averaged across days 3, 6, and 9, including known clogging events, with increasing Ca^{2+}+Mg^{2+}:P dosage ratios of 0.25:1, 0.5:1, and 1:1 were 46%, 49%, and 62%, respectively. However, to determine the effects $Ca(OH)_2$ addition at 5 LPM, the clogging events can be taken out of consideration by taking the average of the triplicate samples collected on day 9 (three full days of unclogged chemical feed). The corrected OP-P removal efficiencies measured were then 60% for the 0.25:1 dosed tank, 53% for the 0.5:1 dosed tank, and 85% for the 1:1 dosed tank. Unfortunately, the 0.5:1 dosed tank was still believed to have clogging issues as evidenced by the obstructed chemical flow in the feed line during cleaning at the end of the test. As this was still determined to be more accurate than accepting the data containing five days of known clogs, these corrected day 9 OP-P values were included in Figure 9 and fall in line with expected values as compared to the other tests completed. Now, the same percent yield analysis can be calculated of actual OP-P removal measured compared to the removal expected after subtracting off the baseline OP-P removal achieved in the control of this test, which was 36%. The 0.25:1 dosed tank achieved 96% of the expected OP-P removal, the 0.5:1 dosed tank achieved 34% of the expected OP-P removal and the 1:1 dosed tank achieved 49% of the theoretical OP-P removal (Equation 28). Discounting effects from $Ca(OH)_2$ clogging in the 0.5:1 dosed tank, the $Ca(OH)_2$ dosed test aerated at 5 LPM performed similarly to the $Mg(OH)_2$ test completed at 5 LPM, with no statistical difference in OP-P removal across each tank in steady state. Also similar was the highest dosed tank with $Ca(OH)_2$ at 1:1 aerated at 5 LPM had the highest OP-P removal overall, but the lowest dosed tank at 0.25:1 yielded the most OP-P removal per amount of chemical added.

Lessons learned from this first $Ca(OH)_2$ test were kept in mind when the test was repeated at a DO setpoint of 0.2 mg/L. A higher dilution was used for the $Ca(OH)_2$ chemical make down for injection and chemical dose volume checks were completed daily to discourage clogging. No clogging was observed throughout the test. In the $Ca(OH)_2$ dosed test aerated at a DO setpoint of 0.2 mg/L, with increasing Ca^{2+}+Mg^{2+}:P dosage ratios of 0.25:1, 0.5:1, and 1:1 the OP-P removal increased to 66%, 76%, and 83%, respectively. However, with the unexpected high OP-P removal of 55% seen in the control of this test, possibly linked to a fouled diffuser, the percent yield of the OP-P removal measured versus expected cannot be accurately calculated for this test. However, similar to the $Mg(OH)_2$ dosed tests, the aeration setting of constant as compared to a DO setpoint in the $Ca(OH)_2$ supplemented tests showed no statistically significant difference in terms of OP removal at the higher 1:1 dosed tank, but led to a significant statistical difference in the 0.25:1 dosed tank (corrected after clogging in campaign 3). Campaign 3 may need to be repeated to fully understand its performance without clogging events.

Overall, OP-P removal increased as the chemical dose increased for both chemicals tested and under both aeration settings tested, which was expected. In the control tanks, aeration on a DO setpoint of 0.2 mg/L contributed to increased OP-P removal as compared to constant aeration at 5 LPM. However, the increase in OP-P removal was only statistically significant in the comparison of campaigns 3 and 4, which were at the latter end of this testing period and could have been due to a fouled diffuser over time. Both $Ca(OH)_2$ and $Mg(OH)_2$ performed similarly in OP-P removal once the clogging events were mitigated, and had no significant difference between them at either aeration setting when the chemical dose was as high as a Ca^{2+}+Mg^{2+}:P dosage ratio of 1:1. According to results from campaigns 1-3, the lower dosed tanks, most notably the 0.25:1 dosed tanks, yielded more OP-P removal per amount of chemical added and showed more effects from chemical choice and aeration as compared to the equal molar dosed tanks. This could indicate an opportunity for chemical savings, which is further discussed in a cost-benefit analysis conducted in section 6.

Campaign 4.1 measured the effects of no mixing on OP-P removal. For an additional three full days at the end of campaign 4, the mixing pumps to all four tanks were unplugged and no longer operated. Chemical addition was continued via daily manual injection. Online data recording was lost due to an issue with the PLC for the majority of this test except for the last day. This test was aerated on a DO setpoint following campaign 4. In campaign 4, with mixing on, the aeration demand plus air entrapment and turbulence from the mixing was enough to reach the DO setpoint daily in each tank. With no mixing, aeration alone was not enough to reach the DO setpoint, so the aeration demands in each tank increased to the maximum LPM allowed of 15 for the entire last day to increase DO levels. This led to the increase in pH from averages of about 8.4 and 8.5 up to about 8.7 and 8.8 (Table 5 and Figure 60 in Appendix A).

A decrease in OP-P was also measured with no mixing. In campaign 4 with mixing, aeration on a DO setpoint of 0.2 mg/L and addition of $Ca(OH)_2$, the OP-P removal rates in the control, 0.25:1, 0.5:1, and the 1:1 dosed tank were 55%, 66%, 76%, and 83%, respectively. Now after three days of no mixing, the OP-P removal percentages decreased to 41%, 44%, 50%, and 58%, respectively. This means up to 25% OP-P removal measured in these experiments may have been due to the mixing intensity provided by the mixing pumps alone. Because the DO was no longer able to hit the setpoint of 0.2 mg/L, it was assumed that the mixing pumps were the larger contributor to achieving a measurable DO than the aeration alone. The mixing pumps could be entrapping oxygen into solution, they could be dispersing the fine bubbles into solution by keeping it well mixed, and/or they could be decreasing the boundary layer around the bubbles to better facilitate interfacial transfer of oxygen to water (Brutsaert and Jirka, 1984). Now that aeration was isolated, it was also assumed that mixing does not contribute as significantly to CO_2 stripping as aeration does, seen in the increase in pH values (Figure 60). With an increase in pH, one would assume an increase in OP-P removal would follow suit. However, this is not the case, therefore, this could mean there is a dependence on the agitation provided by mixing. Studies have shown mixing and agitation can induce crystal nucleation in precipitation reactions (Mullin, 1992). At about the same supersaturation ratio with and without agitation, the induction time for struvite crystallization increased from 42 minutes to 24 hours (Bouropoulos and Koutsokos, 2000; Abbona and Boistelle, 1985). Therefore, at the same SRT of 3 days, perhaps without mixing OP-P removal decreased due to the increase in struvite induction time required, leading to less phosphorus precipitation overall, despite the higher pH value. Another explanation could be that the shear forces from the mixing pumps were liberating additional cations, possibly those bound to organic matter or present as other mineral precipitates, leading to increased free cations available to bind with OP-P. In the absence of mixing, fewer cations were released to assist in OP-P removal. However, not enough information was available to confirm these theories.

Campaign 5 was conducted in the same manner as campaign 2, aerated on a DO setpoint of 0.2 mg/L, and dosed with $Mg(OH)_2$, but was now overdosed to Ca^{2+}+Mg^{2+}:P ratios of 0, 1:1, 1.3:1, and 1.6:1 to determine how much OP-P removal was attainable. Figure 11 below shows the steady state OP-P concentrations and removal percentages in comparison with the first four campaigns.

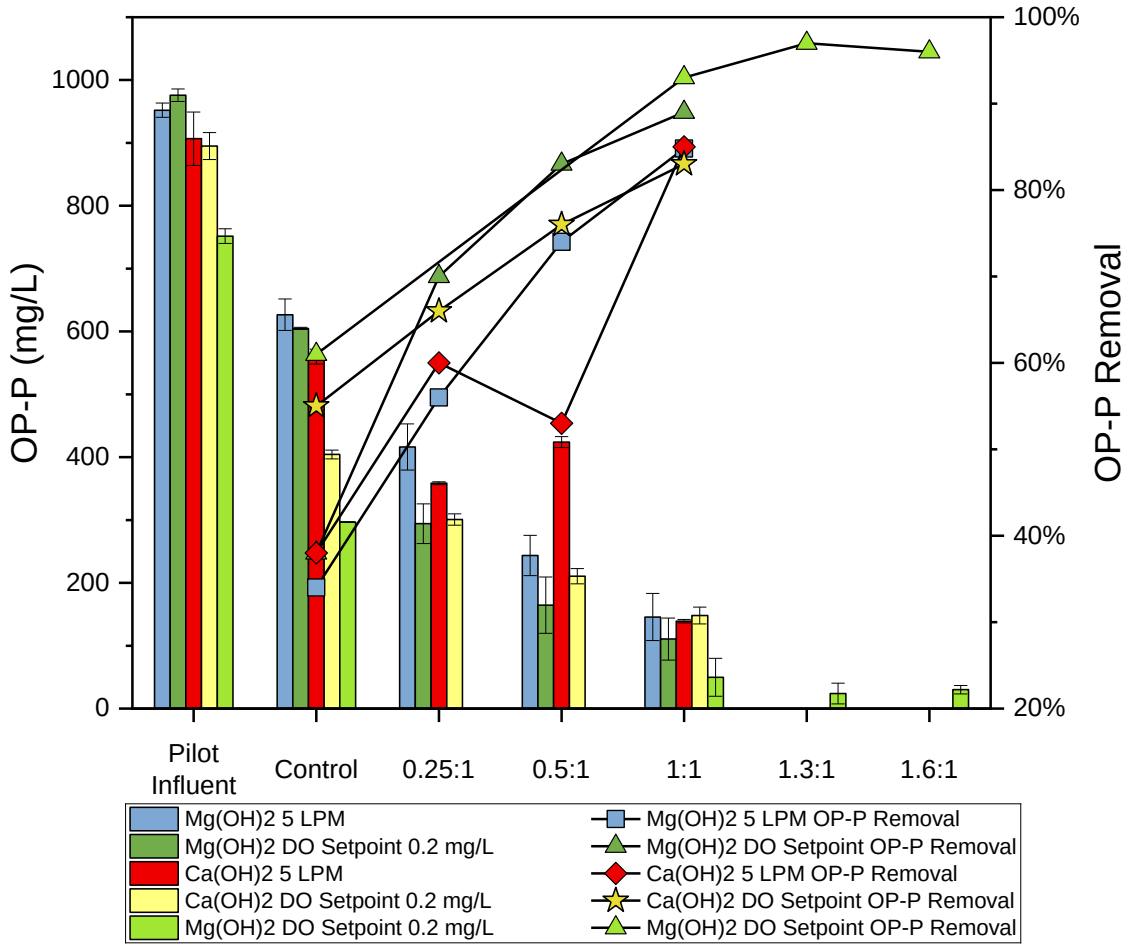

Figure 11: OP-P (mg P/L) averaged across the steady state period of each test and the OP-P removal efficiency of each pilot tank from the pilot influent for campaigns 1-5 at Ca^{2+}+Mg^{2+}:P dosage ratios of 0, 0.25:1, 0.5:1, 1:1, 1.3:1, and 1.6:1.

The OP-P removal measured in the steady state portion of this test in the control, the 1:1, 1.3:1, and 1.6:1 dosed tank was 61%, 93%, 97%, and 96%. Similar to campaign 4, the baseline of OP-P removal in the control was unexpectedly high, in fact this was the highest OP-P removal measured in a control case aerated on a DO setpoint. In the case of campaign 4, this was believed to be due to fouled diffusers due to not conducting a full pilot clean out over the course of these first four campaigns. This theory was supported by the much higher air demands required to hit the same DO setpoint in campaign 4 as compared to campaign 2 as shown in Table 5. Following campaign 4 and prior to campaign 5, a full pilot clean out was conducted. Therefore, in the case of campaign 5 the opposite may be the cause for this enhanced OP-P removal in the control. The diffusers were clean and may have led to enhanced oxygen transfer efficiency. This is supported by the now much lower air demands required to hit the same DO setpoint as compared to campaigns 2 and 4. With the knowledge that the baseline of OP-P removal was higher than previous tests during the startup period of

this test, the chemical dosing was able to be adjusted to lower volumes than the previous tests, as described in the dosing procedures in Section 3.1.5. Thus, the OP-P removal measured of 93% in the 1:1 dosed tank is similar to the measured 89% OP-P removal in the experimentally duplicated 1:1 tank in campaign 2. With overdosing up to 1.3:1 and 1.6:1, almost complete OP-P removal was achieved. The 1.3:1 dosed tank achieved similar OP-P removal to the higher 1.6:1 dose, exceeding it by 1%. This indicates that the maximum achievable OP-P removal on this scale is approximately 97%, which can be effectively reached with the 1.3:1 Ca^{2+}+Mg^{2+}:P dose.

Figure 11 is significant as it can act as guide to the desired OP-P removal based on a WWRF's post treatment goals, and determining what aeration setting, chemical, and dose is required to reach that. If a utility desired to break up the OP-P recycles to the head of the plant with some OP-P removal, this could be achieved with aeration and minimal chemical dose. For example, to achieve around 55-70% OP-P removal, the lower chemical dose of 0.25:1 could be utilized. In this section of the graph, there was more significant difference between chemical choice and aeration choice, so for optimal OP-P removal in this range, aeration on a DO setpoint and $Mg(OH)_2$ was the most successful and chemical saving could be made with the lower dose of 0.25:1. If a utility desired more OP-P removal around 80-85% perhaps to enhance nutrients in biosolids, this would require a higher dose of around 1:1, however the choice between aeration setting and chemical dosed were not significantly different at this dosage. So, savings in utilizing the lower aeration setting of constant 5 LPM, and the cheaper chemical at that time could be available. Lastly, if a utility wanted the maximum OP-P removal around 97% perhaps for mineral harvesting, this is also achievable with aeration on a DO setpoint and $Mg(OH)_2$ at a higher Ca^{2+}+Mg^{2+}:P dose of 1.3:1.

Campaign 6 was well mixed and aerated on pH setpoints of 7.5, 8, 8.5, and 9 with no chemical addition. Figure 12 below shows the steady state OP-P concentrations and removal percentages across the steady state period of the test.

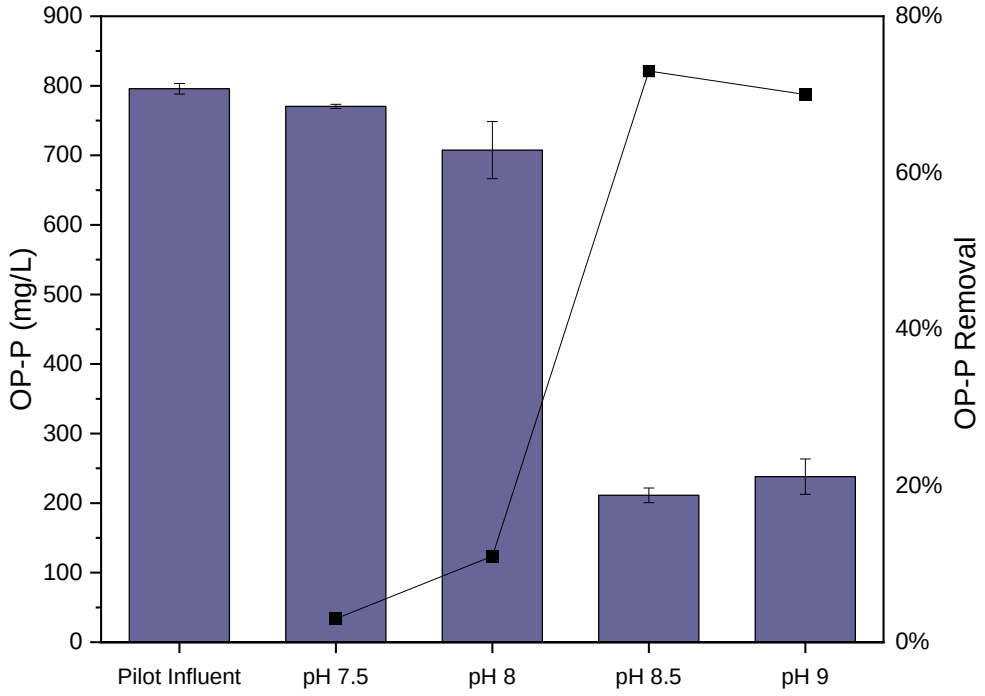

Figure 12: OP-P (mg P/L) averaged across the steady state period of campaign 6 and the OP-P removal efficiency for each pilot tank from the pilot influent for campaign 6 aerated at pH setpoints of 7.5, 8, 8.5, and 9.

The OP-P removal measured in the steady state portion of this test from the pilot influent in the tanks aerated at pH setpoints of 7.5, 8, 8.5, and 9 was 3%, 11%, 73%, and 70%. The tank aerated to a pH setpoint of 7.5 resulted in the diffusers not dispensing air for the entirety of the test, yet the pH in this tank averaged 7.9 ± 0.52. This could be why little to no OP-P removal was measured here from the pilot influent. The tank aerated at pH 8 was also barely aerated to reach this setpoint, but averaged the correct setpoint of 8.0 ± 0.53, meaning that a difference in about 0.1 pH points led to an additional 8% OP-P removal. The tanks aerated at pH setpoints 8.5 and 9 did not average the desired setpoints either, and averaged pH values of 8.3 ± 0.56 and 8.6 ± 0.54, respectively. Despite not reaching the pH setpoints, the air demands were much higher than previous tests, which led to similar OP-P removal values that were measured in campaigns 1-5 with the aid of chemical addition. The tank aerated to the pH of 9 struggled with over foaming and volume loss, which could have resulted in the slightly less OP-P removal measured than the lower pH setpoint tank of 8.5. This indicates that an OP-P removal of around 73% was the maximum OP-P removal achievable via aeration without the aid of chemical addition and before encountering foaming issues. Similar results were seen in Strumpf et al. (2008), where airflow rates of 5 and 8.33 LPM were tested in an airlift pilot reactor to determine the effects on phosphorus recovery as struvite. A general trend emerged: higher airflow rates led to faster and increased phosphorus precipitation. After about

2 hours, the 8.33 LPM air flowrate achieved about 90% OP-P removal and a pH of 8.9, the 5 LPM trial achieved a similar OP-P removal efficiency of 87% and a pH of 8.5. The authors concluded phosphorus removal directly depended on the amount of CO_2 stripped, which was controlled by aeration rate. This is a significant finding as it demonstrates that the same amount of OP-P can be removed from digestate through aeration alone, by maintaining a pH of 8.3 (average air demand required of 17.5 ± 7.14 LPM), as can be achieved with constant aeration at 5 LPM combined with $Mg(OH)_2$ dosing at a Ca^{2+}+Mg^{2+}:P ratio of 0.5:1. Therefore, substantial OP-P removal is possible in this experimental setup through multiple approaches, offering flexibility in operational strategies to optimize phosphorus recovery.

4.4.3 Ammonia Removal

The pilot reactors reached a steady state in NH_3-N removal after the first SRT in the tests. Thus, the NH_3-N concentrations (mg N/L) and removal efficiencies displayed in Figure 13 were averaged across the steady state period, which includes triplicate samples taken on days 3, 6, and 9 for the pilot influent and effluents of campaigns 1-4. The measured ammonia removal could be due to three mechanisms investigated: ammonia stripping, nitrification, and nitrogen precipitation as struvite. Moderate ammonia stripping was available depending on the aeration setting operated and no nitrogen removal via nitrification was observed. Nitrogen removal increased as chemical was introduced to the system, indicating that the primary removal mechanism was via precipitation as struvite. Data from the $Ca(OH)_2$ dosed campaign at 5 LPM again include only the triplicate samples collected on the last day of the test to disregard effects from chemical clogging.

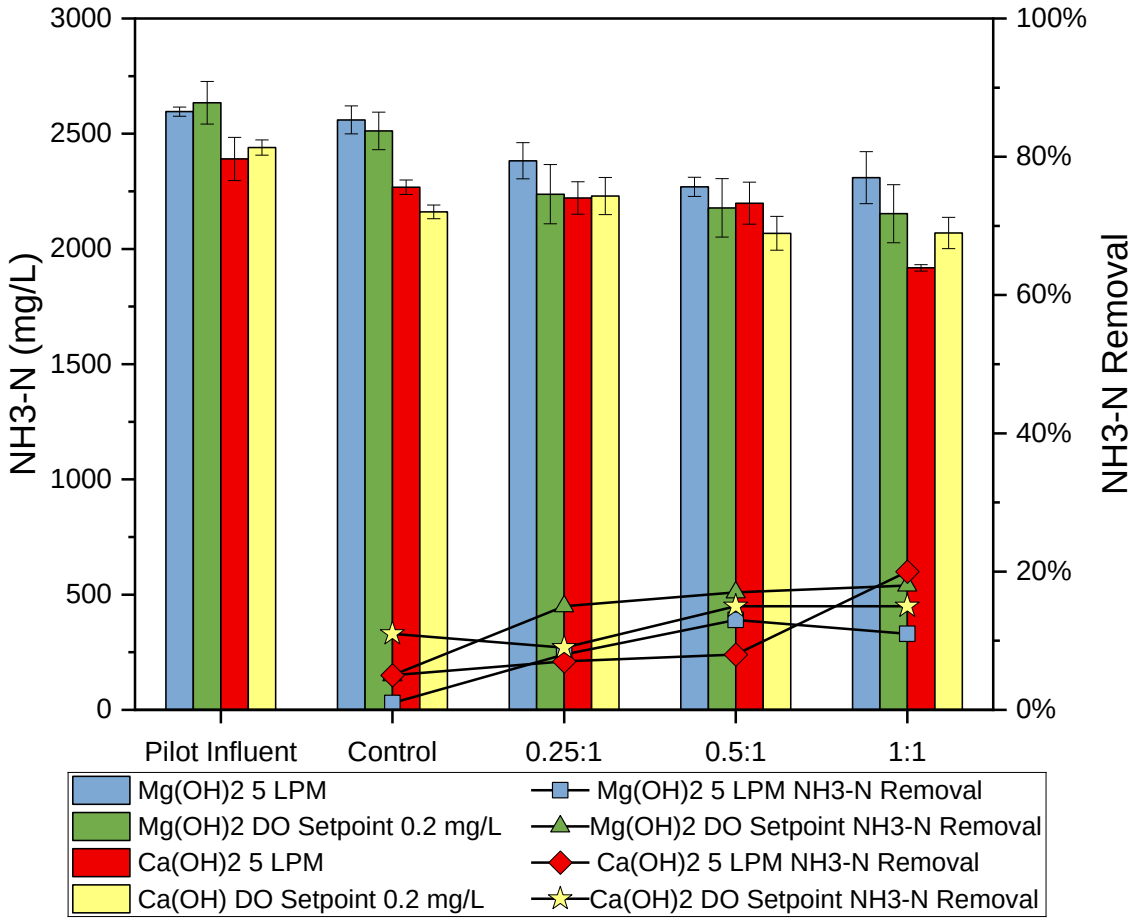

Figure 13: NH_3-N (mg N/L) averaged across the steady state period of each test and the NH_3-N removal efficiency of each pilot tank from the pilot influent for campaigns 1-4 at Ca^{2+}+Mg^{2+}:P dosage ratios of 0, 0.25:1, 0.5:1, and 1:1.

Ammonia removal due to volatilization was evaluated by comparing the pilot influent to the control tanks in each test which were mixed and aerated. Research findings suggested that moderate amounts of ammonia volatilization were available and increased as aeration increased (aeration at constant 5 LPM to a DO setpoint of 0.2 mg/L), most likely due to increased pH. This was illustrated in both of the control tanks in the tests dosed with $Mg(OH)_2$ and $Ca(OH)_2$ at the lower constant aeration setting of 5 LPM. In the $Mg(OH)_2$ dosed test, the control tank measured about 1% ammonia removal at an average pH reached of 8.3 ± 0.49 from aerobic treatment at 5 LPM. In the $Ca(OH)_2$ dosed test, the control tank measured slightly higher around 5% ammonia removal at an average pH reached of 8.3 ± 0.83 from aerobic treatment at 5 LPM, which indicated that about a quarter of the total ammonia removal measured in this test was accounted for in the control via stripping. The ammonia removal in the control cases of both the $Mg(OH)_2$ and $Ca(OH)_2$ dosed tests with aeration on a DO setpoint were higher overall than their respective chemical tests at constant aeration. This

resulted in 5% NH_3-N removal in the control of the $Mg(OH)_2$ dosed test on a DO setpoint, and 11% NH_3-N removal in the control of the $Ca(OH)_2$ dosed test on a DO setpoint. This increased ammonia removal could be explained by the unconstrained airflow allowing for more CO_2 stripping and the average pH values across the tests to increase to 8.4 ± 0.13 in the $Mg(OH)_2$ control tank and to 8.5 ± 0.11 in the $Ca(OH)_2$ control tank. This demonstrated that in the tests aerated on a DO setpoint, one quarter to three quarters of the total ammonia removal measured could be attributed to ammonia volatilization as measured in the controls. Following Equations 17 and 18 from Section 2.3.3.1 and the Henderson-Hasselbach equation, even a small increase in pH such as this can lead to a higher percent of ammonium converted to ammonia available for volatilization. This equilibrium is continuously satisfied as ammonia is volatilized and as the pH changes. As ammonia is stripped from the solution, the reduction in ammonia concentration drives the conversion of ammonium to ammonia, potentially ensuring a sustained supply of ammonia available for further stripping.

$$Percent\ NH_3 = \frac{[NH_3]}{[TAN]} \times 100 = 1 - \frac{1}{(1+10^{pH-pKa})} \times 100 \quad (29)$$

At a pH of 8.3 compared to 8.4 we theoretically have a 2% increase in available ammonia to volatilize:

$$\frac{[NH_3]}{[TAN]} = 1 - \frac{1}{(1+10^{8.3-9.3})} \times 100 = 9.1\%\ NH_3$$

$$\frac{[NH_3]}{[TAN]} = 1 - \frac{1}{(1+10^{8.4-9.3})} \times 100 = 11.2\%\ NH_3$$

Therefore, the difference in aeration setting could explain this rise in ammonia removal recorded across the control tanks.

Campaign 4 and 4.1 measured the effects of mixing on ammonia volatilization. In campaign 4 with mixing, aeration on a DO setpoint of 0.2 mg/L and addition of $Ca(OH)_2$, the NH_3-N removal rates in the control, 0.25:1, 0.5:1, and the 1:1 dosed tank were 11%, 9%, 15%, and 15%, respectively. After three days of no mixing, the NH_3-N removal percentages decreased to 7%, 6%, 10%, and 10%, respectively. This means about a third of NH_3-N removal measured in these experiments may be due to the mixing intensity provided by the mixing pumps alone contributing to ammonia stripping. This may be most contributed to the mixing pump's ability to disperse the fine bubbles into solution by keeping it well mixed, and they could be decreasing the boundary layer around the bubbles to better facilitate interfacial transfer of oxygen to water (Brutsaert and Jirka, 1984). This proves a reliance on mixing as an important factor to ammonia removal in these pilot campaigns.

No signs of nitrification or partial nitrification were observed throughout these tests, which could be due to inhibition of nitrification due to many factors such as alkalinity, DO, temperature, SRT, or free ammonia. Influent alkalinity to the pilot is around 7000 mg/L as $CaCO_3$ due to solids degradation in anaerobic digestion. The maximum amount of alkalinity

removal measured in these tests was about 40% and is discussed in section 4.4.6. This is well above the minimum required alkalinity concentration of 100 mg/L as $CaCO_3$ for nitrification to occur, and thus not an issue here (Biesterfeld et al., 2003). Nitrification is also dependent on SRT, which is heavily dependent on oxygen concentration and temperature. Using Equation 30 and the temperature conversion in Equation 31 listed below, the washout SRT, or minimum SRT required for nitrification to occur at a temperature of 35°C used for pilot testing can be determined.

$$\Theta_{c\,min} = \frac{K_{NH}+S_{SO}}{S_{SO}(\hat{\mu}_A - b_A) - K_{NH} \cdot b_A} \tag{30}$$

Using the temperature correction equation below, from 20°C to 35°C, the new coefficients can be solved for:

$$k_{35°C} = k_{20°C} \cdot \theta^{(35℃-20℃)} \tag{31}$$

Following Grady et al., (2011), the values at 20°C of $\hat{\mu}_A = 0.032\ hr^{-1}$, $K_{NH} = 1.0 \frac{mg}{L} as\ N$, and $b_A = 0.004\ hr^{-1}$ were used. Using the temperature coefficients, θ, of 1.114, 1.125, and 1.114 for $\hat{\mu}_A$, K_{NH}, and b_A, respectively, we can solve for new values at 35°C using Equation 31. Plugging back into Equation 30, and using an ammonia-N concentration of 2500 mg/L, the minimum aerobic SRT required for nitrification to occur would be:

$$\Theta_{c\,min} = \frac{5.852\ mg\ N/L + 2500\ mg\ N/L}{2500\ mg\ N/L(0.162\ hr^{-1} - 0.02\ hr^{-1}) - 5.852\ mg\ N/L \cdot 0.02\ hr^{-1}} = 7.1\ hours$$

Now, this is assuming the DO concentration is not limited. If this is the case for the pilot, which has a total SRT of 3 days, this should not be limiting. However, the pilot was oxygen limited, as shown in Figure 9. The same calculation can be applied for the minimum SRT required for nitrification at a DO of 0.2 mg/L and a constant temperature of 20°C. The $\hat{\mu}_A$ must first be adjusted to the lower oxygen concentration using Equation 32 below.

$$\hat{\mu}_A \left(\frac{S_{NH}}{K_{NH}+S_{NH}}\right)\left(\frac{S_O}{K_{O,A}+S_O}\right) X_{B,A} \tag{32}$$

Following Grady et al., (2011), the values at 20°C of $\hat{\mu}_A = 0.032\ hr^{-1}$, $K_{NH} = 1.0 \frac{mg}{L} as\ N$, $K_{O,A} = 0.75 \frac{mg}{L} as\ O_2$, $X_{B,A} = 1$, and $b_A = 0.004\ hr^{-1}$ were used. Plugging back into Equation 30, and using an ammonia-N concentration of 2500 mg/L, the minimum aerobic SRT required for nitrification to occur would be:

$$\Theta_{c\,min} = \frac{1\ mg\ N/L + 2500\ mg\ N/L}{2500\ mg\ N/L(0.0067\ hr^{-1} - 0.004\ hr^{-1}) - 1\ mg\ N/L \cdot 0.004\ hr^{-1}} = 15.3\ days$$

Considering the availability of oxygen in the pilot but calculated at the lower temperature of 20°C, the pilot SRT of 3 days would be limiting for nitrification to occur. This calculation also assumes a sustained DO of 0.2 mg/L, which was not the case in these experiments. Therefore, despite the aid from the increased temperature, in this suboxic environment on a 3-day SRT, with about half that as the aerobic SRT, nitrifying organisms were not expected to grow.

Nitrification may also be substrate limited, which is ammonia for nitrification. Shown in Figure 13, the influent ammonia levels to the pilot were around 2500 mg as N/L. According to Anthonisen et al. (1976), this value is not limiting, but on the other hand may still be inhibitory due to too much ammonia, referred to as free ammonia inhibition. This may be because thermal hydrolysis pretreatment of the anaerobic digestate as compared to conventional mesophilic anaerobic digestion has been shown to increase the pH in digesters and lead to 5 to 8 times more un-ionized ammonia to be present (Wilson et al. 2011). Free ammonia inhibits nitrobacters (NOB) first at a range as low as 0.1 to 1.0 mg/L and can inhibit nitrosomonas (AOB) at greater FA levels of 10 to 150 mg/L. Influent digestate entered the pilot around a pH of 7.5, and fluctuated between 8.2 to 8.6 during aeration experiments (Figure 9). The temperature was controlled on a setpoint of 35°C. Free ammonia is a function of these values and can be calculated in Equation 33 below (Anthonisen et al., 1976):

$$FA\ as\ NH_3\ \left(\frac{mg}{L}\right) = \frac{17}{14} \times \frac{total\ ammonia\ as\ N\ \left(\frac{mg}{L}\right) \times 10^{pH}}{\frac{K_b}{K_w} + 10^{pH}} \quad (33)$$

Where K_b is the ionization constant of ammonia equilibrium and K_w is the ionization constant of water. Both of which depend on temperature and can be described as Equation 34:

$$K_b : K_w = e^{\left(\frac{6344}{273+C^\circ}\right)} \quad (34)$$

Therefore, when applied to this system, free ammonia can be calculated as follows with Equations 34 and 34.

$$K_b : K_w = e^{\left(\frac{6344}{273+35^\circ}\right)} = 8.81 \times 10^8$$

$$FA\ as\ NH_3\ \left(\frac{mg}{L}\right) = \frac{17}{14} \times \frac{2500\left(\frac{mg-N}{L}\right) \times 10^{7.5}}{8.81 \times 10^8 + 10^{7.5}} = 105.1\ mg/L$$

Therefore, even when the pH is as low as 7.5 in this system, both AOB and NOB are inhibited by free ammonia, and, therefore, no nitrification nor nitritation was expected to occur.

Lastly, ammonia removal due to struvite precipitation was evaluated by comparing additional ammonia removal measured in the chemically dosed tanks to the mixed and aerated controls of each test. Research findings suggested that as chemical was introduced to the pilot system, nitrogen removal increased to a greater extent, most likely due to struvite or other coprecipitation reactions. In the $Mg(OH)_2$ dosed test with constant aeration at 5 LPM, the tanks at Ca^{2+}+Mg^{2+}:P ratios of 0.25:1, 0.5:1, and 1:1 reached slightly higher pH ranges and resulted in ammonia-N removal efficiencies of 8%, 13%, and 11% respectively. Subtracting the 1% NH_3-N removal seen in the control can isolate the additional removal via $Mg(OH)_2$ injection. This gives 7% ammonia removal due to the 0.25:1 dose, 12% due to the 0.5:1 dose, and 10% due to the 1:1 dose. In the $Mg(OH)_2$ dosed test with aeration on a DO setpoint of 0.2 mg/L, the tanks at Ca^{2+}+Mg^{2+}:P ratios of 0.25:1, 0.5:1, and 1:1 reached similar higher pH

ranges, maintained them for longer, and resulted in increased NH_3-N removal efficiencies of 15%, 17%, and 18% respectively. The unconstrained airflow could be contributing to more ammonia stripping in all four tanks, and if the 5% ammonia removal seen in the control of this test is subtracted, this gives 10% ammonia removal due to the 0.25:1 dose, 12% due to the 0.5:1 dose, and 13% due to the 1:1 dose. These ammonia removal percentages due to each $Mg(OH)_2$ dose in the DO setpoint test are similar to the respective values in the 5 LPM test. Although the ammonia removal efficiencies were higher overall for the DO setpoint aerated $Mg(OH)_2$ addition test as compared to the constant 5 LPM aerated test, when a t-test was conducted on the removal efficiencies per tank across steady state, no statistically significant difference due to aeration setting was found. The additional nitrogen removal was likely precipitated out of solution in the form of struvite and will be calculated in the following section.

Campaign 5 was again aerated on a DO setpoint of 0.2 mg/L and injected $Mg(OH)_2$ now at increased ratios of 0, 1:1, 1.3:1, and 1.6:1 to determine the effects of overdoing chemical on ammonia removal. As compared to the experimental duplicates of the control and 1:1 dosed tanks with $Mg(OH)_2$ in campaign 2, which resulted in NH_3-N removal efficiencies of 5% and 18%, respectively, campaign 5 resulted in similar NH_3-N removal efficiencies of 10% and 14% , respectively. Subtracting the 10% NH_3-N removal seen in the control in campaign 5 can isolate the additional removal via $Mg(OH)_2$ injection. This gives 4% ammonia removal due to the 1:1 dose as compared to the 10% ammonia removal due to the 1:1 dose in campaign 2, indicating some slight difficulties in replicating these tests. In campaign 5, with Ca^{2+}+Mg^{2+}:P ratios increased to 1.3:1 and 1.6:1, increased NH_3-N removal was expected to coincide with the additional OP-P removal measured in this test due to additional struvite formation. However, this did not occur. NH_3-N removal measured with overdosing was 14% in the 1.3:1 dosed tank and 16% in the 1.6:1 dosed tank. The expected result may not have occurred, but significant ammonia removal was still measured with $Mg(OH)_2$ addition, and predicted struvite formation will be calculated and discussed in the following section.

Ammonia removal in the $Ca(OH)_2$ dosed tanks at both aeration conditions was expected to be lower, as the precipitate to form in these cases was more likely to be a calcium phosphate, which does not contribute to nitrogen removal as struvite does. Although, in the $Ca(OH)_2$ dosed test with constant aeration of 5 LPM, the tanks at Ca^{2+}+Mg^{2+}:P ratios of 0.25:1, 0.5:1, and 1:1 reached slightly higher ammonia-N removal efficiencies of 7%, 8%, and 20% respectively. When isolating the effects of calcium injection on increased NH_3-N removal, the control removal percentage of 5% can be subtracted to give 2% in the 0.25:1 dosed tank, 3% in the 0.5:1 dosed tank, and 15% in the 1:1 dosed tank. The 1:1 dosed tank with $Ca(OH)_2$ achieved an abnormally high amount of ammonia removal in this constant aeration test. This value may have been collected in error as this was the test reanalyzed after clogging. Another explanation could be the unexplainable higher DO values reached in this tank of an average of 0.15 ± 0.29 mg/L as compared to the other tanks in this test remaining

under 0.10 on average. These values are difficult to compare due to incidences of clogging as well as this outlier. In the $Ca(OH)_2$ dosed test with aeration on a DO setpoint, the tanks at Ca^{2+}+Mg^{2+}:P ratios of 0.25:1, 0.5:1, and 1:1 reached ammonia-N removal efficiencies of 9%, 15%, and 15% respectively. When isolating the effects of calcium injection on increased NH_3-N removal, the control removal percentage of 11% achieved can be subtracted to give -2% in the 0.25:1 dosed tank, 4% in the 0.5:1 dosed tank, and 4% in the 1:1 dosed tank. According to this test, calcium had minimal to no additional impact on ammonia removal beyond the effects of aeration at a DO setpoint. Overall, continued ammonia removal throughout the calcium supplemented tests was unexpected, however, insignificant when the effects from clogging, variable pilot aeration control, and outliers were removed from consideration. More pilot testing may be required to determine this.

Campaign 6 measured the effects of aeration at pH setpoints of 7.5, 8, 8.5, and 9 on NH_3-N removal efficiencies. The NH_3-N removal measured in the steady state portion of this test from the pilot influent in the tanks aerated at pH setpoints of 7.5, 8, 8.5, and 9 was 0%, 0%, 15%, and 18%, respectively. In both tanks aerated to pH setpoints of 7.5 and 8, the diffusers did not dispense air throughout the test, meaning little to no ammonia stripping could have occurred. However, some OP-P removal was still observed in these tanks. The lack of ammonia removal suggests that neither ammonia volatilization nor struvite precipitation occurred, indicating that the minimal OP-P removal detected could be due to the formation of other minerals. The tanks aerated at pH setpoints 8.5 and 9 did not average the desired pH setpoints, however the air demands were high (17.5 ± 7.1 and 19.2 ± 15.9 LPM, respectively) and led to the higher NH_3-N removal rates measured. The tank aerated to the pH of 9 struggled with over foaming and volume loss, meaning an average air demand of around 20 LPM could be the maximum for ammonia stripping. Due to the high OP-P removal also measured in these high pH setpoint tanks, this maximum NH_3-N removal measured of 18% could be from a mixture of ammonia stripping as well as struvite formation.

Therefore, substantial NH_3-N removal was achievable in this experiment. Three mechanisms of ammonia removal were investigated: ammonia stripping, nitrification, and nitrogen precipitation as struvite. Ammonia stripping accounted for up to a quarter of the total ammonia removal measured in the tests aerated at 5 LPM and up to three quarters of the total ammonia removal measured in the tests aerated on a DO setpoint. Nitrogen removal via nitrification/nitritation was assumed not able to occur due to free ammonia inhibition. Nitrogen removal increased as chemical was introduced to the system, indicating that the primary removal mechanism was via precipitation as struvite.

4.4.4 Calcium and Magnesium

Dissolved calcium and magnesium were measured in each pilot test. The Ca^{2+} and Mg^{2+} concentrations (mg/L) and uptake efficiencies displayed in Figure 14 were averaged across the

steady state period, which includes triplicate samples taken on days 3, 6, and 9 for the pilot influent and effluents of campaigns 1-4. Campaigns 1 and 2 dosed with $Mg(OH)_2$ are displayed on top and campaigns 3 and 4 dosed with $Ca(OH)_2$ are displayed on the bottom of the figure.

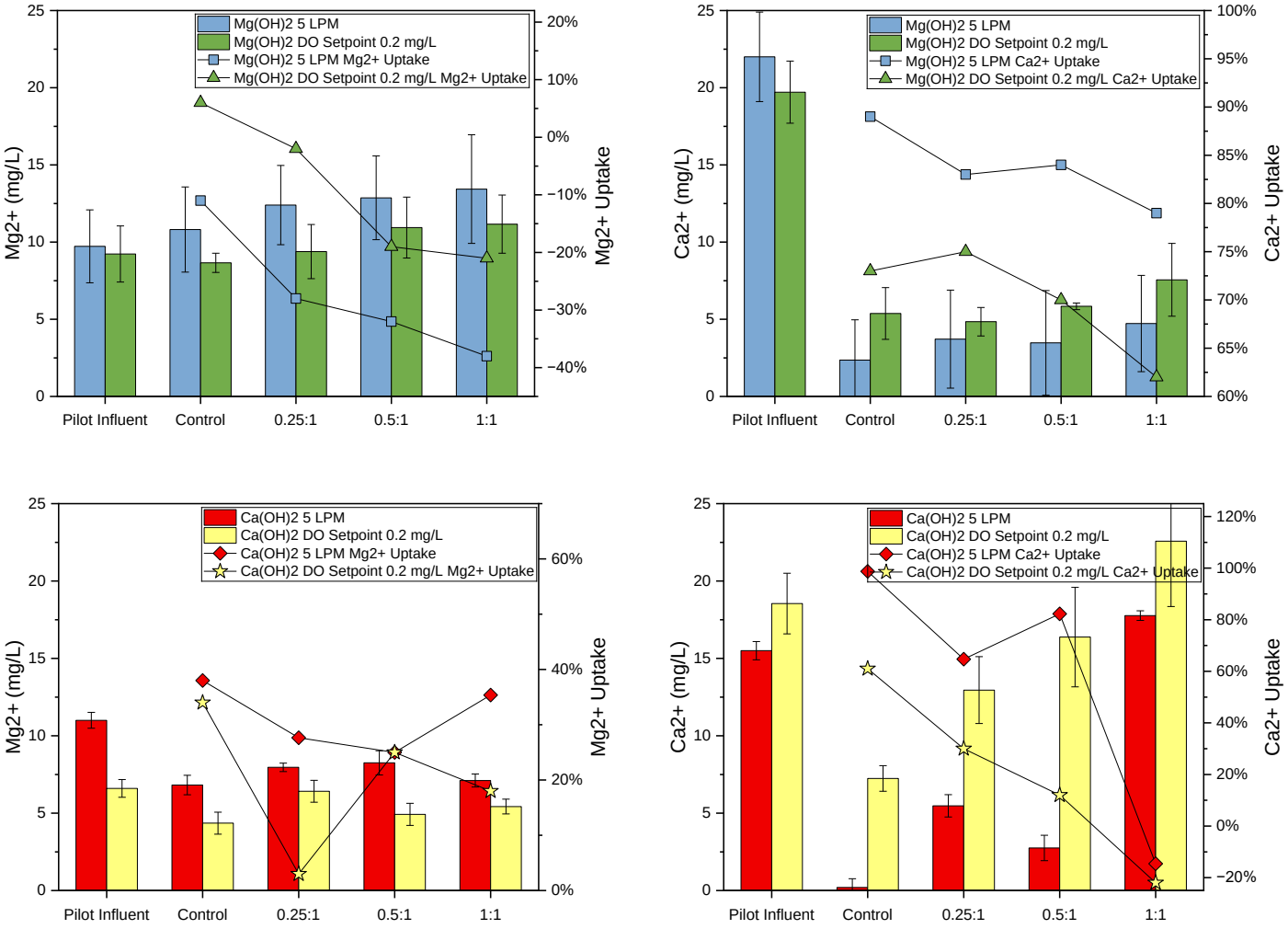

Figure 14: Dissolved Mg^{2+} and Ca^{2+} (mg/L) averaged across the steady state period of each test and the Mg^{2+} and Ca^{2+} uptake efficiency of each pilot tank from the pilot influent for campaigns 1-4 at Ca^{2+}+Mg^{2+}:P dosage ratios of 0, 0.25:1, 0.5:1, and 1:1.

Influent soluble Mg^{2+} in each test was around 10 mg/L, and influent dissolved Ca^{2+} was about double that of Mg^{2+}. Influent total Mg^{2+} and Ca^{2+} to the pilot was much higher, at approximately 280 mg/L total Mg^{2+}, approximately 880 mg/L total Ca^{2+}. As $Mg(OH)_2$ was added in campaigns 1 and 2, Mg^{2+} concentrations remained fairly consistent, meaning all $Mg(OH)_2$ dosed was consumed for precipitation reactions. Likewise as $Mg(OH)_2$ was dosed, Ca^{2+} was substantially removed in each tank, ranging from 60-90% uptake, pointing to the formation of a calcium precipitate as well, without the need of supplemental Ca^{2+}. As

$Ca(OH)_2$ was added in campaigns 3 and 4, Mg^{2+} uptake ranged from 3-38%, indicating magnesium precipitate formation was also possible without supplemental Mg^{2+}. Likewise, as $Ca(OH)_2$ was dosed, Ca^{2+} was significantly scoured in the control and Ca^{2+} levels continued to increase as the dosage increased, indicating the added Ca^{2+} was consumed in precipitation reactions as well. It is significant to note that in each test there was substantial removal of calcium from the pilot influent to the control tank effluents under suboxic, mixed conditions. Overall, these data for dissolved Ca^{2+} and Mg^{2+} removal in the control cases do not justify the phosphorus removal for the controls in each test as discussed in Section 4.4.2. This showcases the complexity of dynamic phosphorus precipitation reactions occurring in this study and indicates it cannot be explained solely by tracking magnesium and calcium phosphorus precipitates.

4.4.5 Predicted Struvite Formation in the Magnesium Supplemented Tests

Struvite formation can be predicted in the three magnesium supplemented tests to determine which aeration setting had the largest effect on struvite. Struvite forms most readily at a $Mg:NH_4^+:P$ ratio of 1:1:1, so this calculation was completed on the equimolar dosed tanks of $Mg(OH)_2$. Predicted struvite was also calculated for the over dosed tanks in campaign 5. The mineral has a molecular weight of 245.4 g/mol, which means that when struvite is formed every pound of phosphorus yields 7.9 lbs of struvite, and every pound of magnesium and ammonium-N yields 10.1 and 17.5 lbs of struvite, respectively. Therefore, the amount of struvite formed was limited by either the amount of OP-P removal measured, or the amount of NH_3-N removal measured.

In campaign 1, $Mg(OH)_2$ was supplemented to a Ca^{2+}+Mg^{2+}:P ratio of 1:1 and aerated constantly at 5 LPM. The equimolar dosed tank achieved 85% OP-P removal, and 11% NH_3-N removal, which based on the average influent concentrations during this steady state testing period was 806.3 mg P/L removed, and 286.7 mg N/L removed, respectively. Converting both concentrations to pounds using the pilot tank volume, the amount of struvite formed in the pilot test can be predicted by each nutrient removal in the equations below.

$$Struvite\ Yield = P\ removed\ \left(\frac{mg\ P}{L}\right) \times 165.2\ L \times 2.20462e^{-6}\ \frac{lbs\ P}{mg\ P} \times 7.9\ \frac{lbs\ Struvite}{lbs\ P} \quad (35)$$

$$Struvite\ Yield = N\ removed\ \left(\frac{mg\ N}{L}\right) \times 165.2\ L \times 2.20462e^{-6}\ \frac{lbs\ P}{mg\ P} \times 17.5\ \frac{lbs\ Struvite}{lbs\ P} \quad (36)$$

Following the equations above, via P removal, this test theoretically yielded 2.3 pounds of struvite, and via N removal, the test theoretically yielded 1.8 pounds of struvite. Therefore, the maximum amount of struvite potentially formed in campaign 1 was limited by ammonia removal and was 1.8 pounds of struvite. The amount of additional P removed that was not attributed to struvite can then be back calculated. This could indicate that theoretically 182.5

mg P/L removed in this test was additionally precipitated from solution as a different mineral other than struvite. This ultimately indicated that the precipitation process was complex, and many other coprecipitation reactions may have occurred in the background of these experiments.

The same struvite formation prediction can be calculated for campaign 2, which was supplemented with $Mg(OH)_2$ and aerated on a DO setpoint of 0.2 mg/L. The equimolar dosed tank achieved 89% OP-P removal, and 18% NH_3-N removal, which based on the average influent concentrations during this steady state testing period was 856.4 mg P/L removed, and 481.8 mg N/L removed, respectively. Following the same equations above to calculate potential struvite yield from P removed or N removed, this test theoretically yielded 2.5 pounds of struvite via P removal, and 3.1 pounds of struvite via N removal. Therefore, 2.5 pounds of struvite were theoretically formed in this test, which was now limited by P removal.

The same struvite formation prediction can be calculated for campaign 5, which was supplemented with $Mg(OH)_2$ and aerated on the same DO setpoint. The equimolar dosed tank achieved 93% OP-P removal, and 14% NH_3-N removal, which based on the average influent concentrations during this steady state testing period was 701.9 mg P/L removed, and 336.4 mg N/L removed, respectively. Following the same equations above to calculate potential struvite yield from P removed or N removed, this test theoretically yielded 2.0 pounds of struvite via P removal, and 2.1 pounds of struvite via N removal. Therefore, 2.0 pounds of struvite were theoretically formed in this test, which was again limited by P removal.

The 1.3:1 dosed tank achieved 97% OP-P removal, and 14% NH_3-N removal, which based on the average influent concentrations during this steady state testing period was 727.8 mg P/L removed, and 352.4 mg N/L removed, respectively. Following the same equations above to calculate potential struvite yield from P removed or N removed, this test theoretically yielded 2.1 pounds of struvite via P removal, and 2.2 pounds of struvite via N removal. Therefore, 2.1 pounds of struvite were theoretically formed in the 1.3:1 dosed tank in this test, which was again limited by P removal.

Lastly, the 1.6:1 dosed tank achieved 96% OP-P removal, and 16% NH_3-N removal, which based on the average influent concentrations during this steady state testing period was 721.7 mg P/L removed, and 393.1 mg N/L removed, respectively. Following the same equations above to calculate potential struvite yield from P removed or N removed, this test theoretically yielded 2.1 pounds of struvite via P removal, and 2.5 pounds of struvite via N removal. Therefore, 2.1 pounds of struvite were theoretically formed in this test, which was again limited by P removal.

In both tests aerated on a DO setpoint, in each tanks case, theoretical struvite formation was limited by P removal rather than N removal. This assumes that Mg is not a limiting factor, however, this is a complex scenario as it is likely that not all Mg contributes to struvite formation due to competing reactions. Due to the higher airflow rate available in the aeration

setting on a DO setpoint, additional N was removed. It was hypothesized in Section 4.4.3 of this paper that this additional N removal could be attributed to ammonia volatilization. The amount of additional N removed that was not attributed to struvite formation was then back calculated for the equimolar and over dosed tanks in campaigns 2 and 5. In the equimolar tank in campaign 2, after assuming the N removal via struvite (limited by P removal) an additional 90.6 mg N/L was removed in this test. This equimolar tank dosed with $Mg(OH)_2$ aerated on a DO setpoint of 0.2 mg/L achieved an average pH value of 8.5 ± 0.13 during this test. Following Equation 29 from Section 4.4.3, the amount of ammonium converted to ammonia that could be available for volatilization at this pH can be calculated.

$$\frac{[NH_3]}{[TAN]} = 1 - \frac{1}{(1 + 10^{8.5-9.3})} \times 100 = 13.4\% \, NH_3$$

Therefore, 13.4% of the N removed could be due to volatilization, which is 64.6 mg N/L. A nitrogen mass balance is inherently complex due to the equilibrium that exists between TAN and unionized ammonia, as well as the dynamic flux of ammonia between dissolved and gaseous states. However, at this average pH, the fraction of ammonia potentially available for volatilization could explain the additional N removal measured after struvite formation.

In the equimolar tank in campaign 5, after assuming the N removal via struvite (limited by P removal) an additional 19.1 mg N/L was removed in this test. This equimolar tank dosed with $Mg(OH)_2$ aerated on a DO setpoint of 0.2 mg/L achieved an average pH value of 8.2 ± 0.20 during this test. Following Equation 29 from Section 4.4.3, the amount of ammonium converted to ammonia that could be removed via volatilization at this pH can be calculated.

$$\frac{[NH_3]}{[TAN]} = 1 - \frac{1}{(1 + 10^{8.2-9.3})} \times 100 = 7.4\% \, NH_3$$

Therefore, 7.4% of the N removed could be due to volatilization, which is 24.9 mg/L. A nitrogen mass balance is complex, however, at this average pH, the fraction of ammonia potentially available for volatilization could help explain the additional N removal measured after struvite formation.

In the 1.3:1 dosed tank in campaign 5, after assuming the N removal via struvite (limited by P removal) an additional 23.4 mg N/L was removed in this test. This 1.3:1 tank dosed with $Mg(OH)_2$ aerated on a DO setpoint of 0.2 mg/L achieved an average pH value of 8.3 ± 0.12 during this test. Following Equation 29 from Section 4.4.3, the amount of ammonium converted to ammonia that could be removed via volatilization at this pH can be calculated.

$$\frac{[NH_3]}{[TAN]} = 1 - \frac{1}{(1 + 10^{8.3-9.3})} \times 100 = 9.1\% \, NH_3$$

Therefore, 9.1% of the N removed could be due to volatilization, which is 32.1 mg/L. Again, a nitrogen mass balance is complex, but at this pH, ammonia volatilization likely accounts for the additional N removal observed after struvite formation.

In the 1.6:1 dosed tank in campaign 5, after assuming the N removal via struvite (limited by P removal) an additional 66.9 mg N/L was removed in this test. This 1.6:1 tank dosed with $Mg(OH)_2$ aerated on a DO setpoint of 0.2 mg/L achieved an average pH value of 8.3 ± 0.12 during this test. As shown above, 9.1% of ammonium was converted to ammonia potentially available for volatilization at this pH. Therefore, 9.1% of the N removed could be due to volatilization, which is 35.8 mg/L. Overall, in each test aerated on a DO setpoint, additional N removal was observed after assumed struvite formation, which could possibly be further explained by ammonia volatilization.

4.4.6 Alkalinity

The alkalinity concentrations (mg as $CaCO_3$/L) and removal efficiencies reported in Figure 15 were averaged across the steady state period, which includes triplicate samples taken on days 3, 6, and 9 for the pilot influent and effluents of campaigns 1, 2, and 4. Campaign 3 data is the averaged triplicate samples taken on only the last day of the test to omit results affected by clogging. Alkalinity consumption was driven most by aeration control, with increased alkalinity consumption estimated and measured in the tanks aerated on a DO setpoint of 0.2 mg/L than aerated constantly at 5 LPM.

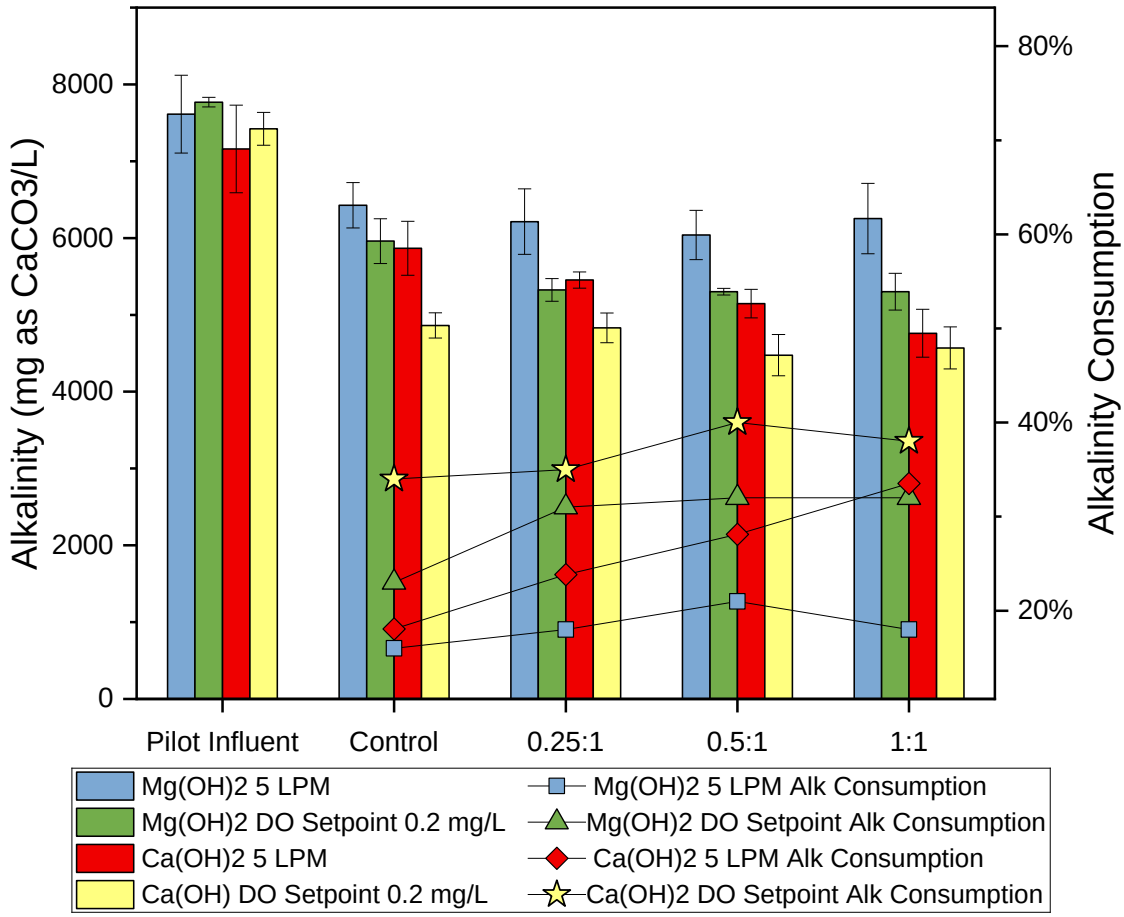

Figure 15: Alkalinity (mg $CaCO_3$/L) ± the standard deviation averaged across the steady state portion of each test for the pilot influent and tank effluents at Ca^{2+}+Mg^{2+}:P dosage ratios of 0, 0.25:1, 0.5:1, and 1:1.

Aeration control had an effect on alkalinity consumption, with more alkalinity consumption occurring in the $Mg(OH)_2$ and $Ca(OH)_2$ dosed tests aerated on a DO setpoint of 0.2 mg/L than constantly at 5 LPM. The alkalinity consumed in both the $Mg(OH)_2$ and $Ca(OH)_2$ dosed tests aerated constantly at 5 LPM began similarly in the lower dosed tanks, with 16% and 18%, respectively, in the control, 18% and 24% in the 0.25:1 dosed tank, but while the alkalinity consumption in the $Mg(OH)_2$ dosed test began to plateau, with 21% in the 0.5:1 dosed tank, and 18% in the 1:1 dosed tank, the alkalinity consumption in the $Ca(OH)_2$ dosed test continued to increase, with 28% in the 0.5:1 dosed tank, and 34% in the 1:1 dosed tank. For the $Mg(OH)_2$ and $Ca(OH)_2$ dosed tests aerated on a DO setpoint of 0.2 mg/L, the alkalinity consumption measured were higher overall at 23% and 34%, respectively, in the control, 31% and 35% in the 0.25:1 dosed tank, 32% and 40% in the 0.5:1 dosed tank, and 32% and 38% in the 1:1 dosed tank. With each chemical tested, the alkalinity consumption was higher when aerated on a DO setpoint rather than when aerated constantly. However, due

to the clogging events in campaign 3, a t-test was only conducted on the magnesium dosed tests to prove this. The alkalinity consumption measured in all four tanks on days 3, 6, and 9 aerated at either constant or a DO setpoint in the magnesium supplemented tests were all significantly different from each other (p values = 0.02, 0.01, 0.01, and 0.02 in the control, 0.25:1, 0.5:1, and 1:1 dosed tanks, respectively), indicating that aeration setting did have an impact on alkalinity consumption.

To make sense of this trend, alkalinity consumed and added was accounted for. The formation of many precipitates consume alkalinity, namely struvite as shown in Equation 1, as well as hydroxides, vivianite, and calcite. Alkalinity consumption could also be attributed to partial nitrification occurring and gaining some benefits from PAD, which destroys 7.14 g of alkalinity as $CaCO_3$ for each g of nitrogen oxidized from ammonia-N to nitrate-N. However, signs of nitrification had not been observed and had been shown not likely to occur in previous sections. Alkalinity was also added in these tests in the chemical dosed tanks in the form of $Mg(OH)_2$ or $Ca(OH)_2$. No alkalinity was added to the control tanks in each test. According to Premier Magnesia®, thioguard contained 13.2 lbs/gallon of alkalinity as $CaCO_3$. The carbide lime slurry was reported by Arc3 Gases® as 115% effective $CaCO_3$ equivalent, meaning 1 dry gram of the carbide lime slurry provided 1.15 g alkalinity as $CaCO_3$. The percent total solids was reported as 46.8% and the density was reported as 1.317 g slurry/mL. Using the spike volume of chemical added (chemical volume in each tank at steady state conditions), the alkalinity added can be solved for using the following equations.

$$\frac{Mg(OH)_2\ volume\ added\ (mL)}{Tank\ volume\ (L)} \times \frac{gal\ Mg(OH)_2}{3785\ mL\ Mg(OH)_2} \times \frac{13.2\ lbs\ CaCO_3}{gal\ Mg(OH)_2} \times \frac{453592\ mg\ CaCO_3}{lb\ CaCO_3} = \frac{mg}{L}\ as\ CaCO_3 \quad (37)$$

$$\frac{Ca(OH)_2\ volume\ added\ (mL)}{Tank\ volume\ (L)} \times \frac{1.317\ g\ Ca(OH)_2\ slurry}{mL\ Ca(OH)_2} \times \frac{0.468\ g\ Ca(OH)_2\ dry}{g\ Ca(OH)_2\ slurry} \times \frac{1.15\ g\ CaCO_3}{g\ Ca(OH)_2\ dry} \times \frac{1000\ mg\ CaCO_3}{g\ CaCO_3} = \frac{mg}{L}\ as\ CaCO_3 \quad (38)$$

Taking the same approach of assuming the amount of struvite formed from the limiting constituent of either P or N removal as described in Section 4.4.5, the amount of alkalinity consumed attributed to struvite formation can be calculated for each tank in each test with the following equation.

$$Alkalinity\ consumption\ \left(\frac{mg}{L} as\ CaCO_3\right) = mmoles\ of\ struvite\ \times 50\frac{mg}{mmol}\ as\ CaCO_3 \quad (39)$$

Once the alkalinity added from chemical addition and consumed from struvite formation are calculated, the estimated alkalinity consumption can be calculated as subtracting the added from the consumed alkalinity. This provides a positive number for net alkalinity removal, and a negative number for net alkalinity gained, which occurred most in the higher chemically

dosed tanks. The estimated alkalinity consumption can be compared to the measured alkalinity consumption for each tank as described in Figure 15 above. The difference in the estimated alkalinity consumption from the measured alkalinity consumption described any alkalinity consumption that could have occurred unrelated to struvite formation. As shown in Table 6, all tanks underestimated alkalinity removal based on struvite formation. This is indicative of possibly other precipitates forming such as vivianite or a calcium phosphate to account for the additional OP removal if a tank was limited in struvite formation by nitrogen removal, and calcite for any remaining alkalinity consumption. This will be expanded upon in Chapter 5 with confirmation in Visual MINTEQ precipitate formation.

Table 6: Alkalinity consumption estimated from struvite formation, alkalinity addition from $Mg(OH)_2$ or $Ca(OH)_2$ addition, and measured alkalinity consumption in mg/L as $CaCO_3$.

		Struvite Formed (mmol/L)	*Alk Consumption due to Struvite (mg/L as $CaCO_3$)*	*Alk added as Chemical (mg/L as $CaCO_3$)*	*Estimated Alk Consumption (mg/L as $CaCO_3$)*	*Measured Alk Consumption (mg/L as $CaCO_3$)*	*Alk Consumption Difference (mg/L as $CaCO_3$)*
Campaign 1	Tank 1	2.6	128.6	0	128.6	1186.7	1058.1
	Tank 2	15.2	761.9	468.2	293.7	1400.0	1106.3
	Tank 3	22.9	1143.7	995.0	148.7	1573.3	1424.7
	Tank 4	20.5	1023.8	2048.7	-1024.9	1360.0	2384.9
Campaign 2	Tank 1	8.8	438.1	0	438.1	1808.9	1370.8
	Tank 2	22.0	1100.9	497.6	603.3	2444.4	1841.2
	Tank 3	26.2	1310.3	1050.6	259.7	2466.7	2207.0
	Tank 4	27.9	1397.1	2156.5	-759.4	2466.7	3226.0
Campaign 3	Tank 1	8.8	438.1	0	438.1	1293.3	855.2
	Tank 2	12.1	604.8	474.9	129.8	1706.7	1576.8
	Tank 3	15.6	779.3	975.7	-196.4	2013.3	2209.8
	Tank 4	24.8	1239.5	1977.2	-737.7	2400.0	3137.7
Campaign 4	Tank 1	15.9	792.5	0	792.5	2560.0	1767.6
	Tank 2	15.0	750.8	297.1	453.7	2591.1	2137.4
	Tank 3	22.1	1105.1	633.7	471.4	2946.7	2475.3
	Tank 4	24.1	1205.8	1306.9	-101.1	2853.3	2954.4
Campaign 4.1	Tank 1	11.8	587.7	0	587.7	1386.7	799.0
	Tank 2	12.8	639.3	297.1	342.2	2200.0	1857.8
	Tank 3	14.6	729.7	633.7	96.0	2146.7	2050.6
	Tank 4	16.9	842.5	1306.9	-464.4	1960.0	2424.4
Campaign 5	Tank 1	14.7	734.5	0	734.5	2613.3	1878.9
	Tank 2	22.7	1133.3	987.3	146.1	2626.7	2480.6
	Tank 3	23.5	1175.0	1297.3	-122.3	2809.3	2931.6

Tank 4	23.3	1165.2	1607.4	-442.2	2746.7	3188.9

As compared to each respective tank between the tests aerated constantly at 5 LPM (campaigns 1 and 3) to the tests aerated at a DO setpoint of 0.2 mg/L (campaigns 2, 4, and 5), more struvite was estimated to have formed in the tanks aerated on a DO setpoint, which led to more alkalinity consumption overall. This corresponds to the similar trend in increased alkalinity consumption measured in the tanks aerated on a DO setpoint as compared to the measured alkalinity consumption measured in the tanks aerated at 5 LPM. Therefore, the higher airflow rate delivered to the tanks not only lead to more estimated struvite formed, but a larger difference between the alkalinity consumption estimated and measured, indicating an increase in other precipitate formation as well. Unconstrained airflow rates could be driving struvite and other mineral precipitation reactions forward, which drive the consumption of alkalinity. Alkalinity addition to each tank from $Mg(OH)_2$ injection in campaigns 1 and 2 were similar to the alkalinity addition to each tank from $Ca(OH)_2$ addition, and no significant difference in alkalinity accounting was attributed to choice of chemical. The decrease in alkalinity removal measured as well as predicted struvite formation in campaign 4.1 compared to campaign 4 indicates again the dependence on mixing to help drive precipitation reactions forward.

4.4.7 COD and Volatile Acids

COD and Volatile Acids (VA) concentrations (mg/L) and removal efficiencies were measured for each test. Total COD and sCOD were measured for all tests, and when little to no sCOD removal was measured across the pilot reactors, the colloidal COD fraction was included in measurements for campaigns 3 and 4. The VA measured was also converted from acetic acid to COD to determine the amount of VA contributed to sCOD measured. Figure 16 below first plots the total COD and sCOD to show the particulate and soluble COD fractions for each test as well as the total COD removal measured relative to digestate. Overall, test results point to COD removal across the pilot being linked to both physical and biological mechanisms.

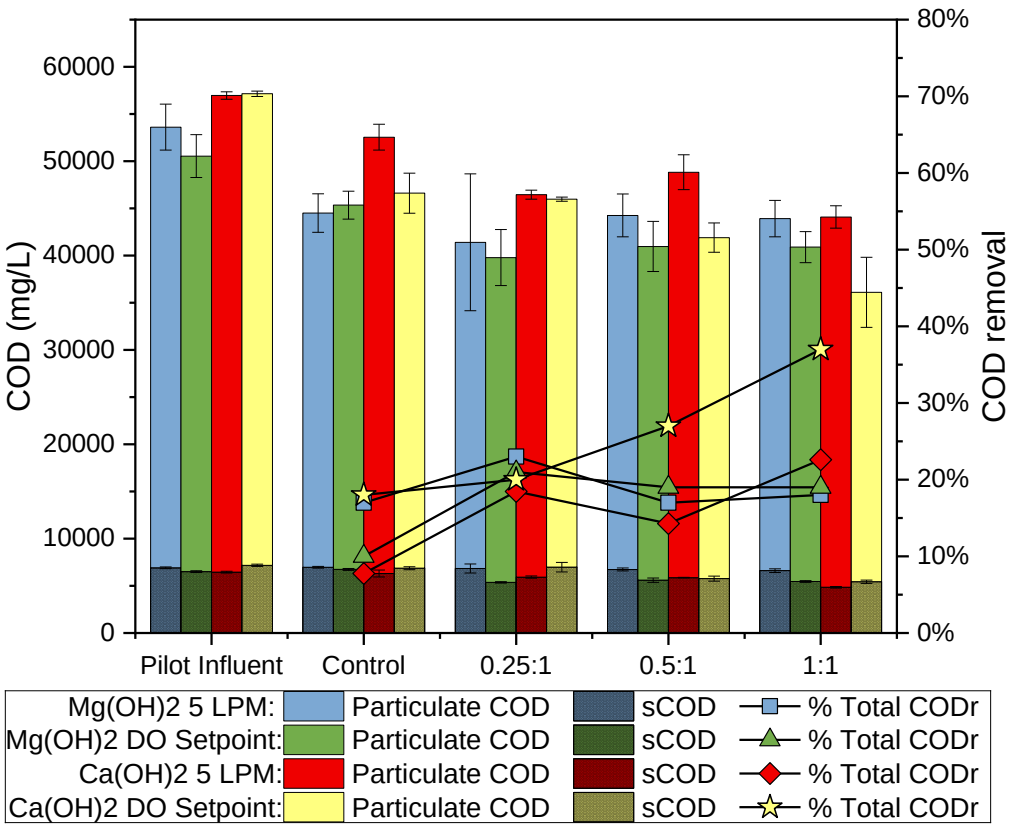

Figure 16: Particulate and soluble COD ± the standard deviation averaged across the steady state portion of each test for the pilot influent and tank effluents at Ca^{2+}+Mg^{2+}:P dosage ratios of 0, 0.25:1, 0.5:1, and 1:1. Total COD removal for each test is plotted on the right y-axis.

Soluble COD (sCOD) defined at a 0.45 µm filter pore size was subtracted from the total COD measured to calculate particulate COD. Total COD measured in the pilot influent was between 50,000 and 58,000 mg/L. The sCOD measured in the pilot influent ranged from 6,400 to 7,200 mg/L, indicating that approximately 88% of the influent COD was particulate and 12% was soluble across all tests. Total COD removal in the first three tests all hovered closely around 20% and increased up to a maximum COD removal observed in campaign 4 of 37%. In a similar PAD experiment at a temperature of 36°C, an SRT of 6 days, and aeration at a DO setpoint of 1 mg/L, an average of 16% COD removal was measured (Parravicini et al., 2008). A 20% reduction in total COD is significant, as it directly impacts the amount of residual solids requiring management. Soluble COD removal for the $Mg(OH)_2$ dosed test aerated constantly at 5 LPM had little to no removal across the pilot with no statistical difference measured. Yet, in the $Ca(OH)_2$ dosed test aerated constantly at 5 LPM, sCOD removal increased as the Ca^{2+}+Mg^{2+}:P dosage ratios increased, up to 25% in the 1:1 dosed tank. In the $Mg(OH)_2$ dosed test aerated on a DO setpoint of 0.2 mg/L, no sCOD removal was measured in the control, but as the Ca^{2+}+Mg^{2+}:P dosage ratios increased, sCOD removal increased to 17% in the 0.25:1 tank, 14% in the 0.5:1 tank, and 16% in the 1:1 dosed tank. In

the $Ca(OH)_2$ dosed test aerated on a DO setpoint of 0.2 mg/L, sCOD increased to 3% in the 0.25:1 tank, 20% in the 0.5:1 tank, and 24% in the 1:1 dosed tank. This sCOD removal seems variable, but when placed in perspective of the contribution to total COD removal, the fraction of that from sCOD removal was never above 3% and was mostly due to removal in the particulate fraction.

A continuous supply of bubbles can satisfy oxygen demand, while also maintaining mixing in the reactor to allow corresponding substances (i.e., COD, NO_3^-, VFAs, etc.) contact with microorganisms (Rosso, 2018). This is significant COD removal at not only both a low aeration rate or low DO setpoint, but a low aerobic SRT according to measurable DO shown in Figure 9. This finding suggests two possible factors may be working together to contribute to COD removal. The physical mechanism of shear in this system due to the mixing intensity of the pumps could be contributing to the degradation or hydrolyzation of particulate COD into soluble COD. This now soluble COD could then be biodegraded by some aerobic heterotrophic activity in a mostly anaerobic or micro aerobic environment. Any particulate COD that was hydrolyzed possibly by shear was then rendered readily biodegradable compounds for heterotrophs to metabolize. A supporting theory linked to PAD is the belief some solids are only digestible under aerobic conditions due to the specific biopolymer fraction associated with the digestion process (Park et al., 2006b). The possibility of aerobic heterotrophic activity is important to note to the oxygen demand of the system and whether additional solids degradation is possible in this PAD-like process. Further analysis was required to better understand these COD fractions and how it will affect the aeration requirement on the full scale if the plant chooses to implement a similar system.

Therefore, beginning at campaign 3 and on, sCOD at a filter pore size of 1.5 μm was also measured for each sample, which the 0.45 μm sCOD could then be subtracted from to give the colloidal sCOD measurement, defined here as: 1.5 μm > Colloidal sCOD > 0.45 μm. Each COD fraction along with particulate COD are shown together in Figure 17 below for campaigns 3 and 4.

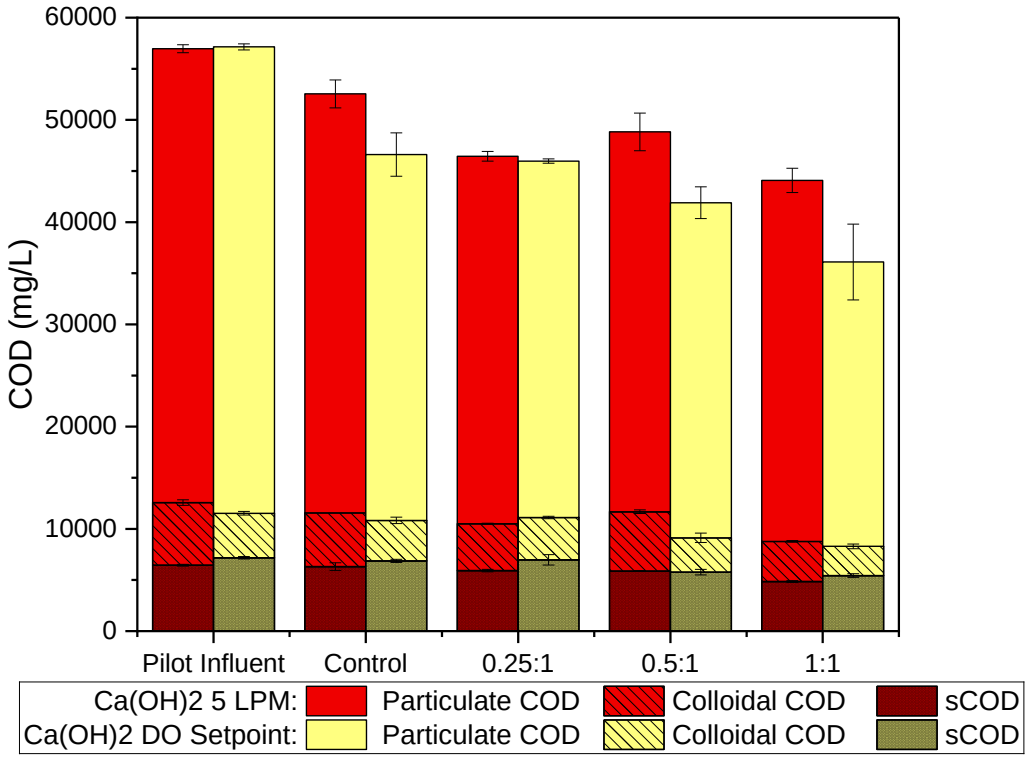

Figure 17: Incremental column graph for particulate and soluble COD fractions ± the standard deviation averaged across the steady state portion of campaigns 3 and 4 for the pilot influent and tank effluents at Ca^{2+}+Mg^{2+}:P dosage ratios of 0, 0.25:1, 0.5:1, and 1:1.

Colloidal COD measured in the pilot influent ranged from 4,200 to 6,200 mg/L, indicating that approximately 79% of the influent COD was particulate, 9% was colloidal, and 12% was soluble across all tests. Therefore, the smallest percentage of total COD was colloidal. Total COD removal on average across each tank was higher in the $Ca(OH)_2$ dosed test aerated at a DO setpoint than aerated constantly at 5 LPM. This could presumably be due to hydrolysis of organic solids during aeration to be favored by a higher oxygen concentration applied (Parravicini et al., 2008).

Soluble COD removal for the campaigns 3 and 4 increased as chemical dose increased, but again only contributed up to 3% of the total COD removal measured. Colloidal COD removal in the $Ca(OH)_2$ dosed test aerated on a DO setpoint also generally increased as chemical addition increased, up to 36% removal in the 1:1 dosed tank. The $Ca(OH)_2$ test aerated constantly at 5 LPM followed this increasing colloidal COD removal as chemical dose increased except for tank 3, which was the tank where chemical clogging was observed. Ultimately, the colloidal COD removal was similar to the sCOD removal in that both contributed very little to the total COD removal observed, reaching a maximum of 4% contribution to total COD removal relative to the influent. This again points to the possibility of shear in this test hydrolyzing particulate COD to sCOD that was then degraded by aerobic

heterotrophs. If this particulate COD reduction was only due to physical shear from the mixing pumps, one might expect an increase in sCOD from the pilot influent to all of the other tanks in each test that was aerated and mixed. However, sCOD remains fairly unchanged between the influent and the mixed tanks, indicating the presence of aerobic heterotrophic organisms that may be degrading the now readily available sCOD.

Campaign 4.1 with no mixing tested this physical shear hypothesis. After three days of continued aeration and chemical addition but no mixing, another sample was collected to measure COD fractions. With mixing in campaign 4, total COD removal from the pilot influent for the control, 0.25:1, 0.5:1 and 1:1 dosed tanks was 18%, 20%, 27% and 37%, respectively. Without mixing, these COD removal percentages decreased to 10%, 11%, 12%, and 15%, respectively. This means about half of the total COD removal was due to help from mixing intensity. Which further indicates the physical shear was helping hydrolysis of particulate COD to soluble COD to then be degraded by heterotrophs. However, it is important to note the decrease in total COD reduction did not stabilization after the one additional SRT tested without mixing (Figure 61). Therefore, it is possible with more time unmixed, the solids that were exposed to the high shear environment could be washed out from the system, and total COD removal via aerobic heterotrophic activity and aeration would be even less. More testing is required to determine this.

VA uptake can also be discussed here as readily biodegradable compounds and were converted to COD to determine the VA contribution to sCOD, calculated as theoretical oxygen demand. The VA values reported in Figure 18 below were measured at end of each test once steady state was achieved. The samples were analyzed by the CEL, with no replicates completed for the pilot influent and effluents of campaigns 1 through 4.

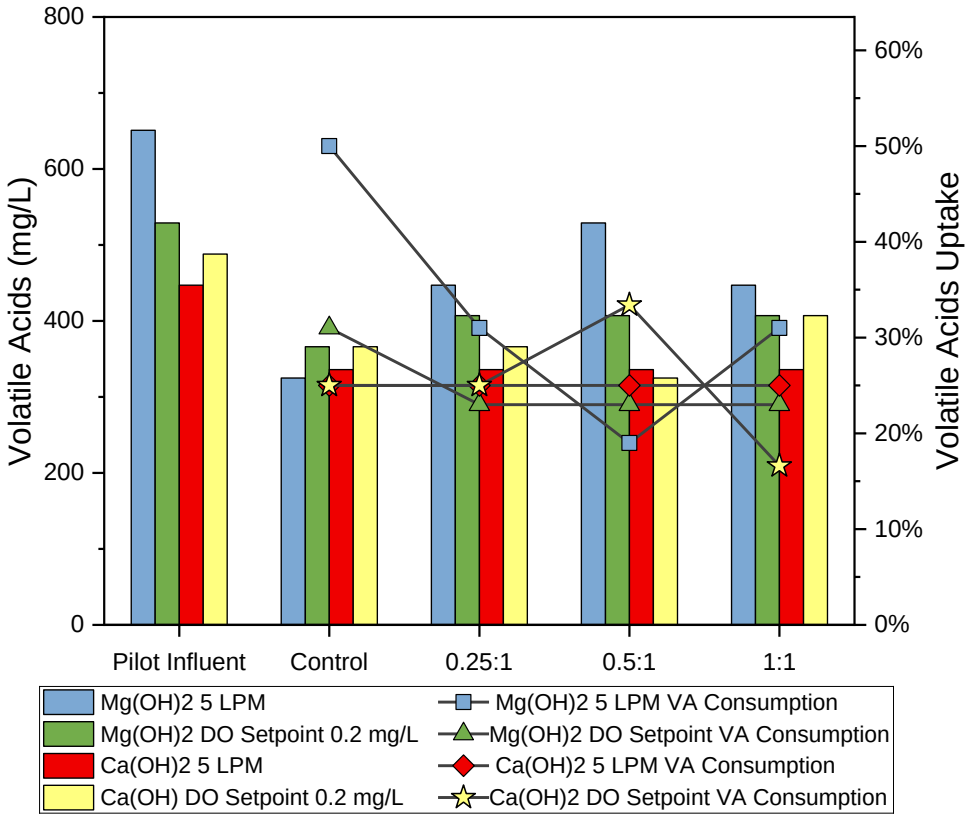

Figure 18: Volatile Acids (mg/L) at the end of the steady state portion of each test for the pilot influent and tank effluents at Ca^{2+}+Mg^{2+}:P dosage ratios of 0, 0.25:1, 0.5:1, and 1:1.

Volatile Acids uptake for each test hovered mostly around 20-30% relative to the pilot influent. The $Mg(OH)_2$ dosed test aerated at a constant 5 LPM had the most variability in VA uptake, with 50% in the control tank, 31% in the 0.25:1 dosed tank, 19% in the 0.5:1 dosed tank, and 31% in the 1:1 dosed tank. In the $Mg(OH)_2$ dosed test aerated on a DO setpoint of 0.2 mg/L, the VA uptake was less variable across dosages, with the highest VA uptake in the control of 31%, and 23% VA uptake in the 0.25:1, 0.5:1, and the 1:1 dosed tanks. The $Ca(OH)_2$ dosed test aerated constantly at 5 LPM had the least variability in VA uptake across dosages, with all tanks achieving a 25% VA uptake efficiency. Lastly, the $Ca(OH)_2$ dosed test aerated on a DO setpoint had VA uptake efficiencies of 25% in both the control tank and the 0.25:1 dosed tank, 33% in the 0.5:1 dosed tank, and the lowest VA uptake of 17% in the 1:1 dosed tank. No trend appears to be present on the effects on volatile acids uptake from chemical choice, dosage, or aeration setting, and due to the lack of replication in samples available for this analysis, no strong conclusions were drawn here. However, the uptake of VA across all tests in each tank consistently measured was significant in the suggestion of uptake as a readily available carbon source for aerobic heterotrophic organisms that may be at play here.

VA measured were then assumed to be all acetic acid and converted COD units using the conversion of 1 g of acetic acid = 1.07 g of COD (Wu et al., 2020). The VA contributing to sCOD could then be compared to the non-VA sCOD in Figure 19 below.

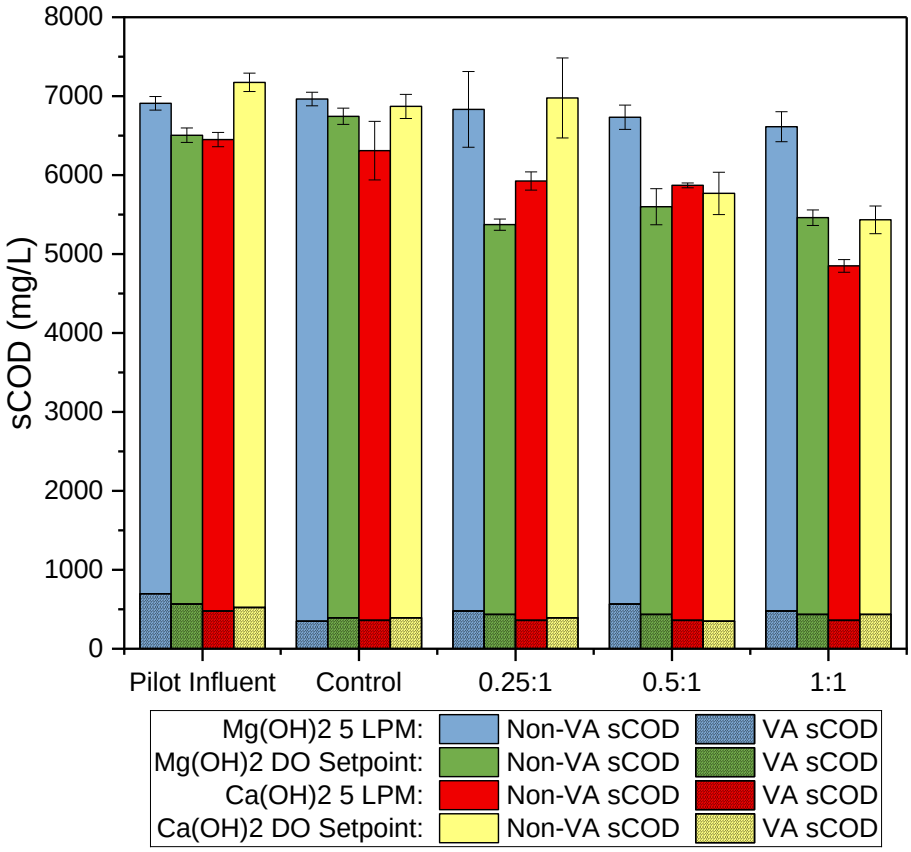

Figure 19: VA sCOD and non-VA sCOD ± the standard deviation averaged across the steady state portion of each test for the pilot influent and tank effluents at Ca^{2+}+Mg^{2+}:P dosage ratios of 0, 0.25:1, 0.5:1, and 1:1.

VA as sCOD measured in the pilot influent ranged from 450 to 700 mg/L, indicating that approximately 8% of the pilot influent sCOD was due to VA and 92% was not due to VA for each test. Despite the significant VA uptake shown in Figure 18 above, the VA removal measured when converted to sCOD units only accounted for up to 5% of the measured sCOD removal across the pilot and was, therefore, not considered significant in effects on COD removal.

Overall, total COD removal across the pilot was significant and averaged around 20% for campaigns 1-4 when subjected to mixing and aeration. The results from campaign 4.1 point to evidence of shear from the mixing pumps to aid in about half of the total COD removal measured in these tests. Shear from the mixing pumps may be inducing hydrolysis of the particulate COD fractions down to soluble COD for aerobic heterotrophic degradation. On a full-scale implementation of this system, one might expect around 10% total COD removal

across this process, which is a notable outcome given the microaerobic environment and low SRT PAD. This has a substantial potential impact on future solids management.

4.4.8 Total and Volatile Solids

Total and volatile solids were measured throughout each test and the averages, along with calculated volatile solids fraction (VSF) and VSR across the steady state period for each test are presented in Table 19 in Appendix A. These parameters were measured with the intention of collecting evidence of organic degradation across the pilot, to be able to compare and validate the measured total COD removal discussed in the previous section. The substantial COD removal measured should be due to any additional VSR from PAD due to endogenous decay (McNamara et al., 2022). However, no meaningful trend in VSR calculated by TS and VS measurements presented itself. Likewise, a COD/VS ratio of 1.5 was used to estimate the amount of VSR measured that contributed to total COD removal, and all calculations were less than 1% (Parker et al., 2008). VSR calculations via TS and VS measurements based on the assumption that fixed solids are unaltered by anaerobic digestion have been proven to be heavily influenced by the systematic artifact caused when ammonium bicarbonate, ammonium carbonate, and some salts decompose during TS analysis (Beall et al., 1998). The ammonium and six water molecules within struvite have also been observed to decompose when exposed to thermal heating. Mass loss begins at 55°C and is complete at 250°C (Bhuiyan et al., 2008). Therefore, due to the many artifacts surrounding TS and VS measurements within this test, COD removal was taken as the primary parameter to explain the degradation of organics within this project.

4.5 Conclusions

Through pilot testing, operational settings such as aeration, mixing, chemical addition choice, and dose have been shown to affect precipitation reactions in terms of OP-P removal, NH_3-N removal, and alkalinity. Pilot testing results demonstrated:

- Aeration on a DO setpoint provided more stability to pH and DO measurements than constant aeration. With aeration on a DO setpoint, due to the higher airflow demand, pH was able to hit a maximum faster, and maintain it for longer, which improved OP-P removal, NH_3-N removal, precipitate formation, and alkalinity removal.
- 34-61% OP-P removal was achieved via aeration and mixing alone, indicating influent soluble magnesium and calcium concentrations were not limiting in these dynamic precipitation reactions.
- OP-P removal increased with both $Mg(OH)_2$ and $Ca(OH)_2$ addition as dose increased, with a maximum of 97% at a Ca^{2+}+Mg^{2+}:P ratio of 1.3:1 with $Mg(OH)_2$ addition and aeration on a DO setpoint.

- The lower chemical dosages were more efficient in achieving OP-P removal per unit of chemical added due to the stoichiometric balance between the supplemented cations and the higher residual OP-P available for removal.
- $Mg(OH)_2$ was marginally more efficient at OP-P removal than $Ca(OH)_2$, but by the higher 1:1 dosage, there was no significant statistical difference between the chemicals or aeration choice.
- NH_3-N removal averaged around 10-20%, with more efficient removal seen in tests aerated on a DO setpoint. The primary nitrogen removal mechanism suggested here was struvite formation, with moderate ammonia stripping occurring.
- Alkalinity removal in each test surpassed what was consumed by predicted struvite formation and considering the alkalinity addition from chemical injection, indicating that another source of alkalinity consumption was at play and could be due to further coprecipitates forming in solution.

When further investigating other effects of aeration and mixing, it was observed that:

- Implementing aeration and mixing consistently achieved about 20% total COD removal across the pilot.
- Without mixing, about 10% total COD removal was achieved. This supports the hypothesis that physical shear from mixing pumps contributed to the hydrolysis of particulate COD to sCOD which was then aerobically degraded.

These testing efforts prove the goals of this project to be achievable, such as phosphorus removal to break up internal recycle patterns, struvite and other scaling mineral control to protect downstream equipment and treatment efficiency, as well as additional N removal and VSR achieved from PAD. Significant OP-P removal was achieved in this experimental setup through multiple approaches, offering flexibility in operational strategies to optimize phosphorus recovery. Striking the balance between these goals and costs from chemical addition and aeration can be done utilizing the lessons learned from the pilot scale. When equating the results from the pilot scale to full scale plant modifications, further research on phosphorus sequestration to Class A biosolids, whether fines loss could occur, and other downstream effects may be necessary.

5. Manuscript 2 – Modeling Phosphorus Mineral Formation in Aerated Anaerobic Digestate Using Visual MINTEQ

Intended Authorship of this manuscript: Caitlyn Harris, Shubhashini Oza, Chris Wilson

- *Harris: Conceptualization, experimental design, data collection, modeling, analysis, writing lead*
- *Oza: Conceptualization, analysis*
- *Wilson: Conceptualization, experimental design, analysis, writing support, review*

5.1 Abstract

Common phosphate minerals in wastewater treatment plants such as struvite (magnesium ammonium phosphate (MAP), $MgNH_4PO_4 \cdot 6H_2O$), calcium phosphates such as amorphous calcium phosphate (ACP, $Ca_3(PO_4)_2$), and iron salt precipitates such as vivianite ($Fe_3(PO_4)_2 \cdot 8H_2O$) have been recognized as a maintenance and operational nuisance for their tendency to scale and deposit within anaerobic digesters, in pipe bends, and on dewatering equipment downstream of anaerobic digesters. Precipitation of these minerals occur if the concentrations of the ionic constituents exceed the solubility product (K_{sp}) of the solid which is measured as scaling tendency (ST) or scaling index (SI). Phosphorus equilibrium chemistry is complex, and the solubility of these precipitates is dependent on factors such as pH, temperature, other competing ions, and available nucleation sites. Chemical thermodynamic modeling could be used in evaluating the parameters that contribute to scaling and, thereby, safeguard process equipment from scaling-induced damage, improve treatment efficiency, and regulate phosphorus sequestration to produce nutrient-rich biosolids.

In this study, the commercially available model Visual MINTEQ Version 4.0 was evaluated (Gustafsson, 2008). A pilot-scale experimental setup evaluated the impact of aeration at multiple settings, mixing, and chemical addition to thermally hydrolyzed pretreated, anaerobically digested solids on phosphorus removal at Hampton Roads Sanitation District's (HRSD) Atlantic Treatment Plant (ATP). Critical parameters such as pH, temperature, alkalinity, orthophosphate (OP), ammonia (NH_3), and major cations and anions concentrations were measured during pilot testing and used as model inputs. The solids formed during these evaluations were characterized by X-Ray Diffraction (XRD), Scanning Electron Microscopy (SEM)/Energy Dispersive X-Ray Spectroscopy (EDS), and Raman Spectroscopy to validate the model.

Sensitivity analyses for pH and temperature were conducted for both unaerated anaerobic digestate (pilot influent) and aerated anaerobic digestate (pilot effluent) in the modelling software. Chemical addition of $Mg(OH)_2$ and $Ca(OH)_2$ was also added in the model at the Ca^{2+}+Mg^{2+}:P ratios tested on the pilot to determine the precipitates formed under each dosing scenario. Visual MINTEQ consistently predicted struvite formation, which was confirmed by XRD analysis. Visual MINTEQ also predicted calcium and iron compounds such as octacalcium phosphate, calcite, and vivianite. The model showed that phosphorus

mineral formation in aerated digestate directly depends on pH but does not significantly depend on temperature within the ranges tested. Visual MINTEQ closely predicted OP-P removal for the $Mg(OH)_2$ dosed pilot tests via struvite formation, but failed to correctly predict OP-P removal for the $Ca(OH)_2$ dosed tests due to predicting calcite formation rather than a Ca-P that could have contributed to the OP-P removal measured in the pilot. Therefore, the selection of appropriate model input parameters and understanding of solubility chemistry is required to accurately predict scaling tendency at WRRFs.

5.2 Introduction

While scaling compounds can be harmful to plant processes and equipment, they have also been recognized as a beneficial phosphorus recovery option from water resource recovery facilities (WRRFs). Struvite harvesting and sequestration is a common and commercialized technology for the removal and recovery of phosphorus, with brushite ($CaHPO_4 \cdot 2H_2O$) and vivianite recovery emerging as another popular recovery route for phosphorus. Before beneficial harvesting, it is vital to characterize the solids stream at WRRF, since precipitation reactions are complex and dependent on several physio-chemical parameters.

There are three main groups of compounds likely to precipitate at WRRF: phosphates, carbonates, and sulfides/sulfates. This paper focuses on scaling minerals most likely to form within anaerobic digesters, downstream of digestion in solution of anaerobically digested sludge, and in aerated anaerobic digested sludge (PAD). The chemical equations, conditions for formation, and solubility constants of scalants observed at WRRF are presented in Table 1.

Struvite, k-struvite ($KMgPO_4 \cdot 6H_2O$), dittmarite ($MgNH_4PO_4 \cdot H_2O$), newberyite ($MgHPO_4 \cdot 3H_2O$), bobierrite ($Mg_3(PO_4)_2 \cdot 8H_2O$), and cattiite ($Mg_3(PO_4)_2 \cdot 22H_2O$) have all been noted in solutions containing magnesium, ammonium, and phosphate ions (Massey et al., 2009; Daneshgar et al., 2018). Of these, only struvite was considered in these models as struvite precipitates at neutral and higher pH values and at Mg:NH_4:P ratio of 1:1:1 (Musvoto et al., 2000).

Calcium phosphates include a large and complex variety of potential scaling minerals. This family includes amorphous calcium phosphate (ACP – $Ca_3(PO_4)_2$), as well as crystalline minerals such as: dicalcium phosphate dihydrate, commonly referred as brushite (DCPD – $CaHPO_4 \cdot 2H_2O$), monetite (DCP – $CaHPO_4$), tricalcium phosphate, commonly referred to as whitlockite (TCP – $Ca_3(PO_4)_2$) octacalcium phosphate (OCP – $Ca_8H_2(PO_4)_6 \cdot 5H_2O$), hydroxyapatite (HAP – $Ca_{10}(PO_4)_6(OH)_2$) (Daneshgar et al., 2018). In order of increasing solubility these are: hydroxyapatite, whitlockite, octacalcium phosphate, monetite, and brushite (Abbona et al., 1986). However, studies have shown that brushite and ACP are the first phases to precipitate, before slowly transforming into a more stable phase, such as hydroxyapatite. This transformation to hydroxyapatite has been observed to proceed slowly, extending beyond the typical timescale of solids handling in WRRF, and is therefore not likely to form (Musvoto et al., 2000).

Iron can also precipitate phosphate as vivianite. Vivianite ($Fe_3(PO_4)_2 \cdot 8H_2O$), like struvite, is increasing in popularity as a highly valuable wastewater recovery product that has beneficial slow release, fertilizer-like qualities when land applied (Wu et al., 2019). The pH range of insolubility of vivianite overlaps with struvite (pH 6-9). They have been noted to coprecipitate together, therefore, vivianite was included in the models (Wilfert et al., 2015). Both iron and aluminum oxides and hydroxides can remove orthophosphate by binding OP-P onto their solid surfaces via adsorption complexes. Diaspore (AlO(OH)), boehmite (AlO(OH), and gibbsite ($Al(OH)_3$) can adsorb phosphate in the pH range of 2 to 9, and are, therefore, relevant minerals to these models (Tanada et al., 2003).

Carbonates such as calcite ($CaCO_3$) and magnesite ($MgCO_3$) are both thermodynamically stable in the conditions present in anaerobic digestate and aerated anaerobic digestate, and therefore both were considered (Musvoto et al., 2000). Since the solubility range for siderite ($FeCO_3$) overlaps with vivianite, and it was considered in modeling efforts (Postma, 1980).

Lastly, sulfur compounds are important to consider within and around digesters. There are three naturally occurring iron sulfides minerals to note: mackinawite ($Fe_{(1+x)}S$, where x = 0.0057 to 0.06), pyrrhotite (ranging from Fe_7S_8 to FeS), and pyrite (FeS_2). Mackinawite forms in the initial pH range of 6.5 to 8.8 (Sardisco and Pitts, 1965). Generally, the formation order is a mackinawite scale which is then transformed to pyrrhotite and pyrite (Meyer et al., 1958). Finally, barite ($BaSO_4$) has been shown to precipitate at a pH > 2, with increasing precipitation rates between the pH of 2-5, and was considered in the modelling evaluation (Esteves et al., 2023).

Precipitate formation is most predominantly determined by the pH as it is related to both the solids solubility product (K_{sp}) and the saturation in solution (Snoeyink and Jenkins, 1980). Several authors have shown that the solubility of struvite decreases as pH increases, with maximum likelihood of formation in the wide pH range of 7-11, depending on the type of wastewater and plant operating conditions (Buchanan et *al*., 1994, Moulessehoul et *al*., 2017). The pH of a solution can be manipulated via CO_2 stripping from agitation and aeration as demonstrated by Merkel and Krauth, 1999, allowing for controlled struvite formation without additional reagents. The effectiveness of CO_2 removal varies with factors like temperature, initial dissolved CO_2 levels, and aeration flow rates (Korchef et al., 2011), and CO_2 solubility decreases with increasing temperature, further enhancing CO_2 volatilization and promoting conditions favorable to struvite crystallization (Snoeyink and Jenkins, 1980). The formation of struvite also affects pH. According to Equation 40, the reaction of struvite formation causes a release of protons, which leads to a reduction in pH of the solution (with n = 0, 1, or 2, dependent on the solution pH). Therefore, the pH change can be used as an indicator of the nucleation of struvite (Bouropoulos and Koutsoukos, 2000).

$$Mg^{2+} + NH_4^+ + H_nPO_4^{n-3} + 6H_2O \rightarrow MgNH_4PO_4 + 6H_2O + nH^+ \quad (40)$$

Temperature has a significant effect on mineral solubility, morphology, and kinetics. Studies show an inverse relationship between struvite solubility and temperature, indicating that struvite is more likely to form at lower temperatures (Burns and Finlayson, 1982; Bhuiyan et al., 2007). Additionally, high temperatures can promote the formation of alternative mineral phases, such as newberyite formation instead of struvite, especially in solutions with high magnesium concentrations and low pH levels (Babic-Ivancic et al., 2002). Jones, 2002 noted that the rate of precipitation is often increased at higher temperatures. Likewise, Boistelle et al.,1983 demonstrated struvite crystal growth to differ with temperature, with a "rectangular and prismatic" crystal structure at 25°C and more "square and thick" growth was seen at the increased temperature of 37°C.

Visual MINTEQ is a chemical equilibrium model that has a vast thermodynamic database that can calculate the speciation, solubility, and equilibrium of solid and dissolved phases of minerals in an aqueous solution (Gustafsson, 2008). Visual MINTEQ has been utilized to study interactions between PO_4, Mg, ammonia, and pH (Buchanan et al., 1994), and struvite crystal formation and precipitation kinetics (Jia et al., 2017; Ali et al., 2003). Jia et al., 2017, demonstrated that experimental results from a bench-scale study using synthetic wastewater aligned closely with Visual MINTEQ model predictions regarding ammonium recovery efficiency, struvite formation, and alkalinity dosages. Similarly, Celen et al., 2007, examined Visual MINTEQ's ability in determining the optimal operational changes to enhance struvite precipitation from liquid swine manure. However, other studies have discussed the importance of precipitation kinetics when modeling mineral formation and have stated that supersaturation in Visual MINTEQ is not a sufficient condition. Romero-Guiza et al., 2015, used Visual MINTEQ to conclude that struvite precipitation was influenced more by reaction kinetics than the solubility of magnesium and phosphate sources. Other studies emphasize that precipitate formation order is governed by kinetic factors such as pH effects in phosphate precipitation (Musvoto et al. 2000, Koutsoukos et al., 1980).

Many plants struggle with these scaling minerals and desire to reduce their harmful effects or even harvest them for nutrient recycling and recovery. However, due to the complex nature of these precipitates, difficulties in mineral characterization and the control of when and where these precipitates form remain. Limited research exists on the mechanisms involved in phosphorus precipitation in PAD combined with predictive modeling work on precipitation formation and confirmation with solids analysis. Therefore, a pilot experimental setup utilized aeration for pH control and chemical addition of $Mg(OH)_2$ and $Ca(OH)_2$ to thermally hydrolyzed anaerobic digestate collected from Hampton Road Sanitation District's Atlantic Treatment Plant (ATP) on a 3-day SRT. Parameters measured in each pilot test were modeled with the chemical equilibria software Visual MINTEQ to determine operational effects on minerology. The precipitates formed within pilot testing were then analyzed with Scanning Electron Microscope (SEM), Energy Dispersive X-ray Spectroscopy (EDS), X-Ray Diffraction Analysis, and Raman Spectroscopy to confirm the model results. The study had two primary objectives:

1) to evaluate and understand the impacts of pH, temperature, and chemical addition of two chemicals at various Ca^{2+}+Mg^{2+}:P ratios on phosphorus removal and mineral formation utilizing the modeling software Visual MINTEQ and

2) to characterize the solids formed with SEM/EDS, XRD, and Raman Spectroscopy to calibrate and validate the model.

The results of this study will enhance our understanding regarding scaling minerals likely to form within anaerobic digestion pretreated with Cambi THP, downstream of anaerobic digestion and on dewatering equipment, as well as in a potential PAD setup. A validated model could then be used to predict scaling potential and characterize minerals formed at other WRRFs to better treat these nuisance scaling minerals and determine their potential for harvesting/sequestration as a nutrient-rich product. Furthermore, this research will enhance the understanding of phosphorus mineral formation in biosolids, providing valuable insights for more sustainable and efficient modeling of phosphorus management in wastewater treatment, which is crucial for the future of solids handling.

5.3 Materials and Methodology

5.3.1 Sample Collection from Pilot Testing

The pilot setup at ATP consisted of four tanks (Figure 20). Each tank was 11 feet tall and with a volume of about 44 gallons. The tanks were operated as daily batch fed continuously stirred tank reactors (CSTR) mixed by pump recirculation with a 3-day SRT. The pilot tanks were well mixed with a turnover rate of less than two minutes (Equation 62 in Appendix B). Digestate was first passed through a 2-mm basket screen prior to being fed to each of the tanks one at a time to protect downstream pilot equipment. The tanks were aerated with fine bubble diffuser membranes at the base of each tank which could be operated at constant or intermittent air flow rates, on a DO setpoint, or pH setpoint. Each tank contained probes to record online measurements of temperature, DO, and pH (INSITE IG®). ORP was measured in the unaerated and aerated anaerobic digestate using the INSITE IG® ORP Sensor. The pilot was temperature controlled with a Non-Potable Water (NPW) heat exchanger at a setpoint of 35°C to best match the temperature of digestate. Effluent samples from each tank, as well as the pilot influent (e.g. anaerobic digestate), were collected throughout each test at the end of the 24-hour batch waste and feed timer to track steady state characteristics. The samples were analyzed for orthophosphate (TNT 845), ammonia (TNT 833), total alkalinity (TNT 870), total chemical oxygen demand (COD) (TNT 823), and soluble COD (TNT 822), all with HACH TNTplus Vial Tests, as well as soluble metals via filtering and ICP-AES (EPA 200.7 rev 4.4), volatile acids via standard methods (5560C-2011), and total solids (TS), and volatile solids (VS) via standard methods (1684).

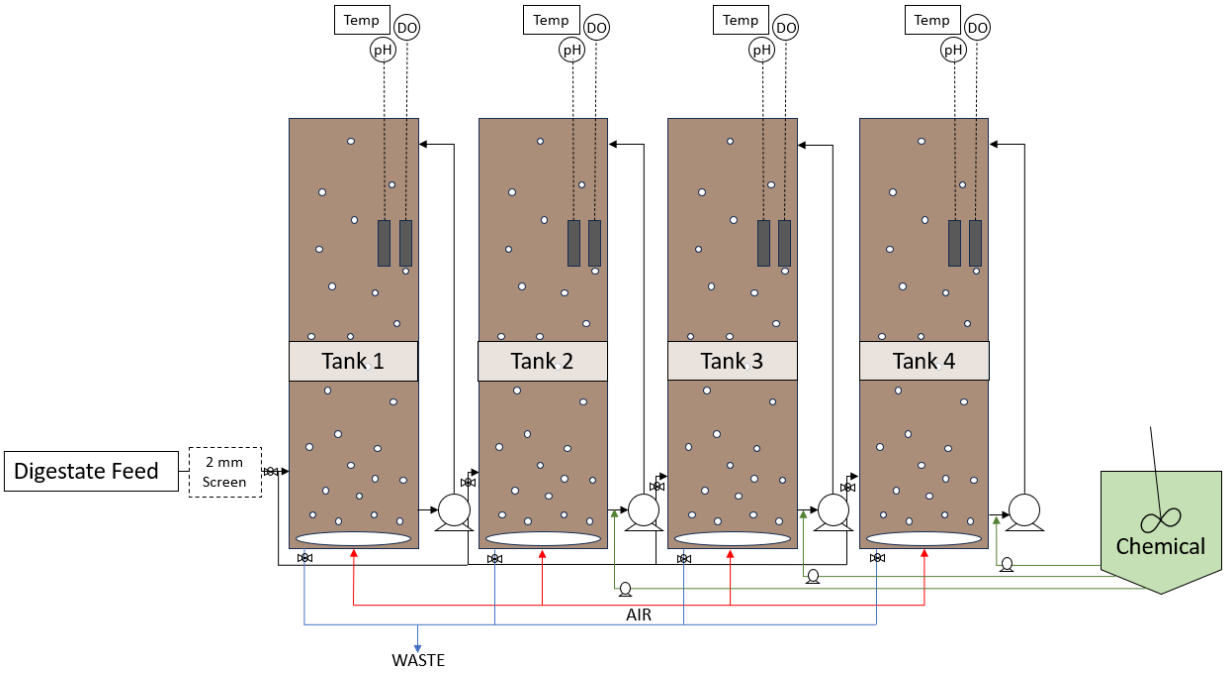

Figure 20: Pilot scale schematic featuring the control tank 1, and tanks 2, 3, and 4 from left to right, waste and feed lines, diffusers, probes, mixing pumps, and chemical injection.

5.3.2 Sample Characterization

Four samples of the minerals formed were analyzed with XRD, EDS/SEM, and Raman Spectroscopy. To determine what precipitate is currently formed at ATP, a scale sample was collected from the inside of a final dewatering centrifuge and evaluated. The second sample was collected from grit build up off of the base of the pilot tanks after being aerated at a DO setpoint of 0.3 mg/L and well mixed, prior to chemical injection tests to determine what precipitate formed in aerated anaerobic digestate. And the last two grit samples were similarly collected from the base of the pilot tanks after a $Mg(OH)_2$ dosed test and a $Ca(OH)_2$ dosed test, respectively, to determine the precipitate formation depending on the chemical injected. For the chemically dosed samples, grit was collected from the tank dosed to a Ca^{2+}+Mg^{2+}:P ratio of 1:1 for maximum scale possibility. Grit was collected off the surface of the diffuser during pilot clean out and placed in a 2-gallon Vevor® vacuum chamber attached to a GAST® pump for a few days to dry the sample.

The samples were sent to Ohio University's Institute for Corrosion and Multiphase Technology for XRD, EDS/SEM, and Raman spectroscopy analysis for quantification and crystalline phases identification. XRD analysis to identify the crystalline phases was conducted on a Rigaku MiniFlex 600 instrument at a current of 15 mA, a voltage of 35 kV, a scan speed of 3°/min, a step size of 0.02° and CuK_α radiation. EDS to determine the chemical composition of the samples was conducted on a Bruker® energy dispersive spectroscopy (EDS) analyzer attachment to SEM. SEM was utilized to determine the morphology of the samples and was conducted on a JEOL JSM-6390™ scanning electron microscope. Finally, the

phase characterization was determined by Raman spectroscopy using a Bruker Senterra II Raman microscope.

Middles of the samples were chosen for chemical and morphological analyses. Figure 21 displays the Infinite Focus Microscope (IMF) images of each sample.

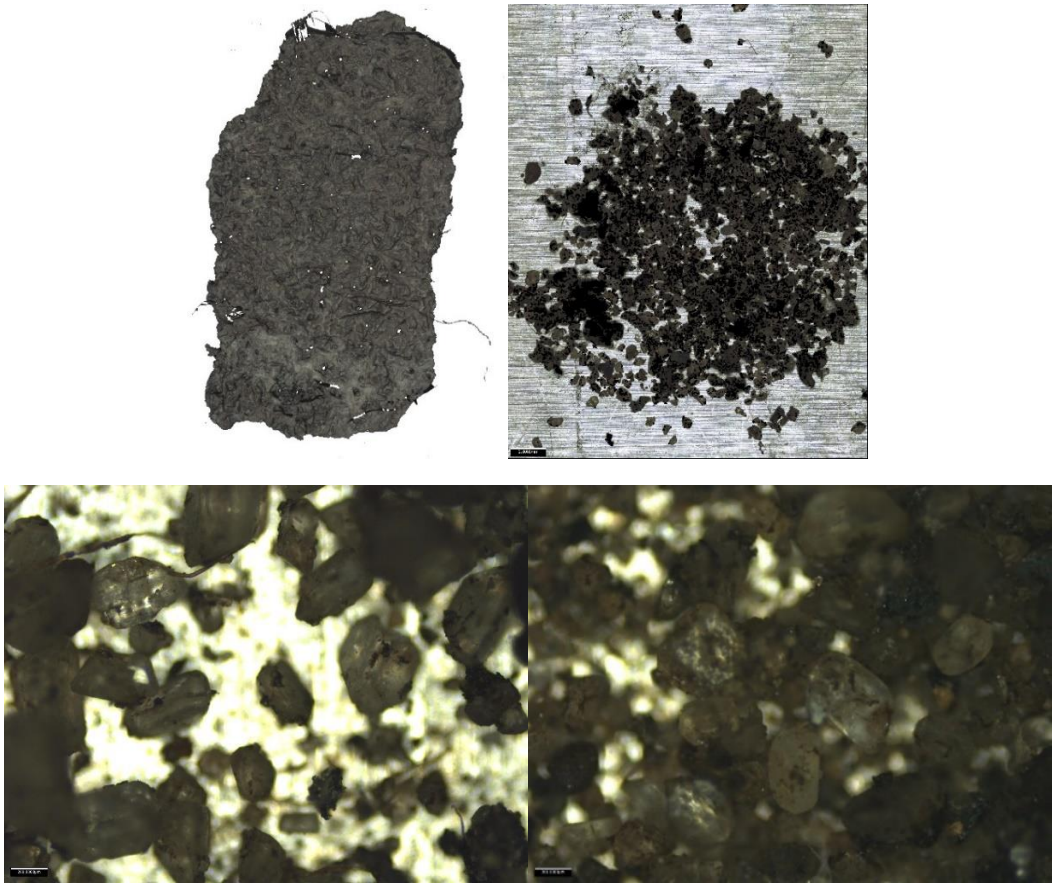

Figure 21: IFM images for the samples analyzed for (left to right, top to bottom): Final dewatering centrifuge scale, aerated pilot grit, $Mg(OH)_2$ dosed aerated grit, $Ca(OH)_2$ dosed aerated grit.

5.3.3 Visual MINTEQ Set Up

Visual MINTEQ is a chemical equilibrium model that has a vast thermodynamic database that can calculate the speciation, solubility, and equilibrium of solid and dissolved phases of minerals in an aqueous solution (Gustafsson, 2008). Visual MINTEQ v4.0 (KTH Vetenskap Och Konst, Stockholm, Sweden) was used to predict the precipitates formed in anaerobic digestate samples, as well as pilot effluent samples that were aerated and/or chemically dosed at ATP.

To set up the Visual MINTEQ model, the default equilibrium constants of complexes and precipitates in the Visual MINTEQ database were used, the Debye-Huckel method was selected for activity correction due to its acceptance as an appropriate method in the research

community (Buchanan et al., 1994). Other default settings were chosen such as defining the input concentrations based on the solution rather than the solids, and checking the box stating, "Oversaturated solids are not allowed to precipitate (Exceptions: Solids specified as infinite, finite, or possible)". This setting allows the user to have more control of the solids that are allowed to precipitate, based on first checking the saturation indexes of solids that can precipitate and later specifying them as possible solids. The drawback with using the default option is that it has poorer convergence characteristics, which could be a problem if you have many solids that precipitate. Because Visual MINTEQ does not account for kinetics, the slow-forming minerals, such as hydroxyapatite, dolomite, bobierrite, and cattiite, were not selected as possible precipitates even if they were listed as oversaturated in Visual MINTEQ. This step acted as model calibration. The ionic strength was calculated by the program, and pH and temperature sweeps were conducted to determine the precipitates formed across a pH range of 7-9 and 20-40°C, respectively. Cation and anion components such as sodium or ammonium and chloride were altered in these models to ensure the difference in charge was below 10%.

Oxidative Reduction Potential (ORP) is an important parameter to insert into these models as it measures if the environment is oxidized or reduced, and therefore determines the speciation of components such as iron and sulfur. A low redox potential promotes the reduction of ferric to ferrous iron and sulfate compounds to sulfide, which can create more ideal environments for compounds such as vivianite (Mingzhao et al. 2021). A more oxidized environment can have the opposite effect and lead to more iron sulfate compounds or barite. ORP was measured in the unaerated and aerated anaerobic digestate using the INSITE IG® ORP Sensor. Soluble Chemical Oxygen Demand (sCOD) can also be inserted into Visual MINTEQ as an approximated value for Dissolved Organic Carbon using the Stockholm Humic Model (SHM) but must be converted from a measure of "demand" for oxygen to a measure of CO_2 using Equations 41-43 (Rittmann and McCarty, 2001).

$$C_nH_aO_bN_c + \frac{2n+0.5a-b-1.5c}{2} O_2 \rightarrow nCO_2 + cNH_3 + \frac{a-3c}{2} H_2O \quad (41)$$

Then, the ratio of required oxygen for oxidation to dry mass of the organics is:

$$\frac{COD\prime}{Mass} = \frac{(2n+0.5a-b-1.5c)16}{12n+a+16b+14c} \quad (42)$$

The formula for standard biomass ($C_5H_7O_2N$) was assumed. So the $\frac{COD\prime}{Mass}$ = 1.42. The measured value for sCOD can then be divided by this ratio to get the amount of biomass converted to CO_2. This was then converted to CO_2 produced as C, following Equation 43.

$$DOC\ (SHM) = \frac{sCOD\ (\frac{mg}{L})}{\frac{COD\prime}{Mass} ratio} \div MW_{Biomass} \times n \times MW_C \quad (43)$$

Titration manager was used to model chemical injection experiments of $Mg(OH)_2$ and $Ca(OH)_2$ at Ca^{2+}+Mg^{2+}:P ratios tested on the pilot scale of 0.25:1, 0.5:1, 1:1, 1.3:1 and 1.6:1. To titrate each chemical in as done on the pilot scale, the original model inputs used were the same for the aerated anaerobic digestate at either aeration setting. In titration manager, the

volume of solution to be titrated was set to the pilot tank volume of 165 L, the volume of titrant was set to be 0.01 L increments, and the concentrations of the titrant composition in molal were inserted as measured. The box stating not to add titrant until the second step was checked. Each chemical was titrated in the model to match the volume injected in the pilot trial to reach the desired Ca^{2+}+Mg^{2+}:P ratio. When solving a titration model, the pH mode was changed from fixed to calculated from mass balance. For this option to yield correct results, the charge balance for all entered components must be zero. Therefore, ammonia and chloride were adjusted until this was satisfied. This set up is described in Table 7 for both the $Mg(OH)_2$ and $Ca(OH)_2$ chemical injection models.

Table 7: Titration manager setup for Visual MINTEQ for each chemical trial.

Component	Concentration (mol/L)
$Mg(OH)_2$ chemical titration set up	
Ca^{2+}	0.54
Mg^{2+}	14.89
H^+	-29.78
$Ca(OH)_2$ chemical titration set up	
Ca^{2+}	7.08
Mg^{2+}	0.01
H^+	-14.16

The set up steps for each run were followed as:

1. Enter all the components measured in the samples from Table 8, including organic components such as: Acetate-1 for the volatile acids measured, DOC (SHM) for the sCOD measured following the conversion Equations 41-43.
2. Set the pH and temperature as starting values of sweeps.
3. Specify alkalinity as mg/L as $CaCO_3$ and select the normal option for calculation.
4. Specify pe and Eh as Fixed Eh (mV) with the measured ORP value.
5. Run model and check the saturation indices of those solids that were oversaturated.
6. Now return to the home page, and unspecify alkalinity to reinterpret it as the total CO_3^{2-} concentration. This will now allow you to specify solids that are allowed to precipitate.
7. From the Solid phases and excluded species menu, specify 12 or less of those solids that were previously oversaturated as possible solids phases.
8. Set up pH or temperature sweep and determine which minerals formed.
9. Set up titration manager to model chemical injection at each Ca^{2+}+Mg^{2+}:P ratio using Table 7.

5.3.4 Model Operational Conditions

The modeling process for Visual MINTEQ was based on pilot operational conditions: anaerobic digestate (pilot influent), aerated anaerobic digestate (control tank effluent) constantly at 5 LPM, and aerated anaerobic digestate (control tank effluent) on a DO setpoint of 0.2 mg/L. The inputs of these operational conditions were collected during pilot tests as described in chapter 4 and averaged to insert into the model (Table 8).

Table 8: Operational conditions inserted as inputs in Visual MINTEQ.

Component	1. Anaerobic Digestate - Concentration (mg/L)	2. 5 LPM Aerated Anaerobic Digestate – Concentration (mg/L)	3. 0.2 mg/L Aerated Anaerobic Digestate – Concentration (mg/L)
Temperature set for pH sweep (°C)	35	35	35
pH set for temperature sweep	7.5	8.3	8.4
ORP (mV)	-442	-200	-200
DOC (SHM)	2546.3	2488.9	2609
Total Alkalinity (as $CaCO_3$)	7617	6147	5887
Volatile Acids (Acetate-1)	529	331	366
Al^{3+}	4.7	2.3	4.6
B(III)	0.7	0.8	0.6
Ba^{2+}	0.4	0.2	0.5
Ca^{2+}	54.6	28.1	40.3
Cl^-	131	136	136
Cu^{2+}	0.5	0.8	1.0
Fe^{2+}	47.3	46.2	108
K^+	446	471	376
Mg^{2+}	9.4	9.4	6.5
Mn^{2+}	0.3	0.2	0.3
Na^+	85.5	83.6	74.6
N (NH4+)	2538	2414	2443
P (PO4)	878	593	454
S (-II)	300	36	36
S (SO4)	1	1880	1880
Si^{4+}	66.1	35.3	-
Sr^{2+}	0.3	0.2	0.3
Zn^{2+}	2.9	3.0	4.7

5.4 Results and Discussion

5.4.1 Condition 1: Anaerobic Digestate

Anaerobic digestate (pilot influent) was modeled to determine the scaling tendency prior to aerobic treatment. The objective of this run was to determine what scaling compounds may have formed in the DSST and downstream at ATP. The Visual MINTEQ set up steps were followed, and the following minerals were listed as possible precipitates: Al_2O_3(s), $AlPO_4 \cdot 1.5H_2O$, barite, boehmite, $Ca_3(PO_4)_2$ (am1) and $Ca_3(PO_4)_2$ (am2) (ACP), $Ca_4H(PO_4)_3{:}3H_2O$ (OCP), $CaHPO_4$ (monetite), $CaHPO_4{:}2H_2O$ (brushite), calcite, diaspore, FeS, gibbsite, mackinawite, pyrite, SiO_2, siderite, struvite, variscite, and vivianite. First, a solubility diagram of these solids allowed to form can be determined in Visual MINTEQ. Figure 22 below shows the percent of the total concentration each solid may form across the pH spectrum from 5-10, at a constant temperature of 35°C. Visual MINTEQ predicts that out of all the possible solids to form listed, SiO_2, variscite, pyrite, monetite, calcite, struvite, diaspore, and OCP were the only ones likely to precipitate in solution. SiO_2, variscite, pyrite, monetite, OCP, and diaspore were dominant at lower pHs, but switched to calcite as the dominant mineral around pH 8, along with pyrite, struvite and diaspore.

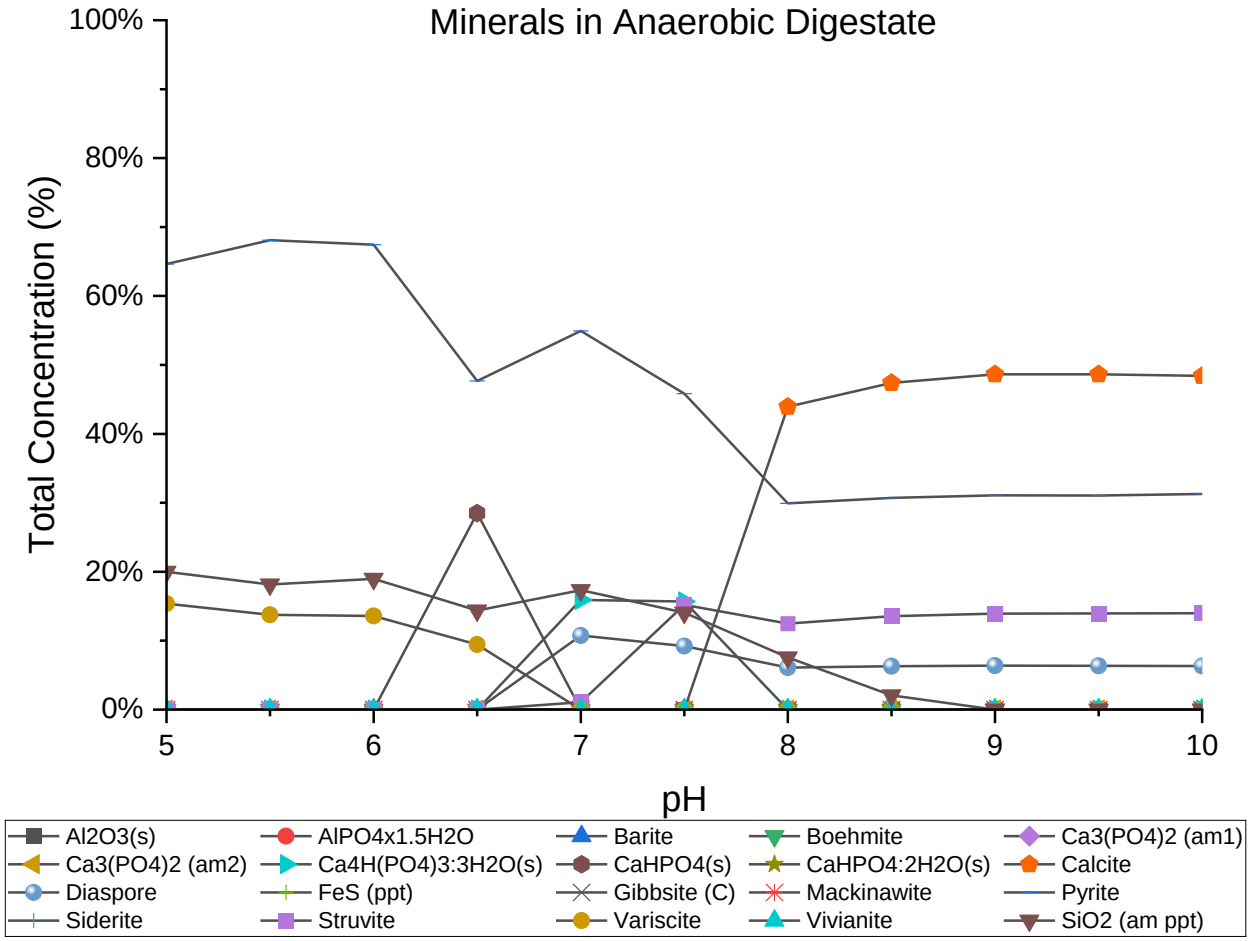

Figure 22: Percent of the total concentration of minerals predicted to form in Visual MINTEQ in anaerobic digestate.

For the pH sensitivity analysis, a constant temperature of 35°C was set, and for the temperature sensitivity analysis a constant pH of 7.5 was set. These were the average values measured for unaerated anaerobic digestate over the course of this study. Figure 23 and Figure 24 below provides a summary of the results at key points through the sensitivity analysis in the model: pH 7.5 and 8.5, and temperatures 20, 30, and 40°C, respectively.

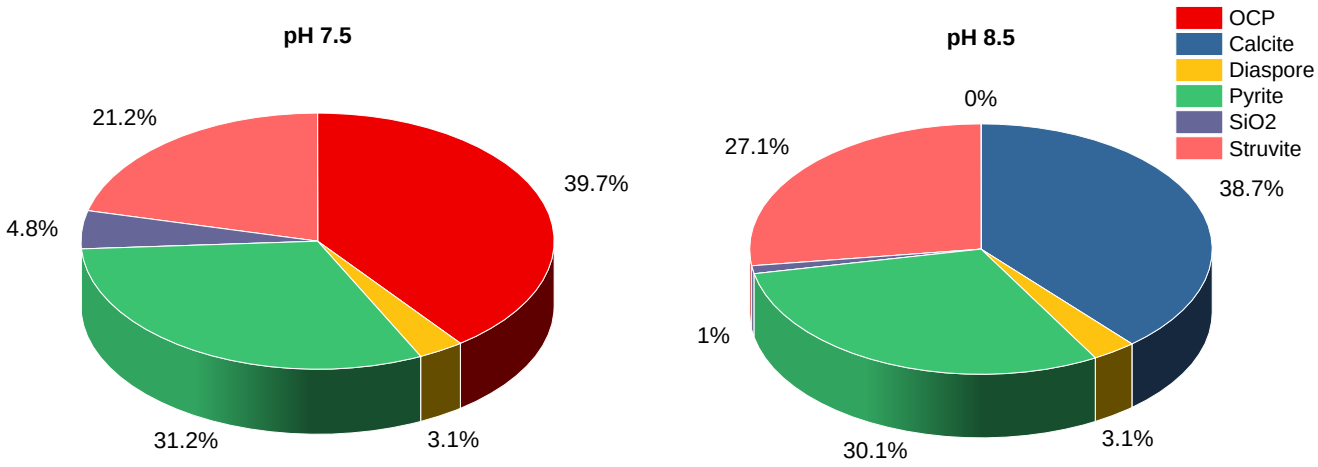

Figure 23: Summary of mineral formation in anaerobic digestate - pH sensitivity analysis results from Visual MINTEQ performed at a constant temperature of 35°C.

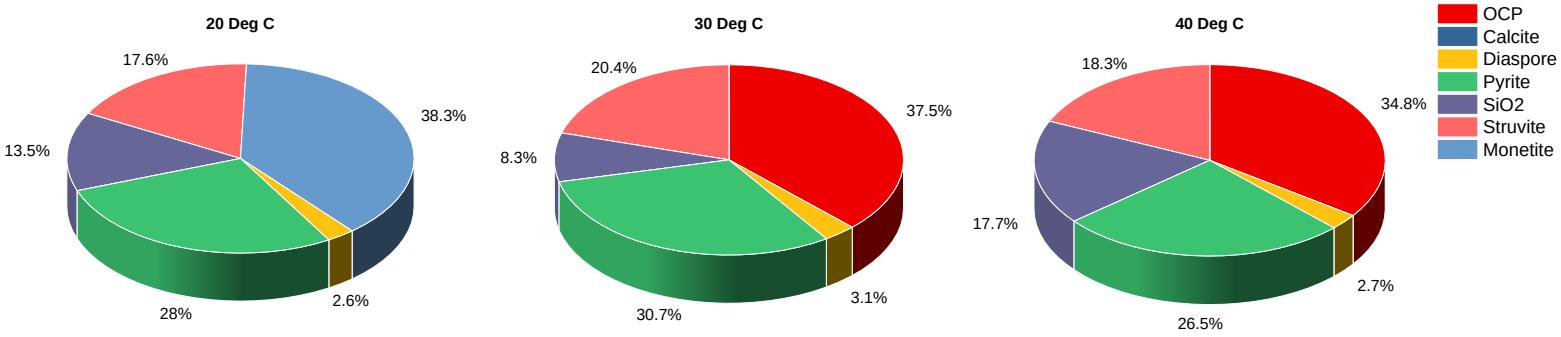

Figure 24: Summary of mineral formation in anaerobic digestate - temperature sensitivity analysis results from Visual MINTEQ performed at a constant pH of 7.5.

According to Visual MINTEQ at a pH of 7.5 and a temperature of 35°C, the dominant mineral formed was OCP, which was followed by pyrite, struvite, SiO_2, and diaspore. As pH increased, the dominant calcium mineral formed switched from OCP to calcite around pH 7.9. This is a reasonable prediction with the influent Ca^{2+} concentration and pH range of insolubility for each mineral. Struvite formed at both pH values, as expected in this range of insolubility for this mineral. Struvite increased as pH increased in this range, which also aligns with literature (Munch and Barr, 2000; Buchanan et al., 1994). At a temperature of 35°C, Visual MINTEQ predicts pH heavily determines the degree of phosphorus removal via struvite alone or if additional phosphorus was removed in the form of OCP.

In Visual MINTEQ, at a constant pH of 7.5 and 20°C, the dominant mineral formed was monetite, however, it transitioned to OCP at higher temperatures of 30°C and 40°C.
A similar phenomenon was reported in a calorimetric study conducted by Mitsionis and Vaimakis, 2010 of the temperature effects on calcium phosphate phases. They found with XRD analysis that at the lower temperatures they tested (30 and 40°C), brushite and monetite

were apparent, but when the temperature was raised to 50 and 60°C, both mineral phases disappeared, and only hydroxyapatite and OCP were present. Visual MINTEQ predicted calcite will not form over OCP until pH 7.9. Therefore, in this temperature sensitivity analysis conducted at pH 7.5 to best model the initial pH measured in anaerobic digestate, temperature does not affect calcite formation. Otherwise, Visual MINTEQ at a pH of 7.5 predicted minimal effects from temperature on pyrite, struvite, and diaspore formation.

5.4.1.1 Physical Scale Analysis for the Final Dewatering Centrifuge Sample

Model results for anaerobic digestate were validated with XRD, EDS/SEM, and Raman spectroscopic analysis from the sample collected post digestion off the final dewatering centrifuges. The XRD peaks identified for the sample are presented below (Figure 25).

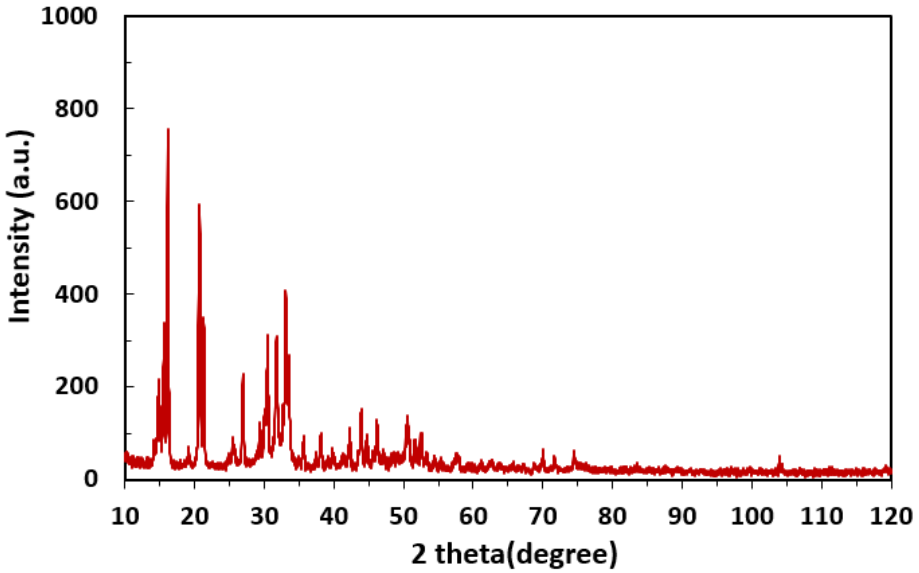

Figure 25: XRD peaks measured for ATP scale collected.

The analysis most closely resembled struvite, with slight variability in peak position and intensity. Struvite most notably has peak XRD peak locations at 15, 16, 17, 21, 22, 27, 31, 32, and 33 degrees, which almost all line up with the XRD pattern for this sample, as shown in the struvite standard (The RRUFF™ Project). The peak at 30 degrees, as well as the minor peaks between 42 and 52 degrees may also be correlated to calcite or Ca_3PO_4 (The RRUFF™ Project). The most intense peak for pyrite appears at 33 degrees and could be contributing to the peak around the same location in the XRD analysis for ATP plant scale (The RRUFF™ Project).

EDS and SEM indicated the presence of metal phosphates, with a potential presence of carbonates (Figure 26,Figure 27, Table 9). The prominent atomic percentages found with

EDS analysis was that of P, Mg, Fe, and Ca, which correlate well with struvite or calcium phosphate compounds. Nitrogen content was too insignificant at the specimen surface to be detected. However, it was noted by the lab conducting this analysis that EDS has limitations with light elements, which might also render these values for oxygen and calcium less reliable.

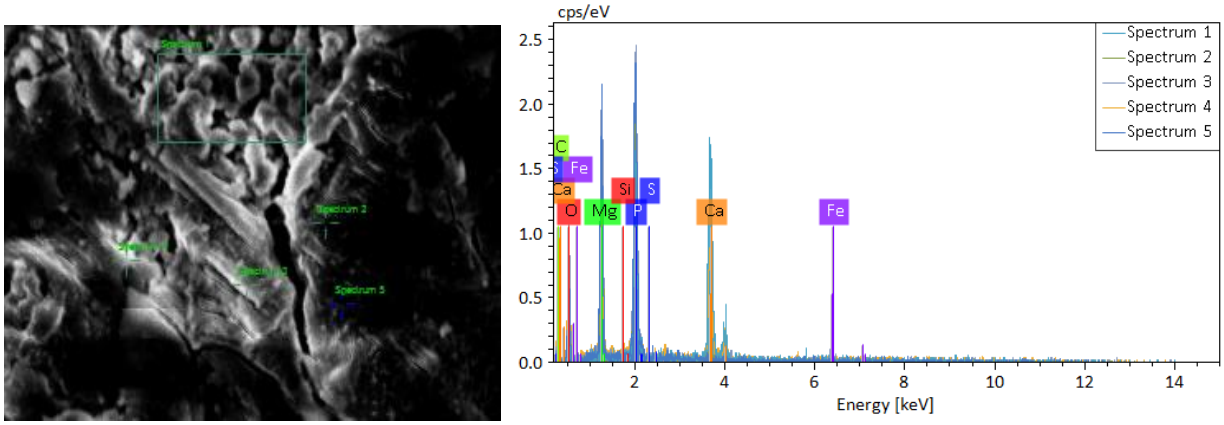

Figure 26: EDS chemical composition for the ATP scale collected.

Table 9: EDS chemical composition for the ATP scale collected.

Spectrum	C	O	Mg	Si	P	S	Ca	Fe
1	0.00	0.00	5.36	0.80	77.10	0.29	16.44	0.00
2	4.65	30.78	24.10	0.88	33.11	0.00	4.41	2.07
3	16.05	32.86	17.02	0.22	26.72	0.00	1.87	5.26
4	20.58	29.81	3.52	0.66	41.47	0.87	3.08	0.00
5	0.00	30.84	18.43	0.00	27.58	0.00	0.78	22.37
Mean	8.26	24.86	13.69	0.51	41.20	0.23	5.32	5.94

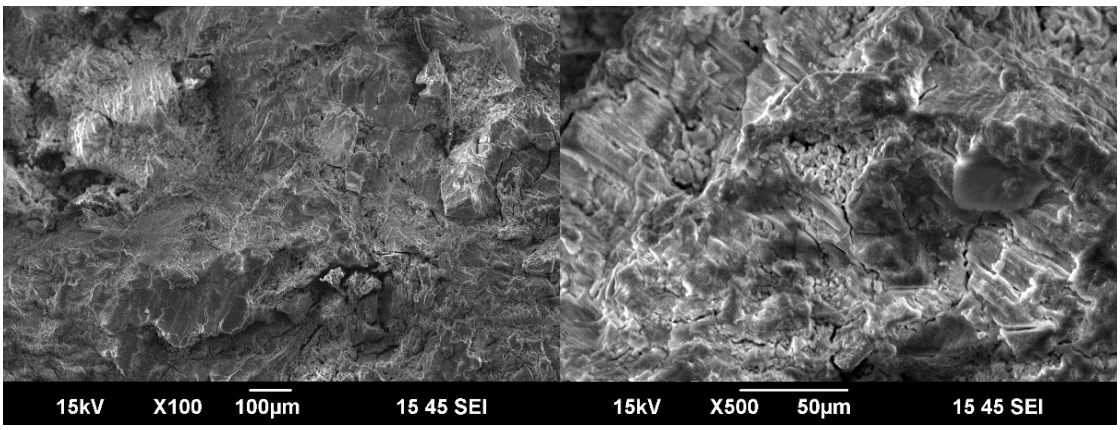

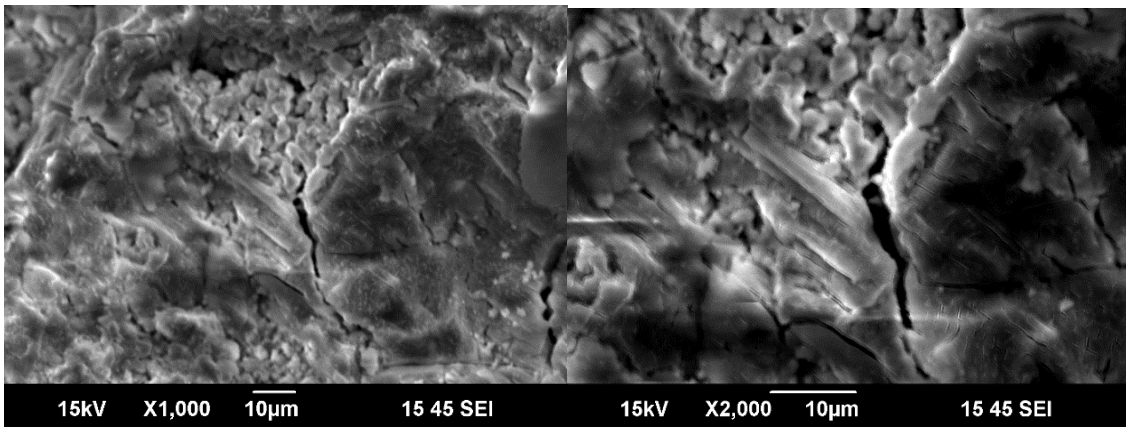

Figure 27: EDS chemical composition for the ATP scale collected.

Lastly, this specimen strongly emitted under laser irradiation during Raman spectroscopy analysis, however, this dwarfed any possible Raman peaks from phases, functional groups, or polyatomic species. Therefore, it is not included. Overall, the physical scale analysis predicted struvite as the dominant species and validates struvite formation predicted by the Visual MINTEQ model. The EDS atomic percentages verified carbon, magnesium, silica, phosphorus, calcium, and iron as the dominate elements present in this sample. When coupled with the XRD peak locations this could be indicative of the presence of calcite, tricalcium phosphate, and pyrite like in the model predictions, but is unconfirmed due to minor shifts in peak locations and intensities.

5.4.2 Condition 2: Anaerobic Digestate Aerated Constantly at 5 LPM

Anaerobic digestate was subjected to aerobic treatment constantly at 5 LPM in the pilot during campaigns 1 and 3. Post aeration and mixing, the samples were analyzed for the parameters used as model inputs listed in the methods section. The following minerals were listed as possible precipitates in Visual MINTEQ: Al_2O_3(s), $AlPO_4 \cdot 1.5H_2O$, barite, boehmite, $Ca_3(PO_4)_2$ (am1) and $Ca_3(PO_4)_2$ (am2) (ACP), $Ca_4H(PO_4)_3 \cdot 3H_2O$ (OCP), $CaHPO_4$ (monetite), $CaHPO_4 \cdot 2H_2O$ (brushite), calcite, diaspore, FeS, gibbsite (C), mackinawite, pyrite, SiO_2, siderite, struvite, variscite, and vivianite.

A solubility diagram of these solids allowed to form can be determined in Visual MINTEQ. Figure 28 below shows the percent of the total concentration each solid may form across the pH range of 5-10, at a constant temperature of 35°C. Compared to this diagram for unaerated digestate in Figure 22, this figure suggests an increase in complexity of mineral formation in PAD solids. Along with variscite, pyrite, calcite, struvite, diaspore, and OCP, Visual MINTEQ now predicts vivianite to form between pH values 5.5 – 10. SiO_2 no longer was predicted to form. Pyrite, OCP, diaspore, and vivianite were dominant at lower pHs, but again switched to calcite as the dominant mineral around pH 8 – 10, followed by pyrite, struvite, diaspore, and vivianite. Between pH 8 – 10, struvite consisted of a higher percentage of the total concentration as compared to unaerated anaerobic digestate.

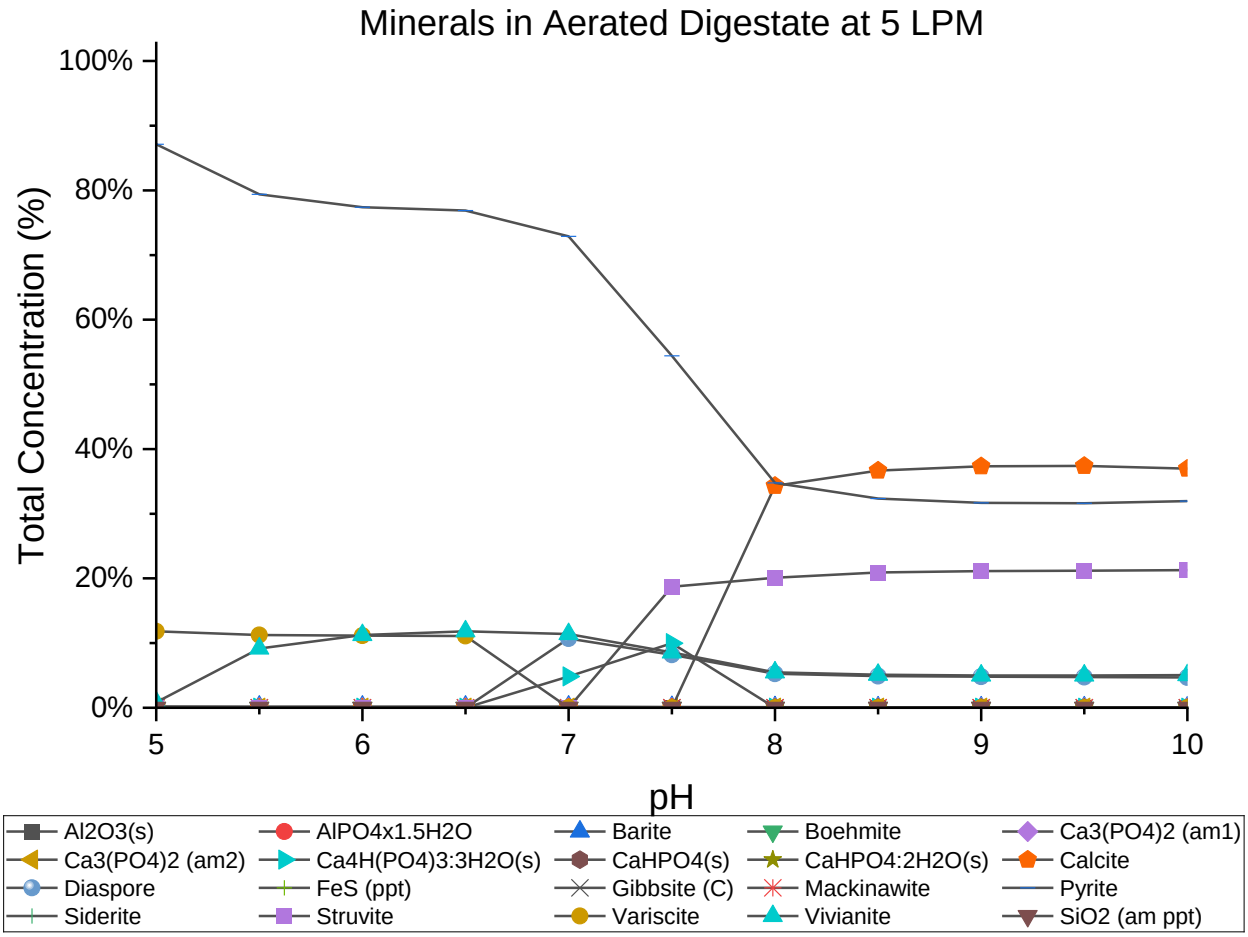

Figure 28: Percent of the total concentration of minerals predicted to form in Visual MINTEQ in anaerobic digestate aerated constantly at 5 LPM.

For the pH sensitivity analysis, a constant temperature of 35°C was set, and for the temperature sensitivity analysis a constant pH of 8.3 for aerated anaerobic digestate at 5 LPM was set. Figure 29 and Figure 30 below shows a summary of results found at key points through the analyses in each model: pH 7.5 and 8.5, and temperatures 20, 30, and 40°C, respectively.

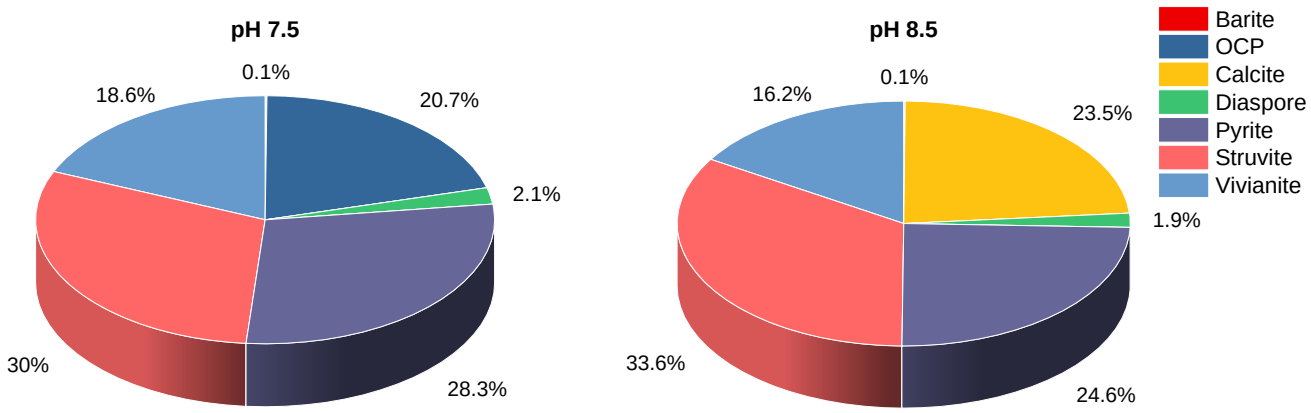

Figure 29: Summary of mineral formation in anaerobic digestate aerated at 5 LPM - pH sensitivity analysis results from Visual MINTEQ conducted at a constant temperature of 35°C.

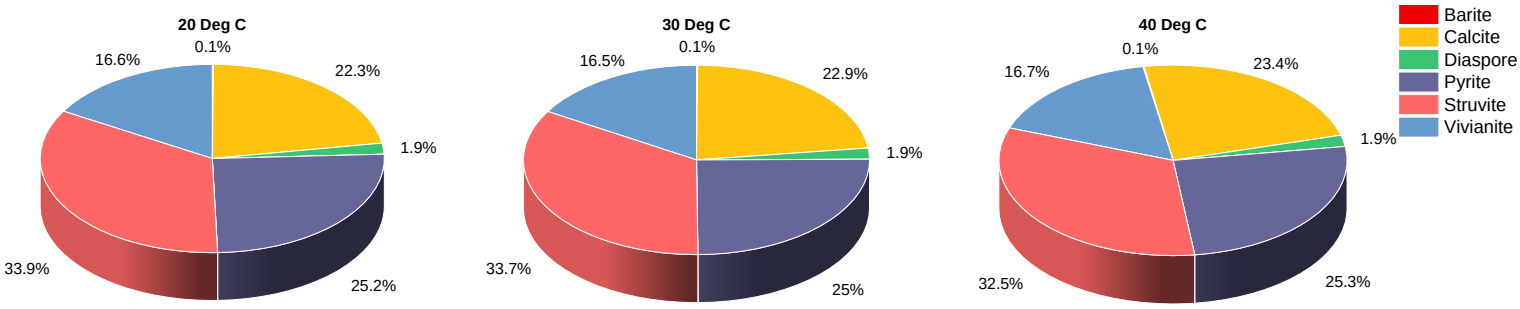

Figure 30: Summary of mineral formation in anaerobic digestate aerated at 5 LPM - temperature sensitivity analysis results from Visual MINTEQ conducted at a constant pH of 8.3.

According to Visual MINTEQ at a pH of 7.5 and a temperature of 35°C, under constant aerated operation at 5 LPM, the dominant mineral formed was struvite, followed by pyrite, OCP, vivianite, diaspore, and barite. As the pH increased to 8.5, the dominant minerals formed were the same except OCP switched to calcite. Similar to the first model run, the calcium mineral formed switched from OCP to calcite at pH 7.9. Struvite formation increased as pH increased. Unlike the first model run, vivianite was predicted to form as a means of phosphorus removal in similar amounts at both pH 7.5 and 8.5, which could be due to the increase in the measured ORP in this more oxidized environment as shown in Table 8. Struvite increased in formation at 35°C from pH 7.5 to 8.5 by approximately 10.5% of the total concentration. Therefore, Visual MINTEQ predicts pH at a constant temperature of 35°C to have an effect on precipitate formation, especially in terms of compounds as a means of phosphorus removal. At a pH below 7.9, OCP, struvite, and vivianite were predicted to precipitate phosphorus from solution, as compared to struvite and vivianite alone at higher pH values.

According to Visual MINTEQ at a constant pH of 8.3 and a temperature sensitivity analysis across 20°C, 30°C, and 40°C under aerated operation, the dominant mineral formed remained struvite, followed by pyrite, calcite, vivianite, diaspore and barite. The concentration of struvite formation decreased slightly as temperature increased, which aligns with the literature (Aage et al., 1997; Burns and Finlayson, 1982; Bhuiyan et al., 2007). Otherwise, there was little to no differences in precipitate formation across the temperature sensitivity analysis conducted across 20 – 40°C. Therefore, it could be concluded that at a pH of 8.3, the effect of temperature is minimal on precipitation of scaling compounds in anaerobic digestate aerated at 5 LPM.

5.4.2.1 $Mg(OH)_2$ Titration to Anaerobic Digestate Aerated at 5 LPM

Utilizing the same inputs from run 2, a titration experiment was set up to model the effects of $Mg(OH)_2$ addition on mineral formation in the pilot. The titration steps were followed, and the concentration of each mineral formed was solved for. Combined with the model predictions from the run for unaerated anaerobic digestate at a temperature of 35°C and a pH of 7.5, and the aerated digestate at 5 LPM at a temperature of 35°C and a pH of 8.3, the predicted minerals formed at the Ca^{2+}+Mg^{2+}:P ratios tested of 0.25:1, 0.5:1 and 1:1 in the pilot, along with the pH predicted in the model and measured in campaign 1 are shown in Figure 31 below.

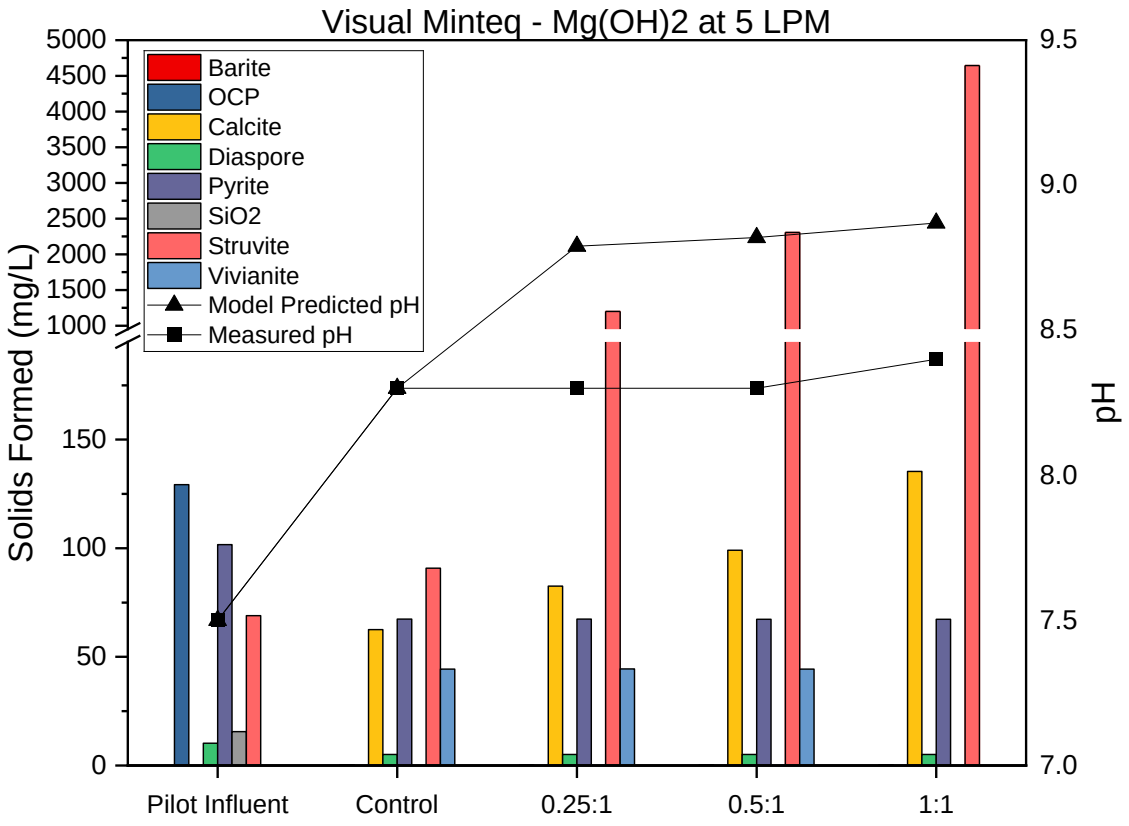

Figure 31: Mineral formation and pH predicted by Visual MINTEQ in the anaerobic digestate (pilot influent), aerated digestate at 5 LPM (control), and aerated digestate at 5 LPM with Mg(OH)2 addition to the Ca^{2+}+Mg^{2+}:P ratios tested of 0.25:1, 0.5:1 and 1:1.

The mineral predicted to form and the concentrations for the pilot influent and control were discussed in Sections 5.4.1 and 5.4.2. As $Mg(OH)_2$ was introduced at various Ca^{2+}+Mg^{2+}:P, the minerals formed stayed the same as the control in the 0.25:1 and 0.5:1, except at the higher ratio tested of 1:1, vivianite was no longer predicted to form as it was depleted by struvite formation. Struvite remained the dominant mineral predicted to form, and increased as $Mg(OH)_2$ was added up to 4643 mg/L in the 1:1 dosed tank. Calcite also increased as $Mg(OH)_2$ was added, but to a lesser extent up to 135 mg/L. However, Visual MINTEQ overpredicted the pH calculated at each Ca^{2+}+Mg^{2+}:P ratio than what was measured in the pilot, which could be overpredicted these mineral concentrations as well. Where the measured pH averaged around pH 8.3 in the control, 0.25:1, and 0.5:1 dosed tanks and 8.4 in the 1:1 dosed tank, the calculated pH from the mass balance in Visual MINTEQ was 8.8 for both the 0.25:1 and the 0.5:1 dosed tanks, and was 8.9 for the 1:1 dosed tank. This could indicate that the pilot tanks were more well buffered by background environmental conditions than what was predicted in the model solely based on the component inputs measured and alkalinity in the $Mg(OH)_2$ chemical. A study done by Lui et al., 2018 measured the effects of struvite formation on pH change and determined this to be more difficult in real wastewaters, due to the existence of alkaline ions and other foreign substances that impose different pH decreases due to buffer capacity.

In each model output, OP-P in the effluent was also predicted by Visual MINTEQ to validate the model results back to the pilot test conducted. Table 10 below displays the predicted results compared to the measured results for OP-P removal in this model run and campaign 1.

Table 10: Visual MINTEQ predicted OP-P removal compared to measured OP-P removal for campaign 1.

	Visual MINTEQ Predicted OP-P Removal (%)	Measured OP-P Removal (%)
Control	37%	34%
0.25:1	52%	56%
0.5:1	68%	74%
1:1	99%	85%

Overall, the model was able to closely predict OP-P removal measured in the first pilot test. The model more closely predicted OP-P removal in the control and lowest Ca^{2+}+Mg^{2+}:P ratio tested and got less accurate as the ratio increased. The model overpredicted OP-P removal for the control and 1:1 dosed tank, and underpredicted OP-P removal in both the 0.25:1 and 0.5:1 dosed tanks. Visual MINTEQ can be accurate in predicting OP-P removal in aerated digestate supplemented with $Mg(OH)_2$ via struvite formation.

5.4.2.2 $Ca(OH)_2$ Titration to Anaerobic Digestate Aerated at 5 LPM

Utilizing the same inputs from run 2, a titration experiment was set up to model the effects of $Ca(OH)_2$ addition on mineral formation in the pilot. The titration steps were followed, and the concentration of each mineral formed was solved for. Combined with the model predictions from the run for unaerated anaerobic digestate at a temperature of 35°C and a pH of 7.5, and the aerated digestate at 5 LPM at a temperature of 35°C and a pH of 8.3, the predicted minerals formed at the Ca^{2+}+Mg^{2+}:P ratios tested of 0.25:1, 0.5:1 and 1:1 in the pilot, along with the pH predicted in the model and measured in campaign 3 are shown in Figure 32 below.

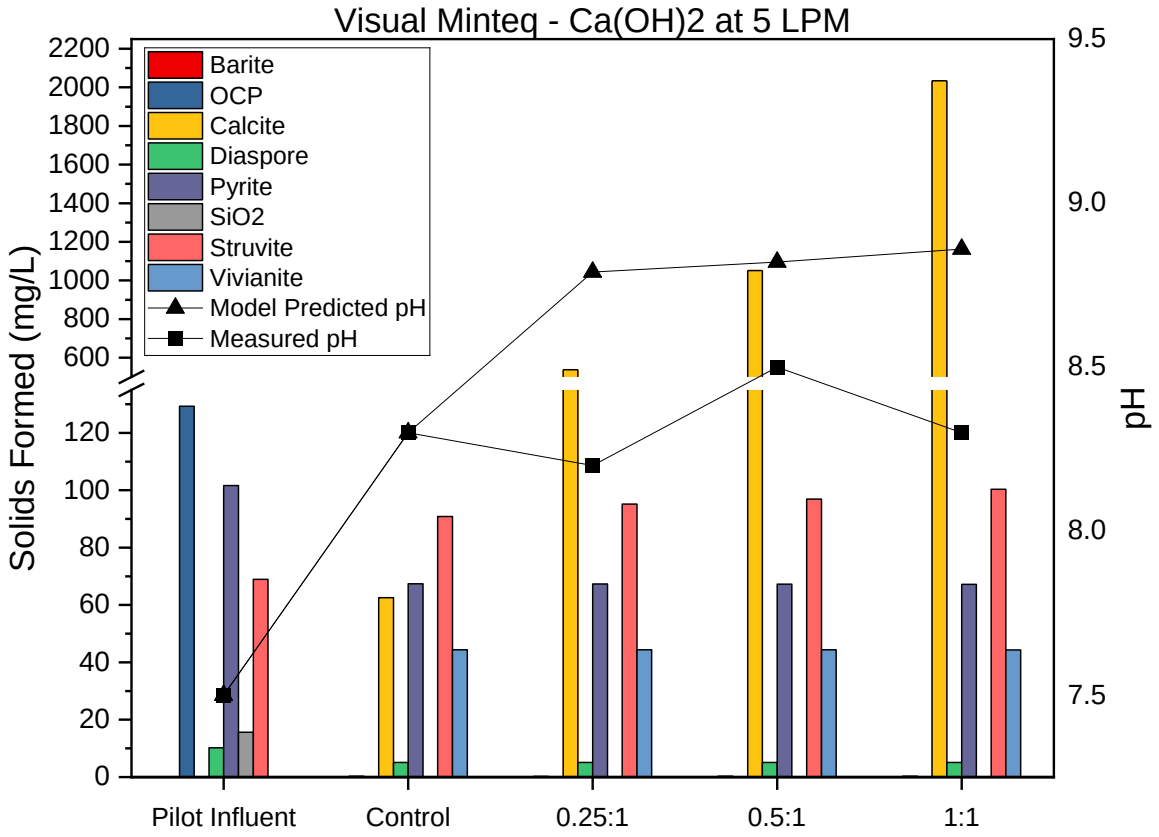

Figure 32: Mineral formation and pH predicted by Visual MINTEQ in the anaerobic digestate (pilot influent), aerated digestate at 5 LPM (control), and aerated digestate at 5 LPM with Ca(OH)2 addition to the Ca^{2+}+Mg^{2+}:P ratios tested of 0.25:1, 0.5:1 and 1:1.

The mineral predicted to form and the concentrations for the pilot influent and control were discussed in Sections 5.4.1 and 5.4.2. As $Ca(OH)_2$ was introduced at various Ca^{2+}+Mg^{2+}:P, the minerals formed stayed the same as the control in the all the tested ratios of 0.25:1 and 0.5:1 and 1:1. Where struvite was the dominant mineral predicted to form in the control, the supplemented calcium as $Ca(OH)_2$ immediately caused an increase in calcite in the chemically dosed tanks to become the new dominant mineral formed. Calcite increased as the Ca^{2+}+Mg^{2+}:P ratio increased up to 2033 mg/L in the 1:1 dosed tank. Struvite also

minimally increased as $Ca(OH)_2$ was added by about 10 mg/L. There were no other changes to the minerals formed or concentrations due to $Ca(OH)_2$ addition predicted. This was a critical result as it predicted no other calcium phosphate mineral to form due to the $Ca(OH)_2$ supplementation, which led to no change in OP-P removal past the control. Visual MINTEQ again overpredicted pH calculated at each Ca^{2+}+Mg^{2+}:P ratio than what was measured in the pilot. Where the measured pH for the control, 0.25:1, 0.5:1, and the 1:1 dosed tanks averaged pH 8.3, 8.2, 8.5, and 8.3, respectively, the calculated pH from the mass balance in Visual MINTEQ was 8.8 for both the 0.25:1 and the 0.5:1 dosed tanks, and was 8.9 for the 1:1 dosed tank.

In each model output, OP-P in the effluent was also predicted by Visual MINTEQ to validate the model results back to the pilot test conducted. Table 11 below displays the predicted results compared to the measured results for OP-P removal in this model run and campaign 3.

Table 11: Visual MINTEQ predicted OP-P removal compared to measured OP-P removal for campaign 3.

	Visual MINTEQ Predicted OP-P Removal (%)	**Measured OP-P Removal (%)**
Control	37%	38%
0.25:1	37%	60%
0.5:1	37%	53%
1:1	37%	85%

In this run, the model was only able to closely predict OP-P removal measured in the third pilot test in the control tank. No further OP-P removal past 37% was predicted in the model due to calcite formation dominating in all the $Ca(OH)_2$ dosed trials. Even after allowing all other calcium phosphate minerals to form within the model, at this pH all minerals were undersaturated with respect to calcite, except for hydroxyapatite. Hydroxyapatite was not allowed to form in this model due to many sources claiming the formation rate of hydroxyapatite to be too slow for a wastewater treatment timeline and that hydroxyapatite is characteristically suppressed in anaerobic digestate (Muster et al., 2013; Ferguson and McCarty, 1971; Musvoto et al., 2000). Due to Visual MINTEQ not accounting for kinetics in the model, hydroxyapatite must remain omitted from the possible precipitates allowed to form, and no work around was determined to correct these false phosphorus levels reported by the model. Therefore, Visual MINTEQ has limitations when predicting phosphorus removal via calcium phosphates and will incorrectly favor calcite formation in aerated digestate supplemented with $Ca(OH)_2$.

5.4.3 Condition 3: Anaerobic Digestate Aerated on a DO Setpoint of 0.2 mg/L

Anaerobic digestate was subjected to aerobic treatment on a DO setpoint at 0.2 mg/L in the pilot during campaigns 2, 4, and 5. Post aeration and mixing, the samples were analyzed for the parameters used as model inputs listed in the methods section. The following minerals were listed as possible precipitates in Visual MINTEQ: Al_2O_3(s), $AlPO_4 \cdot 1.5H_2O$, barite, boehmite, $Ca_3(PO_4)_2$ (am1) and $Ca_3(PO_4)_2$ (am2) (ACP), $Ca_4H(PO_4)_3{:}3H_2O$ (OCP), $CaHPO_4$ (monetite), $CaHPO_4{:}2H_2O$ (brushite), calcite, diaspore, FeS, gibbsite (C), mackinawite, pyrite, SiO_2, siderite, struvite, variscite, and vivianite.

A solubility diagram of these solids allowed to form can be determined in Visual MINTEQ. Figure 33 below shows the percent of the total concentration each solid may form across pH 5-10, at a constant temperature of 35°C. Compared to this diagram for aerated digestate at a constant rate of 5 LPM, the same minerals were predicted to form, but with now a large increase in vivianite in more aerated PAD solids. Along with barite, variscite, pyrite, calcite, struvite, diaspore, and OCP, Visual MINTEQ now predicts vivianite to make up a greater percentage of the total concentration than struvite. Barite, pyrite, OCP, diaspore, and vivianite were dominant at lower pHs, but similarly switched to calcite as the dominant mineral around pH 8 – 10.5, followed by pyrite, and vivianite.

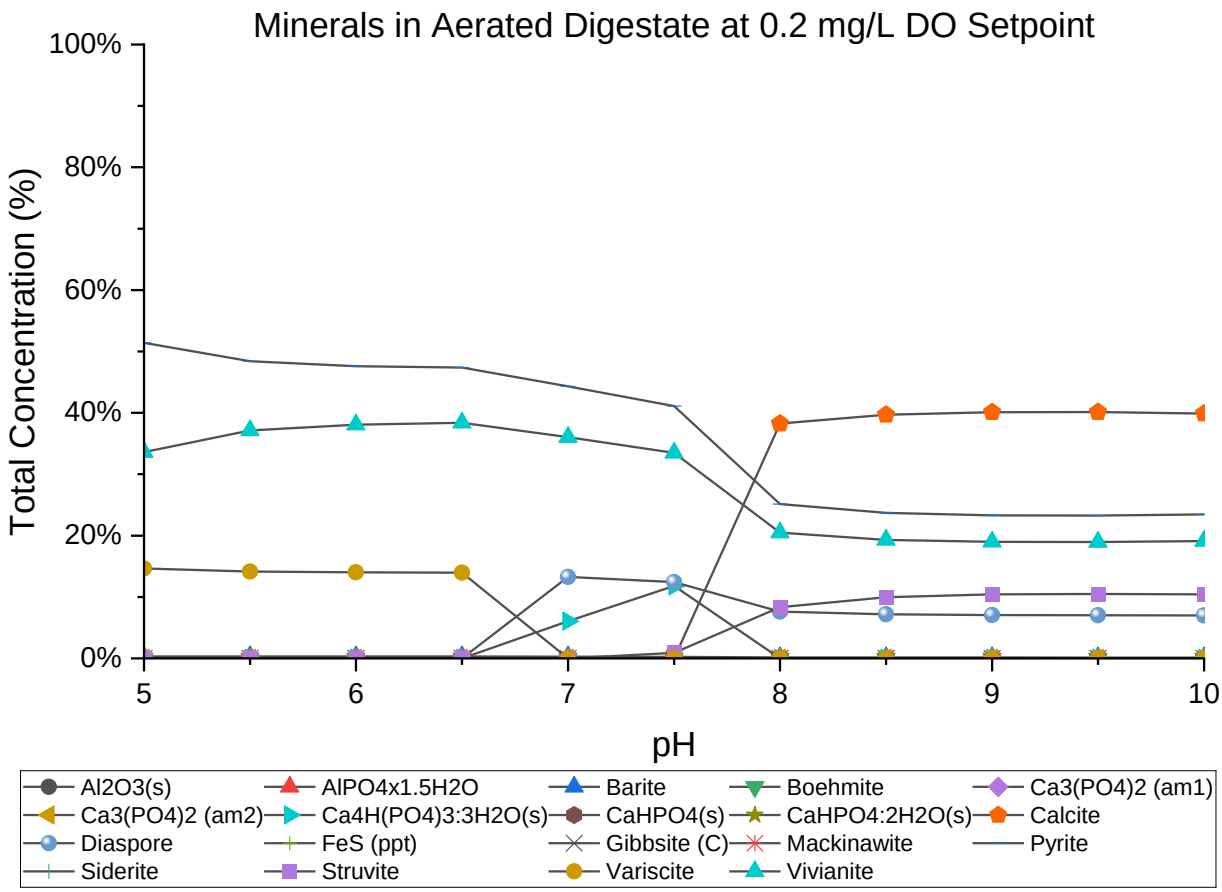

Figure 33: Percent of the total concentration of minerals predicted to form in Visual MINTEQ in anaerobic digestate aerated at a DO setpoint of 0.2 mg/L.

For the pH sensitivity analysis, a constant temperature of 35°C was set, and for the temperature sensitivity analysis a constant pH of 8.4 for aerated anaerobic digestate at a DO setpoint of 0.2 mg/L was set. Figure 34 and Figure 35 below show a summary of results found at key points through the analyses in each model: pH 7.5 and 8.5, and temperatures 20, 30, and 40°C, respectively.

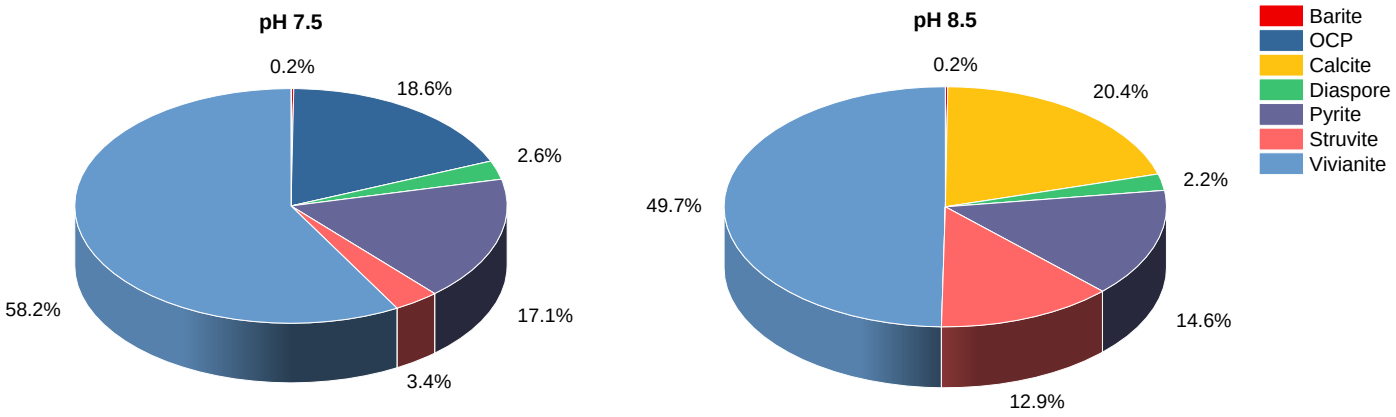

Figure 34: Summary of mineral formation in anaerobic digestate aerated at a DO setpoint of 0.2 mg/L - pH sensitivity analysis results from Visual MINTEQ conducted at a constant temperature of 35°C.

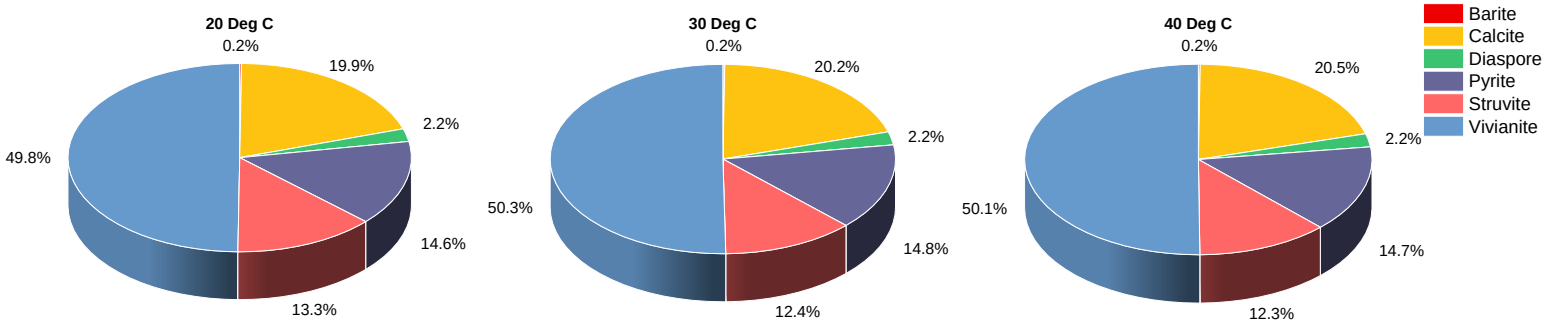

Figure 35: Summary of mineral formation in anaerobic digestate aerated at a DO setpoint of 0.2 mg/L - temperature sensitivity analysis results from Visual MINTEQ conducted at a constant pH of 8.4.

According to Visual MINTEQ at a pH of 7.5 and a temperature of 35°C, under constant aerated operation at a DO setpoint of 0.2 mg/L, the dominant mineral formed was now vivianite, followed by OCP, pyrite, struvite, diaspore, and barite. Contrary to the model run for aerated digestate at a constant 5 LPM, vivianite now dominants over struvite formation, which could be due to the increase in the measured soluble iron concentration in this more heavily aerated environment as shown in Table 8. As the pH increased to 8.5, the dominant minerals formed were the same except OCP switched to calcite, as was in previous pH

sensitivity analyses. Although no longer the dominant mineral, struvite formation still increased at 35°C from pH 7.5 to 8.5 by approximately 9.5% of the total concentration. Vivianite formation remained stable from pH 7.5 to 8.5, and, therefore, decreased in terms of percent of the total concentration to account for the increase in struvite. Like the previous runs, Visual MINTEQ predicts pH at a constant temperature of 35°C to influence precipitate formation in terms of the concentration of struvite formation and the formation of compounds as a means of phosphorus removal. At a pH below 7.9, vivianite, OCP, and some struvite were predicted to precipitate phosphorus from solution, as compared to vivianite and struvite alone at higher pH values.

According to Visual MINTEQ at a constant pH of 8.4 and a temperature sensitivity analysis conducted across 20°C, 30°C, and 40°C under aerated operation, the dominant mineral formed remained vivianite, followed by calcite, pyrite, struvite, diaspore and barite. The concentration of struvite formation decreased slightly as temperature increased, which aligns with the literature, and the concentration of calcite slightly increased (Aage et al., 1997; Burns and Finlayson, 1982; Bhuiyan et al., 2007). Otherwise, there was little to no differences in precipitate formation across the temperature sensitivity analysis conducted across 20 - 40°C. Therefore, it could be concluded that at a pH of 8.4, the influence of temperature is minimal on precipitation of scaling compounds in anaerobic digestate aerated at a DO setpoint of 0.2 mg/L.

5.4.3.1 Physical Scale Analysis of Anaerobic Digestate Aerated on a DO Setpoint of 0.2 mg/L

Model results for anaerobic digestate aerated at a DO setpoint of 0.2 mg/L were validated with XRD, EDS/SEM, and Raman spectroscopic analysis on the scale sample collected from the pilot aerated at a similar DO setpoint (0.3 mg/L) prior to chemical injection tests. XRD analysis identified peaks similar to that of struvite, with more intense XRD peaks when compared to the final dewatering centrifuge sample, indicating a more crystalline sample (Figure 36).

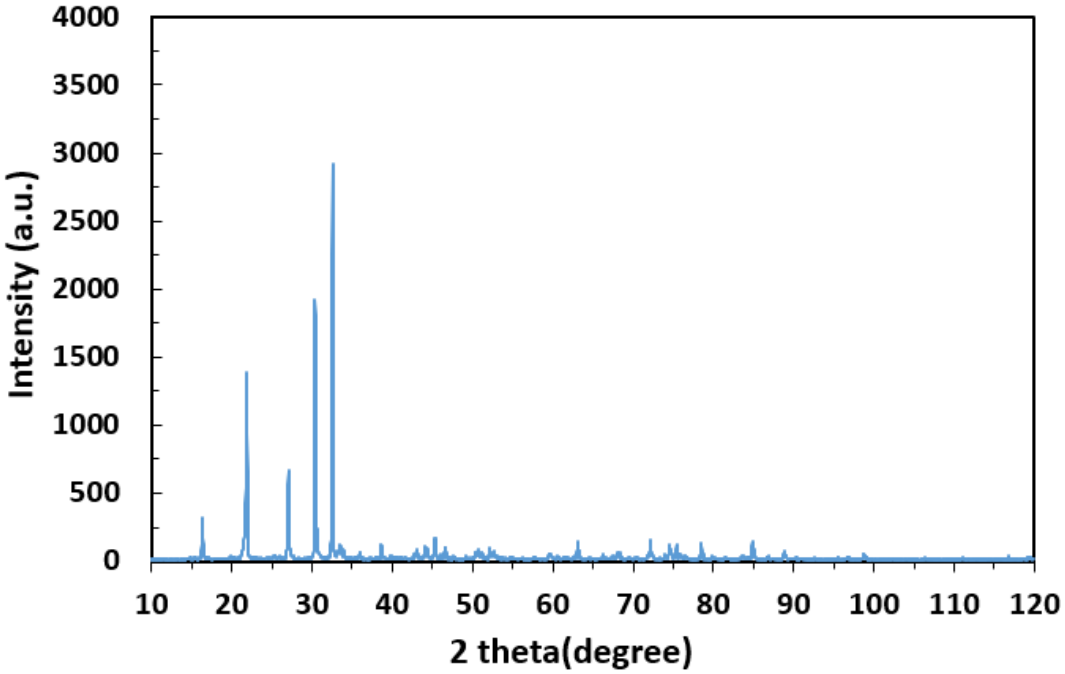

Figure 36: XRD peaks measured for the sample collected from pilot grit aerated at a DO setpoint of 0.3 mg/L.

The analysis most closely resembled struvite, with slight variability in peak position and intensity. Struvite most notably has peak XRD peak locations at 16, 21, 27, 31, and 33 degrees, which all line up with the XRD pattern for this sample (The RRUFF™ Project). The most notable peak for vivianite appears at 13 degrees, which was unable to be determined in this sample. The peaks that correspond with calcite were also not present in this XRD analysis. The most intense peak for pyrite appears at 33 degrees and could be contributing to the peak around the same location in the XRD analysis for aerated anaerobic digestate.

EDS/SEM again indicated the presence of metal phosphates, with a stronger potential presence of carbonates, which matched the higher percentages for calcite predicted by the Visual MINTEQ model. The images provided by the SEM analysis for this pilot grit sample also appeared more crystalline and orthorhombic in structure, which is classic to struvite minerals (Le Corre et al., 2009).

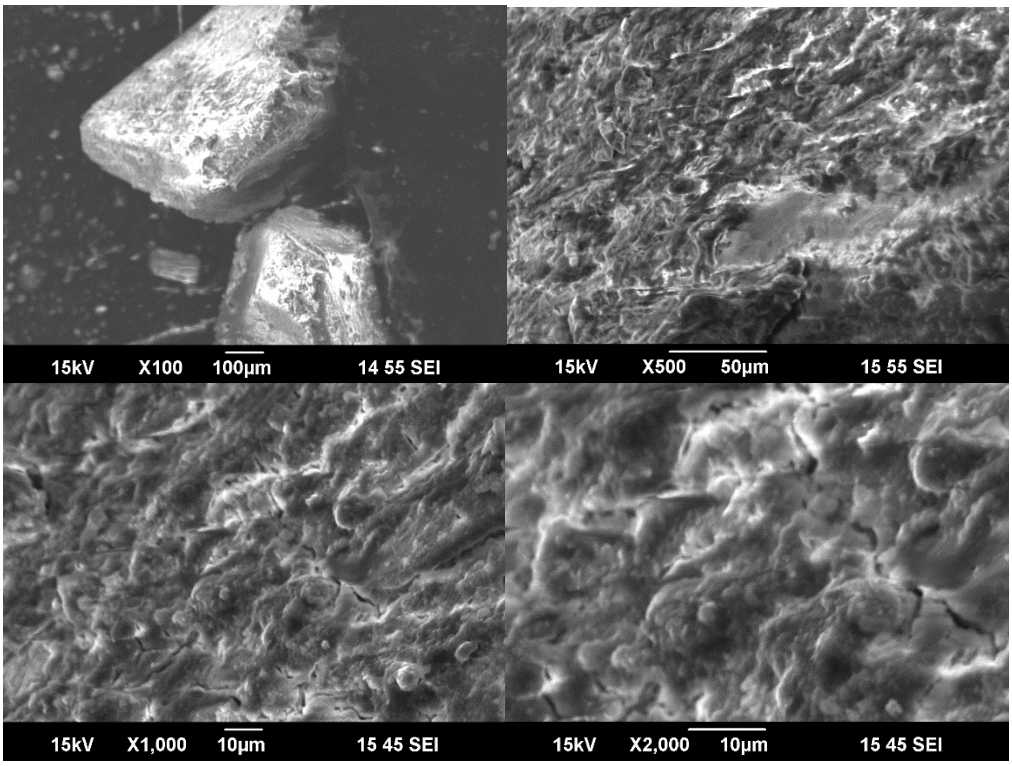

Figure 37: SEM images for the aerated anaerobic digestate sample.

This could be due to the controlled pilot setting exposing the mineral formed to less impurities than in the plant-wide mineral formed on the final dewatering centrifuges. The prominent atomic percentages found with EDS analysis was that of P, Fe, Ca, Mg, and S (Table 12). These elements correspond with the dominant minerals predicted of vivianite, OCP, calcite, struvite, and pyrite.

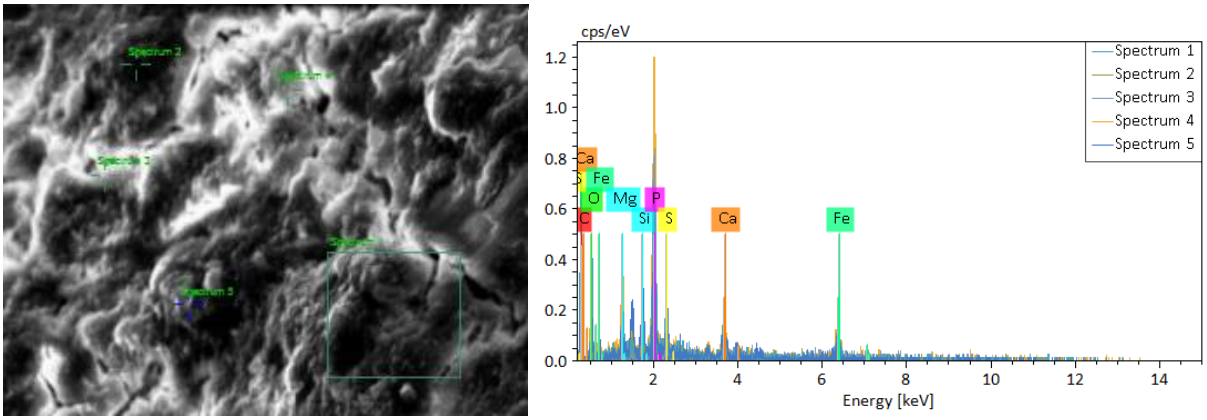

Figure 38: EDS chemical composition for the aerated anaerobic digestate sample.

Table 12: The most prominent atomic percentages picked identified by EDS for the aerated pilot grit scale collected.

Spectrum	C	O	Mg	Si	P	S	Ca	Fe
1	62.52	16.58	3.51	0.76	11.53	2.61	2.28	0.20
2	61.94	12.43	1.87	0.60	11.62	6.03	4.61	0.91
3	28.87	3.30	5.80	3.79	47.13	1.41	1.80	7.90
4	48.96	14.10	3.55	0.77	19.20	2.80	3.08	7.54
5	52.73	16.87	1.63	3.73	6.09	1.68	7.79	9.50
Mean	51.00	12.65	3.27	1.93	19.11	2.91	3.91	5.21

Lastly, this specimen strongly emitted under laser irradiation during Raman spectroscopy analysis, however, again this dwarfed any possible Raman peaks from phases, functional groups, or polyatomic species. Overall, the physical scale analysis predicted struvite as a dominant species and was significantly more crystalline compared to the final dewatering centrifuge scale.

5.4.3.2 $Mg(OH)_2$ Titration to Anaerobic Digestate Aerated on a DO Setpoint of 0.2 mg/L

Utilizing the same inputs from run 3, a titration experiment was set up to model the effects of $Mg(OH)_2$ addition on mineral formation in the pilot. The titration steps were followed, and the concentration of each mineral formed was solved for. Combined with the model predictions from the run for unaerated anaerobic digestate at a temperature of 35°C and a pH of 7.5, and the aerated digestate at a DO setpoint of 0.2 mg/L at a temperature of 35°C and a pH of 8.4, the predicted minerals formed at the Ca^{2+}+Mg^{2+}:P ratios tested of 0.25:1, 0.5:1 and 1:1 in the pilot in campaign 2, and the increased ratios of 1.3:1 and 1.6:1 from campaign 5, along with the pH predicted in the model and measured in each test are shown in Figure 39 below.

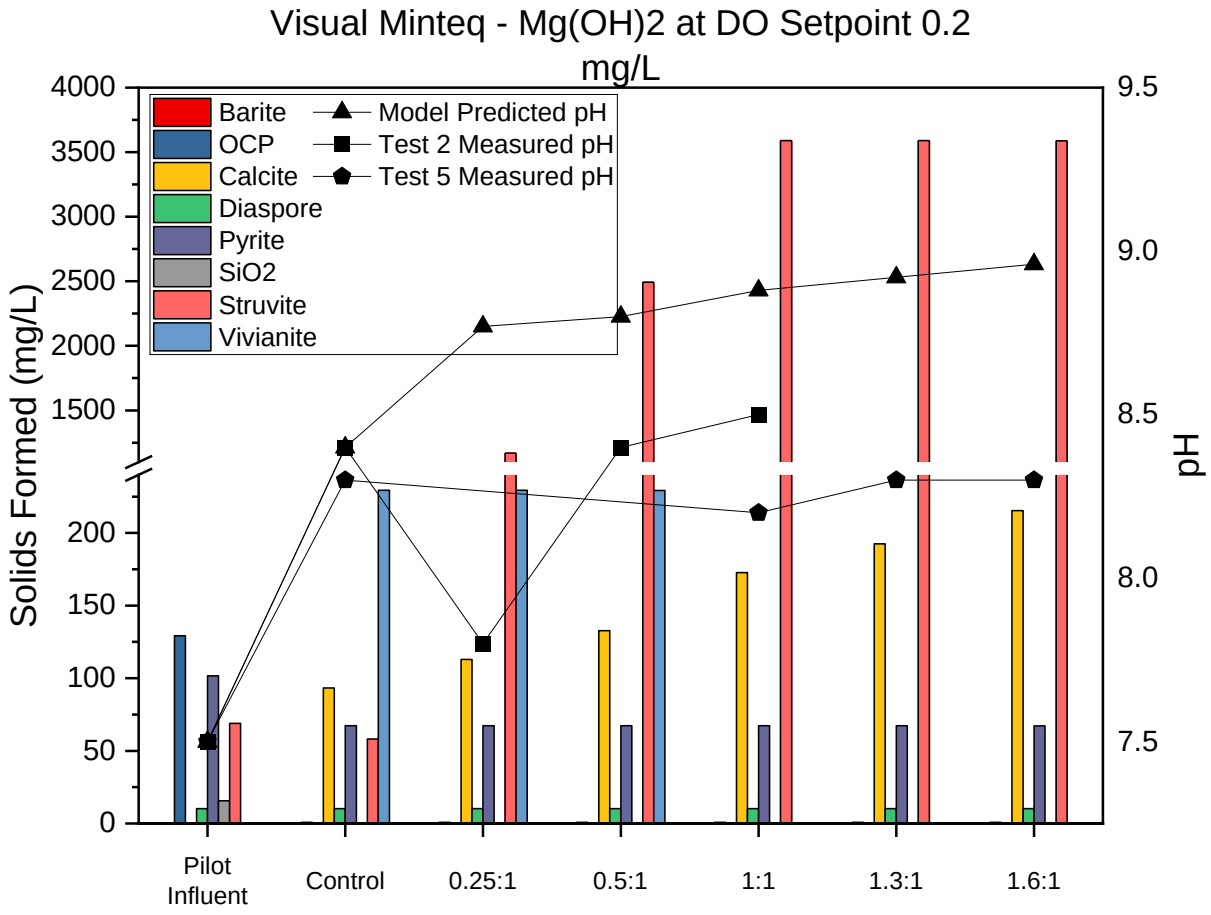

Figure 39: Mineral formation and pH predicted by Visual MINTEQ in the anaerobic digestate (pilot influent), aerated digestate at a DO setpoint of 0.2 mg/L (control), and aerated digestate at a DO setpoint of 0.2 mg/L with Mg(OH)2 addition to the Ca^{2+}+Mg^{2+}:P ratios tested of 0.25:1, 0.5:1, 1:1, 1.3:1, and 1.6:1.

The minerals predicted to form and the concentrations for the pilot influent and control were discussed in Sections 5.4.1 and 5.4.3. As $Mg(OH)_2$ was introduced at various Ca^{2+}+Mg^{2+}:P, the minerals formed stayed the same as the control in the 0.25:1 and 0.5:1, except at the higher ratios tested of 1:1 and higher, vivianite was no longer predicted to form as it was depleted by struvite formation. Struvite remained the dominant mineral predicted to form, and increased as $Mg(OH)_2$ was added until a maximum was reached at 3589 mg/L in the 1:1 dosed tank. Past that dosage, no additional struvite was predicted to form in the 1.3:1 and 1.6:1 dosed tanks. Calcite also increased as $Mg(OH)_2$ was added, up to 215 mg/L in the 1.6:1 dosed tank. Visual MINTEQ overpredicted the pH calculated at each Ca^{2+}+Mg^{2+}:P ratio than what was measured in the pilot in both campaigns 2 and 5. Where the measured pH in campaign 2 in the control, 0.25:1, 0.5:1 and 1:1 dosed tanks averaged pH 8.4, 7.8 (malfunctioned pH probe), 8.4, and 8.5, respectively, the measured pH in campaign 5 in the control, 1:1, 1.3:1, and 1.6:1 was 8.3, 8.2, 8.3, and 8.3 respectively. In the experimental

replicate of the 1:1 dosed tank, the measured pH was different in campaign 2 than campaign 5, which implies the difficulty in the consistent repeatability of these tests, and therefore, difficulty in precisely modeling them. The calculated pH from the mass balance in Visual MINTEQ was 8.8 for both the 0.25:1 and the 0.5:1 dosed tanks, 8.9 for the 1:1 and 1.3:1 dosed tanks, and 9.0 in the 1.6:1 dosed tank. This predicted increase in pH as chemical was introduced indicates some error in the model's ability to correctly account for the alkalinity and buffering capacity in the pilot.

In each model output, OP-P in the effluent was also predicted by Visual MINTEQ to validate the model results back to the pilot test conducted. Table 13 below displays the predicted results compared to the measured results for OP-P removal in this model run, campaign 2, and campaign 5.

Table 13: Visual MINTEQ predicted OP-P removal compared to measured OP-P removal for campaign 2 and 5.

	Visual MINTEQ Predicted OP-P Removal (%)	**Measured OP-P Removal (%) (Campaign 2, Campaign 5)**
Control	54%	38%, 61%
0.25:1	70%	70%
0.5:1	88%	83%
1:1	100%	89%, 93%
1.3:1	100%	97%
1.6:1	100%	96%

Overall, the model was able to closely predict OP-P removal measured in pilot campaigns 2 and 5. For campaign 2, the model overpredicted OP-P removal in the control, exactly predicted the 70% OP-P removal measured in the 0.25:1 dosed tank, and slightly over predicted OP-P removal in the 0.5:1 and 1:1 dosed tanks. In campaign 5, the OP-P removal measured in the control was more success than previous tests, as hypothesized due to the most recent clean out. Therefore, the model underpredicted OP-P removal in the control, but very closely predicted the nearly 100% OP-P removal measured in the 1:1, 1.3:1, and 1.6:1 dosed tanks. At the 1:1 dose and higher the model predicted struvite to be at a maximum formation point, therefore aligning with the 100% OP-P removal predicted in these tanks. The Visual MINTEQ model has a tendency to overpredict OP-P removal than what can truly be achieved on an experimental level, but can be mostly accurate when modeling aerated digestate supplemented with $Mg(OH)_2$ by predicting the formation of struvite.

5.4.3.2.1 Physical Scale Analysis of Anaerobic Digestate Aerated on a DO Setpoint of 0.2 mg/L Supplemented with $Mg(OH)_2$

The model results for anaerobic digestate aerated at a DO setpoint of 0.2 mg/L and supplemented with $Mg(OH)_2$ at were validated with XRD, EDS/SEM, and Raman spectroscopic analysis on the scale sample collected from the pilot aerated at a DO setpoint of 0.2 mg/L and dosed to a Ca^{2+}+Mg^{2+}:P ratio of 1:1 collected from campaign 5. XRD analysis shown in Figure 40 below identified peaks highly suggestive to that of struvite.

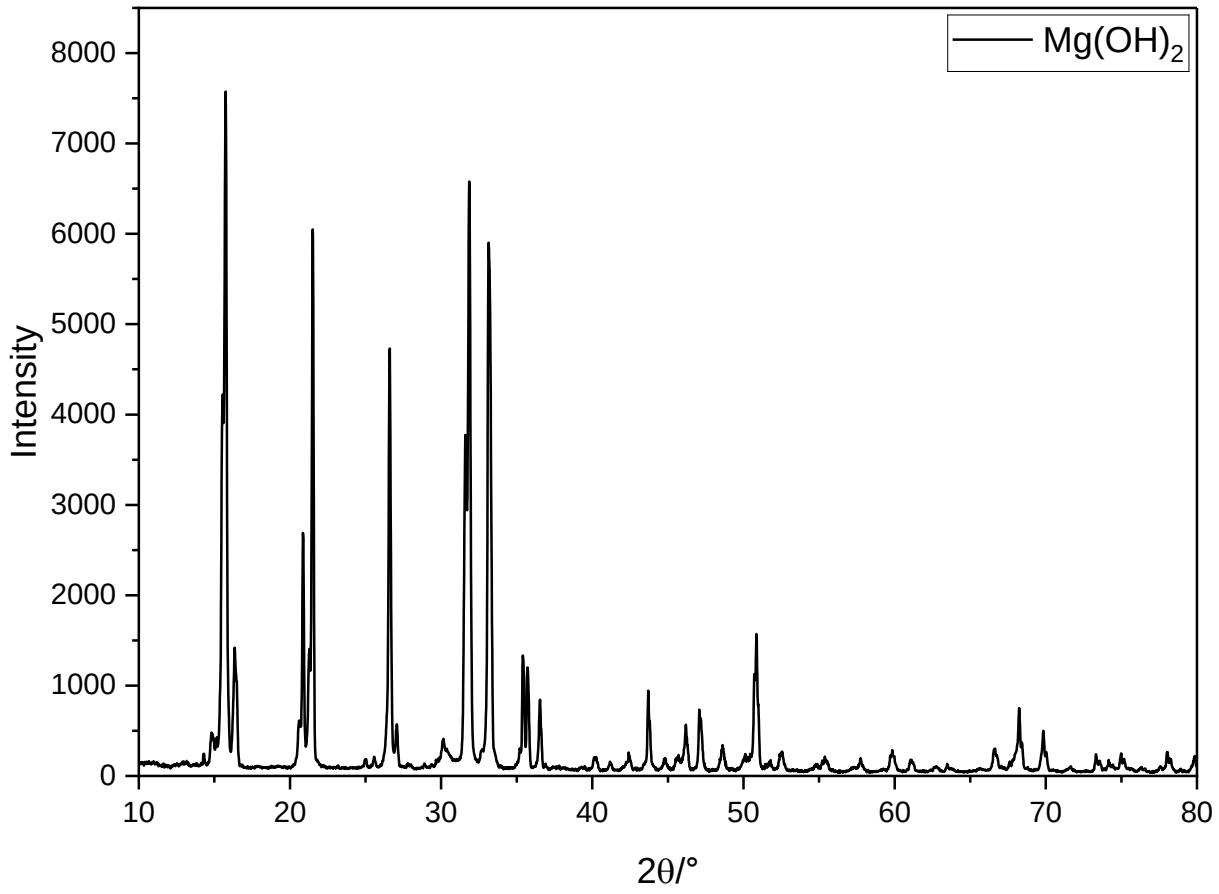

Figure 40: XRD peaks measured for the sample collected from pilot grit aerated at a DO setpoint of 0.2 mg/L and dosed with $Mg(OH)_2$ to a Ca^{2+}+Mg^{2+}:P ratio of 1:1.

The analysis most closely resembled struvite, with slight variability in peak position and intensity. Struvite most notably has peak XRD peak locations at 15, 16, 17, 21, 22, 27, 31, and 33 degrees, which all line up with the XRD pattern for this sample (The RRUFF™ Project). Calcite has XRD peak locations at 26, 29, 36, 44, 48, and 49 degrees, which were identified to some degree in this XRD analysis. The most intense peak for pyrite appears at 33 degrees and could be contributing to the peak around the same location in the XRD analysis for aerated

anaerobic digestate. Therefore, these XRD peaks strongly validate struvite in the model results and may suggest the presence of calcite and pyrite as well.

The data collected from EDS were consistent with mixed metal phosphates, dominated by Ca, Mg, and Fe. The atomic percentages in Table 14 show the large amounts of P and Mg to be contributing to struvite, as well as C, O, and Ca which may be indicative of calcite, and the elevated Fe may be indicative or pyrite or vivianite, however no S was detected here. The images provided by the SEM analysis for this pilot grit sample were unclear to any specific crystal structure.

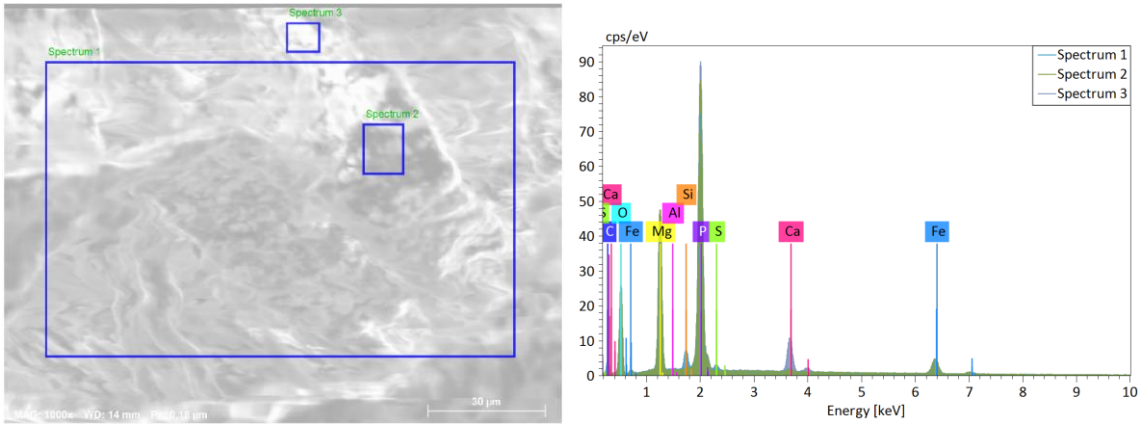

Figure 41: EDS chemical composition for the scale sample collected at a DO setpoint of 0.2 mg/L and dosed with $Mg(OH)_2$ to a Ca^{2+}+Mg^{2+}:P ratio of 1:1.

Table 14: The most prominent atomic percentages picked identified by EDS for the scale sample collected at a DO setpoint of 0.2 mg/L and dosed with $Mg(OH)_2$ to a Ca^{2+}+Mg^{2+}:P ratio of 1:1.

Spectrum	C	O	Mg	P	Ca	Fe
1	17.14	29.12	7.22	25.92	2.56	18.05
2	3.88	30.22	8.23	33.92	2.17	21.57
3	13.13	25.93	6.04	25.92	14.25	14.73
Mean	11.38	28.42	7.16	28.59	6.33	18.12

Lastly, Raman spectroscopy analysis was conducted to determine peaks from phases, functional groups, or polyatomic species. The most intense peak shown in Figure 43 below occurred as ca. 950 cm^{-1}, which is consistent with phosphate polyatomic anions. The Raman figure most closely matches that of struvite by the similar peaks in the ca. 200 and 570 cm^{-1} areas (The RUFF™ Project).

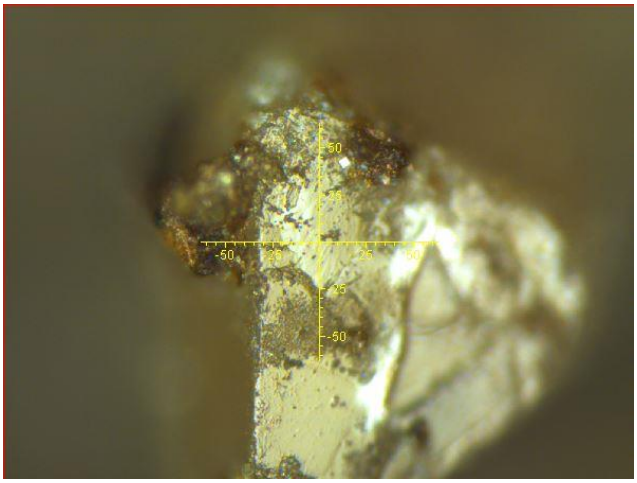

Figure 42: Raman microscope image for the scale sample collected at a DO setpoint of 0.2 mg/L and dosed with $Mg(OH)_2$ to a Ca^{2+}+Mg^{2+}:P ratio of 1:1.

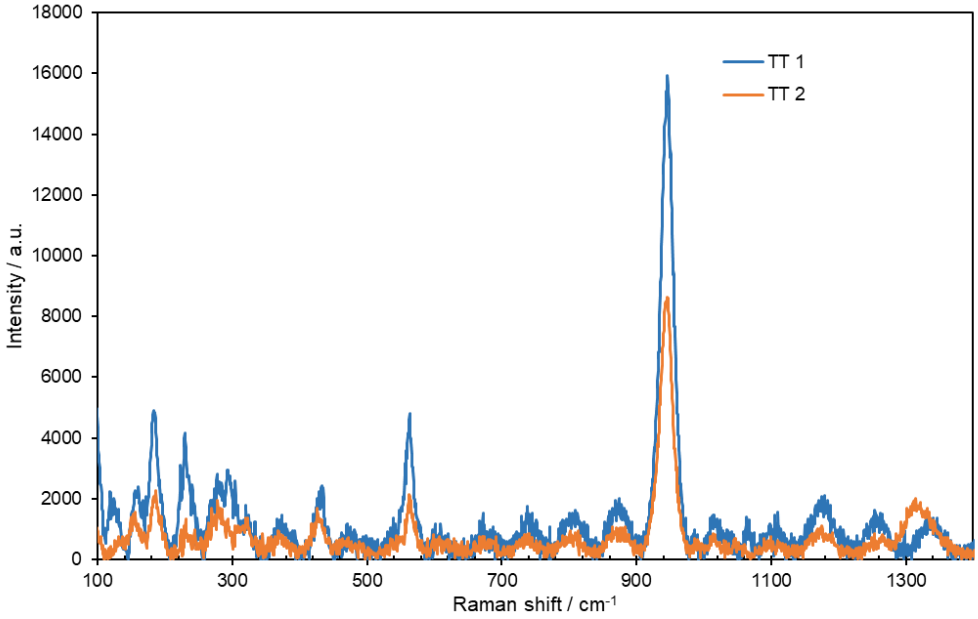

Figure 43: Raman spectra for the scale sample collected at a DO setpoint of 0.2 mg/L and dosed with $Mg(OH)_2$ to a Ca^{2+}+Mg^{2+}:P ratio of 1:1.

Overall, the physical scale analysis suggests struvite as the dominant species and validates struvite formation predicted by the Visual MINTEQ model. The EDS atomic percentages verified carbon, magnesium, phosphorus, calcium, and iron as the dominate elements present in this sample. The XRD peak locations also strongly suggests struvite and could be indicative of the presence of calcite and pyrite like in the model predictions.

5.4.3.3 $Ca(OH)_2$ Titration to Anaerobic Digestate Aerated on a DO Setpoint of 0.2 mg/L

Utilizing the same inputs from run 3, a titration experiment was set up to model the effects of $Ca(OH)_2$ addition on mineral formation in the pilot. The titration steps were followed, and the concentration of each mineral formed was solved for. Combined with the model predictions from the run for unaerated anaerobic digestate at a temperature of 35°C and a pH of 7.5, and the aerated digestate at a DO setpoint of 0.2 mg/L at a temperature of 35°C and a pH of 8.4, the predicted minerals formed at the Ca^{2+}+Mg^{2+}:P ratios tested of 0.25:1, 0.5:1 and 1:1 in the pilot, along with the pH predicted in the model and measured in campaign 4 are shown in Figure 44 below.

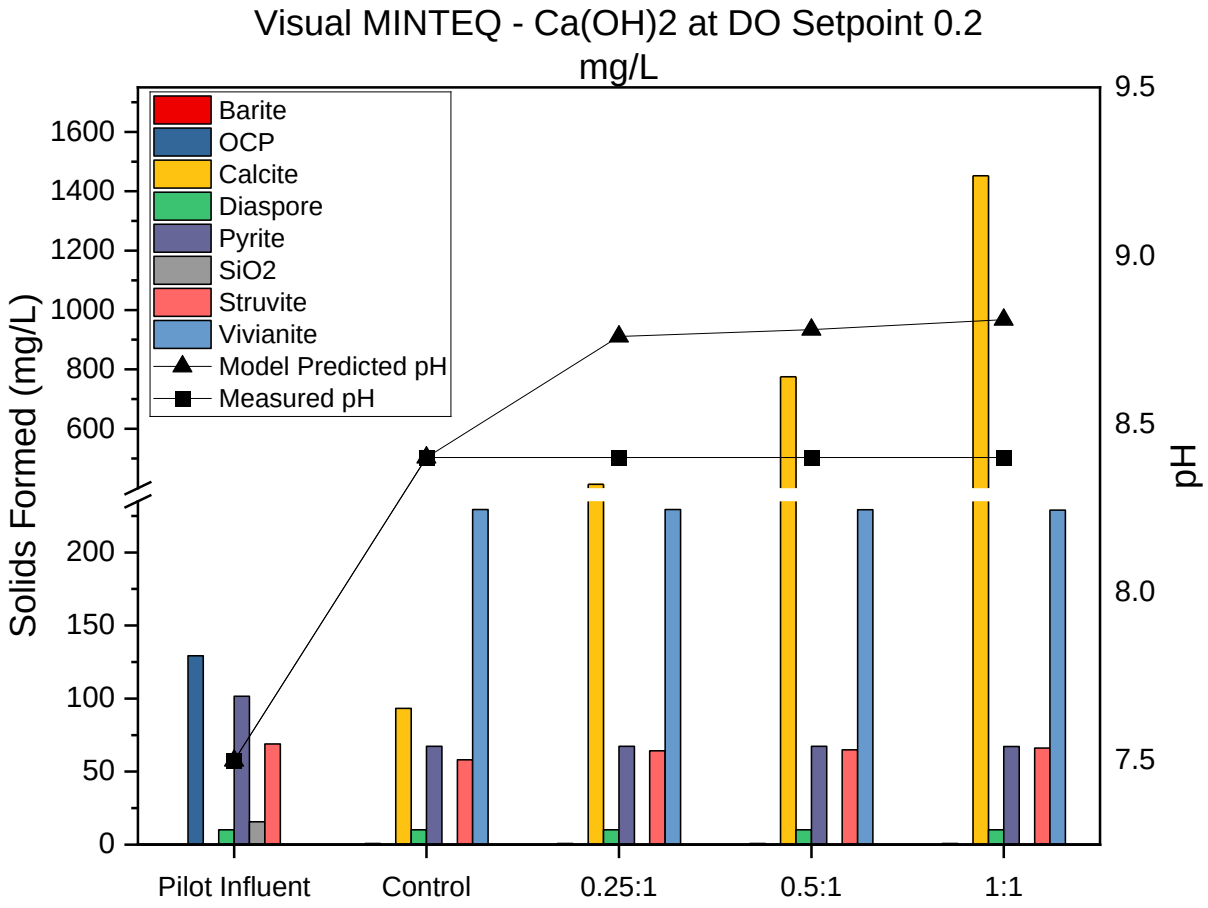

Figure 44: Mineral formation and pH predicted by Visual MINTEQ in the anaerobic digestate (pilot influent), aerated digestate at a DO setpoint of 0.2 mg/L (control), and aerated digestate at a DO setpoint of 0.2 mg/L with $Ca(OH)_2$ addition to the Ca^{2+}+Mg^{2+}:P ratios tested of 0.25:1, 0.5:1, 1:1.

The minerals predicted to form and the concentrations for the pilot influent and control were discussed in Sections 5.4.1 and 5.4.3. As $Ca(OH)_2$ was introduced at various Ca^{2+}+Mg^{2+}:P, the minerals formed stayed the same as the control in all of the tested ratios of 0.25:1 and 0.5:1 and 1:1. Where vivianite was the dominant mineral predicted to form in the control, the supplemented calcium as $Ca(OH)_2$ immediately caused an increase in calcite as the new dominant mineral in the chemically dosed tanks. Calcite continued to increase as the Ca^{2+}+Mg^{2+}:P ratio increased up to 1452 mg/L in the 1:1 dosed tank. Struvite also minimally increased as $Ca(OH)_2$ was added. Otherwise, there were no other changes to the minerals formed or concentrations due to $Ca(OH)_2$ addition predicted. Similar to the previous $Ca(OH)_2$ addition run at 5 LPM, this tendency for Visual MINTEQ to favor calcite to form rather than any calcium phosphate is a critical result as it predicts no change in OP-P removal past the control. Visual MINTEQ again overpredicted pH calculated at each Ca^{2+}+Mg^{2+}:P ratio than what was measured in the pilot. Where the measured pH for the control, 0.25:1, 0.5:1, and the 1:1 dosed tanks all averaged pH 8.4, the calculated pH from the mass balance in Visual MINTEQ was 8.8 for the 0.25:1, 0.5:1, and the 1:1 dosed tanks.

In each model output, OP-P in the effluent was also predicted by Visual MINTEQ to validate the model results back to the pilot test conducted. Table 15 below displays the predicted results compared to the measured results for OP-P removal in this model run and campaign 4.

Table 15: Visual MINTEQ predicted OP-P removal compared to measured OP-P removal for campaign 4.

	Visual MINTEQ Predicted OP-P Removal (%)	**Measured OP-P Removal (%)**
Control	54%	55%
0.25:1	54%	66%
0.5:1	54%	76%
1:1	54%	83%

In this run, the model was only able to closely predict OP-P removal measured in the fourth pilot test in the control tank. No further OP-P removal past 54% was predicted in the model due to calcite formation dominating in all the $Ca(OH)_2$ dosed trials. All other calcium phosphate minerals within the model at this pH were undersaturated with respect to calcite, except for hydroxyapatite again. Therefore, this further proves Visual MINTEQ has limitations when predicting phosphorus removal via calcium phosphates and will incorrectly favor calcite formation in aerated digestate supplemented with $Ca(OH)_2$.

5.4.3.3.1 Physical Scale Analysis of Anaerobic Digestate Aerated on a DO Setpoint of 0.2 mg/L Supplemented with $Ca(OH)_2$

The model results for anaerobic digestate aerated at a DO setpoint of 0.2 mg/L and supplemented with $Ca(OH)_2$ at were validated with XRD, EDS/SEM, and Raman spectroscopic analysis on the scale sample collected from the pilot aerated at a DO setpoint of 0.2 mg/L and dosed to a Ca^{2+}+Mg^{2+}:P ratio of 1:1 collected from campaign 4. XRD analysis shown in Figure 45 below identified peaks suggestive to that of struvite, calcite, and vivianite.

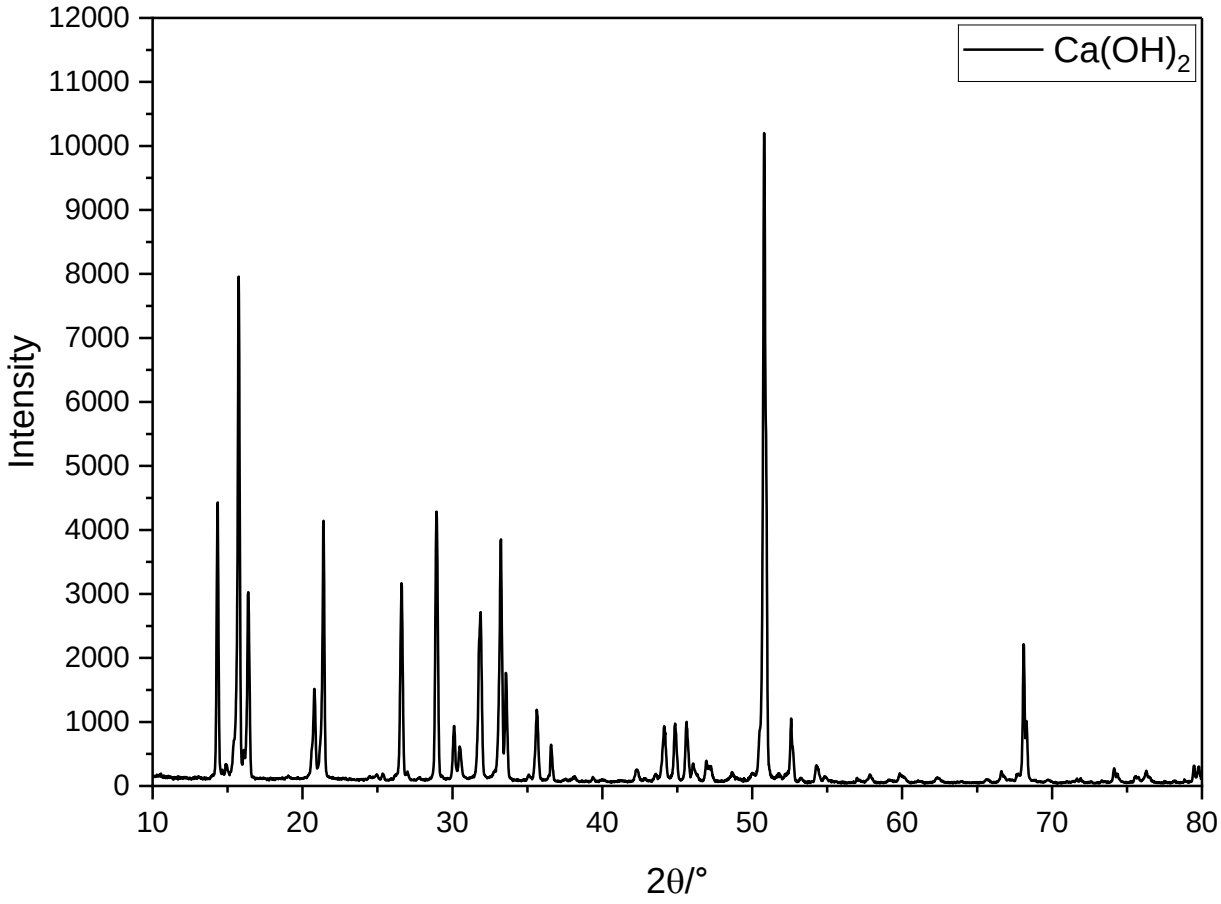

Figure 45: XRD peaks measured for the sample collected from pilot grit aerated at a DO setpoint of 0.2 mg/L and dosed with $Ca(OH)_2$ to a Ca^{2+}+Mg^{2+}:P ratio of 1:1.

The analysis most closely resembled struvite, with slight variability in peak position and intensity. Struvite most notably has peak XRD peak locations at 16, 17, 21, 22, 27, 31, and 33 degrees, which all line up with the XRD pattern for this sample (The RRUFF™ Project). Calcite has XRD peak locations at 26, 29, 36, 44, 48, and 49 degrees, which were identified to some degree in this XRD analysis. OCP also has characteristic XRD peak locations at about 27 and 54 degrees, which may be identified in this analysis. The most notable peak for

vivianite is located around 13 degrees, indicating that could be present in this analysis. The most intense peak for pyrite appears at 33 degrees and could be contributing to the peak around the same location in the XRD analysis for aerated anaerobic digestate. The most intense peak at about 51 degrees was unable to be identified. Therefore, these XRD peaks strongly validate struvite in the model results and may suggest the presence of calcite, vivianite and pyrite as well.

These data collected from EDS were very high in carbonaceous residues and show potential for metal phosphates and sulphates. The atomic percentages in Table 16 show the large amounts of C and some Ca and O that may be contributing to calcite, and P and N to be contributing to struvite, as well as some Fe and S may be indicative or pyrite or vivianite. The images provided by the SEM analysis for this pilot grit sample were unclear to any specific crystal structure.

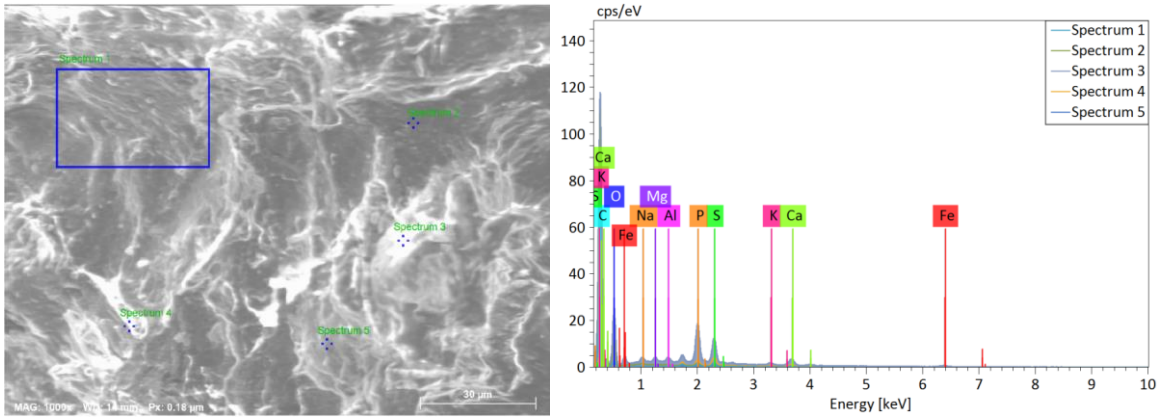

Figure 46: EDS chemical composition for the scale sample collected at a DO setpoint of 0.2 mg/L and dosed with $Ca(OH)_2$ to a Ca^{2+}+Mg^{2+}:P ratio of 1:1.

Table 16: The most prominent atomic percentages picked identified by EDS for the scale sample collected at a DO setpoint of 0.2 mg/L and dosed with $Ca(OH)_2$ to a Ca^{2+}+Mg^{2+}:P ratio of 1:1.

Spectrum	C	N	O	Na	Al	Si	P	S	K	Ca	Fe
1	89.00		7.70	0.78	0.09	0.44	0.67	0.99		0.34	
2	82.17	8.22	9.00		0.01	0.07	0.26	0.27			
3	81.10		12.41	0.45	0.11	0.27	2.42	1.55		0.89	0.80
4	77.81		5.54		0.55	2.65	4.16	6.37	0.66	2.28	
5	84.40		10.44		0.10	0.83	1.42	1.64	0.34	0.82	
Mean	82.90	8.22	9.02	0.61	0.17	0.85	1.78	2.16	0.50	1.08	0.80

Lastly, Raman spectroscopy analysis was conducted to determine peaks from phases, functional groups, or polyatomic species (Figure 48). The processing lab noted that this

specimen locally emitted, which may be due to the high carbonaceous residue present indicated by the purple line. This was confirmed by the high carbon content measured in the atomic concentrations in the EDS analysis. The red spectra had the most intense peak at ca. 950 cm^{-1}, which is consistent with phosphate polyatomic anions. The blue spectra minor peaks in in the ca. 200 and 570 cm^{-1} areas were consistent with struvite. Calcite has the most notable peak at around ca. 1090 cm-1, which very weakly appears in this analysis. The Raman analysis only confirms a presence of phosphate, which could indicate struvite or a calcium phosphate that would help better explain the measured phosphorus removal measured in this pilot test. However, a direct match was unable to be made.

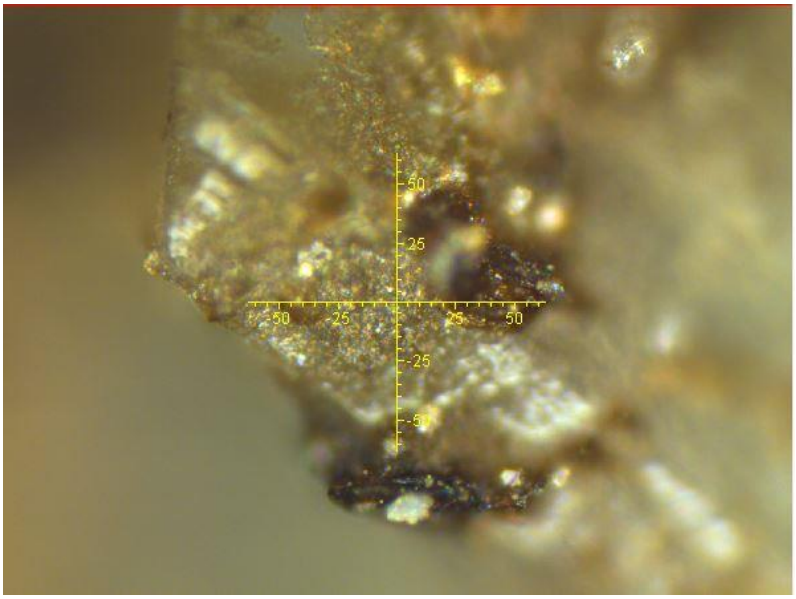

Figure 47: Raman microscope image for the scale sample collected at a DO setpoint of 0.2 mg/L and dosed with $Ca(OH)_2$ to a Ca^{2+}+Mg^{2+}:P ratio of 1:1.

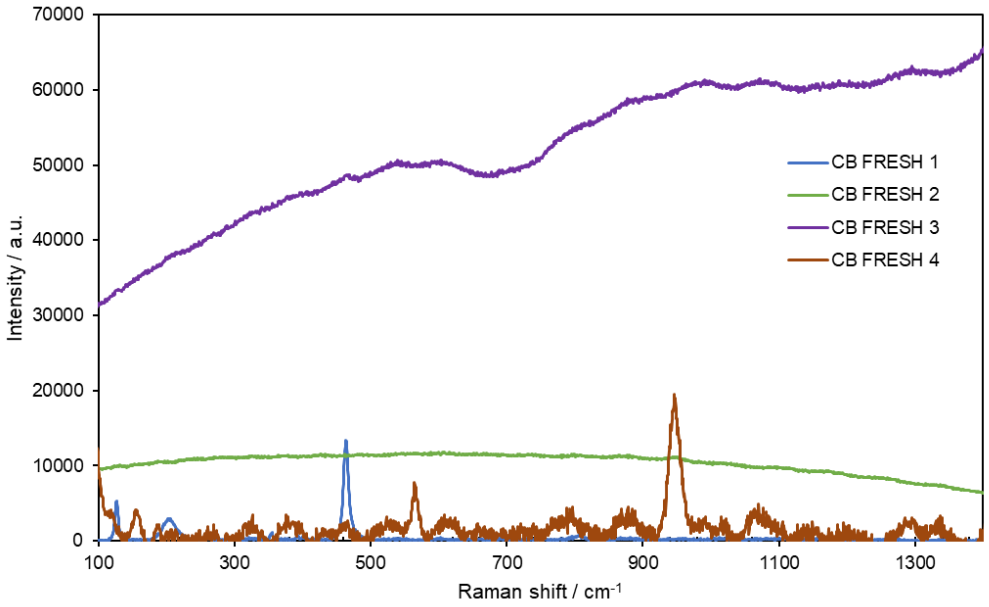

Figure 48: Raman spectra for the scale sample collected at a DO setpoint of 0.2 mg/L and dosed with $Ca(OH)_2$ to a Ca^{2+}+Mg^{2+}:P ratio of 1:1.

Overall, the physical scale analysis suggests struvite, calcite, vivianite, and pyrite minerals that may be present and validates struvite formation predicted by the Visual MINTEQ model. The EDS atomic percentages verified carbon, magnesium, phosphorus, calcium, and iron as the dominate elements present in this sample. The XRD peak locations also strongly suggests struvite and could be indicative of the presence of calcite and pyrite like in the model predictions.

5.4.4 Pilot Test with Aeration at pH Setpoints for Model Validation

Campaign 6 was completed on the pilot utilizing aeration with pH setpoints matching those tested in the Visual MINTEQ model pH sensitivity analysis to confirm the model results. The four available tanks in the pilot were aerated at pH setpoints of 7.5 to best try to match the pH in the anaerobic digesters, 8, 8.5, and 9. Model results from the pH sensitivity analysis from 7-9 for the pilot influent was then compared to determine the OP-P removal predicted to the measured OP-P removal results from the pilot, and mineral formation predicted at each pH by Visual MINTEQ. Figure 49 below displays the OP-P concentrations and OP-P removal efficiencies measured on the pilot in campaign 6 compared to the model predicted OP-P concentrations and OP-P removal predicted from the pilot influent inputs via changing the pH. The model results for OP-P and OP-P removal were calculated at the actual pH averages achieved on the pilot of 7.9, 8, 8.3, and 8.6, respectively, rather than the setpoints for the best comparison.

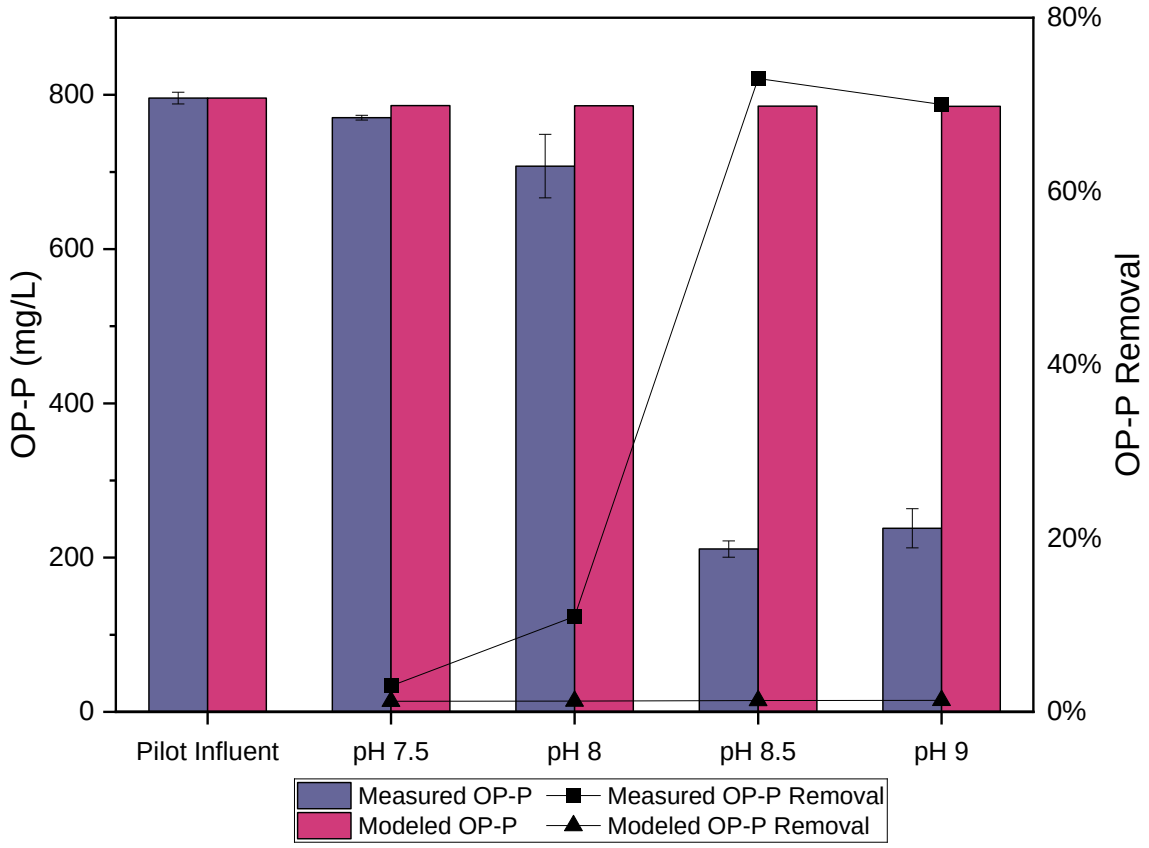

Figure 49: OP-P concentrations measured in campaign 6 in the pilot influent and tanks in aerated at pH setpoints of 7.5, 8, 8.5, and 9, as well as the OP-P removal measured across the pilot, compared to the OP-P concentrations and OP-P removal results predicted rom the model at the actual pH values measured of 7.9, 8, 8.3, and 8.6, respectively.

The measured OP-P removal across the pilot in campaign 6 was 3%, 11%, 73% and 70%, respectively, but the model only predicted 1% OP-P removal for each pH value tested. Therefore, the model was unable to correctly predict phosphorus removal due to pH manipulation alone, revealing more potential limitations with Visual MINTEQ. This may be due to the lack of kinetics integrated in the model, which makes modeling steady state phosphorus removal of a daily batch fed CSTR with an SRT of 3 days quite challenging. Another reason for this disagreement between modeled and measured results could be that the model lacks the ability to model minerals dissolving and reforming in a solution with a changing pH. According to ATP data, about 3302 lbs/day of Mg^{2+} came in the RWI of the plant during the years 2022-2024. About 8% of that Mg^{2+} was measured in the anaerobic digestate, which was about 280 lbs/day. Of this total magnesium content in the digestate, only about 3% of it was measurable as soluble Mg^{2+}, which is what was plugged into the model. This indicated that the soluble Mg^{2+} available to complex OP-P out of solution as struvite consisted of a very small fraction of the total magnesium entering the plant each day.

Magnesium in solution may have been bound in complexes with other minerals or organics that dissolved during the pH shift from aeration, releasing additional Mg^{2+} ions beyond the initially measured soluble amount. This increase in available magnesium could then precipitate as struvite, contributing to the OP-P removal observed in this pilot campaign but not captured in the model simulation.

Despite the model being unable to predict OP-P removal in this test, the soluble metals measured in each tank were still used to model precipitates formed at each average pH reached by the end of campaign 6. The same setup for Visual MINTEQ described in the methods section was followed, and measured inputs in Table 18 were used. Figure 50 below displays the solids predicted to form at each measured pH in campaign 6.

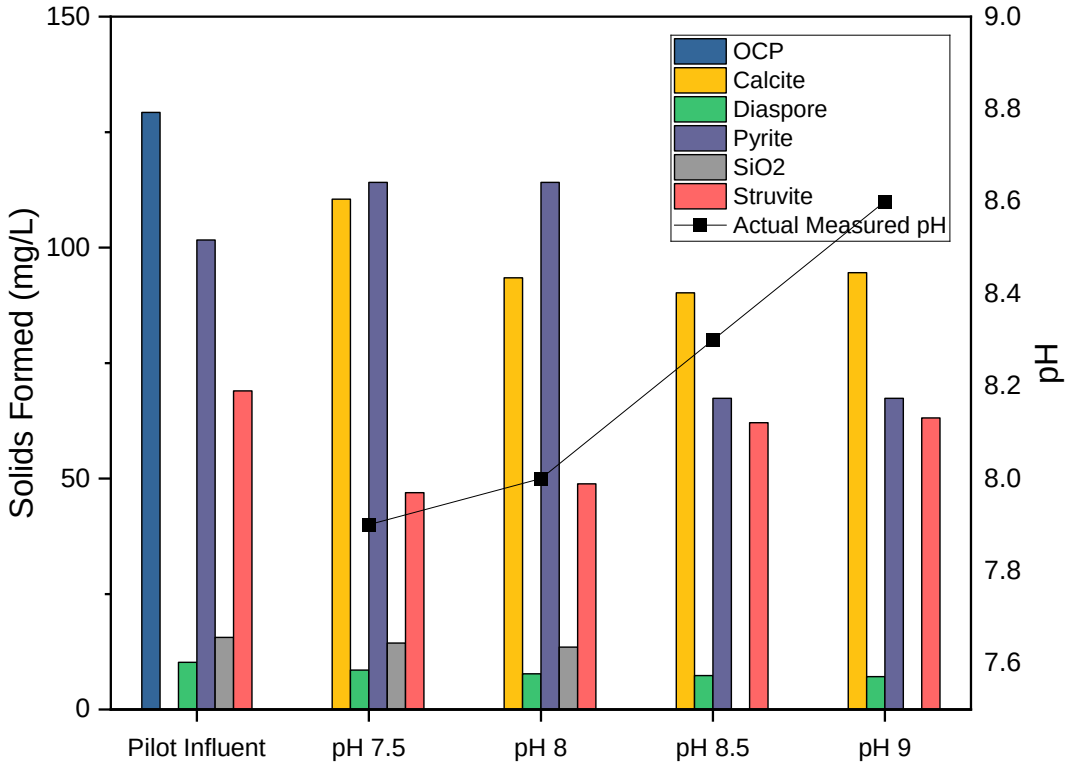

Figure 50: Mineral formation predicted by Visual MINTEQ in the anaerobic digestate (pilot influent), and aerated digestate at pH setpoints of 7.5, 8, 8.5, and 9, and the actual average pH measured in campaign 6 and inserted into the model of 7.9, 8, 8.3, and 8.6.

The minerals predicted to form and the concentrations for the pilot influent were discussed in Section 5.4.1. The tank aerated at a pH setpoint of 7.5 was best simulating the pilot influent but averaged a pH of 7.9 due to the immediate CO_2 stripping caused by the difference in headspace within anaerobic digesters compared to atmospheric CO_2 partial pressure in the pilot headspace. Therefore, the main difference between the two model predictions is the switch from OPC to calcite. The dominant mineral predicted to form in campaign 6 at pH 7.9 and 8 was pyrite. The dominant mineral then shifted to calcite at pH

values of 8.3 and 8.6. Struvite increased minimally from 47 to 63 mg/L as the pH increased from 7.9 to 8.6. Struvite was the only phosphorus mineral predicted to form in this pH range by Visual MINTEQ and at fairly insignificant amounts compared to the struvite concentrations predicted in the chemically injected trials. This lack of struvite predicted to form at these pH ranges corresponds with the low OP-P removal predictions in this run in Figure 49 above. Visual MINTEQ has been shown to work well with OP-P removal and precipitate formation with chemical injection experiments but may have limitations when modeling OP-P removal in steady state conditions via pH manipulation in a daily batch fed CSRT with a 3-day SRT with dynamic precipitation reactions occurring.

5.5 Conclusions

Chemical thermodynamic modeling can be used to evaluate the intricate parameters that influence the solubility of precipitates and predict the scaling potential of common minerals formed at WRRFs. A validated model could then be used to predict scaling potential and characterize minerals formed at other WRRFs to better treat these nuisance scaling minerals and determine their potential for harvest/sequestration as a nutrient-rich product.

This study assessed the commercially available model Visual MINTEQ Version 4.0. Model inputs were collected from a pilot-scale experiment at HRSD's Atlantic Treatment Plant that examined the impact of aeration and mixing on thermally hydrolyzed, anaerobically digested solids regarding scaling tendencies. The solids formed during these evaluations were characterized by XRD, SEM/EDS, and Raman Spectroscopy analysis to validate the predictions of the two models. The study results determined:

- At a temperature of 35°C, pH heavily determined the degree of phosphorus removal via struvite formation alone or if additional phosphorus was removed in the form of OCP.
- At a pH below 7.9, OCP, struvite, and vivianite were predicted to precipitate phosphorus from solution, as compared to struvite and vivianite alone at higher pH values.
- At a constant pH of 7.5 for unaerated digestate, 8.3 for aerated digestate at 5 LPM, and a pH of 8.4 for aerated digestate at a DO setpoint of 0.2 mg/L, temperature minimally affected the formation of pyrite, struvite, and diaspore.
- The physical scale analysis of unaerated anaerobic digestate predicted struvite as the dominant species and validated struvite formation predicted by the Visual MINTEQ model. The EDS atomic percentages verified carbon, magnesium, silica, phosphorus, calcium, and iron as the dominate elements present in this sample. When coupled with the XRD peak locations this could be indicative of the presence of calcite, tricalcium phosphate, and pyrite as the model predicted, but was unconfirmed due to minor shifts in peak locations and intensities.

- Visual MINTEQ closely predicted OP-P removal for the $Mg(OH)_2$ dosed pilot tests via struvite formation, but failed to correctly predict OP-P removal with $Ca(OH)_2$ addition due to predicting calcite formation rather than a Ca-P that contributed to the OP-P removal measured in the pilot.
- The physical scale analysis of the aerated anaerobic digestate dosed with $Mg(OH)_2$ and $Ca(OH)_2$ both strongly validated struvite in the model results as indicted by the XRD peaks, with the suggestion of calcite and pyrite in the $Mg(OH)_2$ dosed sample, and calcite, vivianite and pyrite as well in the $Ca(OH)_2$ dosed sample.
- Non-kinetic modeling and lack of dynamic dissolution and reprecipitation reactions across pH increases may be limitations within Visual MINTEQ modeling OP-P overtime via aeration for pH manipulation in a daily batch fed CSRT with a 3-day SRT.

These testing efforts prove the goals of this project to be achievable, including gaining a deeper understanding of the effects of pH, temperature, and chemical addition on phosphorus precipitation chemistry, utilizing modeling software to predict the scaling tendency of struvite and other minerals for downstream equipment protection and treatment efficiency, and characterizing the precipitated solids through SEM/EDS, XRD, and Raman Spectroscopy. This research provides key insights into phosphorus mineral formation in biosolids, advancing sustainable and efficient phosphorus management in wastewater treatment.

6. Engineering Significance

Understanding which operational strategies improve phosphorus sequestration in biosolids is crucial as phosphorus resources are becoming increasingly depleted. WRRFs that handle solids, especially those employing EBPR, a THP, and anaerobic digestion, that do not harvest these enhanced phosphorus loads may be struggling with large phosphorus recycle loads around the plant that are being continuously treated, nuisance scaling within and post digestion, and are missing out on recovering this potentially valuable product. Phosphorus recovery from wastewater via precipitation into class A biosolids addresses these issues by improving treatment efficiency, mitigating scaling, and producing a marketable biosolid product.

Using plant data from 2022-2024, a total phosphorus (TP) mass balance was modeled for ATP in a previously calibrated full plant SUMO model (Figure 51) (Dynamita, 2022). Based on influent characteristics and the TP removal rates, the model predicted about 1688 lbs P/day to exit with the cake. Due to increased loading to the digesters from a THP and soluble phosphorus in dewatering filtrates/centrates, TP in the recycle lines have increased over time, leading to continuous treatment of about 325 lbs P/day in the GBT filtrate, 1907 lbs P/day in the pre-dewatering centrate, and 878 lbs P/day in the final dewater centrate. This heavy recycle load increases the phosphorus available around the plant to form scaling precipitates that lead to the phosphorus sinks within digesters and on dewatering equipment that can clog

and damage equipment, as shown in Figure 3. This increases maintenance and clean out costs and hinders treatment efficiency overall.

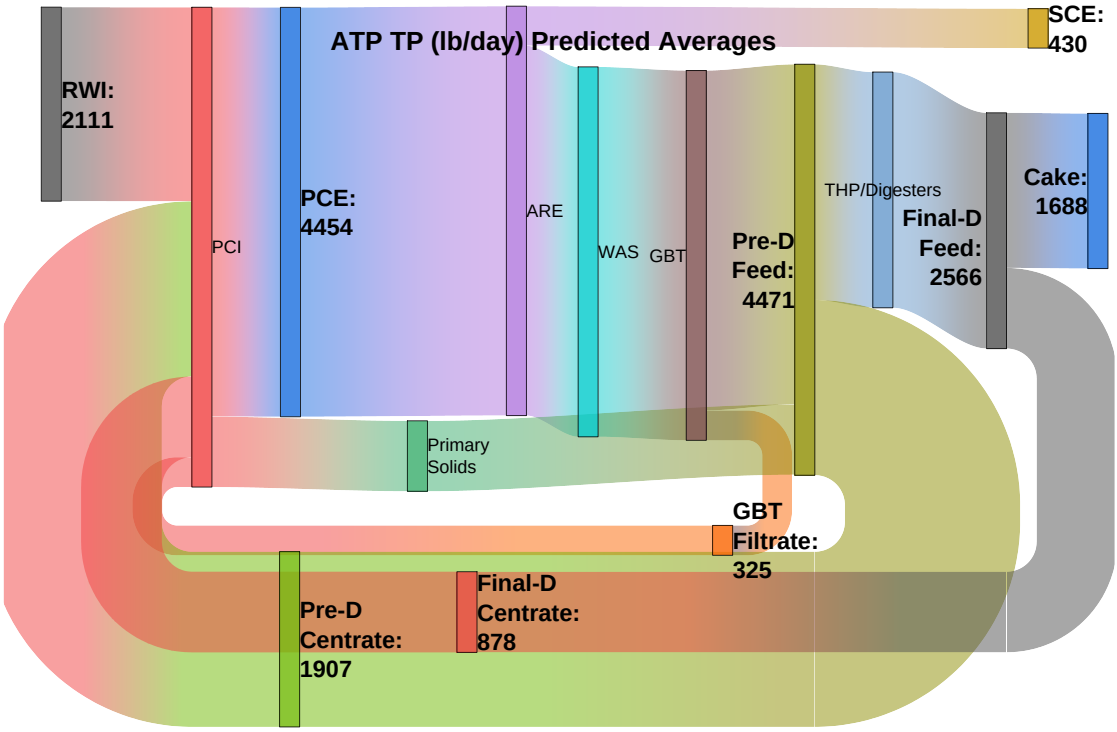

Figure 51: SUMO model predicted Total Phosphorus (TP) mass balance in the form of a Sankey diagram for the current operation of the Atlantic Treatment Plant.

As a means to solve this issue at ATP, multiple phosphorus removal strategies were tested at the pilot scale such as various aeration settings and chemical addition at different Ca^{2+}+Mg^{2+}:P ratios. Figure 52 below displays the decreases in OP-P measured from the pilot influent for each aeration setting and treatment strategy tested and discussed in this paper.

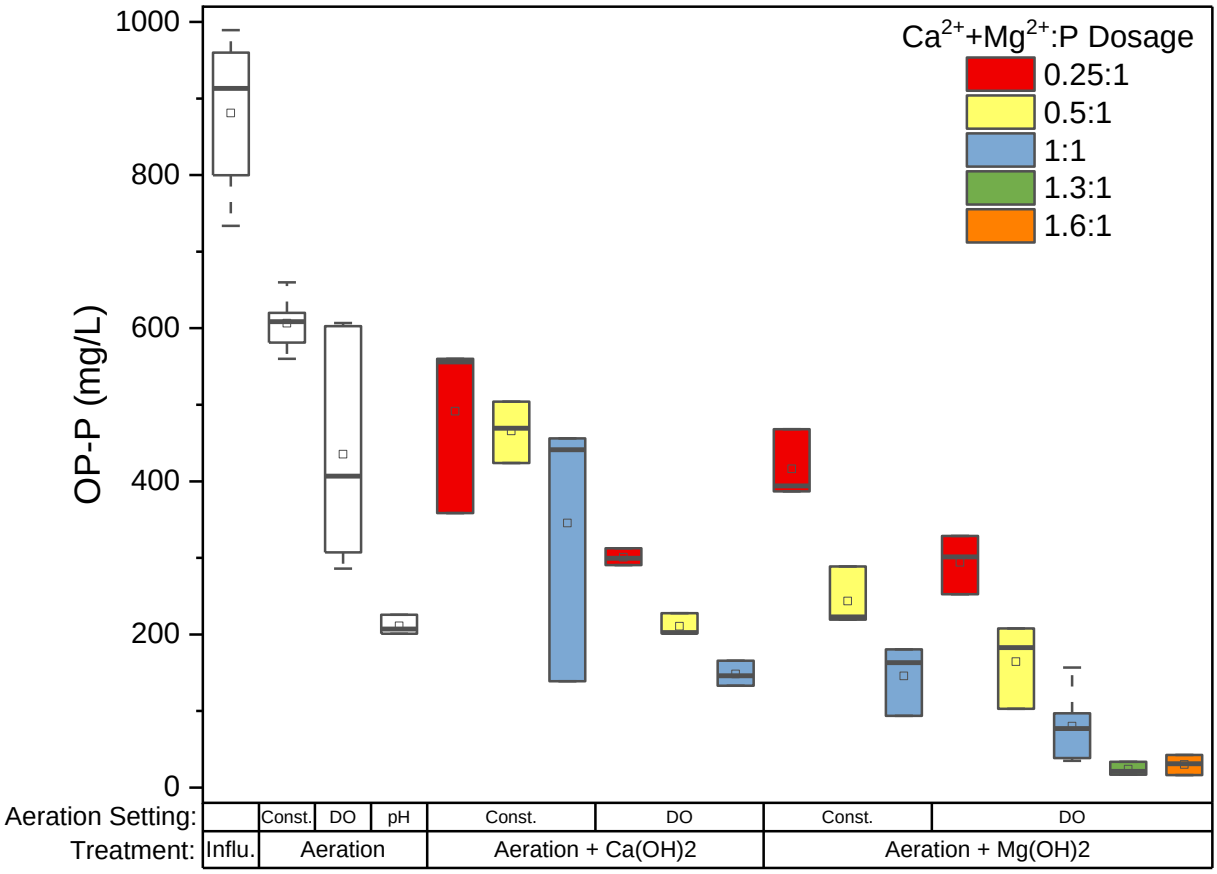

Figure 52: Box and Whisker plot of the OP-P in mg/L measured across the pilot for each treatment strategy tested. The aeration settings are constant aeration at 5 LPM, aeration on a DO setpoint of 0.2 mg/L, and aeration on a pH setpoint of 8.5.

Based on the desired OP-P removal for a WRRF's post treatment goals, this figure can be used as a guide to determine optimal aeration setting, chemical, and chemical dosage required. The benefit of phosphorus removal can then be weighed against the cost of aeration and chemical addition. The following cost-benefit analysis was completed on the 0.5 MGD DSST at ATP. The current annual cost was calculated based on the Virgina SCAT Regulations of a well-mixed tank of this size, calculated as an SCFM of 1337 (9VAC25-790-590). The projected annual cost of aerating the DSST was calculated based on the carbonaceous oxygen demand of the DSST representing full equilibrium with the atmosphere and biological COD removal, calculated as a SCFM of 9801 (Wilson et al., 2010). This aeration cost was simplified in this manner and does not distinguish between constant aeration or DO or pH setpoint based aeration. General pricing was used from Univar Solutions for $Ca(OH)_2$ and $Mg(OH)_2$ of $0.16 per pound at 35% solution strength for $Ca(OH)_2$ and $0.35 per pound delivered at 60% solution strength for $Mg(OH)_2$. These chemical costs were converted to cost per liter using the densities and active percentage of each chemical. The cost per liter was then

used to determine the annual cost of DSST operation if aerated and chemically supplemented. All calculations can be found in Appendix A Section 7.3. Table 17 below describes a summary of the cost benefit analysis for percentages of OP-P removal measured via aeration and aeration plus chemical addition as compared to the current cost of DSST operation.

Table 17: Cost-Benefit analysis for the current DSST operation versus OP-P removal treatment strategies tested in this pilot study.

Treatment	OP-P Removal (%)	Annual Cost (USD/year)
Mixed DSST (Current)	0%	$16,125
Aerated DSST	36-73%	$118,225
Aerated DSST + $Ca(OH)_2$ 0.25:1 Dose	66%	$133,920
Aerated DSST + $Ca(OH)_2$ 0.5:1 Dose	76%	$151,701
Aerated DSST + $Ca(OH)_2$ 1:1 Dose	83%	$187,262
Aerated DSST + $Mg(OH)_2$ 0.25:1 Dose	70%	$166,863
Aerated DSST + $Mg(OH)_2$ 0.5:1 Dose	83%	$220,892
Aerated DSST + $Mg(OH)_2$ 1:1 Dose	89%	$328,998

This cost-benefit analysis for OP-P removal in the DSST highlights a range of treatment options. The current operation of the mixed DSST offers no OP-P removal at an estimated low operation cost of about $16,125 per year. Switching to an aerated DSST without chemical addition provides moderate OP-P removal (36-73%) for about $118,225 annually. This range of OP-P removal was based on the control tanks in each pilot test and depends on the aeration setting, with the least amount of OP-P removal measured at constant aeration at 5 LPM, moderate OP-P removal measured with aeration on a DO setpoint of 0.2 mg/L, and the most OP-P removal measured at a pH setpoint of 8.5. Enhanced removal rates were achieved with chemical addition. Operation consisting of aeration with $Ca(OH)_2$ addition offers a cost-effective balance, with OP-P removal rates ranging from 66% at $133,920 per year, to 83% at $187,262 per year, as the Ca^{2+}+Mg^{2+}:P dose increased. In comparison, aeration and $Mg(OH)_2$ addition also improved OP-P removal, but costs were notably higher, reaching $328,998 annually for 89% OP-P removal at a 1:1 dose. Although $Mg(OH)_2$ achieved slightly higher OP-P removal efficiencies, its steep cost rise makes it less cost-effective than $Ca(OH)_2$ for achieving comparable OP-P removal results. Aeration with $Ca(OH)_2$ addition provided improvements in OP-P removal with a manageable rise in cost, specifically, $Ca(OH)_2$ at a 1:1 dosage offered a mid-range cost solution with strong OP-P removal.

Therefore, to determine an example of the benefits of this OP-P removal on the full plant scale, a DO setpoint of 0.2 mg/L and $Ca(OH)_2$ dosage at a Ca^{2+}+Mg^{2+}:P ratio of 1:1 was added to a calibrated plant SUMO model for ATP. The Figure 53 below displays how the phosphorus mass balance would change to reflect the updated steady state operation of the DSST with aeration and $Ca(OH)_2$ at a Ca^{2+}+Mg^{2+}:P ratio of 1:1. The significant change in the total phosphorus load due to an 83% OP-P removal across the DSST can be seen in the much

smaller TP recycle lines in the GBT filtrate an the final dewatering centrate. The TP in the cake increased to 1703 lbs P/day, and the TP in the recycle lines have decreased, leading to about 20% less TP continuously treated in the GBT filtrate, 11% less TP in the pre-dewatering centrate, and 67% less TP in the final dewater centrate. At a cost of $187,262/year, the TP mass balance at ATP could transform from Figure 51 to Figure 53.

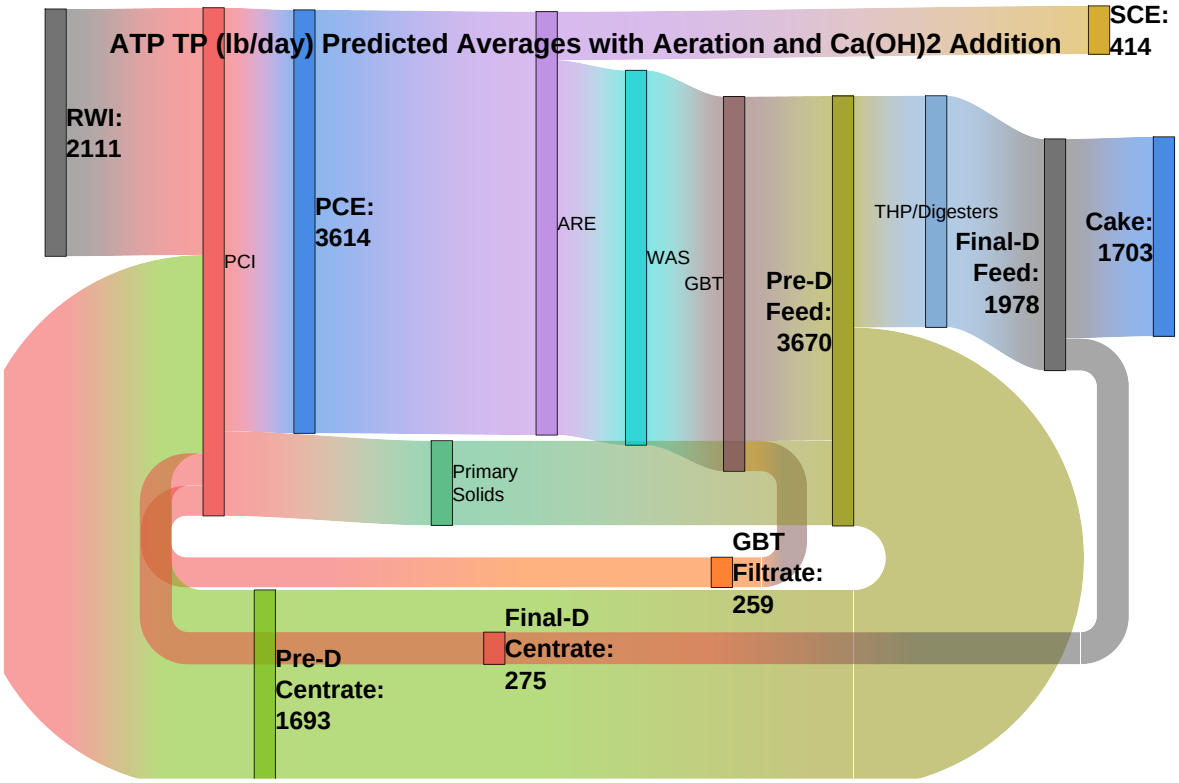

Figure 53: SUMO predicted Total Phosphorus (TP) mass balance in the form of a Sankey diagram for the Atlantic Treatment Plant with aeration and $Ca(OH)_2$ addition at a $Ca^{2+}+Mg^{2+}$:P ratio of 1:1 to the DSST.

The engineering significance of this research lies in its potential to transform phosphorus management at HRSD's Atlantic Treatment Plant and other WRRFs aiming to reduce phosphorus recycle loads and minimize nuisance scaling around the plant. Therefore, a pilot experimental setup utilized aeration for pH control and chemical addition of $Mg(OH)_2$ and $Ca(OH)_2$ to thermally hydrolyzed, anaerobic digestate on a 3-day SRT to optimize phosphorus removal, understand the effects on N and COD removal, and characterize the minerals formed. Figure 52 displays the many ways successful OP-P can be achieved. The pilot results demonstrated effective OP-P removal, with additional benefits such as about 10-20% nitrogen and 20% total COD reduction relative to anaerobic digestate at a 3-day SRT, establishing a practical balance between operational costs and treatment efficiency. This OP-P removal approach also offers downstream benefits in final dewatering by improving polymer demand and cake solids, as discussed by many studies (Higgins et al., 2014; Shimp et al., 2013). There are other nuanced benefits to increased phosphorus content in biosolids, such as enhancing the

marketability of a nutrient-rich soil blend for land application in states with agricultural regulations based on nitrogen limits, and reducing biosolids hauling costs to states that are phosphorus limited. Additionally, the mitigation of nuisance precipitates improves equipment longevity and maintenance costs, providing savings that vary across WRRFs. Based on the cost benefit analysis above, the optimal operation of the DSST can be selected to achieve the desired OP-P removal at the cheapest chemical addition and aeration cost. The integration of Visual MINTEQ modeling further strengthened this approach by enabling predictive insights into mineral scaling, facilitating informed decisions on chemical dosing and pH adjustments, and determining a mineral's potential for harvesting/sequestration as a nutrient-rich product. Furthermore, this research offers valuable insights for WRRFs seeking to reduce phosphorus loads in solids recycle lines and mitigate nuisance scaling in a more cost-effective way than many commercially available technologies. By advancing phosphorus recovery mechanisms in biosolids, this work supports efficient resource management and contributes to the broader objective of sustainable nutrient recovery, both of which are imperative in the future of solids handling.

7. References

Aage, H., Andersen, B., Blom, A., and Jensen, I. (1997). "The Solubility of Struvite". *Journal of Radioanalytical and Nuclear Chemistry.* 223, 213-215. https://doi.org/10.1007/bf02223387

Abbona, F. and Boistelle, R. (1985). "Nucleation of struvite MgNH4PO4.6H2O Single Crystals and Aggregates". *Crystal Research and Technology*, 20, 133–140. https://doi.org/10.1002/crat.2170200204

Abbona Lundager Madsen, H. E., and Boistelle, R. (1982). "Crystallization of Two Magnesium Phosphates, Struvite and Newberyite: Effect of pH and Concentration". *Journal of Crystal Growth.* 57, 6-14. https://doi.org/10.1016/0022-0248(82)90242-1

Abbona, F., Lundager Madsen, H. E., and Boistelle, R. (1986). "The Initial Phases of Calcium and Magnesium Phosphates Precipitated from Solutions of High to Medium Concentrations". *Journal of Crystal Growth.* 74, 581-590. https://doi.org/10.1016/0022-0248(86)90205-8

Aka, R. Jr. N., Hossain, M., Yuan, Y., Agyekum-Oduro, E., Zhan, Y., Zhu, J., Wu, S. (2023). "Nutrient Recovery Through Struvite Precipitation from Anaerobically Digested Poultry Wastewater in an Air-Lift Electrolytic Reactor: Process Modeling and Cost Analysis". *Chemical Engineering Journal.* Vol. 465, 142825. https://doi.org/10.1016/j.cej.2023.142825

Ali, M. D. I., Schneider, P. A., Hudson, N. (2003). "Nutrients Recovery from Piggery Effluents". *International Journal for Engineering Modelling.* 16, (1-2), 71-76. https://hrcak.srce.hr/316079

Alleman, J. E. (1985). "Elevated Nitrite Occurrence in Biological Wastewater treatment Systems". *Water and Science Technology*. 17, 2-3, 409-419. https://doi.org/10.2166/wst.1985.0147

Andrade, A. and Schuiling, R. D. (2001). "The Chemistry of Struvite Crystallization" *Mineralogical Journal of Ukraine.* 23, 37-46.

Anthonisen, A. C., Loehr, R. C., Prakasam, T. B. S., and Srinath, E. G. (1976). Inhibition of Nitrification by Ammonia and Nitrous Acid. *Journal - Water Pollution Control Federation.* 48, 835– 852. https://www.jstor.org/stable/25038971

Arnold, P. W. (1950). "The Nature of Precipitated Calcium Phosphate". *Trans Faraday Society.* 46, 1061-1073. https://doi.org/10.1039/TF9504601061

Atalay, A. and Whitehead, B. (2018). "Thermodynamic Principles of Dittmarite Precipitation". *Journal of Environmental Science and Engineering* B 7. 331-336. doi:10.17265/2162-5263/2018.09.002

Azam, H. M., Alam, S. T., Hasan, M., Yameogo, D. D. S., Kannan, A. D., Rahman, A., Kwon, M. J. (2019). "Phosphorus in the Environment: Characteristics with Distribution and Effects, Removal Mechanisms, Treatment Technologies, and Factors Affecting Recovery as Minerals in Natural and Engineered Systems". *Environmental Science and Pollution Research.* Vol. 26, pp 20183-20207. https://doi.org/10.1007/s11356-019-04732-y

Babic-Ivancic, V., Kontrec, J., Kralj, D., Brecevic, L. (2002). "Precipitation Diagrams of Struvite and Dissolution Kinetics of Different Struvite Morphologies". *Croatica Chemica Acta*. 75, 89-106.

Bauer, H., Johnson, T. D., Johnson, B. R., Oerke, D., Graziano, S. (2016). "Comparison of Sidestream Treatment Technologies: Post Aerobic Digestion and Anammox". *Water Science and Technology.* 73. 11. 2789-2803. https://doi.org/10.2166/wst.2016.079

Beall, S., Jenkins, D., Vidanage, S. (1998). "A Systematic Analytical Artifact that Significantly Influences Anaerobic Digestion Efficiency Measurement". *Water Environment Research*. 70, 5, 1019-1024. https://doi.org/10.2175/106143098X123345

Berner, R. (1967). "Thermodynamic Stability of Sedimentary Iron Sulfides". *American Journal of Science.* 265, 773-785.

Bhuiyan, M. I. H., Manvinic, D. S., and Beckie, R. D. (2007). "A Solubility and Thermodynamic Study of Struvite". *Environmental Technology.* 28, 9, 1015-1026. https://doi.org/10.1080/09593332808618857

Bhuiyan, M. I. H., Manvinic, D. S., and Koch, F.A. (2008). "Thermal Decomposition of Struvite and its Phase Transition". *Chemosphere.* 70, 1347-1356. https://doi.org/10.1016/j.chemosphere.2007.09.056

Biesterfeld, S., Farmer, G., Russell, P., Figueroa, L. (2003). "Effect of Alkalinity Type and Concentration on Nitrifying Biofilm Activity". *Water Environment Research.* 75, 3, 196-204. https://doi.org/10.2175/106143003X140971

Boistelle, R., Abbona, F., Lundager Madsen, H. E. et al. (1983). "On the Transformation of Struvite into Newberyite in Aqueous Systems". *Physics and Chemistry of Minerals.* 9, 216-222. https://doi.org/10.1007/BF00311958

Booker N.A., Priestley A.J., Fraser I.H. (1999). "Struvite Formation in Wastewater Treatment Plants: Opportunities for Nutrient Recovery". *Environmental Technology*, Vol. 20, pp. 777-782. https://doi.org/10.1080/09593332008616874

Bouropoulos, N. C. and Koutsoukos, P. G (2000). "Spontaneous precipitation of struvite from aqueous solutions". *Journal of Crystal Growth*, 213, 381–388. https://doi.org/10.1016/S0022-0248(00)00351-1

Brutsaert, W. and Jirka, G. H. (1984). *Gas Transfer at Water Surfaces.* Springer Science + Business Media.

Buchanan, J. R., Mote, C. R., Robinson, R. B. (1994). Thermodynamics of struvite formation. In: Transactions of the ASAE (USA) doi: 10.13031/2013.28121

Burns, R. R. and Finlayson, B. (1982). "Solubility Product of Magnesium Ammonium Phosphate Hexahydrate at Various Temperatures". *Journal of Urology.* 128, 2, 426-428. https://doi.org/10.1016/S0022-5347(17)52952-3

Celen, I., Buchanan, J. R., Burns R. T., Robinson, R. B., Raman, D. R. (2007). "Using a Chemical Equilibrium Model to Predict Amendments Required to Precipitate Phosphorus as Struvite in Liquid Swine Manure". *Water Research.* 41, 1689-1696. https://doi.org/10.1016/j.watres.2007.01.018

"Centrisys CNP – Magprex," Home Page. [Online]. Available: https://www.centrisys-cnp.com/magprex. [Accessed: 12-June-2024]

Cheng, P. T. (1985). "Octacalcium Phosphate Formation in Vitro: Implication for Bone Formation". *Calcified Tissue Int.* 37, 91-94. https://doi.org/10.1007/BF02557685

Chow, L. C. (2001). "Octacalcium Phosphate". *Monographs in Oral Science.* 18, 94-111.

D. Cordell, J. Drangert, S. White, "The story of phosphorus: Global food security and food for thought, Global Environmental Change", Volume 19, Issue 2, 2009, Pages 292-305, ISSN 0959-3780, https://doi.org/10.1016/j.gloenvcha.2008.10.009

Daneshgar, S., Buttafava, A., Capsoni, D., Callegari, A., Capodaglio, A. G. (2018). "Impact of pH and Ionic Molar Ratios on Phosphorus Forms Precipitation and Recovery from Different Wastewaters Sludges". Mdpi Resources 7, 71. https://doi.org/10.3390/resources7040071

Doyle, J. D. and Parsons, S. A. (2002). "Struvite formation, control and recovery", *Water Research*. 36, 3925–3940. https://doi.org/10.1016/S0043-1354(02)00126-4

Dynamita. (2022). *SUMO22: Advanced modeling and simulation platform for wastewater treatment* [Computer software]. Dynamita. Retrieved from https://www.dynamita.com

Eanes, E. D. and Meyer, J. L. (1977). "The Maturation of Crystalline Calcium Phosphates in Aqueous Suspension at Physiologic pH". *Calcified Tissue Res.* 23, 259-269. https://doi.org/10.1007/BF02012795

Eanes, E. D. and Posner, A. S. (1968). "Intermediate Phases in the basic Solution Preparation of Alkaline Earth Phosphates". *Calcified Tissue Res.* 2, 38-48. https://doi.org/10.1007/BF02279192

Eckenfelder, W. W. and Ford, D. L. (1968). "Laboratory and Design Procedures for Wastewater Treatment Process". *The Center for Research in Water Resources – The University of Austin Texas.* EHE-10-6802 CRWR-31.

EPA, 2023 https://www.epa.gov/nutrientpollution/sources-and-solutions-wastewater

Esteves, B. F., Druhan, J. L., Jew, A. D. (2023). "Controls on Barite (BaSO4) Precipitation in Unconventional Reservoirs". *Environmental Science and Technology*. 57, 12869-12878. https://doi.org/10.1021/acs.est.3c02923

Gilmour, J. T., Cogger, C. G., Jacobs, L. W., Evanylo, G. K., Sullivan, D. M. (2003). "Decomposition and Plan- Available Nitrogen in Biosolids: Laboratory Studies, Field Studies, and Computer Simulation". *Journal of Environmental Quality.* 32, 4, 1498-1507. https://doi.org/10.2134/jeq2003.1498

Grady. C. P. L., Daigger, G. T., Love, N. G., Filipe, C. D. M. (2011). *Biological Wastewater Treatment* (Third). CRC Press.

Gustafsson, J.P., Visual MINTEQ Version 2.52, On-line (2008) KTH Royal Institute of Technology, Stockholm, Sweden. https://vminteq.lwr.kth.se/.

Gustin, S. and Marinsek-Logar, R. (2011). "Effect of pH, Temperature, and Air Flow Rate on Continuous Ammonia Stripping of the Anaerobic Digestion Effluent". *Process Safety and Environmental Protection.* 89, 1, 61-66. https://doi.org/10.1016/j.psep.2010.11.001

Guzman, G., Alcantara, E., Barron, V., Torrent, J. (1994). "Phytoavailability of Phosphate Adsorbed on Ferrihydrite, Hematite, and Goethite". *Plant Soil.* 159 (2) 219– 225 https://doi.org/10.1007/BF00009284

Gysin, A., Lycke, D., Wirtel, S. (2018). "The Pearl and WASSTRIP Processes (Cananda)." Chapter 19. [Online]. Available: 9781780408361_359.pdf (iwapublishing.com). [Accessed: 12-June-2024]

Haug, R. T. (1977). "Sludge Processing to Optimize Digestibility and Energy Production". *Journal of Water Pollution Control Federation.* 49, 7, 1713-1721. https://www.jstor.org/stable/25039765

Higgins, M., Bott, C., Schauer, P., Beightol, S. (2014). "Does Bio-P Impact Dewatering after Anaerobic Digestion? Yes, and Not in a Good Way!". *WEF Residuals and Biosolids Conference Proceedings.*

Higgins, M., Beightol, S., Manahar, U., Suzuki, R., Xiao, S., Lu, H., Le, T., Mah, J., Pathak, B., DeClippeleir, H., Novak, J., Al-Omari, A., Murthy, S. (2017). "Pretreatment of a Primary and Secondary Sludge Blend at Different Thermal Hydrolysis Temperatures:

Impacts on Anaerobic Digestion, Dewatering, and Filtrate Characteristics". *Water Research.* 122, 557-569. https://doi.org/10.1016/j.watres.2017.06.016

Hsieh, C., Babcock, R., Stenstrom, M. (1993). "Estimating Emissions of Twenty VOCs: Diffused Aeration". *Journal of Environmental Engineering.* 119, 1099-1118. https://doi.org/10.1061/(ASCE)0733-9372(1993)119:6(1099)

Iijima, M., Kamemizu, H., Wakamatsu, N., Goto, T., Doi, Y., Moriwaki, Y. (1998). "Effects of Ca Addition of the Formation of Octacalcium Phosphate and Apatite in Solution at pH 7.4 and 37C". *Journal of Crystal Growth.* 193, 182-188. https://doi.org/10.1016/S0022-0248(98)00455-2

Jia, G., Zhang, H., Krampe, J., Muster, T., Gao, B., Zhu, N., Jin, B. (2017). "Applying a Chemical Equilibrium Model for Optimizing Struvite Precipitation for Ammonium Recovery from Anaerobic Digester Effluent". *Journal of Cleaner Production.* 147, 297-305. https://doi.org/10.1016/j.jclepro.2017.01.116

C. Z. Jiang, N. J. Tosca, 2019. "Growth Kinetics of Siderite at 298.15 K and 1 Bar". *Earth Sciences Dept, University of Oxford, OX1 3AN, England, United Kingdom.* https://doi.org/10.1016/j.gca.2020.01.047

Johnsson, M. S. A. and Nancollas, G. H. (1992). "The Role of Brushite and Octacalcium Phosphate in Apatite Formation". *Critical Reviews in Oral Biology and Medicine*. 3, 61–82. https://doi.org/10.1177/10454411920030010601

Jones, A. G. (2002). "Crystallization Process System" *Oxford, Great Britian: Butter-worth/Heinemann.*

Kabdasli, I., Parsons, S. A., Tunaya, O. (2006). "Effect of Major Ions on Induction Time of Struvite Precipitation". *Croatica Chemica Acta.* 79, 243-251.

Kamika, I., Coetzee, M., Mamba, B. B., Msagati, T., Momba, M. (2014). "Enhanced Biological Phosphorus Removal (EBPR) Process: A Case Study of Northern Wastewater Treatment Works, Johannesburg", *Int. J. Environ. Res. Public Health* 2014, *11*(3), 2876-2898. https://doi.org/10.3390/ijerph110302876

Korchef, A., Saidou, H., Amor, M. B. (2011). "Phosphate Recovery Through Struvite Precipitation by CO2 Removal: Effect of Magnesium, Phosphate and Ammonium Concentrations". *Journal of Hazardous Materials.* 186, 602-613. https://doi.org/10.1016/j.jhazmat.2010.11.045

Koutsoukos, P., Amjad, Z., Tomson, M. B., Nancollas, G. H. (1980). "Crystallization of Calcium Phosphates. A Constant Composition Study". *Journal of the American Chemical Society*. 102, 5, 1553-1557.

Koutsoukos, P., Kofina, A. N., Klepetsanis, P. (2003). "Exploration of Alternatives for Phosphorus Recovery from Wastewater by Crystallization". *Wasic Workshop.* Istanbul, Turkey.

Kumar, R., Prakash, KH, Cheang, P., Khor, KA. (2004). "Temperature Driven Morphological Changes of Chemically Precipitated Hydroxyapatite Nanoparticles". *Langmuir.* 20, 13, 5196-5200. https://doi.org/10.1021/la049304f

Le Corre, K.S., Valsami-Jones, E., Hobbs, P., Parsons, S.A. (2009). Phosphorus Recovery from Wastewater by Struvite Crystallization: A Review. Critical Reviews in Environmental Science and Technology, 39(6). 433 – 477. https://doi.org/10.1080/10643380701640573

Liu, X., Xu, Z., Peng, J., Song, Y., Meng, X. (2016). "Phosphate recovery from anaerobic digester effluents using CaMg(OH)4", Journal of Environmental Sciences, Volume 44, 2016, Pages 260-268, ISSN 1001-0742. https://doi.org/10.1016/j.jes.2016.02.006

Liu, X., Wen, G., Hu, Z., Wang, J. (2018). "Coupling Effects of pH and Mg/P Ratio on P Recovery from Anaerobic Digester Supernatant by Struvite Formation". *Journal of Cleaner Production*. Vol. 198, pg. 633-641. https://doi.org/10.1016/j.jclepro.2018.07.073

Lu, X. and Leng, Y. (2005). "Theoretical Analysis of Calcium Phosphate Precipitation in Simulated Body Fluid". *Biomaterials* 26, 10, 1097–1108. https://doi.org/10.1016/j.biomaterials.2004.05.034

Mamais, D., Pitt, PA., Cheng, YW., Loiacono, J., Jenkins, D. (1994). "Determination of Ferric Chloride Dose to Control Struvite Precipitation in Anaerobic Sludge Digesters". *Water Environment Research*. 66, 912–918. https://doi.org/10.2175/WER.66.7.8

Markovic, M., Fowler, BO., Brown, WE. (1993). "Octacalcium Phosphate Carboxylates. 1. Preparation and Identification". *Chem Matter*. 5, 1401-1405. https://doi.org/10.1021/cm00034a007

Massey, MS., Davis, JG, Ippolito, JA., and Sheffield, RE. (2009). "Effectiveness of Recovered Magnesium Phosphates as Fertilizers in Neutral and Slightly Alkaline Soils," *Agronomy Journal*. 101, 2, pp. 323–329. https://doi.org/10.2134/agronj2008.0144

Matitike, O (1966). "The Solubility of Some Iron and Aluminum Phosphates in the Acetic Acid-Ammonium Acetate Buffer System." *Annales Agriculturae Fenniae.* 5, 6-11.

McNamara, P., Sabba, F., Redmond, E., Dunlap, P., Worley-Morse, T., Marks, C., Downing, L. (2022). "Post Aerobic Digestion (PAD) is a Solids Sidestream Nutrient Removal Process that Utilizes Native Carbon: Performance and Key Operational Parameters from Two Full-Scale PAD Reactors". *Environmental Science; Advances.* 1, 216-228. DOI: 10.1039/D2VA00045H

Menniti, A., Johnson, B., Leaf, B., Kumar, N., Oerke, D., Crane, T., Dolsby, C. (2010). "Combining Mesophilic Anaerobic Digestion with Post-Aerobic Digestion to Enhance Volatile Solids Reduction and Reduce Sidestream Ammonia". *Water Environment Federation.* 2010, 4, 994-1003.

Merkel, W. and Krauth, K. (1999). "Mass Transfer of Carbon Dioxide in Anaerobic Reactors Under Dynamic Substrate Loading Conditions". *Water Research.* 33, 9, 2011-2020. https://doi.org/10.1016/S0043-1354(98)00434-5

Meyer, FH., Riggs, OL., McGlasson, RL., Sunbury, JD. (1958). "Corrosion Products of Mild Steel in Hydrogen Sulfide Environments". *Corrosion.* 14, 2, 69-75. https://doi.org/10.5006/0010-9312-14.2.69

Meyer, J. (1983). "Phase Transformations in the Spontaneous Precipitation of Calcium Phosphate". *Croatica Chim Acta.* 56, 753-767.

Meyer, J. and Eanes, ED. (1978). "A Thermodynamic Analysis of the Amorphous to Crystalline Calcium Phosphate Transformation". *Calcified Tissue Res.* 25, 59-68. https://doi.org/10.1007/BF02010752

Mihelcic, J., Fry, L., Shaw, R. (2011). "Global Potential for Phosphorus Recovery from Human Urine and Feces". *Chemosphere.* 84, 6, 832-839. https://doi.org/10.1016/j.chemosphere.2011.02.046

Furedi-Milhofer, H., Purgaric, B., Brecevic, LJ., Pavkovic, N. (1971). "Precipitation of Calcium Phosphates from Electrolyte Solutions". *Calcified Tissue Res.* 8, 142-153. https://doi.org/10.1007/BF02010131

Monma, H and Goto, M. (1983). "Succinate-complexed Octacalcium Phosphate". *Bulletin of the Chemical Society of Japan.* 56, 3843-3844. https://doi.org/10.1246/bcsj.56.3843

Morse, JW. and Arakaki, T. (1993). "Adsorption and Coprecipitation of Divalent Metals with Mackinawite". *Geochimica et Cosmochimica Acta.* 57, 15, 3635-3640. https://doi.org/10.1016/0016-7037(93)90145-M

Moulessehoul, A., Gallart-Mateu, D., Harrache, D., Djaroud, S., de la Guardia, M., Kameche, M. (2017). "Conductimetric Study of Struvite Crystallization in Water as a Function of pH". *Journal of Crystal Growth.* 471, 42-52. https://doi.org/10.1016/j.jcrysgro.2017.05.011

Muhmood, A., Wang, X., Dong, R, Wu, S. (2021). "New Insights into Interactions of Organic Substances in Poultry Slurry with Struvite Formation: An Overestimated Concern?". *Science of the Total Environment.* 751, 141789. https://doi.org/10.1016/j.scitotenv.2020.141789

Mullin, JW. (1992). "Crystallization". *Oxford, Great Britian: Butter-worth/Heinemann.*

Munch, EV. and Barr, K. (2000). “Controlled Struvite Crystallisation for Removing Phosphorus from Anaerobic Digester Sidestreams”. *Water Research.* 35, 1, pp. 151-159. https://doi.org/10.1016/S0043-1354(00)00236-0

Musvoto, E.V., Wentzel, M.C., Ekama, G.A. (2000). “Integrated Chemical—Physical Processes Modelling II. Simulating Aeration Treatment of Anaerobic Digester Supernatants”. *Water Research*. 34, 1868–1880. https://doi.org/10.1016/S0043-1354(99)00335-8

Nelson, NO., Mikkelsen, RL., Hesterberg, DL. (2003). “Struvite Precipitation in Anaerobic Swine Lagoon Liquid: Effect of pH and Mg:P Ratio and Determination of Rate Constant”. *Bioresource Technology.* 89, 3, 229-236. https://doi.org/10.1016/S0960-8524(03)00076-2

Nordstrom, A. and Herbert, RB. (2017). “Denitrification in a Low-Temperature Bioreactor System at Two Different Hydraulic Residence Times: Laboratory Column Studies”. *Environment Technology.* 38, 11, 1362-1375. https://doi.org/10.1080/09593330.2016.1228699

Nordstrom, D. K., Plummer, L. N., Langmuir, D., Busenberg, E., May, H. M., Jones, B. F., Parkhurst, D. L. (1990). “Revised Chemical and Equilibrium Data for Major Water-Mineral Reactions and their Limitations”. *Chemical Modeling of Aqueous Systems II.* 31, 3F98-413. **DOI:** 10.1021/bk-1990-0416.ch031

Novak, J., Wilson, C., Banjade, S., Tanneru, C., Murthy, S., Bailey, W. (2009). “A New Solids Technology Train: Can 70% Volatile Solids Reduction and Class A Biosolids be Achieved from Digestion?” *Weftec Proceedings.*

Novak, J., Banjade, S., Murthy, S. (2011). “Combined Anaerobic and Aerobic Digestion for Increased Solids Reduction and Nitrogen Removal”. *Water Research.* 45, 2, 618-624. https://doi.org/10.1016/j.watres.2010.08.014

LeGeros, R. and LeGeros, J. (1984). “Phosphate Minerals in Human Tissues”. *Phosphate Minerals.* 12, 350-385. https://doi.org/10.1007/978-3-642-61736-2_12

Lu, X. and Leng, Y. (2004). “Theoretical Analysis of Calcium Phosphate Precipitation in Simulated Body Fluid”. *Biomaterials.* 26, 1097-1108. https://doi.org/10.1016/j.biomaterials.2004.05.034

Ohlinger, KN., Young, TM., Schroeder, ED. (1998). “Predicting struvite formation in digestion”. *Water Research*, 32, 3607–3614. https://doi.org/10.1016/S0043-1354(98)00123-7

Ohlinger, KN., Young, TM., Schroeder, ED. (1999). "Kinetic Effects on Preferential Struvite Accumulation in Wastewater". *Journal of Environmental Engineering.* 125, 730-737. https://doi.org/10.1061/(ASCE)0733-9372(1999)125:8(730)

Ohlinger, KN., Young, TM., Schroeder, ED. (2000). "Post Digestion Struvite Precipitation Using a Fluidized Bed Reactor". *Journal of Environmental Engineering.* 126, 361-368. https://doi.org/10.1061/(ASCE)0733-9372(2000)126:4(361)

"Ostara Nutrient Recovery – Nutrient Recovery Solutions," Ostara Nutrient Recovery. [Online]. Available: https://www.ostara.com/nutrient-recovery/nutrient-recovery-solutions/. [Accessed: 12-June-2024]

Park, C., Muller, C., Abu-Orf, M., Novak, J. (2006ba). "The Effect of Wastewater Cations on Activated Sludge Characteristics: Effects of Aluminum and Iron in Floc". *Water Environment Research.* 78, 31, 31-40. https://doi.org/10.2175/106143005X84495

Park, C., Abu-Orf, M., Novak, J. (2006b). "The Digestibility of Waste Activated Sludge". *Water Environment Research.* 78, 1, 59-68. https://doi.org/10.2175/106143005X84521

Parker, WJ., Jones, RM., Murthy, S. (2008). "Characterization of the COD/VSS Ratio during Anaerobic Digestion of Waste Activated Sludge: Experimental and Modeling Studies". *Proceedings of the Water Environment Federation.* 524-533.

Parravicini, V., Svardal, K., Hornek, R., Kroiss, H. (2008). "Aeration of Anaerobically Digested Sewage Sludge for COD and Nitrogen Removal: Optimization at Large-Scale". *Water Science and Technology.* 57, 2, 257-264. https://doi.org/10.2166/wst.2008.020

Penn, CJ. and Sims, JT. (2002). "Phosphorus Forms in Biosolid-amended Soils and Losses in Runoff". *Journal of Environmental Quality.* 31, 1349-1361. https://doi.org/10.2134/jeq2002.1349

Peryea, FJ. and Kittrick, JA. (1988). "Relative Solubility of Corundum, Gibbsite, Boehmite, and Diaspore at Standard State Conditions". *Clays and Clay Minerals.* 36, 391-396. https://doi.org/10.1346/CCMN.1988.0360502

Ping, Q., Li, Y., Wu, X., Yang, L., Wang, L. (2016). "Characterization of Morphology and Component of Struvite Pellets Crystallized from Sludge Dewatering Liquor: Effects of Total Suspended Solids and Phosphate Concentrations". *Journal of Hazardous Materials.* 310, 261-269. https://doi.org/10.1016/j.jhazmat.2016.02.047

Postma, D. (1980). "Formation of Siderite and Vivianite and the Pore-Water Composition of a Recent Bog Sediment in Denmark". *Chemical Geology,* vol. 31. pp. 225-244. https://doi.org/10.1016/0009-2541(80)90088-1

Qiong, L., JuMei, L., XiLong, C., DongPu, W., YiBing, M. (2012). "On-Farm Assessment of Biosolids Effects on Nitrogen and Phosphorus Accumulation in Soils". *Journal of Integrative Agriculture.* 11, 9, 1545-1554.

Quintana, M., Sanchez, E., Colmenarejo, MF, Barrera, J., Garcia, G., Borja, R. (2005). "Kinetics of Phosphorus Removal and Struvite Formation by the Utilization of By-Product Magnesium Oxide Production". *Chemical Engineering Journal.* 111, 45-52. https://doi.org/10.1016/j.cej.2005.05.005

Rahaman, MS., Ellis, N., Mavinic, DS. (2008). "Effects of Various Process Parameters on Struvite Precipitation Kinetics and Subsequent Determination of Rate Constants". *Water Science and Technology.* 57, 5, 647- 654. https://doi.org/10.2166/wst.2008.022

Rawn, AM., Banta, AP., Pomeroy, R. (1937). "Multiple-Stage Sewage Sludge Digestion". *Transactions of the American Society of Civil Engineers*. Volume 104, Issue 1 https://doi.org/10.1061/TACEAT.0005148

Rebosura, M., Salehin, S., Pikaar, I., Sun, X., Keller, J., Sharma, K., Yuan, Z. (2018). "A Comprehensive Laboratory Assessment of the Effects of Sewer-Dosed Iron Salts on Wastewater Treatment Processes". *Water Research.* 146, 109-117. https://doi.org/10.1016/j.watres.2018.09.021

Rittmann and McCarty (2001). "Environmental Biotechnology: Principles and Applications". *Second.* McGraw Hill.

Robie, RA. and Waldbaum, DR. (1968). "Thermodynamic Properties of Minerals and Related Substances at 298.15°K (25°C) and One Atmosphere (1.013 Bars) Pressure and at Higher Temperatures". *Geological Survey. United States Department of the Interior.* Bulletin 1259.

Romero-Guiza, MS., Astals, S., Mata-Alvarez, J., Chimenos, JM. (2015). "Feasibility of Coupling Anaerobic Digestion and Struvite Precipitation in the Same Reactor: Evaluation of Different Magnesium Sources". *Chemical Engineering Journal.* 270, 542-548. https://doi.org/10.1016/j.cej.2015.02.057

Root, M. J. (1990). "Inhibition of the amorphous calcium phosphate phase transformation reaction by polyphosphates and metal ions". *Calcified Tissue International* 47 (2), 112e116. https://doi.org/10.1007/BF02555994

Roques, H. and Girou, A. (1974). "Kinetics of the Formation Conditions of Carbonate Tartars". *Water Research.* 8(11), 907-920. https://doi.org/10.1016/0043-1354(74)90105-5

Rosso, D. (2018). "Aeration, Mixing, and Energy: Bubbles and Sparks" *IWA Publishing.*

Rosso, D. and Stenstrom, MK. (2006). “Surfactant Effects on α-factors in Aeration Systems”. *Water Research.* 40, 1397-1404. https://doi.org/10.1016/j.watres.2006.01.044

The RUFF™ Project. https://rruff.info/

Ruiz-Agudo, C., Putnis, CV., Ruiz-Agudo, E., Putnis, A. (2015). “The Influence of pH on Barite Nucleation and Growth”. *Chemical Geology.* 391, 7-18. https://doi.org/10.1016/j.chemgeo.2014.10.023

Sabba, F., McNamara, P., Redmond, E., Ruff, C., Young, M., Downing, L. (2022). “Lab-scale Data and Microbial Community Structure Suggest Shortcut Nitrogen Removal as the Predominant Nitrogen Removal Mechanism in Post-Aerobic Digestion (PAD)”. *Water Environment Research.* 94, 7. https://doi.org/10.1002/wer.10762

Saidou, H., Korchef, A., Moussa, SB., Amor, MB. (2009). “Struvite Precipitation by the Dissolved CO2 Degasification Technique: Impact of the Airflow Rate and pH”. *Chemosphere.* 74, 2, 338-343. https://doi.org/10.1016/j.chemosphere.2008.09.081

Sardisco, J. B. and Pitts, R. E. (1965). “Corrosion of Iron in an H_2S-CO_2-H_2O System Mechanism of Sulfide Film Formation and Kinetics of Corrosion Reaction”. *Corrosion.* 21, 8, 245-253. https://doi.org/10.5006/0010-9312-21.8.245

Sardisco, JB., Write, WB., Greco, E. C. (1963). “Corrosion of Iron in on H_2S-CO_2-H_2O System: Corrosion Film Properties on Pure Iron”. *Corrosion.* 19, 10, 354-359. https://doi.org/10.5006/0010-9312-19.10.354

Shaddel, S., Ucar, S., Andreassen, JP., Osterhus, SW. (2019). “Engineering of Struvite Crystals by Regulating Supersaturation – Correlation with Phosphorus Recovery, Crystal Morphology and Process Efficiency”. *Journal of Environmental Chemical Engineering.* 7, 1, 102918. https://doi.org/10.1016/j.jece.2019.102918

Shih, K. and Yan, H. (2016). “The Crystallization of Struvite and its Analog (K-Struvite) from Waste Streams for Nutrient Recycling”. *Environmental Materials and Waste.* 665-686. https://doi.org/10.1016/B978-0-12-803837-6.00026-3

Shimp, G., Barnard, J., Bott, C., (2013). “Seeking to Understand and Address the Impacts of Biological Phosphorus Removal on Biosolids Dewatering”. *Water Environment Federation*, *Weftec Proceedings.* 5668-5685. DOI:10.2175/193864713813716309

Shraddha, K., Dipika, J., Arti, M. (2018). “Green and Eco-Friendly Materials for the Removal of Phosphorus from Wastewater”. *Life Cycle Assessment of Wastewater Treatment.*

Simpson, D. (1966). Apatite and OCP: Effects of CO2 and Halogens on Formation”. *Science.* 154, 1660-1661. https://doi.org/10.1126/science.154.3757.1660

Smith, J. and Miller, J. (1975). “Nature of Sulphides and their corrosive Effect on Ferrous Metals: A Review”. *British Corrosion Journal.* 10, 3, 136-143. https://doi.org/10.1179/000705975798320701

Snoeyink, V. and Jenkins, D. 1980. “Water Chemistry”. *New York: John Wiley and Sons.*

Song, Y., Dai, Y., Hu, Q., Yu, X., Qian, F. (2014). “Effects of Three Kinds of Organic Acids on Phosphorus Recovery by Magnesium Ammonium Phosphate (MAP) Crystallization from Synthetic Swine Wastewater”. *Chemosphere.* 101, 41-48. https://doi.org/10.1016/j.chemosphere.2013.11.019

Stratful, I., Scrimshaw, M., Lester, J. (2001). “Conditions Influencing the Precipitation of Magnesium Ammonium Phosphate”. *Water Research.* Vol. 35, 17, 4191-4199. https://doi.org/10.1016/S0043-1354(01)00143-9

Strumpf, D., Zhu, H., Heinzmann, B., Kraume, M. (2008). “Phosphorus Recovery in Aerated Systems by MAP Precipitation: Optimizing Operational Conditions”. *Water Science and Technology.* 58, 10, 1977-1983. https://doi.org/10.2166/wst.2008.549

Stuckey, D. and McCarty, P. (1978). “Thermochemical Pretreatment of Nitrogenous Material to Increase Methane Yield”. *Biotechnology Bioengineering Symp.* 8, 219-233

Stumm, W. and Morgan, J. (1996). “Aquatic Chemistry: Chemical Equilibria and Rates in Natural Waters”. *Third Edition.* Wiley Interscience: New York, NY, USA.

Tanada, S., Kabayama, M., Kawasaki, N., Sakiyama, T., Nakamura, T., Araki, M., Tamua, T. (2003). “Removal of Phosphate by Aluminum Oxide Hydroxide”. *Journal of Colloid and Interface Science.* 257, 1, 135-140. https://doi.org/10.1016/S0021-9797(02)00008-5

Tarrago, E., Sciarria, T., Ruscalleda, M., Colprim, J., Balaguer, M., Adani, F., Puig, S. (2018). “Effect of Suspended Solids and its Role on Struvite Formation from Digestated Manure”. *Journal of Chemical Technology and Biotechnology.* 93, 2758-2765. https://doi.org/10.1002/jctb.5651

Ven Rensburg, P., Musvoto, E. Wentzel, M., Ekama, G. (2003). “Modeling Multiple Mineral Precipitation in Anaerobic Digester Liquor”. *Water Research.* 37, 3087-3097. https://doi.org/10.1016/S0043-1354(03)00173-8

Wei, L., Zhang, T., Hong, T., Dong, Y., Ji, D., Lou, L., Li, R., Li, Z., Tang, Y. (2023). “Revealing and Quantifying the Effect of Cattiite Coprecipitation on the Purity of K-struvite in Aqueous Solution” *Journal of Environmental Chemical Engineering.* 11, 109764. https://doi.org/10.1016/j.jece.2023.109764

Wilfert, P., Kumar, P., Korving, L., Witkamp, G., Van Loosdrecht, M. (2015). “The Relevance of Phosphorus and Iron Chemistry to the Recovery of Phosphorus from Wastewater: A

Review". *Environmental Science & Technology*. 49, 16, 9400-9414. https://doi.org/10.1021/acs.est.5b00150

Wilson, C. and Novak, J. (2009). "Hydrolysis of Macromolecular Components of Primary and Secondary Wastewater Sludge by Thermal Hydrolytic Pretreatment". *Water Research.* 43, 18, 4489-4498. https://doi.org/10.1016/j.watres.2009.07.022

Wilson, C., Novak, J., Murthy, S. (2010). "Determination of Oxygen Utilization during Post-Aerobic Digestion of Anaerobically Digested Biosolids". *Proceedings of the Water Environment Federation.* 4, 1018-1032. https://doi.org/10.2175/193864710802766985

Wilson, C., Tanneru, C., Banjade, S., Murthy, S., Novak, J. (2011). "Anaerobic Digestion of Raw and Thermally Hydrolyzed Wastewater Solids Under Various Operational Conditions". *Water Environment Research.* 83, 9, 815-825. https://doi.org/10.2175/106143011X12928814444934

Winkler, M., Bassin, J., Kleerebezem, R., Sorokin, D., Van Loosdrecht, M. (2012). "Unraveling the Reasons for Disproportion in the Ratio of AOB and NOB in Aerobic Granular Sludge". *Applied Microbiology and Biotechnology.* 94, 6, 1657-1666. https://doi.org/10.1007/s00253-012-4126-9

Wisdom, B., Van Anderson, B., Avila, I., Gottschalk, T., Carson, K., Cavanaugh, L. (2017). "Pilot-scale Evaluation of AirPrex® for Digestate Treatment". *Water Environment Federation.* Vol. 2017.

Wu, Y., Luo, J., Zhang, Q., Aleem, M., Fang, F., Xue, Z, Cao, J. (2019). "Potential and Challenges of Phosphorus Recovery as Vivianite from Wastewater: A Review". *Chemosphere.* 2226, 246-258. https://doi.org/10.1016/j.chemosphere.2019.03.138

Wu, S., Wei, W., Sun, J., Xu, Q., Dai, X., Ni, B. (2020). "Medium-Chain Fatty Acids and Long-Chain Alcohols Production from Waste Activated Sludge via Two-Stage Anaerobic Fermentation". *Water Research.* 186, 1. https://doi.org/10.1016/j.watres.2020.116381

Xu, K., Li, J., Zheng, M., Zhang, C., Xie, T., Wang, C (2015). "The Precipitation of Magnesium Potassium Phosphate Hexahydrate for P and K Recovery from Synthetic Urine". *Water Research.* 80, 71-79. https://doi.org/10.1016/j.watres.2015.05.026

Yan, H. and Shih, K. (2016). "Effects of Calcium and Ferric Ions on Struvite Precipitation: A New Assessment Based on Quantitative X-Ray Diffraction Analysis". *Water Research.* Vol. 95, 310-318. https://doi.org/10.1016/j.watres.2016.03.032

Zeng, L. and Li, X. (2006). "Nutrient Removal from Anaerobically Digested Cattle Manure by Struvite Precipitation". *Journal of Environmental Engineering and Science.* 5, 285-294. https://doi.org/10.1139/s05-027

Zhang, T., Bowers, K., Harrison, J., Chen, S. (2010). “Releasing Phosphorus from Calcium for Struvite Fertilizer Production from Anaerobically Digested Dairy Effluent”. *Water Environment Research.* 82, 1, 34-42. https://doi.org/10.2175/106143009X425924

Zhang, F., Yang, H., Wang, J., Lui, Z., Guan, Q. (2018). “Effect of Free Ammonia Inhibition on NOB Activity in High Nitrifying Performance of Sludge”. *RSC Advances.* 8, 56, 31987-31995. DOI: 10.1039/C8RA06198J

8. Appendix A: Supplementary Information

8.1 Phosphorus Removal Data

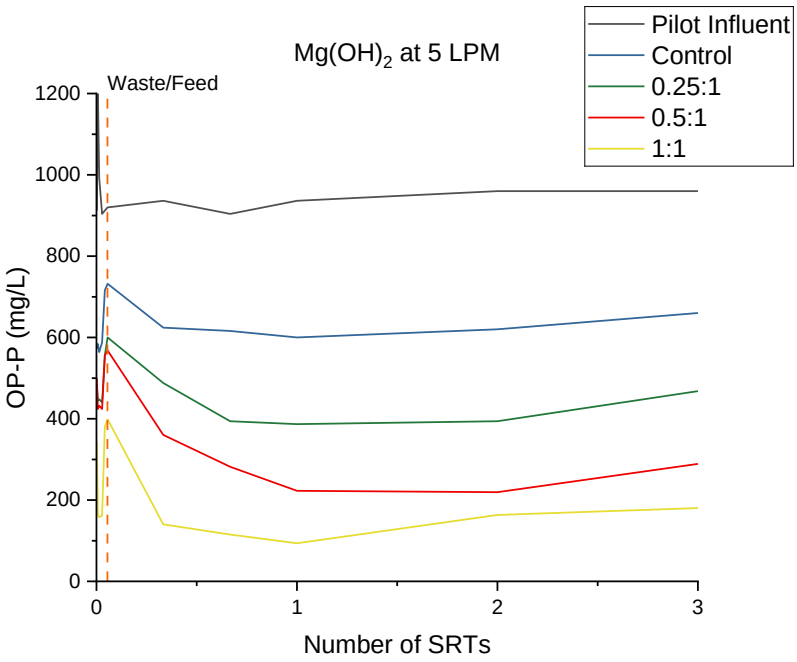

Figure 54: OP-P (mg/L) data sampled throughout campaign 1, aerated at 5 LPM with $Mg(OH)_2$ addition at $Ca^{2+}+Mg^{2+}$:P ratios of 0, 0.25:1, 0.5:1, and 1:1.

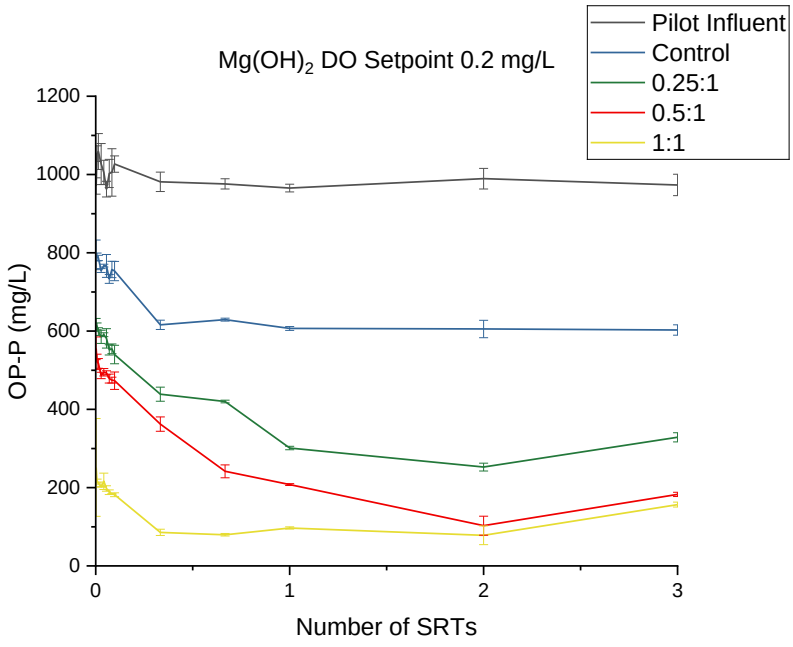

Figure 55: OP-P (mg/L) data sampled throughout campaign 2, aerated at a DO setpoint of 0.2 mg/L, with $Mg(OH)_2$ addition at $Ca^{2+}+Mg^{2+}$:P ratios of 0, 0.25:1, 0.5:1, and 1:1.

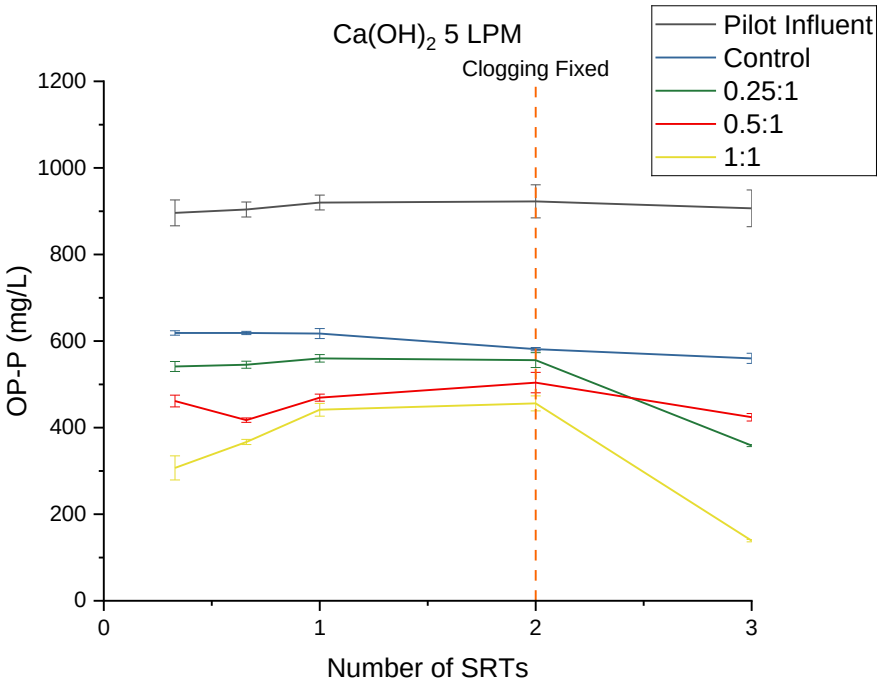

Figure 56: OP-P (mg/L) data sampled throughout campaign 3, aerated at 5 LPM with $Ca(OH)_2$ addition at Ca^{2+}+Mg^{2+}:P ratios of 0, 0.25:1, 0.5:1, and 1:1.

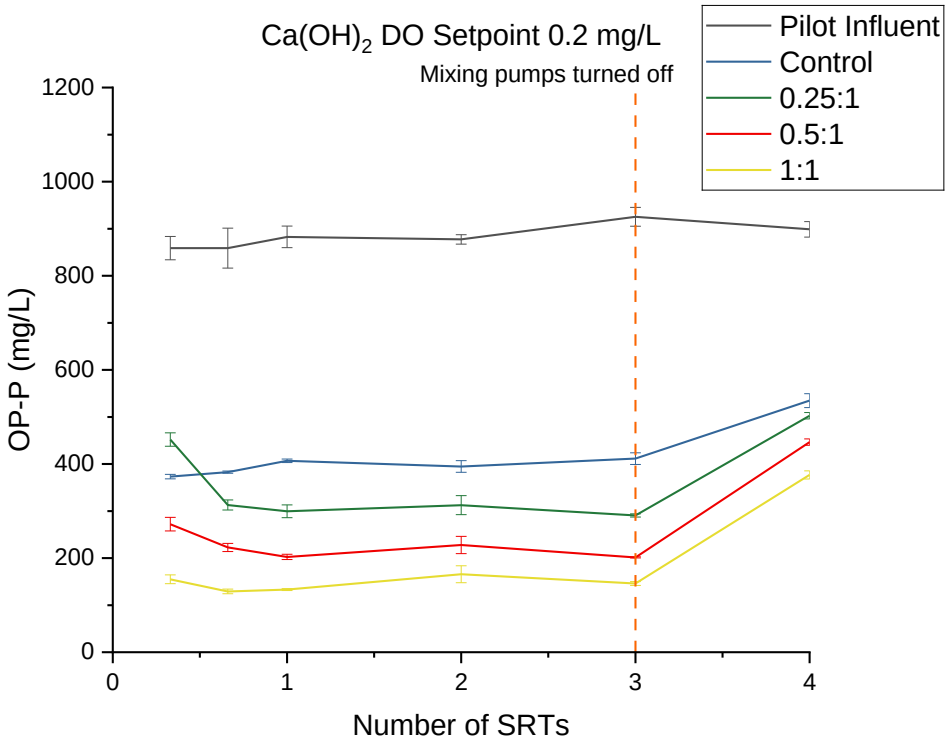

Figure 57: OP-P (mg/L) data sampled throughout campaign 4 and 4.1, aerated at a DO setpoint of 0.2 mg/L with $Ca(OH)_2$ addition at Ca^{2+}+Mg^{2+}:P ratios of 0, 0.25:1, 0.5:1, and 1:1.

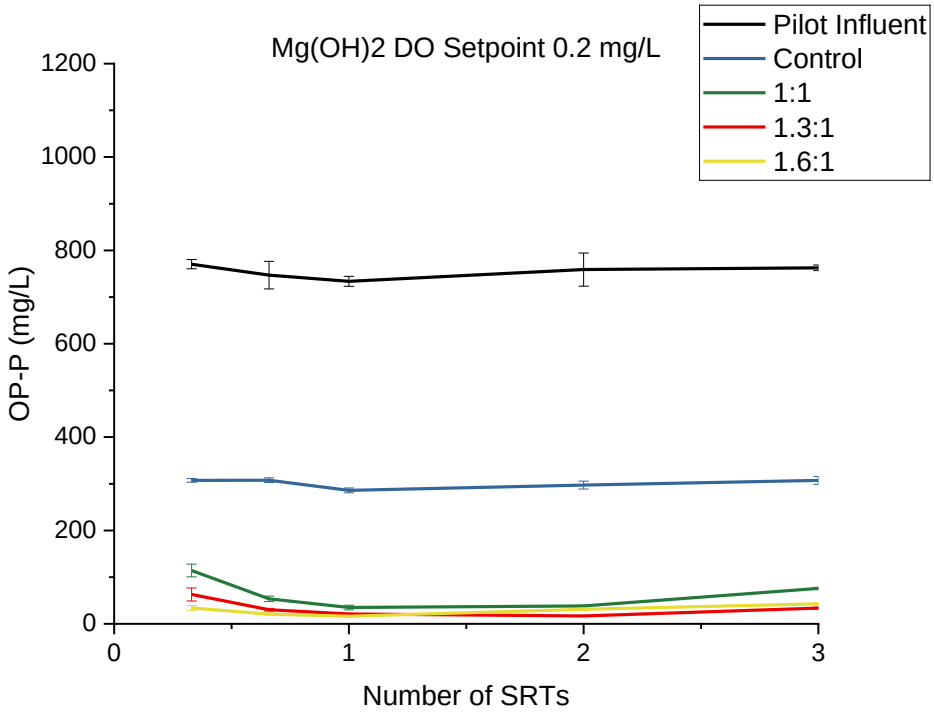

Figure 58: OP-P (mg/L) data sampled throughout campaign 5, aerated at a DO setpoint of 0.2 mg/L with $Mg(OH)_2$ addition at Ca^{2+}+Mg^{2+}:P ratios of 0, 1:1, 1.3:1, and 1.6:1.

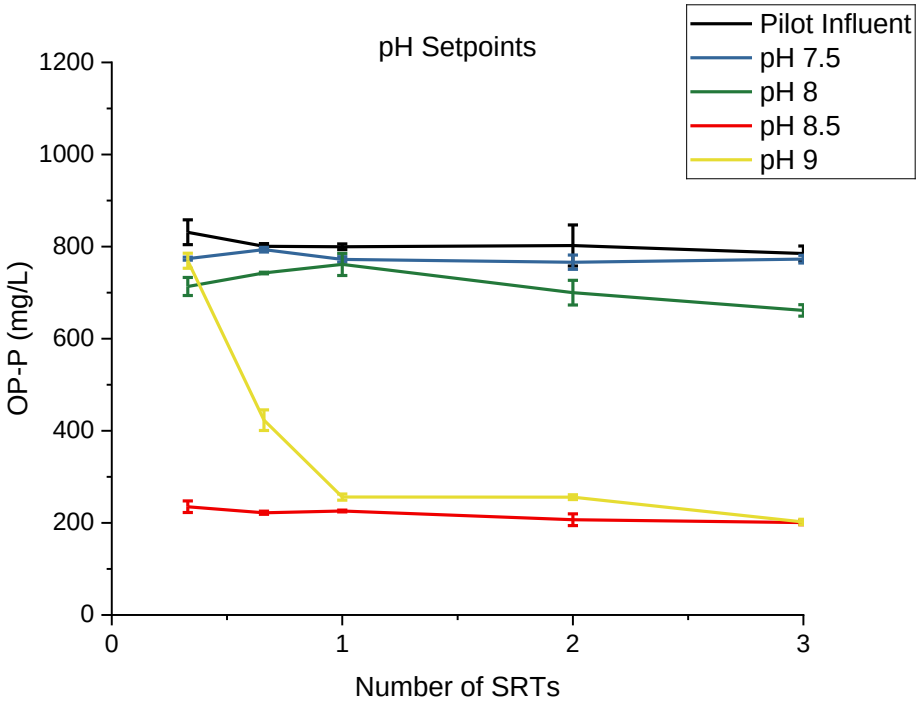

Figure 59: OP-P (mg/L) data sampled throughout campaign 6, aerated at pH setpoints of 7.5, 8, 8.5, and 9.

8.2 Other Data

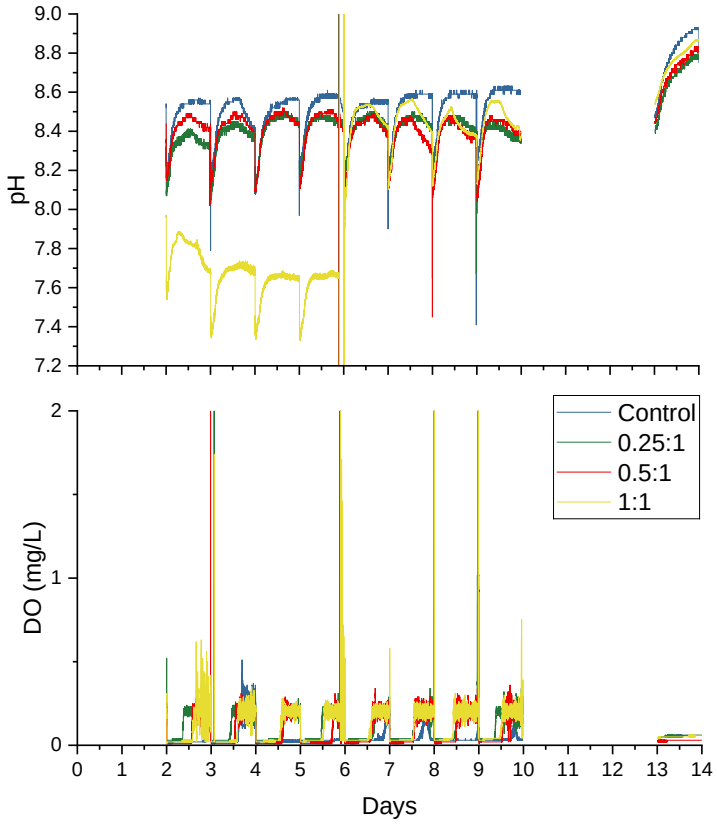

Figure 60: pH and DO online measurements across the 14-day testing period for the control, and chemically dosed tanks at 0.25:1, 0.5:1, and 1:1 Ca^{2+}+Mg^{2+}:P ratios dosed with $Ca(OH)_2$ for campaign 4.1. Mixing pumps were unplugged on day 10.

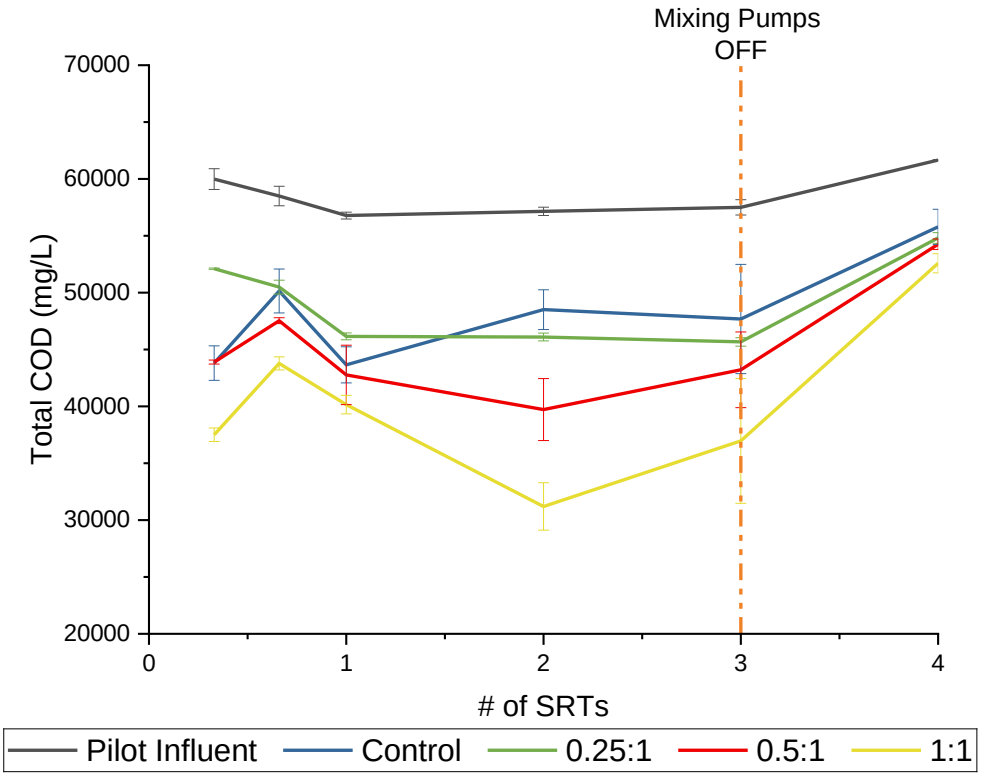

Figure 61: Total COD (mg/L) data sampled throughout campaign 4 and 4.1, aerated at a DO setpoint of 0.2 mg/L with $Ca(OH)_2$ addition at Ca^{2+}+Mg^{2+}:P ratios of 0, 0.25:1, 0.5:1, and 1:1.

Table 18: Visual MINTEQ model inputs for campaign 6.

Component	pH 7.5	pH 8	pH 8.5	pH 9
Temperature (°C)	35	35	35	35
Average pH	7.9	8	8.3	8.6
ORP (mV)	-442	-442	-200	-200
DOC (SHM)	2895	2761	2207	3204
Total Alkalinity (as $CaCO_3$)	8008	8031	4043	5240
Volatile Acids (Acetate-1)	508	285	244	264
Al^{3+}	3.9	3.5	3.3	3.2
B(III)	0.7	0.7	<1.5	<1.5
Ba^{2+}	0.5	0.5	0.4	0.4
Ca^{2+}	49.8	41.8	40	40.3
Cl^-	131	131	136	136
Cu^{2+}	0.4	0.8	0.9	1.49
Fe^{2+}	53.1	53.1	105	112
K^+	383	352	337	342
Mg^{2+}	5.6	6.2	7.5	7.2
Mn^{2+}	0.4	0.4	0.4	0.4

Na^{+}	87	81.8	73.9	76
N (NH4+)	2652	2573	2170	2095
P (PO4)	770.4	707.6	211.2	238
S (-II)	300	300	36	36
S (SO4)	1	1	1880	1880
Si^{4+}	-	-	-	-
Sr^{2+}	0.3	0.2	0.2	0.2
Zn^{2+}	2.9	2.8	4.8	5.4

8.3 Solids Data

Table 19: TS and VS and the standard deviation averaged across the steady state portion of each test for the pilot influent and tank effluents at Ca^{2+}+Mg^{2+}:P dosage ratios of 0, 0.25:1, 0.5:1, and 1:1. The VSF, VSR, and percent of VSR that contributed to CODr was also calculated.

	%TS	Std.	%VS	Std.	VSF	VSR (mass balance)	% of VSR contributing to CODr
Campaign 1:							
Pilot Influent	4.28%	0.19%	3.03%	0.21%	71%		
Control	4.26%	0.06%	3.06%	0.22%	72%	-0.99%	-0.01%
0.25:1	4.26%	0.08%	3.06%	0.26%	72%	-0.81%	-0.01%
0.5:1	4.09%	0.18%	2.83%	0.45%	69%	6.82%	0.06%
1:1	4.17%	0.07%	2.88%	0.24%	69%	5.11%	0.04%
Campaign 2:							
Pilot Influent	4.51%	0.54%	3.18%	0.24%	70%		
Control	4.45%	0.07%	3.18%	0.12%	72%	0%	0.00%
0.25:1	4.44%	0.07%	2.89%	0.04%	65%	9%	0.09%
0.5:1	4.52%	0.21%	2.88%	0.04%	64%	9%	0.09%
1:1	4.32%	0.04%	2.86%	0.20%	66%	10%	0.09%
Campaign 3:							
Pilot Influent	4.53%	0.01%	3.08%	0.00%	68%		
Control	4.55%	0.01%	3.14%	0.01%	69%	-2%	-0.02%
0.25:1	4.38%	0.00%	2.98%	0.01%	68%	3%	0.03%
0.5:1	4.21%	0.01%	2.92%	0.01%	69%	5%	0.05%
1:1	4.13%	0.00%	2.71%	0.01%	66%	12%	0.07%
Campaign 4:							
Pilot Influent	4.68%	0.08%	3.24%	0.01%	69%		
Control	4.91%	0.22%	3.37%	0.09%	69%	-4%	-0.03%
0.25:1	4.61%	0.06%	3.18%	0.05%	69%	2%	0.02%
0.5:1	4.46%	0.02%	3.07%	0.03%	69%	5%	0.05%
1:1	4.35%	0.05%	2.91%	0.01%	67%	10%	0.09%
Campaign 5:							

Pilot Influent	4.49%	0.15%	3.07%	0.09%	68%		
Control	4.64%	0.05%	3.23%	0.06%	69%	-5%	-0.24%
1:1	4.61%	0.06%	3.13%	0.08%	68%	-2%	-0.07%
1.3:1	4.55%	0.07%	3.08%	0.07%	68%	0%	-0.01%
1.6:1	4.54%	0.04%	3.04%	0.08%	67%	1%	0.04%
Campaign 6:							
Pilot Influent	4.65%	0.04%	3.13%	0.03%	67%		
pH 7.5	5.10%	0.12%	3.43%	0.07%	67%	-10%	-1.75%
pH 8	4.54%	0.03%	3.06%	0.04%	67%	2%	-0.72%
pH 8.5	4.49%	0.04%	3.06%	0.03%	68%	2%	0.44%
pH 9	4.94%	0.01%	3.55%	0.19%	72%	-13%	-0.90%

8.4 Cost-Benefit Analysis Calculations

The DSST at ATP is a 0.5 MGD, mixed, anaerobic tank. According to the Virginia Sewer Collection and Treatment (SCAT) regulations, "Coarse bubble diffusers should be used for mixing with compressed air. A minimum air supply of 20 scfm per 1,000 cubic feet of tank volume should be provided for adequate mixing" (9VAC25-790-590). Therefore, a SCFM aeration requirement for the current operation of mixing within the DSST can be calculated:

$$500{,}000\ Gal\ \times \frac{1\ ft^3}{7.48\ Gal} \times \frac{20\ SCFM}{1000\ ft^3} = 1336.8\ SCFM \quad (44)$$

The SCFM can then be used to calculate an aeration cost per year based on the following calculation and assumptions: with a tank height of about 15 ft, a psi of 6.5 was assumed, a blower efficiency of 80%, operation of 24 hours per day for 365 days per year, and $0.10/kWh.

$$Horsepower\ (hp) = \frac{1336.8\ SCFM \times 6.5\ psi}{550 \times 0.80} = 19.7\ hp \quad (45)$$

$$kiloWatts\ (kW) = hp \times 0.7457 = 14.7\ kW \quad (46)$$

$$kW\ hours\ (kWh) = 14.7\ kW\ \times 24\ hr \times 365 \frac{days}{year} = 129{,}001.7 \frac{kWh}{year} \quad (47)$$

$$Annual\ Cost = \frac{129{,}001.7 \frac{kWh}{year} \times \frac{\$0.10}{kWh}}{0.80} = \$16{,}125.21/year \quad (48)$$

Next, the cost for aerating the DSST based on the oxygen demand imparted by the measured COD removal can be calculated. The following assumptions were made and input values listed in Table 20 were used: any ammonia released from VS destruction was assumed to be ammonia lost to stripping, which accounted for about 13%, no nitrification was assumed to occur so ammonia in equals ammonia out, and NOx is zero, and the COD reduction is based on the averaged measured across the pilot.

Table 20: Input and assumption values used in the COD mass balance around the DSST.

DSST Volume (L)	1,892,706

HRT (days)	3
Input flow (L/day)	632,164
COD in (mg COD/L)	55,100
NH_3 in (mg N/L)	2,500
xCOD/VSS (g COD/g VSS)	1.5
N/VSS (g N/g VSS)	10%
xCOD/xVSS effluent (g COD/g VSS)	1.2
COD reduction (%)	20%
COD out (mg COD/L)	44,080
NH_3 stripped (%)	13%
NH_3 out (mg N/L)	2,500
NO_X out (mg N/L)	-

A COD and ammonia mass balance around the DSST can then be calculated.

Mass rates in:

$$COD\ in = \ 632{,}164\,\frac{L}{day} \times 55{,}100\,\frac{mgCOD}{L} = 34{,}832{,}223{,}613\,\frac{mgCOD}{day} \quad (49)$$

$$NH_4\ in = 632{,}164\,\frac{L}{day} \times 2{,}500\,\frac{mgN}{L} = 1{,}580{,}409{,}420\,\frac{mgN}{day} \quad (50)$$

NH3 released from VS destruction:

$$NH_3\ released = \left(55{,}100 - 44{,}080\,\frac{mgCOD}{L}\right) \times 632{,}164\,\frac{L}{day} \div \frac{1.5gCOD}{gVSS} \times 10\%\,\frac{gN}{gVSS} = 464{,}429{,}648\,\frac{mgN}{day} \quad (51)$$

Ammonia loss to stripping:

$$NH_3 stripped = (1{,}580{,}409{,}420 + 464{,}429{,}648) * 13\% = 262{,}001{,}112\,\frac{mgN}{day} \quad (52)$$

Mass rates out:

$$COD\ out = \ 632{,}164\,\frac{L}{day} \times 44{,}080\,\frac{mgCOD}{L} = 27{,}865{,}778{,}890\,\frac{mgCOD}{day} \quad (53)$$

$$NH_4\ out = 632{,}164\,\frac{L}{day} \times 2{,}500\,\frac{mgN}{L} = 1{,}580{,}409{,}420\,\frac{mgN}{day} \quad (54)$$

The total oxygen supply needed to the DSST is then calculated as the carbonaceous requirement, representing full equilibrium with the atmosphere and biological COD removal.

Carbonaceous:

$$O_2\,required = 34{,}832{,}223{,}613\,\frac{mgCOD}{day} - 27{,}865{,}778{,}890\,\frac{mgCOD}{day} = 6{,}966{,}444{,}723\ \frac{mgO_2}{day} \quad (55)$$

Total oxygen required:

$$O_2\,required = 6{,}966{,}444{,}723\,\frac{mgO_2}{day} = \mathbf{15{,}358}\ \frac{\boldsymbol{lbO_2}}{\boldsymbol{day}} \quad (56)$$

This total oxygen demand of 15,358 lbsO_2/day is the actual oxygen requirement (AOR) and can be used to calculate the SCFM required using the following equations. First the following equation can be used to solve for the standard oxygen requirement (SOR).

$$AOR = SOR(\alpha)\left[\frac{\left[\beta\left(\frac{P_f}{P_{MSL}}\right)C_{satT}\right]-DO\ field}{C_{sat20}}\theta^{T-20}\right] \quad (57)$$

Where: $\alpha = \frac{KL_a\ wastewater}{KL_a\ tap\ water} = 0.5$

β is the saturation factor = 0.95

P_f is the barometric pressure at the jobsite, P_{MSL} is the barometric pressure at mean sea level

$\frac{P_f}{P_{MSL}} = 1$

DO field is the DO measured in the experiment = 0 mg O_2/L

T is the operating temperature of wastewater = 30°C

C_{sat20} is the surface DO saturation concentration at 20°C and standard conditions for the aeration equipment at the design submergence = 10.2 at 15'

C_{satT} is the surface DO saturation concentration at the design temperature of 30°C and standard conditions for the aeration equipment at the design submergence = 8.2 at 15'

Solving for SOR this is 31,719 lb O_2/day, or 22 lb O_2/min if aerated for 24 hours a day. The oxygen transfer efficiency (OTE) was assumed to be 12% at 15 feet of submergence. Finally, the SCFM can be calculated below.

$$SCFM = \frac{22\frac{lbO_2}{day}\times 53.4\ scf\frac{air}{lb\ O_2}}{0.20} = 9{,}801\ SCFM \quad (58)$$

The SCFM can then be used to calculate an aeration cost per year based on the following calculation and assumptions: with a tank height of about 15 ft, a psi of 6.5 was assumed, a blower efficiency of 80%, operation of 24 hours per day for 365 days per year, and $0.10/kWh.

$$Horsepower\ (hp) = \frac{9{,}801\ SCFM \times 6.5\ psi}{550 \times 0.80} = 145\ hp$$

$$kiloWatts\ (kW) = hp \times 0.7457 = 108\ kW$$

$$kW\ hours\ (kWh) = 108\ kW\ \times 24\ hr \times 365\frac{days}{year} = 945{,}800\frac{kWh}{year}$$

$$Annual\ Cost = \frac{945{,}800\frac{kWh}{year}\times\frac{\$0.10}{kWh}}{0.80} = \$118{,}225/year$$

For chemical addition cost, Univar Solutions was used for general pricing and solution strength information. Ca(OH)2 at 35% was estimated at $0.16 per pound delivered and Mg(OH)2 at 60% was estimated at $0.35 per pound delivered. The following equations were used to convert these into price per liter.

$$\frac{\$}{g} = \frac{\$0.16}{pound}\times\frac{1\ pound}{453.592\ grams} = \frac{\$0.00035}{gram} \quad (59)$$

$$\frac{Grams\ active}{L} = 1.317\frac{kg}{L}\times\frac{1000\ g}{1\ kg}\times 0.35 = 460.95\frac{g}{L} \quad (60)$$

$$\frac{\$}{L} = \frac{\$0.00035}{g} \times 460.95 \frac{g}{L} = \frac{\$0.16}{L} \quad (61)$$

Using the same formulas for $Mg(OH)_2$ and a density of 1.45 kg/L, the price per liter was \$0.67/L for $Mg(OH)_2$. The chemical volume utilized per day in each test was then scaled up to chemical volume per year and multiplied by this cost per liter. The table below displays the projected costs per year for each test.

Table 21: Cost-benefit analysis for each treatment tested.

Test:	OP Removal %	Aeration Cost/Year	Chem Vol (L/year)	Chemical Cost/Year	Total Cost/Year
5 LPM	36%	$ 118,225.00			$ 118,225.00
DO Setpoint	51%	$ 118,225.00			$ 118,225.00
pH Setpoint 8.5	73%	$ 118,225.00			$ 118,225.00
5 LPM + $Ca(OH)_2$ 0.25:1	60%	$ 118,225.00	154,298	$ 25,088.10	$ 143,313.10
5 LPM + $Ca(OH)_2$ 0.5:1	53%	$ 118,225.00	316,978	$ 51,539.21	$ 169,764.21
5 LPM + $Ca(OH)_2$ 1:1	85%	$ 118,225.00	642,351	$ 104,443.41	$ 222,668.41
5 LPM + $Mg(OH)_2$ 0.25:1	56%	$ 118,225.00	68,158	$ 45,754.80	$ 163,979.80
5 LPM + $Mg(OH)_2$ 0.5:1	74%	$ 118,225.00	144,869	$ 97,251.40	$ 215,476.40
5 LPM + $Mg(OH)_2$ 1:1	83%	$ 118,225.00	298,266	$ 200,228.28	$ 318,453.28
DO + $Ca(OH)_2$ 0.25:1	66%	$ 118,225.00	96,530	$ 15,695.39	$ 133,920.39
DO + $Ca(OH)_2$ 0.5:1	76%	$ 118,225.00	205,884	$ 33,475.86	$ 151,700.86
DO + $Ca(OH)_2$ 1:1	83%	$ 118,225.00	424,592	$ 69,036.79	$ 187,261.79
DO + $Mg(OH)_2$ 0.25:1	70%	$ 118,225.00	72,453	$ 48,637.95	$ 166,862.95
DO + $Mg(OH)_2$ 0.5:1	83%	$ 118,225.00	152,935	$ 102,666.51	$ 220,891.51
DO + $Mg(OH)_2$ 1:1	89%	$ 118,225.00	313,973	$ 210,772.63	$ 328,997.63
DO + $Mg(OH)_2$ 1:1 repeat	93%	$ 118,225.00	143,737	$ 96,491.82	$ 214,716.82
DO + $Mg(OH)_2$ 1.3:1	97%	$ 118,225.00	188,875	$ 126,793.55	$ 245,018.55
DO + $Mg(OH)_2$ 1.6:1	96%	$ 118,225.00	234,014	$ 157,095.28	$ 275,320.28

9. Appendix B: Pilot Design and Operation Details

9.1 Pilot Construction

Pilot construction began in June of 2023 and continued until continuous pilot operation was possible into the month of November. Design modifications and maintenance continued for the remainder of the course of this project and throughout 2024. Four reactors were recovered from previous HRSD pilot work and lowered into the basement of the building next to the DSST at ATP as the new pilot location (Figure 62). Each tank was 11 feet tall with a volume of about 44 gallons. Simulating the DSST, the tanks were operated as daily batch fed continuously stirred tank reactors (CSTRs) mixed by pump recirculation with a 3-day SRT. During pilot construction and the preliminary operation phase, the mixing pump choice was critical due to difficult matrix of TH-AD digestate. First, a magnetically-driven pump was trialed, but lead to many clogs due to the bearing in front of the impeller and was quickly phased out. Next, a shaft-driven centrifugal pump was trialed and was much more durable due to less opportunity for clogging from the lack of bearing in front of the impeller, meaning it could handle more fibrous and gritty material. These Goulds pumps lasted for about 4 months of preliminary pilot operation, but ultimately were still not equipped to handle the pilot influent, and lead to clogging and pump overheating events that required routine pump unclogging maintenance almost weekly. In October 2023, a basket screen was inserted upstream of the feed line to screen out fibrous material and additional grit to help protect pilot equipment and promote longevity of these mixing pumps. The basket screen size was 2 mm and had to be manually cleaned daily, and was switched to a 6 mm screen over the weekends which could be cleaned after two days. In February of 2024, the final mixing pump style was selected. The mixing pumps are commercial duty self-priming (to 20 ft. lift) centrifugal pumps by AMT. The pumps have a semi-open clog resistant impeller with an automatic rest thermal protection and are direct coupled to a 3450 RPM motor. At 10 ft of head, the pumps have a flow rate of 55 gal/min. Therefore, at this pilot tank volume the mixing pumps provide a tank turnover rate of less than one minute (Equation 62).

$$Tank\ turnover\ rate\text{:}\ \frac{44\ gal}{55\ gal/min} = 0.8\ mins \tag{62}$$

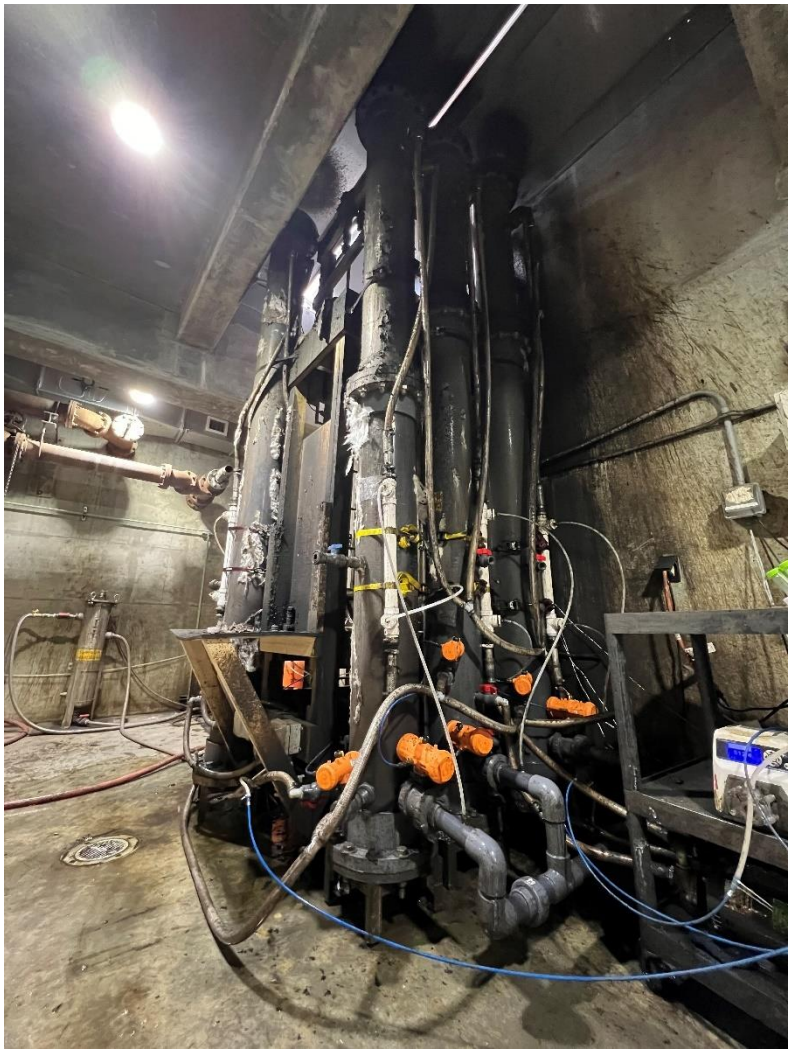

Figure 62: Pilot scale set up featuring the control tank 1, and tanks 2, 3, and 4 from left to right.

Pilot waste and feed of digestate to maintain this 3-day SRT was another design hurdle of this project. Continuous waste and feed was the first trial in August 2023, but due to the flowrate required for this tank volume and target SRT being as low as 38.2 mL/min led to clogging issues (Equation 63).

$$\frac{165\ L}{3\ days} * \frac{1000\ mL}{1\ L} * \frac{1\ day}{1440\ mins} = 38.2\ mL/min \text{ flowrate} \quad (63)$$

Feed lines in 3/8th-inch tubing flowed from the DSST to the feed pumps with T-fittings and into each of the four reactors. The MasterFlex pumps were operated at their lowest speed (level 1) and on continuous on timers for a few seconds and off cycles for minutes to hit the overall flowrate required. Each tank had an overflow drain line that would continuously waste out the volume of digestate as it fed over the tank volume to keep the SRT at 3 days. Due to the slow flows and off periods, this set up under continuous operation would clog after a few hours in both the feed lines

and the overflow waste line (Figure 63). The second iteration was then tried during the months of September and October of 2023. The feed set up was fairly similar in that it was still continuous flow, but in attempts to control the clogging issues, the feed lines were upgraded to 1/2-inch tubing, the T-fittings were traded out for Y-fitting to facilitate smoother flows, and the overflow waste lines fittings were changed from 90° bend fittings to 45° bend fittings for the same reason (Figure 64). However, these clogging events still occurred if the pilot was operated for more than a day.

Finally, later in October of 2023, the final iteration of pilot waste and feed as a daily batch process was settled on. The pilot feed line that pulls directly off a DSST valve in the basement was upgraded to 1-inch braided tubing, flowed through the basket screen, and connected to each tank. As the pilot tanks were also struggling with grit build up at the bases of each tank, 2-inch PVC waste lines were added to the base of each tank a couple of inches above the diffusers. On each of the waste and feed lines, air actuated ball valves powered by a compressed air tank (Hulk by EMAX) opened and closed automatically on a daily relay timer. Once a day, the waste line valve opened to forcefully flush out grit and waste a third of the tank volume then closed. Next, the feed line opened on another timer to fill the tank with a fresh third of digestate until it spilled out of the overflow waste line, and then the next tank in line proceeded in the waste and feed process (Figure 65).

Figure 63: Pilot feed flow setups - the first continuous feed iteration with 3/8th-inch tubing and T-fittings.

Figure 64: Pilot feed flow setups - the second continuous feed iteration with ½-inch tubing and Y-fittings.

Figure 65: Pilot feed flow setups - the final waste and feed iteration with 2-inch and 1-inch, respectively, batched daily powered by air actuated ball valves.

The SRT was checked weekly with a storage bin that could be connected to the waste line to collect and measure the volume wasted (Figure 66). The volume wasted should be a third of each tank, or 55 L per day. This volume is indicated by the orange tape mark on the inside of the waste collection bin, for ease of measuring weekly. Each weekday, the waste and feed process was monitored to ensure the tanks were filled until overflow to gain back the same volume lost. If a

tank did not fill to the overflow line, the tank was manually filled until overflow and the waste and the feed times were adjusted weekly if the volumes were incorrect to maintain the SRT.

Figure 66: Waste volume collection bin for SRT measurement.

The pilot tanks were aerated with fine bubble diffuser membranes at the base of each tank which could be operated at constant or intermittent air flow rates, or via Dissolved Oxygen (DO) or pH set points. The diffusers were the FlexAir™ 7-inch disc diffusers with standard membranes. The oxygen transfer efficiency curve for the diffusers used in the pilot is shown below in Figure 67.

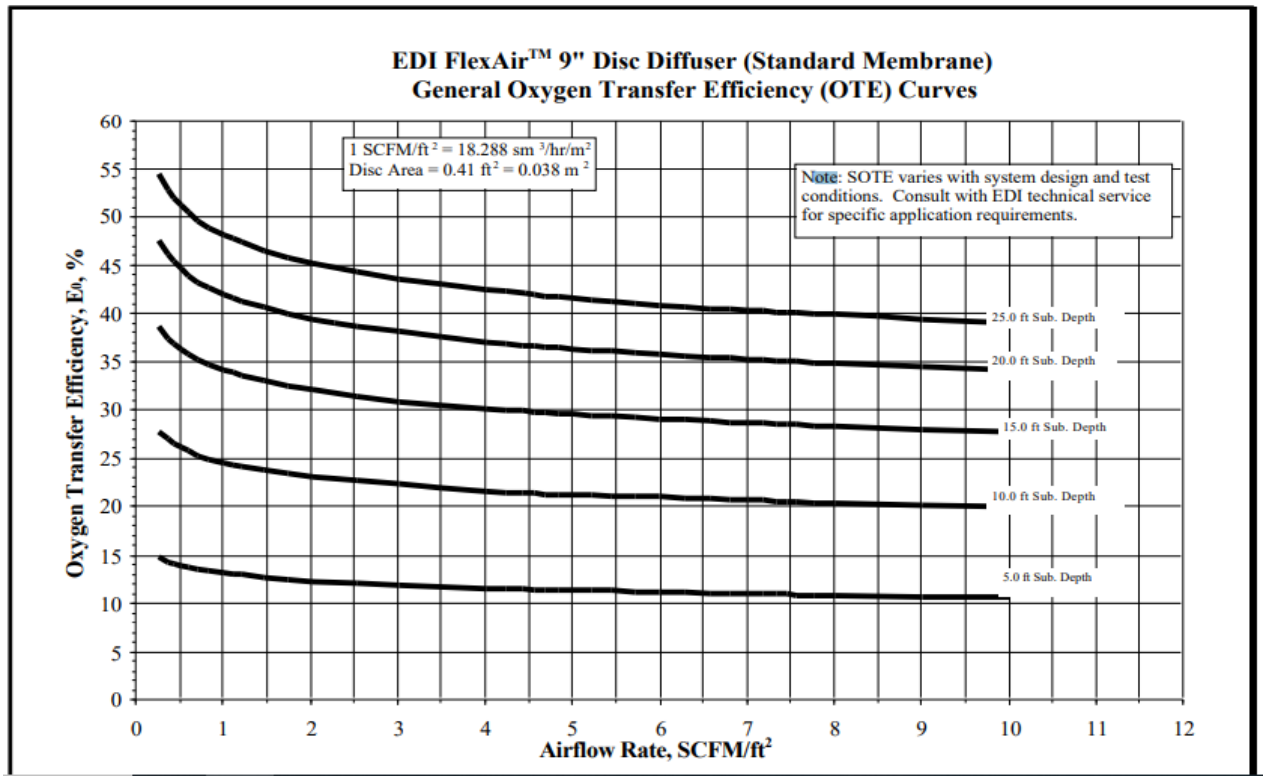

Figure 67: General oxygen transfer efficiency curve for the EDI FlexAir 9" disc diffusers similar to the 7" diffusers used in the pilot. https://www.equind.com.mx/pdfs/edi/Difusor_EDI.pdf

The same compressed air tank used for the waste and feed valves was used to supply air to each diffuser. The air flow rate was controlled by Mass Flow Controllers (MFCs) in the electrical set up and an automated proportional-integrated-derivative (PID) control determined by online pH and DO probes. Each tank contains probes to record online measurements of temperature, DO, and pH (InsiteIG). The online data of these were also recorded onto a flash drive that is available for data recording twice a week.

Figure 68 below shows the pilot operating touch screen home page. The top of the screen displays the 24-hour countdown timer to the next waste and feed cycle (HH:MM:SS) and the air pressure. The air pressure was always maintained above 55 psi to ensure waste and feed as well as aeration capacity. Then, displayed is each of the four available reactors and current airflow output received (LPM) as well as the online DO (mg/L) and pH measurements. At the bottom of the screen, the waste and feed pump timing could be edited to correct the SRT measurement, the reactors could be manually filled and emptied, the 24-hour timer could be turned off and back on, and the chemical feed tank timers could be edited.

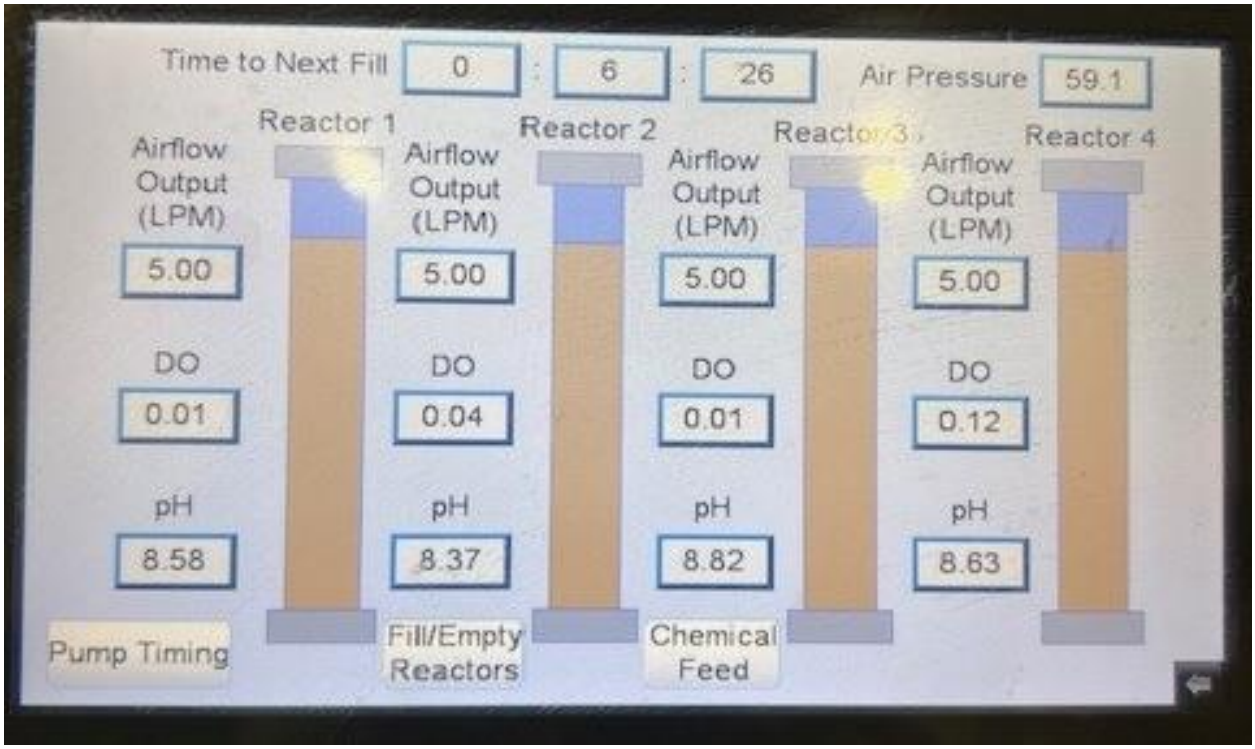

Figure 68: Pilot operating touch screen home page.

From the home page, each tank could be selected independently to choose how it is operated. Figure 69 displays the Tank 1 operation page as an example. Each tank could be aerated in "Time Control Mode" to allow for constant or intermittent aeration, or in "DO Control Mode" to aerate on a DO setpoint.

In the Figure 69 example, tank 1 was operated in Time Control Mode at constant aeration of 5 LPM, indicated by the red button in the right position. The seconds on and off selected could be manipulated on a 1000 second cycle to determine if it was constantly aerating at this Set Value (SV) or intermittently. The output percentage determined how much airflow the tank received based on the maximum value the MFCs were rated for, which was 20 LPM. Therefore, for this test, the output percentage was set to 25% of 20 LPM, so the tank received 5 LPM constantly. To the left of the pictured tank, the SV was 5 LPM, the Point Value (PV) or actual airflow received from the MFC was 5.2 LPM, and the pH and DO at that aeration setting was recorded.

If DO control mode was selected, the DO Setpoint could be set to the desired concentration of DO in the tank in mg/L of oxygen and the tanks would aerate at the airflow value demanded to reach that setpoint. This was controlled by a DO PID based on the online DO probe measurement in each tank and a control loop of just the proportional gain correction term and the integral time correction term, which could be tuned in the top right corner of the screen for each reactor. The "PID Max Airflow %" term on this screen was for the entirety of these experiments set to a maximum of 75%. This means that in order to hit the DO setpoint, the airflow to the tank could aerate only up to 75% of the 20 LPM capacity of the MFCs, which is 15 LPM. This was enacted due to tank volume loss in over foaming events if the full 20 LPM aeration rate was allowed to hit

DO setpoints. In another act to control foaming issues in the tanks, the “Airflow Control Before DO PID Mode” selection was set in place. This was utilized in all pilot experiments on a DO setpoint by switching that button to the right position on red, and by switching the lower right button to the left position on green to “Time Mode”. As indicated by the “Air Flow Setpoints”, for two hours after each waste and feed cycle in this mode, the aeration set point would decrease down to 25% of the “Air Flow % SP”. This required the tanks to operate at 5 LPM for two hours following receiving the fresh third of new digestate to promote a stable transition period prior to allowing the tanks to resume DO Control Mode. Without this setting, the DO concentrations in each tank would drop below the DO setpoint due to the feed volume, and the airflow would immediately increase to the maximum of 15 LPM in order to achieve setpoint again. This would lead to bubbling over or foam events, thus this setting was put in place to acclimate the tanks throughout a DO controlled test.

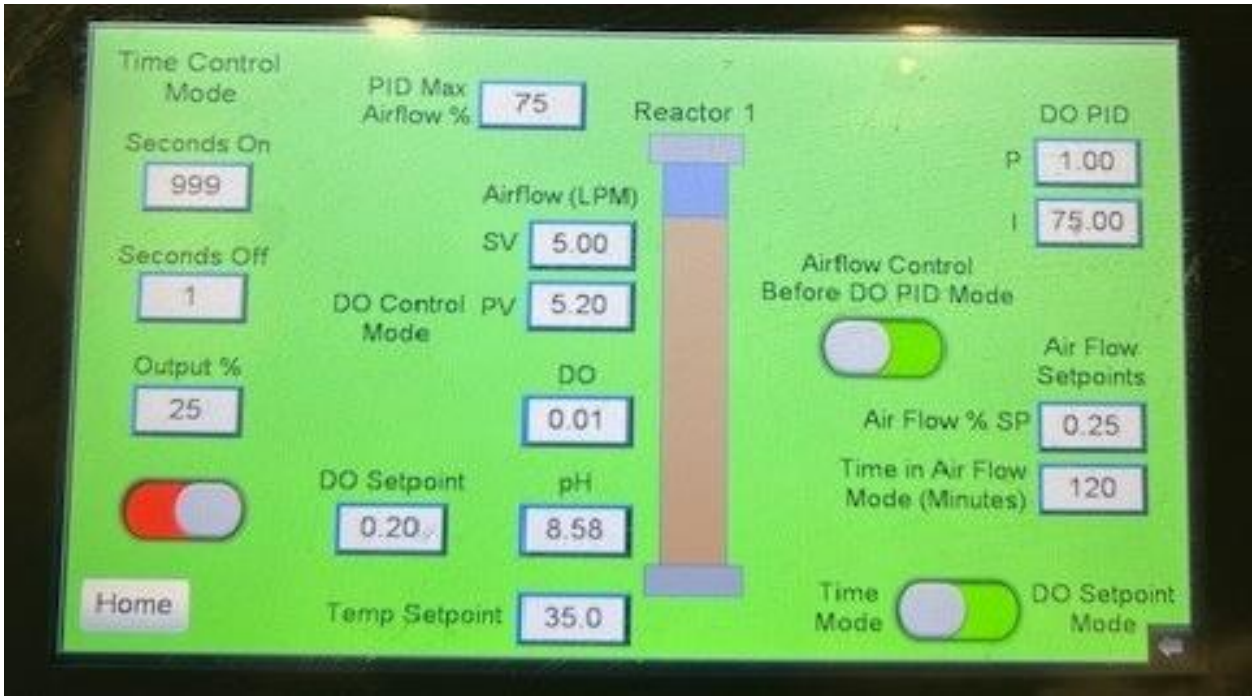

Figure 69: Pilot operating touch screen Reactor 1 settings.

The pilot tanks were temperature-controlled year-round with insulation padding added in the winter and heat exchangers added in the summer (Figure 70). In the winter, fiber glass insulation panels were wrapped around each of the tanks to help maintain heat, and predominantly maintained a temperature range between 25 and 35°C in the months of December, January, and February. In the summer months, temperature was controlled with heat exchangers that circulated cooler NPW in a PVC tube surrounding about two feet each of the mixing lines at a setpoint of 35ºC to best match the temperature in the pilot to the temperature of digestate within the DSST. This temperature setpoint could be manipulated for each reactor, as shown on the Reactor

1 settings example screen in Figure 69. This heat exchanger helped the tanks maintain a temperature range between 30-39°C in the months of June, July, and August.

Figure 70: Pilot temperature control via insulation added for the winter months and NPW heat exchangers for the summer months.